UNIVERSITY OF SOUTHAMPTON

FACULTY OF ENGINEERING AND THE ENVIRONMENT

Energy Technologies Research Group

Development and Operation of an Electrically Rechargeable Zinc-Air Flow Battery

by

Scott Francis Gorman

Thesis for the degree of Doctor of Philosophy

February 2017

UNIVERSITY OF SOUTHAMPTON

ABSTRACT

FACULTY OF ENGINEERING AND THE ENVIRONMENT

Electrochemical Engineering

Thesis for the degree of Doctor of Philosophy

Development and Operation of an Electrically Rechargeable Zinc-Air Flow Battery

Scott Francis Gorman

Due to the limitations of present solutions, there is a demand for cost effective chemical energy storage for grid-scale applications. One promising example in development is the zinc-air flow battery, which could prove to be a key technology in ensuring energy security and the integration of renewable generation. Although the primary zinc-air chemistry is well studied and commercially available to progress the technology into a large-scale electrically rechargeable system requires significant development. Adapting the chemistry for suitability in large secondary systems has seen comparatively little attention and there are very few practical scale systems in operation.

This thesis describes novel procedures for the fabrication of a gas diffusion electrodes suitable for use as a bifunctional oxygen electrode in alkaline secondary batteries.

$NiCo_2O_4$ spinel catalyst was utilised as an alternative to precious metals in both carbon paper based and novel metal based gas diffusion electrodes. Air-electrodes were rapidly screened in a custom electrochemical lab scale half-cell. These electrodes were incorporated into a proof of concept zinc-air flow battery which could act as a preliminary design for future scale up. Electrodes up to 100 cm^2 have be cycled for >24 hours operation at ≤50 mA cm^{-2}. Balancing optimal operating conditions is presently a trade-off between many factors including durability/cycle life, electrochemical performance and electrode fabrication methods/cost. > 90% coulombic efficiently, > 60% voltage efficiency have been demonstrated with catalyst loadings of < 5 mg cm^{-2}.

Table of contents

List of tables

List of figures

DECLARATION OF AUTHORSHIP

I, Scott Francis Gorman declare that this thesis and the work presented in it are my own and has been generated by me as the result of my own original research.

Development and Operation of an Electrically Rechargeable Zinc-Air Flow Battery

I confirm that:

1. This work was done wholly or mainly while in candidature for a research degree at this University;
2. Where any part of this thesis has previously been submitted for a degree or any other qualification at this University or any other institution, this has been clearly stated;
3. Where I have consulted the published work of others, this is always clearly attributed;
4. Where I have quoted from the work of others, the source is always given. With the exception of such quotations, this thesis is entirely my own work;
5. I have acknowledged all main sources of help;
6. Where the thesis is based on work done by myself jointly with others, I have made clear exactly what was done by others and what I have contributed myself;
7. None of this work has been published before submission:

Signed:………………………………………………………………………………………………

Date:…………………………………………………………………………………………………

Acknowledgements

Financial support by the European Commission (*Theme 2010.7.3.1:* **Energy storage systems for power distribution networks,** Grant Agreement no. 256759) is gratefully acknowledged by the POWAIR project. More details are available at *www.powair.eu/*

Project partners / collaborators

- C-Tech Innovation Ltd (UK)
- CEST competence center (Austria)
- FuMA-Tech GmbH (Germany)
- Green Power Tech. Now known as GPTech (Spain)
- University of Seville (Spain)
- DNV KEMA. Now part of DNV·GL (Netherlands)
- Graz University of Technology (Germany)
- E.ON Engineering (UK)

Firstly, I would like to thank my main supervisor Dr Richard Wills, for giving me the opportunity to study for this PhD, his support, advice and putting up with me. I would also like to thank Andrea E. Russell, Frank C. Walsh and Derek Pletcher for their wisdom and guidance. Further I would like to thank everyone who I have worked with in Electrochemistry at the University of Southampton for enriching my time there. I am particularly grateful to Stephen Price, Stephen Thompson and Xiahong Li who went through the highs and lows of POWAIR shoulder to shoulder with me and made my experience positive.

I would not be writing this without Jan, Gilly, Linda and Miss Quinney and to each of them I am forever grateful. To my friends and family for their love and support, and finally to Sarah who has ridden this roller-coaster with me all the way. Thank you.

Definitions and Abbreviations

List of symbols

Symbol	Meaning	Units
Q	Charge	C
I	Current	A
j	Current density	A m^{-2}
F	Faraday constant	96485 C mol^{-1}
ΔG	Gibbs free energy change	J mol^{-1}
k_m	Mass transfer coefficient	m s^{-1}
n	Number of electrons involved in electrode reaction	dimensionless
E	Potential	V
R	Resistance	Ω
T	Temperature	K
W	Work	J

List of acronyms

AEM	Anion exchange membrane
AFC	Alkaline fuel cell
CAES	Compressed air energy storage
CE	Counter electrode
CV	Cyclic voltametry
EDX	Energy-dispersive X-ray spectroscopy
FESS	Flywheel energy storage systems
GDE	Gas diffusion electrode
GDL	Gas diffusion layer
ICRFB	Iron-chromium redox flow battery
IPA	Isopropyl alcohol/isopropanol/propan-2-ol
LSV	Linear sweep voltammetry
MEA	Membrane electrode assembly
OCP	Open circuit potential
OER	Oxygen evolution reaction
ORR	Oxygen reduction reaction
PHES	Pumped hydroelectric energy storage
PTFE	Polytetrafluoroethylene (brand name Teflon)
RE	Reference electrode
RFB	Redox flow battery
SEM	Scanning electron microscope
SCE	Saturated calomel electrode
SHE	Standard hydrogen electrode
SoC	State of charge
UHP	Ultra-high purity
VFB	All-vanadium redox flow battery
WE	Working electrode

Chapter 1: Introduction

1.1 Large-scale energy storage

A growing population and increased industrialisation has resulted in an escalating demand for and mounting dependency on electrical energy on a global scale.[1] Socioeconomic pressures, the development of new technologies and the effects of global warming are forcing a gradual but inevitable transition towards more sustainable electricity generation.[2, 3] Fossil fuel technologies are beginning to see competition from newer, greener alternatives however, to assimilate these modern advances into power distribution networks will require new energy storage and conversion technologies. Both efficient network management and the integration of renewable power generation, may prove crucial in ensuring that supply can match rapidly shifting energy consumption. The ability to store surplus energy when production exceeds consumption, then redistribute it at times of high demand would facilitate effective 'load levelling' within a grid. By de-coupling energy generation from energy supply, it is possible to produce power when it is economically or environmentally advantageous. Energy storage on this scale provides the ability to respond rapidly to local fluctuations in demand and cover periods of down time in production. This shift could ultimately negate the need for fossil fuel powered 'peaking plants', which presently represent some of the most expensive and inefficient energy generation implemented. Large-scale energy storage (also referred to as grid energy storage) is one solution that could form an integral part of this more flexible and stable electrical power network.

Large-scale energy storage refers to methods of storing significant quantities of electrical energy (typically kW h to GW h). Pre-existing technologies for large-scale energy storage have seen limited application to date due to a variety of operational constraints.[1, 4] Some of these technologies including compressed air energy storage (CAES), pumped hydroelectric energy storage (PHES), flywheel energy storage systems (FESS) and a variety of battery systems are evaluated in Table 1.1 in terms of performance as a function of cost and lifespan.

Table 1.1 Comparison of the performance and financial attributes of present large-scale energy storage technologies. (References[5, 6, 7])

Energy storage technology	Power rating	Discharge duration	Efficiency [a]	Capital cost [b]	Cycle cost output	Cycle life at 80% depth of discharge
	kW-GW	h	%	\$ kW h^{-1}	\$ kW h^{-1}	Cycles
Flow batteries	100s kW to MW	1-20	75-80	180–250	0.06–0.2	5,000–14,000[c]
Lead-acid batteries	kW to 10s MW	0.1–4	70–76	350–1,500	0.40–1	200–1,500
Lithium-ion batteries	kW to 100s MW	0.1–1	> 90	850–5,000	0.3–1	5,000–7,000
Sodium sulphur batteries	0.1–100s MW	1–10	85–90	300–950	0.09–0.5	210–4500
CAES	10s MW to GW	0.1–15	60–79	50–110	0.03–0.06 (with gas)	9,000–30,000
PHES	10s MW to GW	> 8	70–85	80–200	0.001–0.02	20,000–50,000
FESS	1-100 kW	0.1-1	> 90	300-5,000	0.05-0.4	> 20,000
Super-capacitors	5-100 kW	0.02–1	> 95	82,000	0.03–0.4	10,000–100,000
Thermal energy storage	MW to 100s MW	1–45	60	\$500/kW	0.035–0.16	4000– 10,000
Superconducting magnet energy storage	10s MW	0.25	90–95	10,000	0.4–1.70	1000– 10,000

[a] Without power electronics, [b] Values from 2011, [c] Up to 270,000 cycles reported for All-Vanadium Redox Battery by Sumitomo Electric Industries, Japan

Many of the most commercially viable large-scale energy storage solutions employ mechanical solutions to the problem of energy storage. Water and compressed gas storage systems being prime examples. They can have low configuration and running costs, as well as very impressive cycle lives, however are bound heavily by nearby geographical features or infrastructure, restricting the number of suitable installation sites that are economically practical. These systems tend to have very low energy density and so to make the system viable for large-scale energy storage requires either a vast area of land or specific local geography.[8]

The other main approach is to utilise chemical energy storage. Conventional battery technologies however, are currently undesirable for use in high power > MW applications, due to factors including high cost per kilowatt hour, toxicity, low energy density and system complexity.[1] Despite this, a number of installations are currently in operation or under construction globally. One example of a large-scale battery technology being used for grid-scale energy storage, is that of lead-acid chemistries, which are currently used to provide a ‘spinning reserve’ for some networks.[9, 10] These installations provide a buffer of several minutes in the event of transmission, or production failures; however, they are unsuitable for applications such as load levelling. Lithium-ion batteries have also seen investment due to their high energy-densities and efficiencies (typically > 90%). A123 SYSTEMS is one example of a lithium-ion battery manufacturer that produces grid-scale ancillary storage systems with capacity in the order of MW h.[11] Presently cost to benefit performance is debatable for such large scale systems and so lithium-ion cells have primarily be used in small consumer electronic devices where size and mass constraints are paramount. The individual Li-ion cells themselves can only be scaled so far before reaching engineering limitations. Typically, Li-ion batteries for applications such as electric vehicles are comprised of a package containing arrays of much smaller cells. To achieve kW to MW powers requires 1000s-100,000s of individual cells. The Tesla model S for example one of the world's bestselling plug in electric vehicles has a battery pack made up of thousands of 18650 form factor Li-ion cells the kind typically found in laptop computers. Controlling this number of cells requires more sophisticated power electronics systems adding complexity and modes of failure. Additionally, the fact that each cell requires individual packaging and cabling reduces system energy density.

The safety and toxicity of present battery chemistries is a significant hurdle to overcome before large-scale battery storage becomes commonplace. Compounds containing metals such as lead, sodium and lithium commonly used in battery construction, can be highly toxic, damaging to the environment and difficult to handle and dispose of safely. Systems containing lithium are also liable to ignite or explode due to its pyrophoric nature and Li-ion's susceptibility to thermal run away. Although these issues are surmountable, concerns related to safety and waste disposal only become heightened when the scale is increased by orders of magnitude. The fact that despite such concerns large scale Li-ion systems are being installed reflects the current market demand for grid-scale energy storage. With legislation like that in the UK with a commitment to reduce carbon emissions 80% by 2050 and international support for the 'Paris agreement' on climate change this demand is only likely to increase.[12]

The ideal candidate for a large-scale energy storage technology would exhibit broad operating conditions, a relatively low start-up and running cost and high-energy efficiency. To ensure successful commercialisation attributes such as low system complexity, a scaleable, modular design and minimal environmental and safety considerations are highly desirable. However, a more pragmatic scenario for the future sustainable energy economy is based on a diverse range of energy-conversion technologies. Many finding a niche distinguished by factors including power output, cost, durability and availability of the energy source.[13] It is therefore unlikely that a single storage technology will dominate the market. An emerging technology with advantages over some of its rivals, which could play a prominent role in the diverse energy storage landscape, is the flow battery.

1.2 Flow batteries

Flow batteries are chemical energy storage systems, which contain one or more of the active materials dissolved in a mobile electrolyte. The electrolyte(s) are pumped through a single or stack of electrochemical cells where the electrochemistry occurs. The flow battery design allows them to be highly scalable, as the system is not limited by the amount of active material that can be packed in the cell stack. Flow batteries are therefore attractive for large-scale energy storage as they are comparatively simple and economical to scale-up compared to other battery architectures. Components such as pumps and flow controls do not scale linearly with system size and so can be expanded with minimal additional expense, complexity and energy requirements. Consequently, once the system reaches sufficient size inefficiencies associated with pumping electrolyte contribute minimally to the overall system efficiency. The electrochemical stacks themselves can also be engineered to be modular with repeating units so power can be increased with minimal design modification. This flexibility in scale and design means that such systems can be deployed almost anywhere and matched to the specific use case.[1] It has been shown that operation in the 10 kW to 10 MW range has cost, mobility, flexibility, depth of discharge, rapid response, and safety advantages over competing battery systems such as lithium-ion and sodium-sulphur.

Modern flow batteries were invented by Thaller in the 1970s at the National Aeronautics and Space Administration (NASA).[14] These early systems however suffered from cross-contamination of the electrolytes resulting in reduced capacity over time. Since then, several other redox flow battery (RFB) chemistries have been reported or developed.[14, 15, 16, 17, 18] Among the types of flow batteries, the only systems that have come close to commercialization are the all-vanadium, iron-chromium, sodium-polysulphide and zinc-bromine systems.[19] These systems have been demonstrated at a few hundred kW power levels and in some cases multi-MW power levels but have yet to achieve wide commercial success.[14]

Using the example of the classical redox flow battery, a simple schematic is depicted in Figure 1.1. In this example, two electrolytes are stored in separate electrolyte tanks. The two electro-active materials are introduced to separate halves (positive and negative electrode chambers) of the cell separated by a membrane.

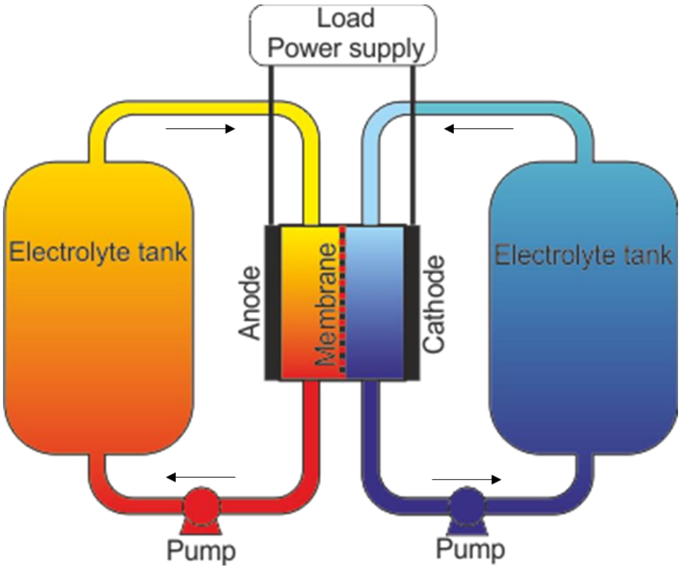

Figure 1.1 Schematic of a conventional redox flow battery system such as the all vanadium redox flow battery. The electrolytes are circulated from their respective tanks through compartments of the cell separated by an ion-puropos membrane. A redox process takes place at each electrode producing an electrical current.

Flow batteries can be categorised as being one of three types:

(a) the classical redox flow battery, e.g. the all-vanadium redox flow battery which separates the two half-cells by a membrane and does not involve a phase change at either electrode surface.[20] Energy is stored in the electrolytes.

(b) a hybrid system where by a redox couple is present at one electrode and a reaction involving a phase change at the other, e.g. zinc-cerium. Energy is stored in both the electrolyte and the electrode.

(c) metal-metal oxide flow battery where by a phase change occurs at both electrodes and the cell is undivided, e.g. soluble lead. Energy is stored in the active material within the electrodes.

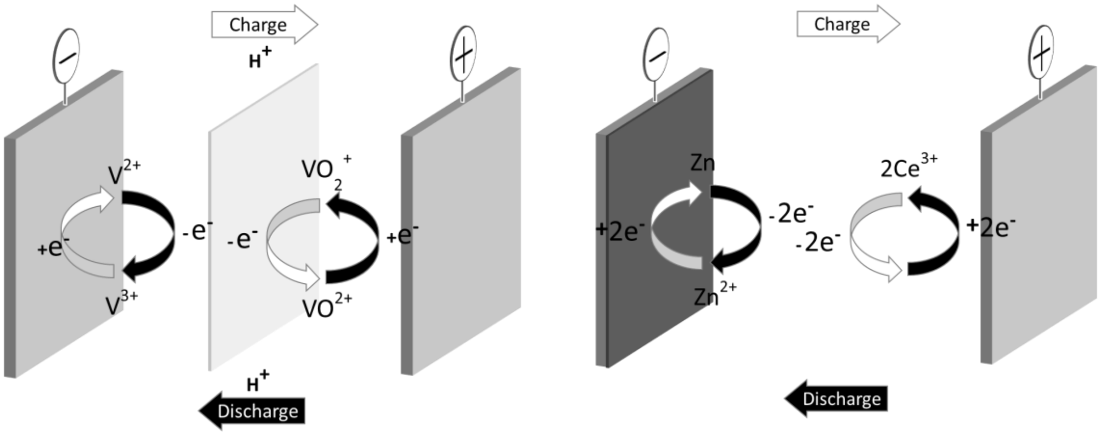

Type A **Type B**

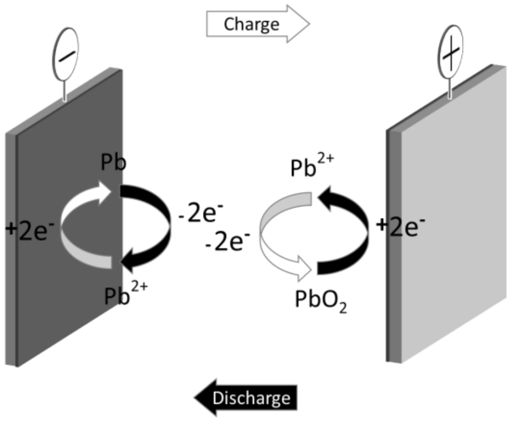

Type C

Figure 1.2 Diagrams showing common types of redox flow battery differentiated by their methods of energy storage. Type A) all-vanadium redox flow battery, Type B) hybrid zinc-cerium flow battery, Type C) lead-lead dioxide flow battery.

Circulation of the electrolytes ensures that there is greatly improved mass transport of the reactants to the electrode surfaces compared to a static electrolyte. Other positive attributes include; comparatively low start-up and running costs, fast response times, and long-life cycles. They display good energy efficiencies (typically > 60%) and higher energy densities than many other large-scale energy storage technologies.[11, 21]

Flow battery design allows for the decoupling of power from energy. Additional capacity can be introduced by increasing the volume of the energy-carrying electrolyte. The electrolyte tanks, which can be placed a small distance from the cells can be made to fit whatever space is available. Ultimately capacity is limited by the amount of zinc which can be deposited in the interelectrode gap prior to the formation of an internal short circuit or blockage of electrolyte flow. Alternatively, the power can be increased by adding more/larger cells to the stack. Flow batteries strike a good compromise between performance and cost compared to many of the alternatives outlined in Table 1.1.

Although requiring additional energy to operate a pump to facilitate electrolyte circulation, the flow of material leads to several operational advantages. A circulating liquid inside each cell helps to remove excess heat from the stack produced as a reaction by-product. Thermal management of the stack is therefore minimised and can be controlled externally at the electrolyte tank.[22] There may also be the potential to recover some of this generated heat and use it constructively either to regulate the temperature of other system components or to generate useful energy helping to mitigate system losses.[22] The considerable increase in electrolyte capacity and the constant mixing of the solution helps to mitigate dramatic fluctuations in moisture content in the cell. This is of particular importance when a membrane is incorporated, as they are often highly moisture sensitive.[23] A further advantage to a flowing electrolyte is that accumulated impurities can easily be filtered out of the electrolyte during cell operation.

Impurities can include carbonates, catalyst particles, and corrosion products among others. If necessary, the entire electrolyte can easily be exchanged after a set period of operation with minimal disruption to the stack.[22]

The metal-air flow battery a (Type B) hybrid flow battery has a greater theoretical energy density than most other flow batteries as it can utilise ambient air or a compressed gas system in place of a secondary electrolyte reservoir. By using the principles of established flow batteries combined with the energy density of the metal-air chemistry there is the possibility of surpassing the commercial appeal and scalability of vanadium systems.

1.3 Metal-air flow batteries

Metal-air batteries are one of the proposed ‘post lithium-ion’ technologies that have recently received a revival in popularity.[3] Metal-air batteries are an attractive energy storage solution because of their higher capacity-to-volume (and mass) ratios than conventional batteries. Metal-air batteries are a specific example of hybrid flow batteries (Type B) that utilise oxygen from the air as one of the reactants negating the need for a second electrolyte tank.[24] Not having to package one of the reactants inside the cell dramatically increases the energy density of the system. During cell discharge, oxygen is reduced at the air (positive) electrode, while material at the metal (negative) electrode, e.g. iron, aluminium, lithium or zinc, is oxidized and dissolves into the electrolyte.[25]

Metal-air batteries can be divided into three main types: primary (non-rechargeable), secondary (rechargeable) and mechanically rechargeable or refuellable cells.[26, 27] This third type operates like a fuel cell with the ability to physically replace the oxidised metal material.[28] It is possible to regenerate the spent fuel so that it can be reused however this need to regularly refuel limits their applications. Examples of mechanically rechargeable systems have seen minor applications and demonstrations for public/agricultural transport.[1, 29, 30, 31]

The first metal-air type battery was developed by Leclanché, in 1868. It utilised a manganese dioxide/carbon positive electrode, a combination that is still prevalent in many metal-air electrodes discussed in recently published literature.[9, 32, 33, 34] The design of an air-electrode and rudimentary primary battery were later commercialised in the 1930s as discussed in a patent by Heise and Schudmacher.[35] Large primary zinc-air cells such as the Thomas A. Edison Industries ‘*Carbonaire*’ type have been used for long duration, low-power applications such as railway signalling, remote communication sites, and navigation buoys.[4] The principles were further developed in parallel to contemporary fuel cell research into more recognisable metal-air batteries as described by Bacon in 1969.[36] Enabling the production of small button and prismatic primary cells with widespread application in hearing aids, pagers, and medical devices to this day, due to their long lifetime and low toxicity.[27, 28, 37, 38] Although the idea of a metal-air battery is not entirely new the prospect of an electrically rechargeable system with the prospective to reach kW scale is still only in development. The progress of rechargeable zinc-air batteries has been primarily limited in the past due to problems of zinc dendrite formation, cell dehydration, and degradation of the air-electrode.

The flowing electrolyte in a metal-air flow battery system has additional benefits over simply increasing mass transport. For example, any gas, which passes through the gas diffusion layer GDE or is formed on the electrolyte facing surface of the electrode can be swept away by the electrolyte flow ensuring that the electrode surface is constantly wetted.[22] The flow of electrolyte also reduces the growth of dendritic metal deposits which have the propensity to cause internal short circuits. Similarly, unwanted by-products on the gas face of the air-electrode such as water, can be removed by the flow of gas. The flow also helps to perturb the formation of carbonate crystals within the electrode produced from the component of CO_2 in the air. Combining metal-air chemistry with the flow battery design could solve some of the key issues preventing the scale-up and efficient rechargeability of metal-air systems.

1.4 The zinc-air flow battery

The zinc-air flow battery is an example of an aqueous alkaline metal-air battery. Unlike conventional batteries, which pack all the necessary reactants inside the cell, zinc-air cells get one of their reactants (oxygen) from the air. In a typical battery, this reactant would have to be present in a liquid electrolyte. The gas is instead introduced via an air-permeable layer (gas-diffusion layer).[39, 40] Extracting a reactant from the air leads to cost, safety and space saving benefits as it removes the need for a second electrolyte tank therefore reducing the size and mass of the battery.

The zinc-air battery chemistry exhibits inherent advantages including comparatively lower cost and toxicity over other metal-air systems.[5, 27, 38, 41] They also produce a flat discharge voltage. Zinc-air cells are environmentally benign containing; no toxic compounds and are neither highly reactive nor flammable. The only reaction product is recyclable zinc oxide which can be hazardous to aquatic life if released but poses almost no hazard to humans. The only component of concern is the corrosive alkaline electrolyte. However, at present there is no viable alternative and it is no worse than the electrolytes found in common consumer batteries currently on the market such as zinc-carbon, lead acid or alkaline cells.

In a primary-cell during discharge, air reaches the cathode surface, where an active electro-catalyst promotes the reduction of oxygen. The gas is introduced via an air-permeable layer (Gas-diffusion layer). Metallic zinc saturated with an alkaline electrolyte, in the form of a paste, is oxidised on the opposite side of the cell (Equation 1.4). During cell operation, a mass of zinc particles forms at the anode. Oxygen from the air reacts at the oxygen (positive) electrode and forms hydroxyl ions which migrate into the zinc paste and form zincate ($Zn(OH)_4^{2}$), releasing electrons (Equation 1.2). The zincate brakes down into zinc oxide and water (Equation 1.3). The water and hydroxyls from the anode are recycled at the oxygen (positive) electrode, so water is not consumed by the process. The theoretical specific energy of the zinc-air battery is 1350 W h kg^{-1}, but its practical specific energy is only about 200 W h kg^{-1}.[42]

- Electrode reactions taking place during discharge/acting as a fuel cell

Cathode:

$$O_2 + 2H_2O + 4e^- \rightarrow 4OH^- \ (E^0 = +0.4\ V) \qquad 1.1$$

Anode:

$$Zn + 4OH^- \rightarrow Zn(OH)_4{}^{2-} + 2e^- (E^0 = -0.625\ V) \qquad 1.2$$

$$Zn(OH)_4{}^{2-}{}_{(aq)} \rightarrow ZnO + H_2O + 2OH^- \qquad 1.3$$

- Overall reaction

$$2\ Zn\ + O_2 \rightarrow 2\ ZnO\ (E_{cell} = 1.65\ V) \qquad 1.4$$

Where E^0 represents the standard electrode potential for each reaction with respect to the standard hydrogen electrode (SHE).

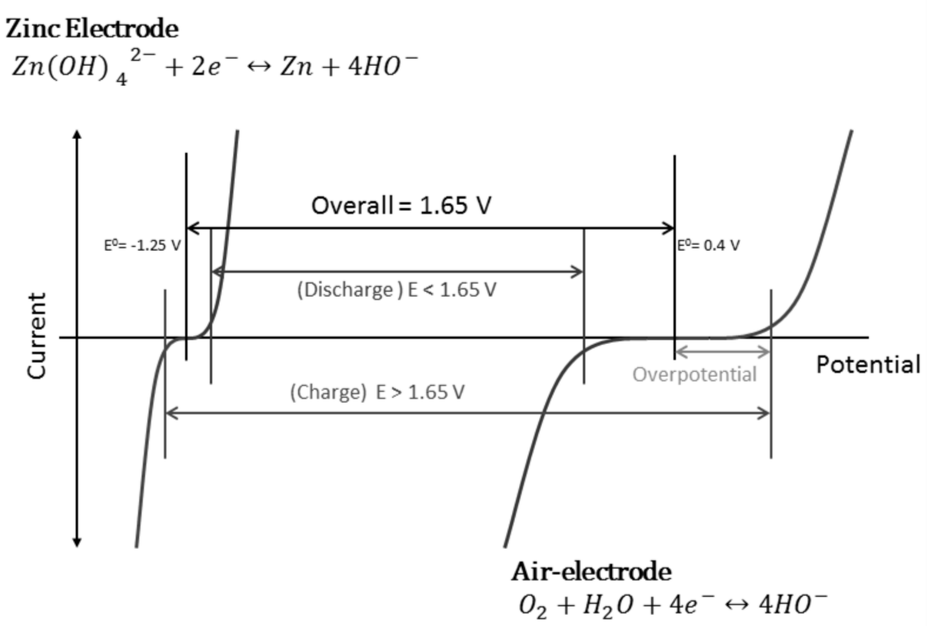

Figure 1.3 Schematic for the oxygen and zinc electrodes in the zinc-air battery.

For electrical energy generation to occur in a zinc-air battery the reaction taking place in Equation 1.1 should be thermodynamically favourable.[27] The overall reaction can be expressed in terms of the potential difference between the anode and cathode which is defined as the cell E_{emf}. The E_{emf} can be related to the electrical work done by Equation 1.5.

$$Electrical\ work\ done\ (W) = -charge\ (Q)\ \times Voltage\ (E_{\mathrm{emf}}) \qquad 1.5$$

Where $Q = nF$ with n being the number of electrons involved in the reaction and F the Faraday constant. In the case of the zinc-air system $n = 2$. For the zinc-air system therefore electrical work done can also be expressed as:

$$W = -2FE_{emf} \qquad 1.6$$

Assuming no losses in the system, the electrical work is equal to the Gibbs free energy change (ΔG).

$$E_{emf} = \frac{-\Delta G}{2F} \qquad 1.7$$

E_{emf} is calculated as:

$$E_{emf} = E^{o}(cathode) - E^{o}(anode) \qquad 1.8$$

The combined electrode reactions produce a theoretical 1.65 V as shown in Equation 1.4 however in practical cells this is generally reduced due to internal losses.[27, 43] Several factors are responsible for this low voltage including ohmic losses, activation losses followed by dendrite formation and carbon dioxide absorption during operation. The open circuit potential (OCP) is obtained when no load is applied and should theoretically equal the E_{emf} however due to potential losses the actual value is often lower at around 1.45 V.[27]

The electrochemical reduction of O_2 is a multiple electron process. There have been over 60 proposed mechanisms however the exact multi step process is not fully understood. In principle the reaction may progress by one of two possible pathways: one involving the transfer of two electrons to produce peroxide (Equation 1.9 and 1.10) and the other involving a direct four-electron pathway to produce hydroxide 1.11.

The $2\ e^-$ peroxide mechanism:

$$O_2 + H_2O + 2\ e^- = HO_2{}^- + OH^- \qquad 1.9$$

$$HO_2{}^- + H_2O + 2\ e^- = 3\ OH^- \qquad 1.10$$

The direct $4\ e^-$ mechanism:

$$O_2 + H_2O + 4\ e^- = 4\ OH^- \qquad 1.11$$

Platinum (an effective catalyst for the reaction) is believed operating primarily through the 4-electron pathway while carbon only the first step of the 2-electron mechanism to HO_2^-. Mixed metal oxide electrocatalysts (a potential replacement for precious metals such as Pt) with metal-oxygen bonded surfaces have been found to behave differently to those with metallic surfaces such as platinum. The oxygen activity is reported to operate with a key step involving a metal bound hydroxy-oxide species. The reaction occurring on perovksites has been suggested by Bockris[44], and further refined by Shao-horn[45] to operate as shown in Figure 1.4.

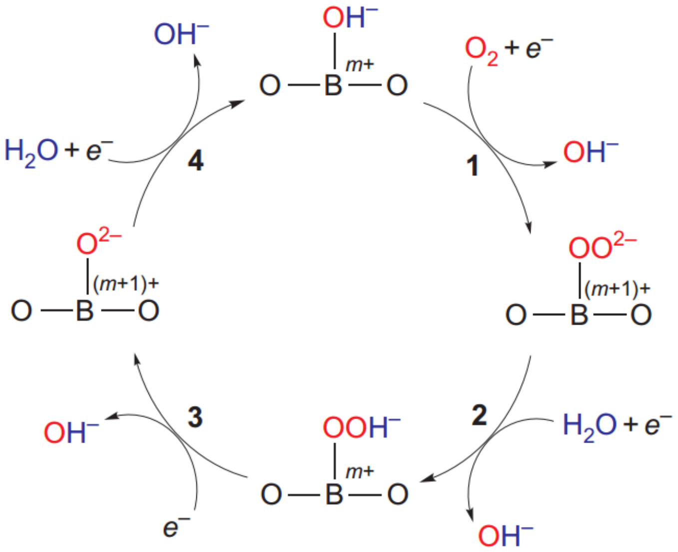

Figure 1.4 A proposed mechanism for the ORR reaction on perovskite electrocatalysts.

To place this theory into context three examples of zinc based primary battery systems are compared in Table 1.2. Due to the air, not being packaged inside the battery it is clear to see that the Zn-air cell has high theoretical and practical energy densities. The real-world performance of a zinc-air battery is however a function of several variables: electrode area, air availability, electrode porosity, and the catalytic activity of the oxygen electrode surface. As a zinc-air battery acquires oxygen from the air to form zinc oxide this will affect the mass and therefore the energy density of the battery. Obtainable practical energy densities are therefore 200 to 400 W h kg^{-1} for primary cells.[46]

Table 1.2 Theoretical and practical operational properties of zinc based primary cells. (Ref.[47])

Battery	Anode	Cathode	Voltage / V	Specific energy / W h kg^{-1}	Energy density / W h L^{-1}
Leclanché	Zn	MnO_2	1.60	358	165[d]
Zinc-air	Zn	Ambient air	1.65	1353	1300[e]
Zinc-O_2	Zn	O_2	1.65	1085	-

d - Cylindrical bobbin-type batteries, e - Button type batteries

Zinc-air flow batteries, such as that shown in Figure 1.5, are a new type of secondary battery which combines attributes of both metal-air and flow batteries (Sections 1.3 and 1.2). A constant flow of electrolyte and gas aids mass transport of the reactants to the electrode surfaces, the use of O_2 from air rather than a second electrolyte tank helps to reduce size and mass. This reduction could result in higher energy density systems with comparatively lower capital costs. The fact that zinc is relatively benign and inexpensive, compared to the all vanadium flow battery for example, makes it a desirable choice for many energy storage applications.

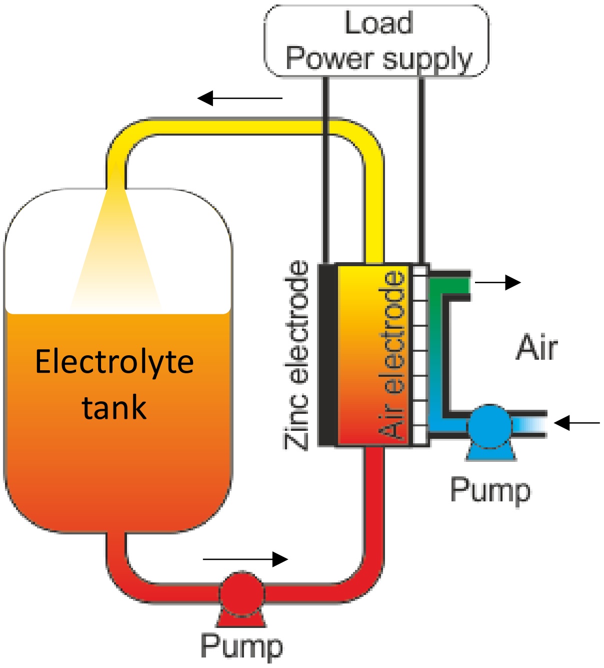

Figure 1.5 Schematic of a zinc-air flow battery design which is an example of a hybrid flow battery (Type B). One of the reactants is oxygen which is readily available in the air and so one of the two electrolyte tanks normally found in a redox flow battery can be replaced by an air pump or compressed gas system.

Chapter 2: Electrodes

2.1 Zinc electrode

The deposition of zinc from alkaline solution is well documented in the academic and patent literature. This is because zinc is one of the metals dominating the electroplating industry.[48] Zinc plating, also referred to as electro-galvanizing, has been used extensively in automotive and other industrial sectors as a protective coating for large quantities of steel wires, strips, sheets, tubes and other fabricated ferrous metal parts.[49,50] The reason for the pre-eminence of zinc in the world of electrodeposition can be attributed to its relative ease of deposition as well as its cost and low toxicity.[51] As the industry has moved away from acidic media and the use of cyanide containing solutions, methods of optimising zincate have become increasingly common. To facilitate this shift a significant research effort has gone into finding suitable additives to aid zinc deposition.[52]

Despite this relatively little research work has focused on improving the anode for application in zinc-air fuel cells / flow batteries.[27] Zinc metal is typically corroded by the alkaline electrolyte.[53] This process leads to parasitic self-discharge of the cell reducing the charge efficiency of the battery. Using the example of KOH, the reaction occurs as follows:

$$Zn + 2KOH + 2H_2O = K_2Zn(OH)_4 + H_2 \qquad 2.1$$

There are presently two ways to overcome the corrosion of the zinc anode in alkaline media. Firstly, adding corrosion inhibitors to the alkaline electrolyte. The corrosion inhibitors adsorb specifically on the zinc electrode surface preventing the corrosion reaction. Lee et al. have suggested the use of phosphoric, tartaric, succinic or acetic acid for perturbing dendritic growth and postponing hydrogen evolution. They report shifting the hydrogen evolution reaction (HER) from − 1.3 V to around − 4.1 V versus Hg/HgO.[54] Secondly subjecting the metal surface to an initial or mechanical treatment. Mercury, lead oxide and cellulose have been examined as additives the electrodes itself during its preparation.[55] Although the additives did influence zinc dissolution, there was limited improvement in both the surface morphology of the zinc deposit and in reduction of dendrite growth. With only minimal improvement in performance toxic heavy metals such as lead and mercury are unlikely to receive adoption for this purpose.

The dissolution process is accelerated at elevated temperatures. This relationship has been demonstrated experimentally in a communication by Pan et al.[56] To minimise the effect of partial self-discharge it was proposed that cell operation should be below 60° C. The preliminary findings indicated that increasing the temperature from 60° C to 80° C resulted in a charge efficiency drop from 95.2% to 89.2%. The other key issue with zinc deposition in the context of a zinc-air battery is the morphology of the deposition. Ideally deposition will occur uniformly across the surface of the electrode and the growth should look mossy in texture. However, it is common for zinc to exhibit dendritic growth. These sharp protrusions can ultimately cause electrical short circuiting within a cell as the zinc eventually bridges the interelectrode gap. This phenomenon should be mitigated by choosing the correct electrolyte conditions. Zincate concentration, electrolyte concentration, temperature, viscosity and velocity of aqueous solution are also limiting factors of dendritic growth. Continuously flowing the electrolyte over the interface should minimise local variations preventing uneven deposition. This is another reason the flow cell design is favoured for scale up of the zinc-air chemistry.

Since the reaction environment is already well defined and studied the zinc electrode does not contribute as significantly to the overall cell efficiency as the air-electrode. For this reason, the focus of this thesis has been on developing the air-electrode as currently this represents the largest inefficiency. Consequently, zinc electrode development has largely fallen outside of the scope of this study.

2.2 Air (oxygen) electrode

For metal/metal oxide-air applications adequate gas diffusion to the oxygen electrode is essential. Oxygen is poorly soluble at atmospheric pressure in the alkaline electrolyte. For example, the solubility in 2 M NaOH is 25000 ppm; therefore, the electrolyte itself is incapable of supplying sufficient oxygen to replenish the active sites at a reasonable rate. A three-phase reaction zone is consequently required to provide oxygen to the active catalyst sites to achieve workable current densities.[57] Air-breathing electrodes are widely used as positive electrodes in energy conversion and storage systems such as fuel cells and metal-air batteries. The nature of their porous structure facilitates the effective mass transport of gaseous reactants and products through the material. This efficient transport of gaseous reactants/products to and from the active catalyst sites increases the kinetics of a reaction.[24]

Secondary zinc-air batteries can operate with either two or three electrodes. In the case of three electrodes, one is used solely for the oxygen reduction reaction (ORR) and another for the oxygen evolution reaction (OER). The third provides an interface for the reactions of the zinc half-cell. For a two-electrode system, a single electrode facilitates both the oxygen reduction and oxygen evolution reactions. It is referred to as a bifunctional electrode.[58] This thesis takes the approach of the bifunctional electrode, as it reduces materials cost and system complexity making it the more desirable option however; it is not without its technical challenges.

An air-electrode is usually comprised of, a current collector, a hydrophobic gas diffusion layer (GDL) and a porous active layer (Figure 2.1).[59, 60] Each component may consist of a single material or be made of a series of layers.[22] Typically one-three diffusion layers and one or two active layers.[22]

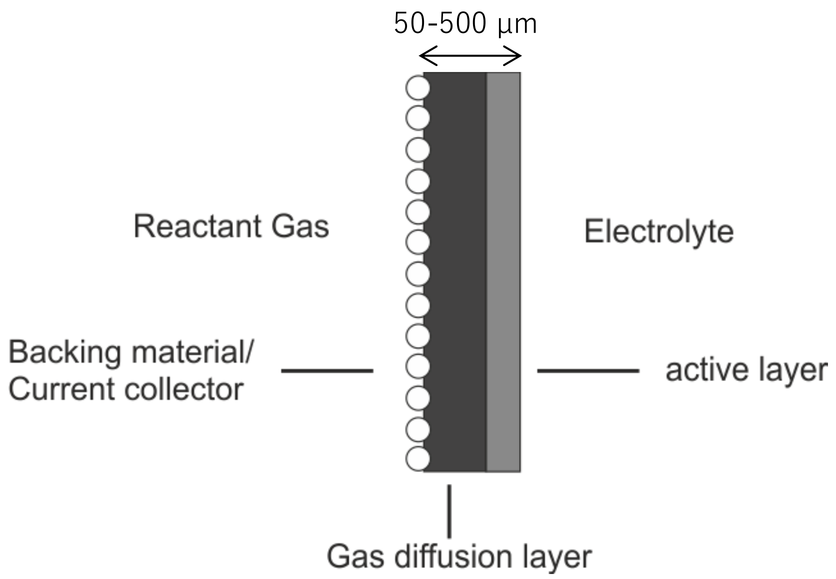

Figure 2.1 Schematic showing the generalised structure of an air-electrode.

If the air-electrode is supplied with atmospheric air (metal-air battery) instead of pure oxygen (metal-oxygen battery) other constituent components of the air need to be considered. Carbon dioxide for example reacts with liquid alkaline electrolyte (LiOH, KOH etc.) leading to carbonate formation.[3, 22, 61]

$$2KOH + CO_2 \rightarrow K_2CO_2 + H_2O \qquad 2.2$$

And/or

$$KOH + CO_2 \rightarrow KHCO_3 \qquad 2.3$$

When these insoluble carbonates precipitate inside the air-electrode structure, active sites become inaccessible and gas channels blocked leading to a decrease in the electrochemical activity.[62] This side reaction has been identified as the main cause of ageing of air-electrodes working in alkaline electrolyte.[63] Performance with atmospheric air tends to be limited to 10s of hours mainly due to the precipitation of carbonates inside the electrode porosity.[64] If the gas entering the cell is significantly cooler than the electrolyte, it can cool the electrode from the gas side, the vapour pressure drops until the water condenses inside the pores of the diffusion layer, no matter if there is a hydrophobic surface or not. This not only blocks the diffusion paths of the fuel gas but also causes the build-up of paths of liquid through the whole electrode. Hence, the fuel gas has to be heated first, using the electrolyte.[22] The most common methods of avoiding the deleterious influence of carbon dioxide are to remove it by using CO_2 scrubbers. This can be easily achieved using soda lime or using an integrated cleaning system. Again, the use of liquid circulating electrolyte is a major advantage, as a certain amount of CO_2 in the feed gas can be accepted (approximately 100 ppm). The type of electrolyte also affects the shape of the crystals formed. NaOH, for example, has a lower solubility of CO_3^{2-} than KOH, but the crystals are smaller and can easily be washed away. In case of K_2CO_3, the crystals remain inside the pores.[22] A build-up of carbonates in the electrolyte can have negative effects on the electrolyte like slower kinetics due to a lower OH^- concentration, a reduced electrolyte conductivity, a reduced O_2 solubility and an increased electrolyte viscosity. Alternatively the electrode can be supplied with pure oxygen via a compressed gas tank.[64] If oxygen is used the majority of the fuel supplied can be recovered during the reverse reaction and stored until needed.

A factor common to many similar fuel cell and battery technologies is that the oxygen electrode (cathode during discharge) constitutes one of the most expensive cell components and is largely responsible for determining the cell performance due to large overpotentials for OER and ORR.[24, 65] The demand for a cost effective (i.e. non-precious metal based) air-breathing electrode has increased development of novel ORR catalysts that are active and durable in alkaline media. There have been a great number of studies[21, 66, 67] addressing the production of effective electro-catalysts for the system, however the scale-up of electrode structures incorporating these materials has seen comparatively less attention.

From previous studies, it has been shown that the design of the air-cathode, encompassing such components as catalyst supports, binding agents, current collectors, membranes, and catalyst layers, has a strong effect on performance.[28, 68] Developments in such components are discussed in the following sections.

2.2.1 Current collector

Current collectors for metal-air batteries commonly consist of or are coated in nickel, which passivates in caustic environments; however, it forms an oxide layer on the surface that increases the internal resistance of the electrode. Nickel-plated steel could also be used however particular care must be taken to ensure the steel is completely encapsulated. Complete protection of the steel and the nickel can only be obtained by layers of gold and other resistant but expensive materials. Examples of pure precious metal plates have been reported but are only used on $< 10\ \text{cm}^2$ scale due to their expense, limiting large-scale applicability.[22] Another approach is to graphite-coat or embed the current collector into the diffusion layer to minimise the area of metal in direct contact with the electrolyte. Current collectors often take the form of meshes, screens and expanded metals.

2.2.2 Catalyst support

One of the key components that can limit the design of the electrode, affect its long-term performance and overall dimensions, is the electrode substrate/catalyst support. Although it does not normally play a role in the chemistry of the cell, properties such as thermal/chemical/electrochemical stability, electrical conductivity and surface area can have multi fold increases on the performance and durability of the electrode. Often a binding material such as polytetrafluoroethylene (PTFE) is required to ensure that the substrate and supporting material adhere to one another.

Table 2.1 summarises the intrinsic properties of the catalyst supports which have been investigated in the literature. Nano-scale powders and fibres are predominantly employed for this purpose. Ideally the optimal material will possess both a large surface area and high electrical conductivity. In general, it is shown that a decrease in particle size results in a greater surface area, however, it should be noted that this is not the only factor which dictates the surface area. Despite having the same particle diameter there is a drastic difference in the reported surface area between Vulcan® XC-72R and Acetylene Black for example.

Table 2.1 Comparison of catalyst support materials found in the academic literature.

Support material	Supplier	Surface area / m^2 g^{-1}	Average Particle size / nm	Apparent density / g cm^{-3}	Specific resistance / Ω cm
Shawinigan Black AB50 [25, 69]	Chevron Chemical Co.	82	40	0.10	0.022, 0.026
Vulcan® XC-72R [25, 69,14]	Cabot Corporation Ltd.	254, 300	30	0.10, 0.26	0.021, 0.035
Black Pearls 2000 [70]	Cabot Corporation Ltd.	1475	15		
Black Pearls 3700 [25]	Cabot Corporation Ltd.	40	55	0.40	
Acetylene Black [71, 72]		70	30-42	0.17-0.23	≤0.25
Carbon nanofibres (HTF150FF-LHT) [73]	Electrovac GmbH		100-200	0.044	
Sub-stoichiometric titanium oxide[74, 75]	Ioroi et al.	~ 1–2	~ 150		
Vapour growth carbon fibre [76]	Showa Denko Corp.	15			
HCF-1 Graphitized [71, 77]		220			
Carbon nanotubes[78]	Not commercially available	42	4 to 50 (diameter)		

2.2.2.1 Carbon

Carbon has been a common component in most fuel cell/metal-air electrode structures since the first commercialised air-electrodes. It was recognized early on in the development of GDE structures that even the type of carbon used had a “great influence on performance”.[35] Carbon based materials have found applications as catalyst supports, a component for gas diffusion layers (GDL) and an aid to electrical conductivity. It is well documented however, that structures that rely on carbon can suffer from low stability in a strongly alkaline environment at the high oxidation potentials associated with oxygen evolution.[71, 77, 79, 80, 81] This low stability manifests itself as degradation in electrochemical performance resulting from physical disintegration of carbon based structures.[60] Carbon is not corroded by KOH but oxidised by O_2 in air at higher temperatures[22] however this is much less apparent at the < 70° C operating temperatures of a typical zinc-air cell. Carbon alone will catalyse the ORR[22] however this activity is far less than that of a catalyst.

Carbon particles can be manufactured via several synthetic routes from a range of feed-stocks. The source and treatment processes can result in considerable performance variations when these carbons are used as catalyst support materials.[25] Details of some commercial and laboratory prepared materials are shown in Table 2.1. Amongst these carbon materials, Shawinigan Black shows superior chemical stability, giving reliable performance for 1000 h under a constant current load of 200 mA/cm^{-2} at 23°C in KOH 7.5 M solution.[25, 69] Comparable systems employing Vulcan® XC-72R and Black Pearls 3700, were shown to degrade in performance and eventually fail due to flooding of the gas supply channels after periods of only a few hundred hours.

The stability data for these supports however is contrary to the findings for their electro-active performance. The use of Vulcan® XC-72R as a support was shown to give enhanced performance over Shawinigan black in terms of electro-activity.[25] There is a difference in oxygen reduction reaction potential of approximately 275 mV between the two un-catalysed materials at 100 mA cm^{-2} based on the study by Maja et al.[25] This is most likely because of its significantly higher surface area compared to similar carbon materials. It should be noted however, that overall, both supports when catalysed showed very similar polarization curves, in this case particle size and electrical conductivity are more significant factors with respect to electrode performance. Kivisaari et al.[70] showed that Black Pearls 2000 have a drastically improved surface area over any discussed by Maja. However, despite also showing good electrical conductivity the pearls resulted in pastes which were too "sticky" to form into effective electrodes. This suggests that there may be an upper limit to the surface area of support which can be implemented.

Studies including those by Ndzebet[82] and Koshiba[83] have shown the utilization of combinations of carbon based materials. In both instances, a combination of carbon black and activated carbon were used in conjunction with a manganese oxide catalyst and a fluorinated polymer binder to form the active layer. It appears that the activated carbon was used as a high surface area support, however, this has a comparatively poor electrical conductivity and so the carbon black is incorporated to improve this. Both studies report improved performance over previous electrode structures; however, it is not made clear in the study to what extent the mixture of carbon powders contributes to this.

To improve the stability of the carbon support, materials that include a higher graphitic character such as graphitized carbon black[71, 77] and carbon nanotubes[84] have been examined. These carbon supports show an intrinsic corrosion rate several-fold lower than conventional carbon supports;[79] however, they still suffer from poor stability under highly oxidative conditions during start–stop cycling. Carbon nanotubes, rods and fibres[78, 85, 86, 87, 88, 89] show promise as support structures in fuel cells due to their unique properties; relatively high electrical conductivity, strength and high surface area. It has been shown that graphite nanofibres can exhibit significantly improved oxidation activities when using a platinum catalyst compared to comparable structures in direct methanol systems.[88, 89, 90] Hacker and co-workers[73] have also demonstrated the use of carbon nanofibres as a catalyst support for cathodes in alkaline fuel cells; successfully loading platinum and silver catalysts onto the fibrous structures. The carbon nanofibres (CNFs) were prepared on the gram scale with loadings of Pt and Ag as low as 0.7 mg cm^{-2} showing that this could be developed to a workable scale however it is not mentioned if larger systems have been achieved or if it would be financially viable.

2.2.2.2 Metals

There is only limited published literature showing electrodes which use a metal substrate not only as a current collector but also as a direct catalyst supporting material. By removing the need for a carbon-based catalyst support the stability could be greatly increased if the adhesion between a catalyst and a metal substrate can be shown to be sufficient. A consideration with metals is galvanic corrosion.

One way to mitigate this is to ensure that all metals used in the electrode have similar standard electrode potentials.

2.2.2.3 Composites

A novel electrode which utilizes fibrous metal–carbon composites was developed at Auburn University. Advantages of these composite electrodes include an increase in electrical conductivity and a significant reduction in the thickness of the electrode structure. The electrodes are fabricated using metal, carbon or cellulose fibres in a process similar to paper making.[91, 92, 93] An example of this type of construction is the use of stainless steel fibres and carbon fibre bundles by Kohler et al.[91] The composite electrode structure was claimed to show a surface area of approximately 760 m^2 g^{-1} of carbon which is more than double that of Vulcan® XC-72R carbon powder as discussed in (Section 0). Ahn et al.[93, 94, 95] also reported the fabrication of stainless steel and carbon-fibre composite structures that were successfully utilized for oxygen reduction in an alkaline electrolyte. It was demonstrated that the steel fibres significantly reduced the electrical resistance of the electrode as well as adding additional structural support. The resulting electrode is significantly thinner than common commercial alternatives. Micro fibrous nickel–carbon composite structures were produced by Zhu et al.[37] The structure combined cellulose, micro-metre diameter nickel fibres (Memtec America), and Black Pearl carbon particles (Cabot Corporation) in an aqueous slurry. A patent by Tatarchuk has shown that a variety of fibrous materials can be combined into network like structures.[96]

The coating of carbon nanotubes in metals has also been suggested as a material which could be used as an electrode support.[47, 88, 90] Gao et al. have tested the aforementioned carbon nanotubes coated in nickel particles in the context of hydrogen storage.[97] Although the performance was promising the structure was found to show a poor charge/discharge cycle life.

Composite materials are an area of interest in finding a substrate solution as presently there is not a single material which appears to satisfy all the desired properties. The ability to combine a group of materials which each show one or more desirable attributes could result in a successful structure however the optimal structure has yet to be developed.

2.2.2.4 Alternatives

Alternative catalyst-support materials based on conducting oxides with highly oxidation-resistant properties, such as sub-stoichiometric titanium oxide,[98, 99] niobium-doped titanium oxide,[100, 101] indium tin oxide,[102] and sulfonated zirconium oxide[103] have been proposed and studied at the laboratory level. Ioroi et al.[98, 104] showed that it is not only catalysed carbon supports which degrade at high oxidation potentials. Tests showing an electrode structure with a carbon containing GDL were found to have significantly worse performance at high potentials compared to an electrode structure which replaced the carbon with titanium. The electrodes were held for periods of 1 h at increasing oxidation potential. At a value of 1.5 V *vs.* a H_2 quasi reference electrode the carbon based GDL was shown to degrade. Sub-stoichiometric titanium oxide was used in place of a carbon support such as Vulcan® XC-72. This improved the stability of the electrode however the particle size of the titanium oxide produced was comparatively large resulting in a surface area which was two orders of magnitude lower than its carbon counterpart. This ultimately reduces the potential of the electrode particularly at high current densities. The paper also admits that the long-term durability should be examined under more practical operating conditions, such as higher current densities, and voltage cycling conditions. Therefore, a valuable expansion to this study would be to attempt to decrease the particle size of the titanium oxide as well as evaluate these systems more extensively in the context of an alkaline electrolyte.

Ebonex® is the commercially recognized trade name for the Magnéli phases of titanium oxide. It encompasses a range of distinct compounds with the generic formula Ti_xO_{2x-1}, where x represents an integer between three and ten.[105, 106] These materials are attractive because of their high electrical conductivity and relative stability in corrosive environments. The electrical conductivity of the material varies with x.[99] The Ti_4O_7 phase exhibits the highest electrical conductivity of these (approximately 1035 S cm^{-1}) at room temperature, which is comparable to that of graphitized carbon.[107] In terms of stability, Ebonex® has a projected half-life of 50 years in 4 mol dm^{-3} H_2SO_4 at room temperature.[108] In addition, Magnéli-phase titanium oxides are known to be highly oxidation-resistant.[109] Due to these conductivity and oxidation-resistant properties, Magnéli-phase titanium oxides may be an attractive replacement for carbon as a durable electrode material for electrochemical applications under harsh conditions.[110]

Vracar[111] reports Pt nanoparticles on Ebonex® show enhanced oxygen reduction compared to polycrystalline platinum electrodes for acid systems. Rotating disc experiments summarised in Table 2.2 show that an electrode coated in Pt supported on Ebonex® displays significantly more positive potentials indicating its higher catalytic activity for oxygen reduction, compared to pure Pt. An apparent gap in the literature however is a conclusive study into the stability of Ebonex® in an alkaline medium. There are a small number of examples of Ebonex® being used in caustic media however they have not explored the stability in any detail.[112, 113] Doping of titanium dioxide has also attracted interest for catalyst support material.[114]

Table 2.2 Rotating disc electrode data for O_2 reduction in a 0.5 mol dm^3 $HClO_4$ solution at: (a) Pt and (b) Ebonex®/Pt (5 μg) electrodes *vs.* a reversible hydrogen electrode (RHE). Disc areas are: 0.196 cm^2 and 0.125 cm^2, and RPM 365 and 383, respectively.

Current density / mA cm^{-2}	Pt *E vs*. RHE / V	Pt/Ebonex® *E vs*. RHE / V
0.10	0.39	0.75
0.20	0.35	0.68
0.30	0.32	0.42

Boron doped diamond (BDD) has attracted interest as a replacement for standard carbon powders in energy storage and conversion system electrodes.[115, 116, 117, 118, 119] BDD combines the strength and stability of diamond with the added boost in electrical conductivity brought by the boron doping. The result is electrodes which have similar performance to their carbon alternatives but likely with increased stability, CO_2 resistance and electrochemical performance with optimisation. There are a few examples of electrodes which incorporate these materials in the literature however only in limited applications.[120] There is potentially an area of scope to expand this although currently the material is not feasibly scalable.

2.2.3 Bi-functional oxygen evolution/reduction catalyst

To promote the evolution and reduction of oxygen a catalyst is required for the reactions at the air (positive) electrode. Active catalyst sites for both reactions are required; the simplest solution is to use two separate catalyst materials; one to promote reduction and one for evolution. This however reduces the area that each catalyst can occupy by half as the surface must be coated with both materials. There is also the possibility that the action of one catalyst may inhibit the performance of the other. The other option is to use a bi-functional catalyst. A bi-functional catalyst describes a material which has two catalytically active sites and is therefore capable of catalysing two reactions. In this instance, the two reactions are the oxygen evolution reaction (OER) and oxygen reduction reaction (ORR). A common issue which is shared by most metal-air systems is that an effective bi-functional catalyst, which has active sites for both the OER and the ORR remains elusive.[121, 122, 123]

MnO_2 was the first material to be utilised as an air-cathode catalyst and is still prevalent today despite debateable long-term stability and promotion of the less favourable peroxide pathway. In terms of performance noble group metals such as Pt, Ru and Pd or their oxides are by far the leading catalysts for this application however these precious metals are not only expensive but also a limited resource.[43] Use of the air-electrode in presence of alkaline electrolyte leads to an increase of the reaction kinetic, and allows the use of cheaper catalysts based on non-noble metals in the active layer. The use of non-noble metals is possible because the ORR in alkaline media is more facile than in acid media.

Silver has been demonstrated to be an active component for the ORR in alkaline solutions. Although Ag is a precious metal, it is one of the cheapest and so some groups have chosen to investigate it as an alternative to Pt. While this would show a significant reduction in the cost over Pt it is unlikely to be cost effective if scaled to a MW system. Silver catalyst has been compared with platinum by Lee et al.[124]

Initial data suggested that silver could be seen to be comparable to Pt under optimized conditions. The silver was also alloyed with Mg which produced even higher current densities. A factor which cannot be overlooked, however, is that Ag metal dissolves in a concentrated alkaline media at open circuit voltages.[22] Unless stabilised Ag may not be an appropriate choice for rechargeable systems.

Developments made stemming from MnO_x have shown that by tweaking the compound it is possible to improve the performance. Yang and Xi,[125] showed that MnOOH has higher ORR activity than oxides such as Mn_2O_3, Mn_3O_4, and Mn_5O_8 due to an increase in the number of active centres. Furthermore, Roche et al.[126] doped Mn_xO with Mg and Ni to significantly improve ORR activity and promote the four-electron pathway. Doping of other metals onto existing structures may allow for improved performance. Currently the most promising replacements for air-cathode catalysts are based on individual metal oxides, or mixtures of these, with a spinel, perovskite, or pyrochlore structure.[28] Examples include MnO_2,[127, 85] Co_3O_4,[14, 128] La_2O_3, $LaNiO_3$[129] and $NiCo_2O_4$.[130, 131] These structures have been found to give good activity for oxygen reduction as well as good stability in a highly caustic medium.

One way to improve the performance and reduce the cost of a catalyst like Pt is to increase its surface area. This can be achieved by producing smaller particle size Pt for example nanoparticles. Pt nanoparticles have been tested on a corrosion resistant carbon support in phosphoric acid fuel cells.[132] Equally important is maximizing the proportion of the active catalytic area which is exposed at the three phase boundary. Active sites which are coated in binder material, attached to or blocked by supporting material or flooded by electrolyte will not be involved in a catalytic reaction. This material which is not active will still contribute to the mass, size and cost of the electrode, however, it will have little effect on performance. Therefore, great care should be taken when adopting methods of catalyst application to maximize active site utilisation.

2.2.4 Active layer binders and additives

Metal–air batteries were not commercially feasible until the development of materials such as PTFE, which allowed the oxygen electrode to operate efficiently. With PTFE, the oxygen electrode could be made thinner, which ultimately allowed the commercialization of zinc-air button cells.[41] A hydrophobic barrier is therefore a necessity. The hydrophobic material needs to coat the pores within the structure to prevent flooding but without blocking them or active sites, preventing gas flow and reducing activity. A porous PTFE layer has been the favoured material for this application in almost all studies. The amount of electrolyte that can penetrate the active layer is inversely proportional to the PTFE content.[72] For most gas diffusion electrodes, the PTFE content is no more than 30%. Different ratios of carbon, catalyst, and binder induce different porosities, wettability of electrolytes, and electrical contact of active materials, resulting in variable electrochemical performance.[43] The wetting of an air-breathing electrode describes its normal operation where by the electrolyte fills the pores of the electrode without entering the GDL. If the electrolyte penetrates through the active layer into the GDL this is referred to as electrolyte weeping and reduces performance of the electrode as electrolyte begins to occupy gas pores. Flooding of the electrode occurs when a sufficient amount of electrolyte has penetrated into the GDL to prevent effective mass transport of O_2 to the active layer of the electrode.[22] Weeping can arise form cracks or other small imperfections in the electrode usually caused in the electrode manufacture of from mechanical damage during operation. It may also be caused by the electrode containing an insufficient hydrophobic content.

Small channels are present in between individual particles, which do not pack completely uniformly. These aggregations of particles form larger structures known as agglomerates and the channels between these agglomerates are larger than the voids found inside the agglomerates themselves.

One wet proofing method is discussed by Zhu et al.[37] where the electrodes were prepared by dipping their dry composite structure in a 12 wt.% dispersion of PTFE for 5 minutes at room temperature, then dried at 110° C for 1 h. The dip-coated electrodes were further heated to 350° C for 20 minutes to remove the surfactants which were present in the solution to keep the PTFE in dispersion. Finally, a PTFE film was lightly pressed onto the gas side of the electrode to control electrolyte weeping through the composite structure.

Plastic binders, including PTFE, are attacked by the hot caustic electrolyte. The electrolyte can contain peroxides, which were produced during incomplete oxygen reduction or through the four-electron pathway (see Chapter 1.4). These peroxides can induce radical chain destruction. Along with the destruction of the polymers the electrode loses mechanical stability (crack formation) and hydrophobicity / weeping. This problem can be diminished by introducing radical collectors into the chains (e.g. styrenes) or using improved catalysts with lower peroxide formation.[22]

Bidault et al.[133] demonstrated that Teflon AF® (amorphous fluoropolymers) shows a modest improvement in performance over previous cathode designs when used as a binder. The compromise for this material is that it comes at significant cost approximately £45 g^{-1} (DuPont), however, Bidault suggested that only a small amount (approximately 1 mg cm^{-2}) was enough to obtain a good gas diffusion layer. This suggests that with further optimization this could still prove a cost-effective solution for large-scale applications.

Often when the binder is added the porosity and consequently the breathability and wettability of the electrode is greatly diminished. One method of enhancing the porosity of the layer is by a sintering process. A pore former such as sugar or ammonium chloride can be mixed into the PTFE solution before its application to the layer.[22] Once heated to approximately 350°C the pore former decomposes forming gas bubbles resulting in voids in the material. Zhang et al.[134] have shown that sodium sulphate can be used as a component in a GDL structure as a pore former. The material is incorporated into a paste which is rolled out to form the GDL. The sulphate particles are then dissolved out by soaking the electrode to create voids that greatly enhance the pore structure of the GDL improving gas diffusion through the electrode. Conversely if additional hydrophobicity is required materials such as paraffin, wax, polyethylene or polysulsone can be incorporated to prevent flooding.[22] Ji et al. reports a more flooding-tolerant electrode which contains water-proof oil, dimethyl-silicone-oil (DMS).[135] The oil lines the pores making them far more hydrophobic while still allowing effective gas flow through the structure.

2.2.5 Anion exchange membranes

An anion exchange membrane (AEM) for application in alkaline fuel cells or metal-air batteries requires the following properties: good mechanical and thermal stability during manufacturing and operation at the high pH conditions necessary for high ionic conductivity, carrier for hydroxyl transport, high ionic conductivity as well as a commercially viable cost. A comprehensive study of current anion exchange membranes with specific applications for alkaline fuel cells (AFC) by Merle[136] compares a wide array of both commercially available membranes and published work on new materials. To standardize and categorize the AEMs the review describes them as being part of one of three groups: heterogeneous, interpenetrated polymer networks and homogenous membranes. It concludes that homogeneous membranes perform better in AFC applications. Homogeneous membranes consist exclusively of the anion-exchanging material, forming a one-phase system.

There are presently a variety of methods for producing AEMs however there are problems with most production methods.[136] The issues include; energy intensive or expensive manufacture arising from processes such as irradiation, hazardous preparation methods involving chemicals such as chloromethyl methyl ether a known carcinogen or produce materials which have defects or poor conductivity. Producing a membrane which displays all the attributes which would be desirable as well as facilitating a manufacturing process which is safe and cost effective on an industrial scale appears to currently be a challenge.

2.2.6 Electrode structures and their fabrication

A common factor with many similar fuel cell and battery technologies is that the oxygen electrode (cathode during discharge) constitutes one of the most expensive cell components and is largely responsible for determining the cell performance due to large overpotentials for OER and ORR.[24, 65] The demand for a cost effective non-precious metal utilizing air-breathing electrode has increased activity in the development of novel ORR catalysts that are active and durable in alkaline media.

There have been a great number of studies that have addressed the issue of producing effective electro-catalysts for the system, however comparatively little work has been published relating to the structure of the electrode itself. The design of the air-cathode, encompassing such components as catalyst supports, binding agents, current collectors, membranes, and catalyst layers, has a strong effect on performance.[28, 68]

The manufacturing process of electrodes can have a significant impact on the overall cell performance. In general, electrodes are manufactured by a method of wet fabrication followed by sintering or by a method of dry fabrication through rolling and or pressing components onto a backing or substrate. Typically, the oxygen electrode design consists of a sandwich of layers each performing a specific purpose. In most cases the resulting electrode consists of a hydrophobic catalysed layer on top of a gas porous conductive layer which is in turn bonded to a porous metallic backing material. A good overview of electrode fabrication methods is described by Kivisaari.[70] In an attempt to find the optimal oxygen electrode structure approximately 30 electrodes were developed and tested. The best results showed half-cell results with current densities of up to 500 mA cm^{-2} without reaching limiting currents. The best results were achieved, when the electrode structure was built up from several layers and most of the current literature describes two-layer fabrication techniques.[59] Maja describes a double-layer PTFE-bonded gas diffusion electrode which was prepared in a single pass wet fabrication process, filtering an alcoholic PTFE-carbon dispersion on a previously prepared active layer to form a dual phase sheet which was dried and sintered under pressure.[25]

Membrane electrode assembly (MEA) structures are commonly fabricated by the "decal method".[137] A layer of the active material and binder is applied to a passive substrate e.g. PTFE. Once dried, a membrane is hot pressed onto the active layer. The membrane and active layer bind preferentially, so the PTFE substrate can be peeled off. Although an MEA structure has many benefits current membrane materials as discussed in the previous section are far from optimal and so there is little literature showing successful structures.

The long-term performance of electrode structures and components is affected by a variety of parameters. Most are a consequence of the harsh conditions of the high pH alkaline electrolyte and the potentials associated with oxygen evolution. Unless adequately mitigated carbonate formation and catalyst poisoning from CO_2 in the air limits the systems lifespan. Although most materials discussed previously have been incorporated into electrodes and electrochemically screened most studies simply report polarisation curves. Although useful for comparing the intrinsic properties of the materials, polarisation curves give little information as to how the electrodes perform over prolonged periods. This information is of great interest as the stability and longevity of the electrode is a key factor to consider when assessing commercial viability. The properties of the electrode can only truly be evaluated in a working battery system with both electrodes present.

Table 2.3 summarises performance and stability data for some electrode structures reported in the literature. Operation at elevated temperatures (typically > 50° C) is common in the systems evaluated. KOH is a common electrolyte and shared by all the systems. It should be noted that out of the samples the max current density achieved was 300 mA cm^{-2} and the longest continual running time was the order of a few hundred hours. Compared to the >10,000 cycles demonstrated by state of the are flow battery systems and current densities of amps per square centimetre shown by current fuel cell technologies there is still a large scope to improve upon the current systems examined below.[138]

Table 2.3 Comparison of electrode performance

Electrode	Catalyst loading / mg	Temp / °C	KOH electrolyte concentration	Reference / counter electrodes	OER / V	ORR / V	Current density / mA cm^{-2}	Stability
CoO beadlike[25]		55	30 wt.%	Hg/HgO	0.475	-0.175	60	250 h max. OER potential limited
Rod like[25]		55	30 wt.%	Hg/HgO	0.580	-0.260	60	
Carbon nanofibres Pt [73]	0.70	80	9 M	RHE				
Silver[73]	0.70	80	9 M	RHE				
Pt/Ti_4O_7	0.24	80		CE as a quasi-reference electrode			0-300	>350 h
Ag-CNC	5.04		30 wt.%	Zn rod			200	

2.3 Research question

The electrically rechargeable zinc-air flow battery is an energy storage technology in development that theoretically has several advantages over similar battery technologies for large-scale energy storage applications. This section highlights the many obstacles still to overcome before the chemistry underpinning commercially available primary zinc-air button cells can be reengineered into a practical flow battery design. This project will discuss the current challenges surrounding the manufacture and testing of novel air-electrode structures and propose developments to overcome them. Ultimately with the aim of integrating promising electrode designs into an operational proof of concept zinc-air flow battery system. The design is intended to demonstrate testing on the order of a few amps but the feasibility of scale up to a multi cell stack with power output on the order of a kW will heavily influence design decisions. The importance of producing an efficient and cost effective bi-functional oxygen electrode is central to this development. Maintaining the three-phase boundary, is crucial to ensure stability and activity therefore balancing the pressures and flow rates of the electrolytes/gasses in the cell. The zinc (negative) electrode also needs to be controlled so that the deposition and stripping of zinc occurs with high efficiency. Finally, the two electrodes must be combined in a flow cell which operates with high cell efficiency, i.e. optimum conditions for each half cell must be balanced.

The work described has incorporated the following aspects:

- Screening of presently available and novel materials including current collector, catalyst, catalyst support, binder, additives and membranes for incorporation into a bi-functional air breathing electrode.

- Production and electrochemical evaluation of 1-2 cm^2 (geometric area) air-electrode architectures.
- Prototyping and characterisation of practical (> 100 cm^2) oxygen (positive) electrode architectures for incorporation into a flow cell.
- Assessment of scale-up feasibility for selected oxygen (positive) electrode architectures.
- Proof of concept combination of oxygen (positive) and zinc (negative) electrodes into an operational secondary battery system.
- Characterisation of the cell performance and design/build a practical, laboratory-scale demonstration system.

Chapter 3: Experimental methodology

Experimental work included materials selection, electrode screening, electrode scale up and ultimately full-scale battery cycling. Early work consisted of high-throughput small-scale testing to select promising materials and structures. Whereas later work was focused on the assembly and operation of a proof of concept battery system utilising the insights from the initial work.

Air-electrode development incorporated the use of catalysts, catalyst supports, membranes, binders, current collectors, gas diffusion layers and other additives (see Chapters 4 & 5). The structures have been analysed using:

- scanning electron microscopy (SEM) imaging
- energy dispersive X-ray spectroscopy (EDX) and spectral mapping
- water-droplet contact angle measurements

These techniques aided in screening for suitability for operation within a cell (see Section 3.2) as well as alluding to failure mechanisms. Electrodes were then tested for their electrochemical activity and stability. Once initial electrode designs had been established, further electrode development was run parallel to flow battery testing and optimisation. Electrodes were grouped in terms of the electrochemical test cell in which they were characterised (see section 3.5).

3.1 Electrode fabrication

Step 1: Substrate preparation

Metal substrates were pre-treated, as described in Figure 3.1, to remove any surface residue or oxide layer. Samples were degreased in isopropanol (IPA) or acetone by sonication at 37 kHz for 15 minutes followed by acid etching in HCl (1-3 M) at 80° C to 100° C for approximately 30 minutes. Samples were subsequently washed in water then IPA to remove any acid residue. Dried substrates were stored in a desiccator until used. All other substrates were used as supplied unless otherwise stated.

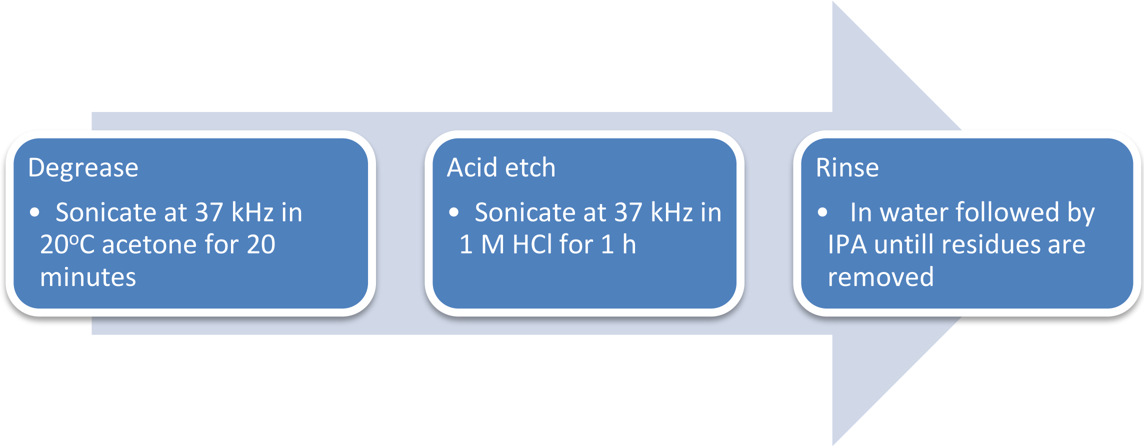

Figure 3.1 The process of pre-treatment followed for preparing metallic substrates prior to active layer application.

Step 2: active layer preparation

The active layer composition was adapted depending on the porosity and wettability of the substrate. Active layer preparations could be described as being in one of two distinct categories, inks or pastes. The term ink in this project, describes dilute solutions with micro or nano particles dispersed homogeneously. Pastes however contain a lower liquid component and range in consistency from pourable slurry, to a mouldable dough, dependant on the liquid content. Standard preparations are discussed for both the ink and paste methods. Details of active layer composition, will accompany data in which deviation from the standard is of significance.

For the standard ink preparation: 500 mg polytetrafluoroethylene (PTFE 60 wt.% dispersion in water, Sigma Aldrich) was added per gram of catalyst powder (finely ground to a ≤ 55 µm particle size) so that the ratio of catalyst to binder (dry solids) was 10:3 by mass. A 5:1 mixture of ultra-high purity (UHP) water (18 MΩ cm) and IPA was then added. The liquid volume added could be adjusted to tailor the ink composition as required. As standard 60 mL of the mixture is added for every 1 g of catalyst. A liquid volume < 25 mL per gram of catalyst produced viscous slurries and a volume ≤ 50 mL of liquid formed a fluid ink. The mixture was then ultra-sonicated (37 kHz Fisher Scientific FB15046) in a stoppered vial for 20 minutes to 30 minutes, to break up agglomerates. Then homogenised (Fisher Scientific Power Gen 1000 fitted with stainless steel generator) for a minimum of 3 s or until the catalyst/PTFE was visibly dispersed throughout the ink. The generator was maintained at 15,000 RPM (no load speed) throughout. Inks were generally used directly after production, because the dispersion would settle out over time. If the ink was not fresh, it was homogenised for a further 3 minutes directly before use.

The paste was prepared as follows; nickel powder (Huizhou Wallyking Battery Ltd, 2–10 μm particle size by SEM)/catalyst powder (15 g) was added to 60 wt.% PTFE dispersed in water (7.5 g) (Sigma Aldrich) followed by a 50:50 ratio of IPA and water (40 mL total liquid volume). The mixture was ultra-sonicated and homogenised as per the inks. The sample was then left to stand overnight allowing the mixture to separate into two distinct layers. The top layer composed of water and IPA was decanted off. The paste was the moist sediment that remained.

Step 3: application of active layer

A layer of the ink/paste was then applied to the substrate surface. To aid bonding between the substrate and the active layer if an ink was used, the substrate surface was pre-wetted with a 50% IPA: 50% water solution to ensure that the ink would adequately wet the surface. Pre-wetting was only required for the initial layer because subsequent layers would adequately adhere to one another. The inks were applied with an Aquafine® AF55 short flat ½-inch synthetic bristle paint brush (small-scale) or screen printing (large-scale). The ink was applied with as few passes as possible to ensure the whole surface is coated evenly and with strokes in the same direction. Overworking the surface with the brush caused delamination of previously deposited layers. An Iwata eclipse G-series 5 pistol-grip Airbrush-gun with a 0.25 L stainless steel reservoir and 0.5 mm stainless steel nozzle fed by a compressed N_2 gas cylinder was later adopted to increase uniformity and the rate of production and. A thin layer of ink, around 0.05 mg cm^2 was applied evenly across the front face of the electrode. The layer was then dried with hot-air gun or on a hotplate at ≈ 100°C (until constant mass) to remove any residual moisture or solvent. The mass of the structure was recorded and, if the desired loading was not achieved, the electrode was rotated by 45° and a further layer of ink was applied and dried. The rotation ensured the surface received an even coating and prevented the buildup of ridges on the surface as an artefact of the application method. This process was repeated until the desired catalyst loading was attained.

For viscous inks and pastes, typically applied to metal foams, the material was spread over the surface of the substrate with a flat blade. These two layers were then subjected to a static force of 7000 kN m^{-2} in a hydraulic press for 30 s. The resulting electrode was then dipped in a solution containing nickel nitrate (Aldrich, 99.999%) and cobalt(II) nitrate (Aldrich, ≥ 98%) in a 1:2 molar ratio (0.5 M:1 M or 1 M to 2 M) for 10 minutes. The solvent for the solution was 50:50 water, IPA. The sample was dried at 25°C for 10 min and then heat treated in a Carbolite ELF 11/6 furnace at 375° C for 10 minutes, to form the $NiCo_2O_4$ spinel. Once removed from the furnace it was allowed to cool to ambient temperature. The dip coating was repeated three times, with the final heat treatment lasting for 3 hours at 375° C. This procedure is detailed in Figure 3.2.

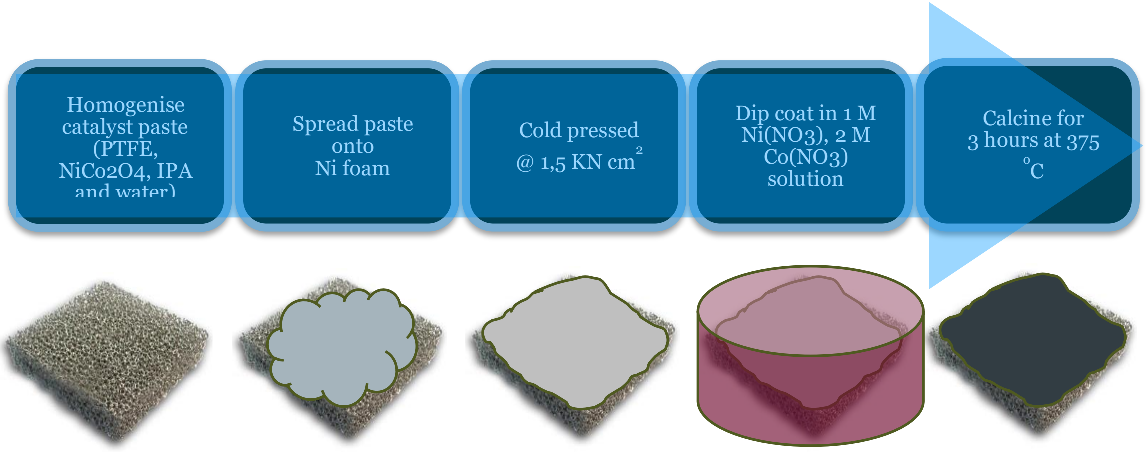

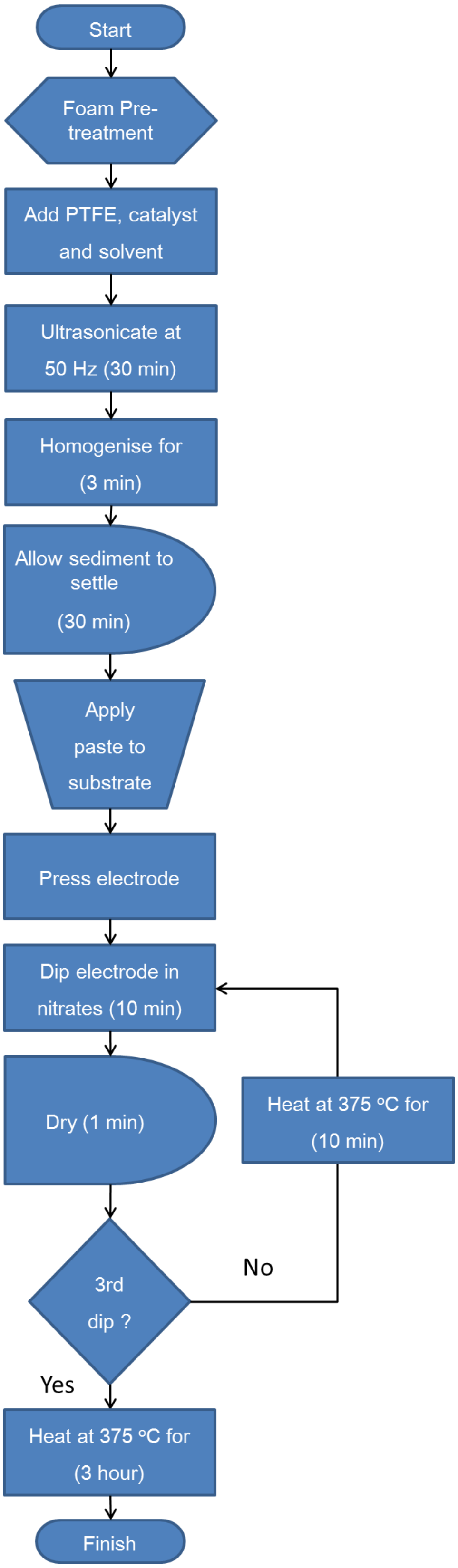

Figure 3.2 Foam-electrode manufacturing process used to produce samples for testing.

Step 4: additional layers

Where appropriate additional layers i.e. membranes or hydrophobic coatings were added at this stage to form the desired structure. Electrodes could then be cut to size and inserted into the cell assembly. Ni mesh (Dexmet) or Ni foam (Goodfellow) detailed in Chapter 4: was often used as an additional current collector to ensure good electrical contact.

3.2 Physical characterisation of electrodes

3.2.1 Surface morphology and composition (SEM, EDX)

Electron microscope imaging was used to observe the fine structure of material surfaces and low-resolution compositional analysis. Scanning electron microscopy (SEM) images were recorded using a JSM 6500F fitted with X-ray energy dispersive analysis (EDX). Both single point and spectral map EDX analysis techniques were used.

3.2.2 Contact angle apparatus

Contact angle measurements describe the degree of interaction between a liquid droplet or vapour and a solid surface. The angle observed at the interface between a liquid droplet and a flat solid surface, is a measure of the materials hydrophobicity. In this project, it has been used to evaluate the wetting properties of the various substrate and electrode materials. The angle θ between the substrate and the tangent of the curve of the droplet where it meets the surface (Figure 3.3) is calculated using Equation 3.1, where γ represents the interfacial energy.[139]

$$\gamma_s = \gamma_L \times cos\,\theta + \gamma_{sL} \qquad 3.1$$

If the droplet immediately spreads out across the surface into a thin film this is a contact angle of 0° and the surface would be described as hydrophilic (high level of wettability). If the droplet remains as intact but forms an interface with the surface creating a hemisphere the angle between the substrate and where the droplet meets the surface is 90°. A contact angle >90° represents a surface which is hydrophobic. Many polymers exhibit hydrophobic surfaces. Highly hydrophobic surfaces made of low surface energy (e.g. fluorinated) materials may have water contact angles as high as ~120° (low wettability).[140]

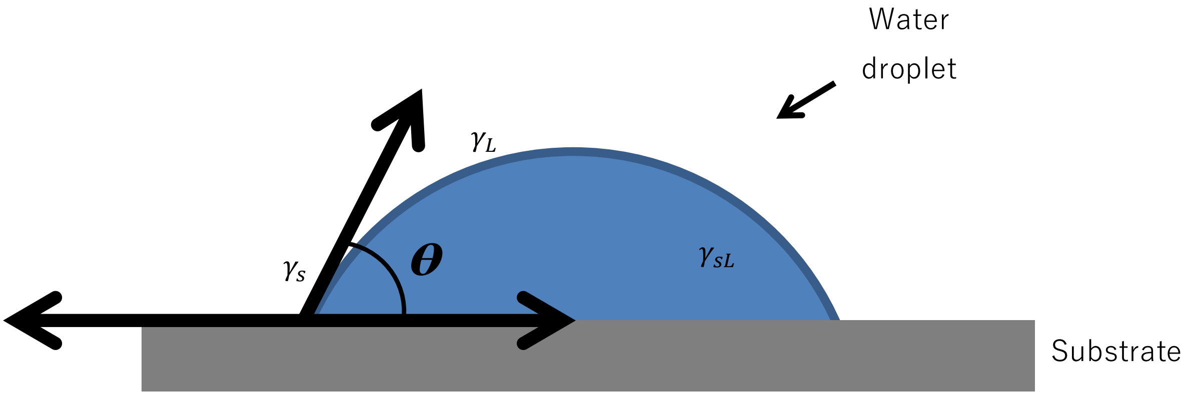

Figure 3.3 Schematic showing a liquid droplet on a flat solid surface and the interfacial energies associated with its contact angle measurement where γ represents the interfacial energy.

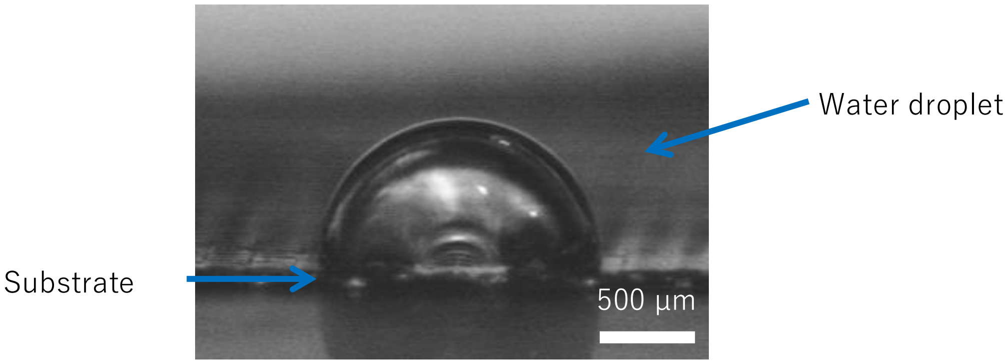

Figure 3.4 Example image of a water droplet on Dexmet Ni mesh obtained using the KRÜSS DSA10. The contact angle displayed is approximately 90˚; this material would consequently be described as hydrophobic.

All measurements were taken using a drop shape analyser (KRÜSS DSA100E) by the static sessile drop method.[141] The technique refers to an immobile drop of liquid that is in contact with the substrate throughout the measurement.[141] 1 µL of UHP water (18 MΩ cm) was dispensed from a 400 µL inverted syringe fitted with capillary (inside diameter ~ 100 µm). The sample was mounted on an X, Y and Z adjustable stage directly below the inverted syringe. The stage was raised so that the substrate contacted the suspended droplet. The stage was then lowered until the droplet detached from the capillary leaving a bead of water on the surface of the substrate around 1 mm in diameter (see Figure 3.4). An image was immediately captured of the drop on the surface of the substrate with a CCD angled to look down on the sample with a deviation of 2° relative to horizontal. This process was repeated at a range of locations across the surface of an electrode/substrate to observe if the hydrophobicity was consistent. The contact angles were calculated using a software-fitting programme using circle-fitting mode. The method calculates the shape and size of the ellipse of the cross-section through the centre of the drop perpendicular to the sample, which would be formed from the segment of a sphere, visible on the surface of the substrate. From the cross-section, a tangent of the calculated curve is taken from the point where the drop would intersect the baseline, that is represented by the substrate. Assuming the substrate surface is flat, the angle between the tangent and the baseline is equal to the contact angle θ (Equation 3.2).

$$\frac{\theta}{2} = tan^{-1}\left(\frac{h}{d}\right) \qquad 3.2$$

The principal assumptions in measurements are that the drop is symmetrical about a central vertical axis, eliminating the direction from which the drop is viewed as a possible variable. Secondly that the drop is not in motion from the point of view that viscosity or inertia are not involved in determining its shape resulting in the fact that the interfacial tension and gravity are the only forces shaping the drop.

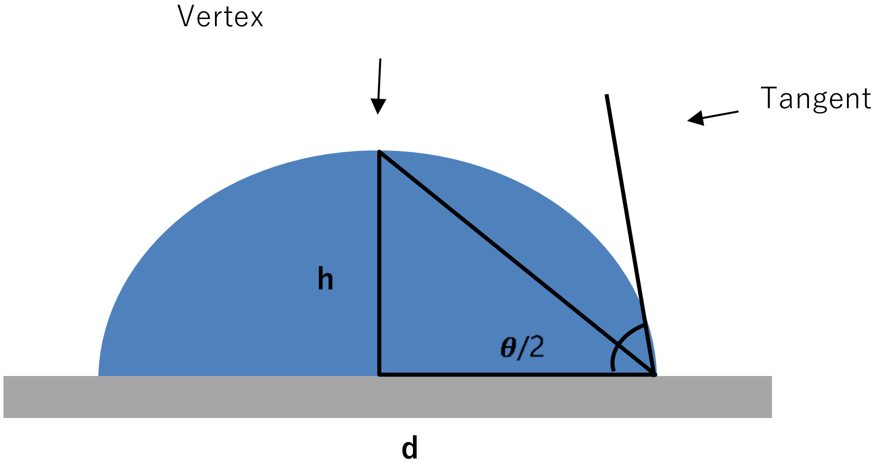

Figure 3.5 Representation demonstrating the $\theta/2$ method for calculation of the contact angle of a liquid drop on a surface described in Equation 3.2.

3.3 Electrolyte

The electrolyte for all experiments was based on either sodium hydroxide (97%, fisher scientific) or potassium hydroxide (85%, Acros organics) pellets. Half-cell experiments typically used pure hydroxide made to the desired concentration. Experiments carried out in the flow cell required Zn in solution to be plated and stripped during cell cycling. ZnO powder (99%, Sigma Aldrich) was therefore dissolved in the hydroxide solution. ZnO concentration was selected in accordance with its saturation point in the chosen electrolyte. The quantity of ZnO used was always at least 0.1 M below the saturation limit to account for slight electrolyte composition variation during cell operation. Initial work started with KOH however, it was consequently discovered that NaOH had nearly double the capacity to dissolve ZnO (0.75 M vs 1.2 M in 8 M hydroxide). NaOH was therefore pursued for its potential benefits for the zinc half-cell. It was also known that NaOH was significantly less expensive and so when scaling the system up the cost of the initial investment may become a deciding factor. However, KOH out performed NaOH after directly comparing the electrolytes in flow-cell tests, and so was selected as the preferred electrolyte in later experiments. Based on preliminary data from a project partner it was suggested that the additive Lugalvan® P aided zinc deposition and so the additives were trialed during flow cell testing. All electrolyte compositions used are collated in Table 3.1.

Table 3.1 Electrolyte compositions used for electrode and flow battery testing.

Electrolyte	**Hydroxide concentration / mol**	**ZnO concentration / mol**	**Additives**
NaOH	8.0	1.0	N/A
NaOH	8.0	1.0	Lugalvan® P
NaOH	8.0	0.5	N/A
NaOH	8.0	0.5	Lugalvan® P
KOH	8.0	0.5	N/A
KOH	8.0	0.5	Lugalvan® P
KOH	8.0	0.7	N/A

3.4 Electrochemical characterisation

Electrochemical measurements in the half-cell were controlled and measured using an Autolab potentiostat/galvanostat PGSTAT12 (Metrohm) in tandem with general-purpose electrochemical software (GPES).

Electrochemical techniques used:

- Cyclic voltammetry
- Linear sweep voltammetry
- Galvanostatic potentiometry

These techniques were used for rapid screening of catalyst/electrode structures. The counter electrode was a Pt gauze and all measurements in the half-cell were made against in-house Hg/HgO reference electrodes.

3.5 Cell designs

Small-scale: Glass cell

In house designed three-electrode, glass cell. Static electrolyte and Pt counter electrode allowed focused development of air-breathing electrode (see Section 3.5).

- 1.23 cm^2 - 1.27 cm^2 circular electrodes, exposed geometric area 0.5 cm^2

Scale up: Flow cell

In house design manufactured by C-Tech Innovation. Incorporated flowing electrolyte and zinc half-cell (see section 3.5).

Mk 1

- 3 cm by 5 cm electrodes, exposed geometric area 8 cm^2

Mk 2

- 13 cm by 12 cm electrodes, exposed geometric area 100 cm^2

Unit cell testing began with non-optimised structures incrementally replaced and improved with the best available information. The initial cell design focused on rapid disassembly and modification enabling testing of a range of electrode structures and operational parameters. The knowledge gained from these tests aimed to aid the design and construction of an optimised scale-up of the cell, which was built with performance and durability in mind.

To examine the intrinsic electrochemical properties of the oxygen electrode, a three-electrode glass cell was fabricated to eliminate the effects of the zinc electrode and focus solely on the gas diffusion electrode. The cell was intended as a high-throughput prototype characterising tool. The small dimensions and rapid assembly facilitated minimal waste of material and accelerated electrode architecture iteration compared to what could be achieved in a unit cell. Oxygen electrode structures were used as the working electrodes (WE) with a platinum mesh as the counter electrode (CE) and a Saturated Calomel Electrode (SCE) or a mercury/mercury oxide (Hg/HgO) in corresponding concentration hydroxide solution as the reference electrode. It was possible to gather information on the electrochemical performance of the oxygen electrode by examining the overpotentials associated with oxygen evolution and oxygen reduction reactions. Insight into the stability of the electrode within the typical operating potentials of the cell could also be evaluated over a moderate time scale (typically < 24 hours). In addition, qualitative information could be obtained on the wetting of the GDL and electrolyte wicking with time. Most experiments were conducted at either, 20° C or 60° C because it was acknowledged that these temperatures were beneficial for the zinc and oxygen electrodes respectively.[56] The focus has been to optimise operation at 60° C because this is an estimated operating temperature for the system when it is scaled to a multi-cell pilot-plant stack. Gas was supplied to the rear face of the electrode by either laboratory air via a compressor or by a supply of bottled O_2 (typical flow rate 200 cm^3 min^{-1}, 1 bar).

3.5.1 Glass Cell Mk I

Initial screening took place in a custom-made glass cell (Figure 3.6), which sandwiched the working electrode between two flanges, allowing for rapid interchange of electrodes. Current was taken from either a tab at the top of the electrode, which protruded past the flanges, or via a current collector that was placed behind the electrode. Gas was supplied to the rear of the electrode via a capillary that terminated approximately 2 mm from the rear of the electrode. This arrangement was non-optimal nonetheless ensured that the rear face was supplied with a regular if unevenly distributed supply of gas. Improvements to gas flow uniformity were made in the flow cell set up. The backpressure of gas in the cell could be crudely controlled by restricting the flow from the outlet. The front face of the electrode was exposed to the electrolyte chamber. The chamber has a port at the top to facilitate the insertion of the counter electrode and a thermometer and an opening for a reference electrode that was connected via a Luggin capillary.

The design was intended to allow rapid testing with minimal waste of materials. The cell was arranged with a circular disc working-electrode clamped between a gas supply channel and the electrolyte-filled cell. An opening in the cell allowed for the counter electrode to be introduced. The RE was connected to the cell by a Luggin capillary. The capillary tip was positioned at approximately 2 mm from the working electrode. This cell allowed for rapid testing, because it was easy to dismantle and reassemble with a fresh electrode, electrolyte and gas, but it was not designed with temperature control in mind. A new cell of similar configuration but incorporating a heated water jacket was designed and manufactured in-house for temperature-controlled experiments.

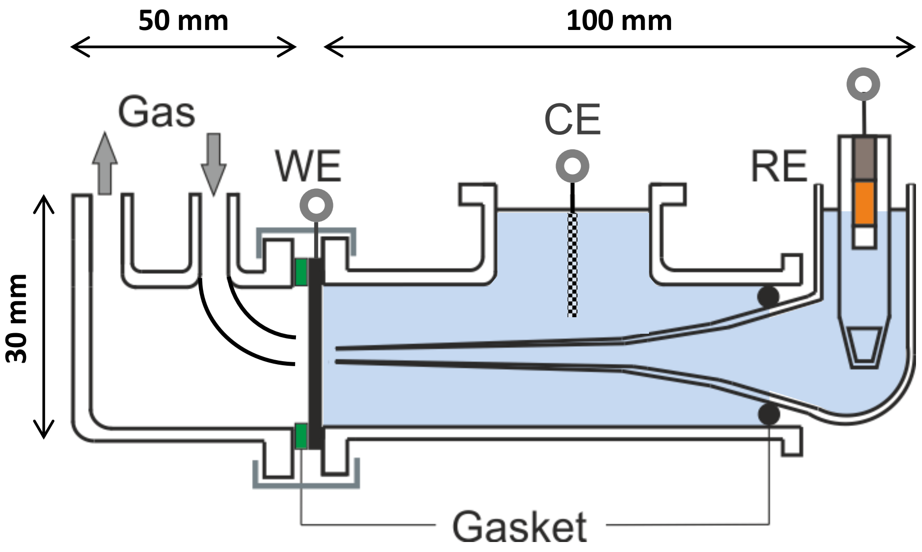

Figure 3.6 Schematic of the cross-sectional view of the Mk I glass cell. A Viton O-ring seal was used to fit the Lugging capillary and KLINGERsil® C-4400 Aramid fibre with a nitrile rubber binder was used as a gasket material to seal the working electrode.

3.5.2 Glass Cell Mk II

A second glass cell (volume ~200 cm^3) that allowed temperature control by the incorporation of a heated water jacket was produced (Figure 3.8). The cell employed the same three-electrode arrangement. A PTFE insert (Figure 3.7) was used to house the oxygen electrode electrical contact and gas supply channels. The insert accommodated circular electrodes up to 1.5 cm^2 though the geometric area exposed to the electrolyte was only 0.5 cm^2. This area is defined by the internal dimensions a Viton® rubber O-ring positioned on the electrolyte face of the electrode. A disc of Ni mesh was placed behind the electrode to act as a current collector and add mechanical support. Electrical contact was made by pressing a circle of nickel wire against the gas-face of the electrode. The wire then ran parallel to the gas channels down its own separate cavity.

All experiments in this arrangement were run under a set of standard conditions unless otherwise stated. These conditions included, static zinc-free alkaline electrolyte thermostatically maintained via the jacked cell fed by a Camlab W14 water re-circulator. An O_2 flow rate of 200 cm^3 min^{-1}, supplied to the rear face of the GDE and controlled via a flowmeter. Platinum gauze was used as the counter electrode and inhouse manufactured Hg/HgO electrodes as the reference.

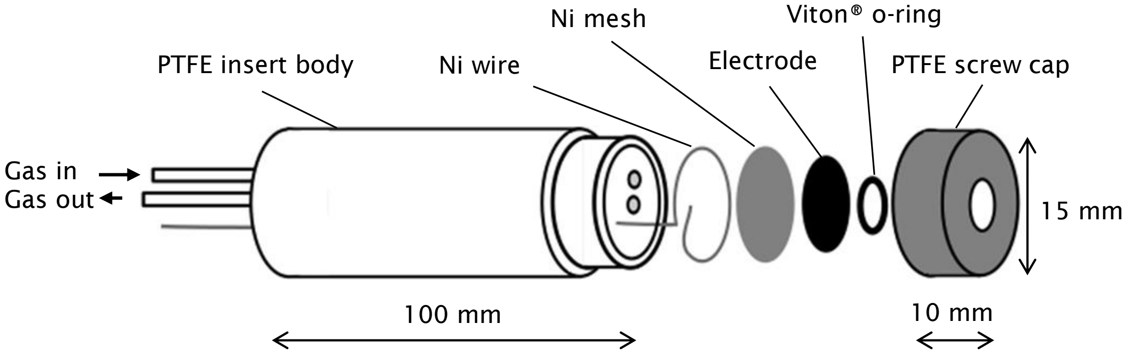

Figure 3.7 Exploded diagram showing the plastic cell insert from the Mk II glass cell which houses the air-electrode in more detail.

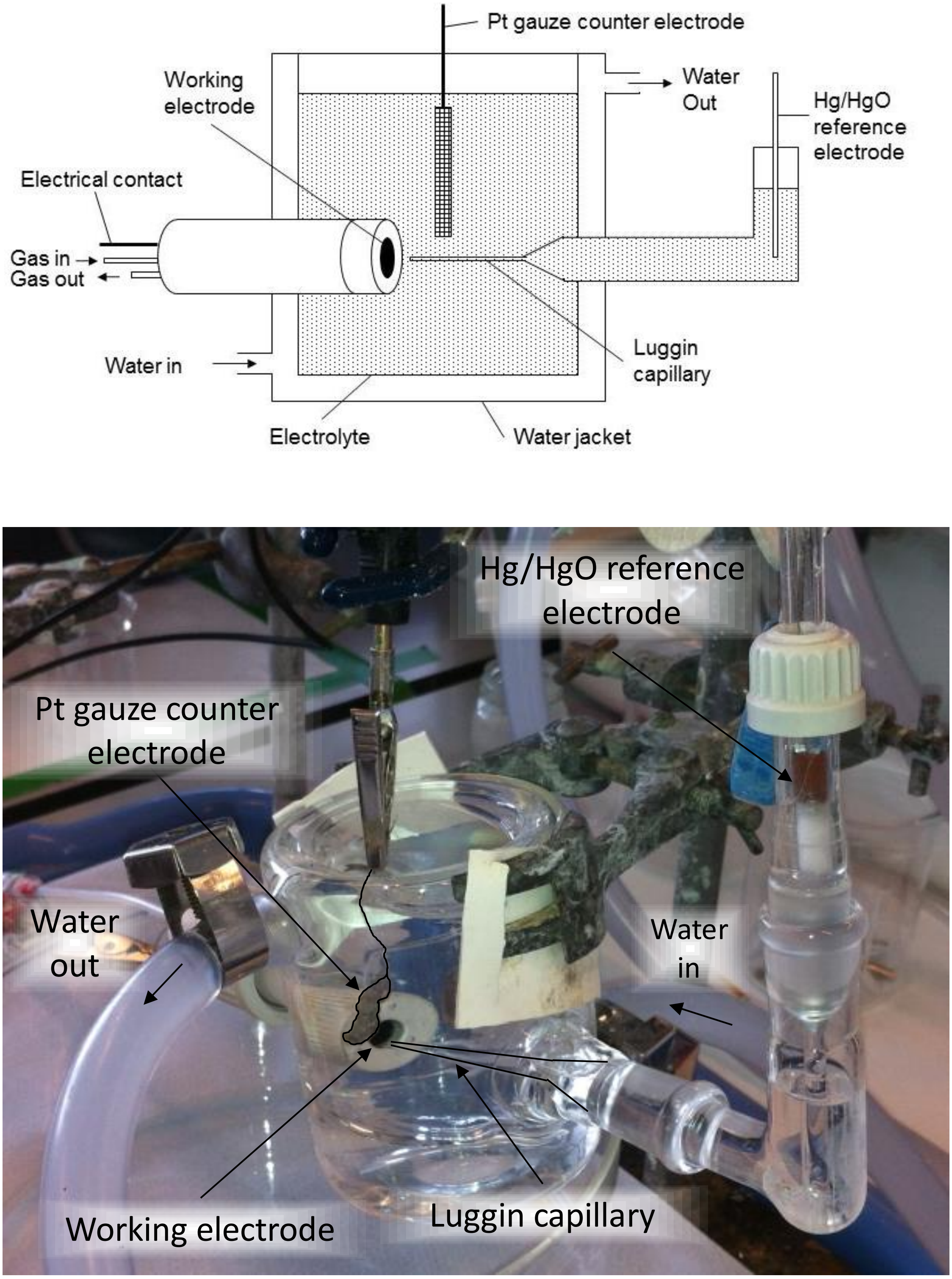

Figure 3.8 (Top) Diagram showing the cross-section of the glass cell Mk II. (Bottom) Photograph of the same set up. The counter electrode and Luggin capillary have been outlined for clarity.

3.5.3 Flow cell design and arrangement

The initial unit flow cell (manufactured at C-Tech Innovation) accommodated a 30 mm x 50 mm electrode. The electrode was sealed around the perimeter leaving an exposed geometric area of dimensions 20 mm × 40 mm. The cell was sandwiched between 20 mm thick stainless steel endplates that provide much of the structure of the cell. The positive and negative electrodes were positioned parallel to each other to ensure even current distribution. The initial inter electrode gap was between 10 mm – 20 mm dependent on separators however this will also vary as a function of state of charge dependant on the volume of zinc deposited. Properties of the electrolyte will also change as a function of SOC as during charging for example Zn will be drawn out of the electrolyte. Ensuring there is an excess of electrolyte would mitigate any variation. Alternatively, electrolyte composition could be monitored to give real time feedback on cell conditions such as depth of discharge and electrolyte moisture content. The cell was operated in an upright position (vertically). Electrolyte was pumped up through the cell whereas the gas was pumped from top to bottom. This allowed for the evacuation of any liquid in the gas side of the cell that may have leaked through the electrode. Conversely, any gas, which was formed on the electrolyte face of the electrode, would flow out of the top of the cell. This was to enable any gas which made its way into the electrolyte to readily escape out through the top of the cell. If the cell had been run horizontally any gas evolved off the electrolyte facing sides of the electrodes could have become trapped inside the cell potentially masking the electrodes. These issues could be eliminated by tilting the cell in such a way as to direct any trapped gas away from the electrodes, altering the cell design or by adding a relief valve to remove any gas which became trapped. However, these solutions were not required by simply setting the cell upright during operation. The anode consisted of a carbon polymer composite structure (SGL Group) with planar geometry; it was mounted flush with the electrolyte flow channel and a metal plate allowed electrical contact to the rear face. The oxygen electrode was mounted to a gasket or separator plate with a window to prevent leaking and ensure that only the desired area of electrode was exposed to the electrolyte. This additional layer however recessed the electrode from the electrolyte flow channel by 1 mm – 2 mm. Although non-optimal, the cell was designed for rapid testing and interchange of electrodes of various dimensions. For a more commercial design, better sealing would be implemented so the electrode sat flush to the flow channel. A flow field plate, which incorporated channels for gas flow and the current collector, was positioned to the rear face of the positive (air) electrode. It consisted of alternating strips of ~3 mm in diameter stainless steel ridges and gas channels running vertically up the electrode. There is a large body of patents filed as well as literature which describes the various designs for flow field plates and flow distributor manifolds.[142, 143, 144, 145, 146] Studies have been performed practically, computationally through simulations and mathematically through theoretical investigation.[146] Two of the most common designs of flow fields found in the literature are parallel and serpentine. It is currently understood that serpentine-style flow fields provide the best performance per cell. However, the associated pressure drop of serpentine flow fields causes a significant parasitic loss especially when stack systems are considered.[142] A radial design has also shown benefits over serpentine if humidity of the gas is an issue.[142] For optimal performance the pressure and flow of electrolyte should remain constant across the rear face of the electrode to ensure even current distribution. The design of such plates has not been extensively explored for the zinc-air system and as the availability of gas to the electrode is critical this could be further explored.

The series of layers described slotted onto posts on the end plates to prevent misalignment of the electrodes. The layers were held together under compression applied by tightening bolts running through both end plates perpendicular to the electrodes. The rig facilitated control of both the gas and electrolyte flow. Oxygen was supplied from either ambient laboratory air via a compressor (flow rate = 10 dm^3 min^{-1}) or direct from a compressed gas cylinder. The 500 cm^3 of electrolyte was circulated from the reservoir through the cell by peristaltic pump (Cole-Pamer MasterFlex® L/S). The pump was fitted with a MasterFlex® L/S EASY-LOAD® 3 pump head. Charge/discharge cycling involved applying a load across a cell for a set period or until the potential reached a predetermined cut off. At this point, the cell was discharged at a constant current and changes in potential were recorded. The cell was controlled using a multi-channel BaSyTec® battery-testing unit that simultaneously measured full cell and individual electrode potentials. Values for individual electrodes were measured against a reference electrode located in the electrolyte reservoir. Although this was nonideal it did provide consistent values which fitted very closely to anticipated values. If the cell were to be redesigned an opening would be made to allow this electrode to be present in the cell itself however prior consideration to how this might affect fluid flow particularly in the inter-electrode region would have to be made.

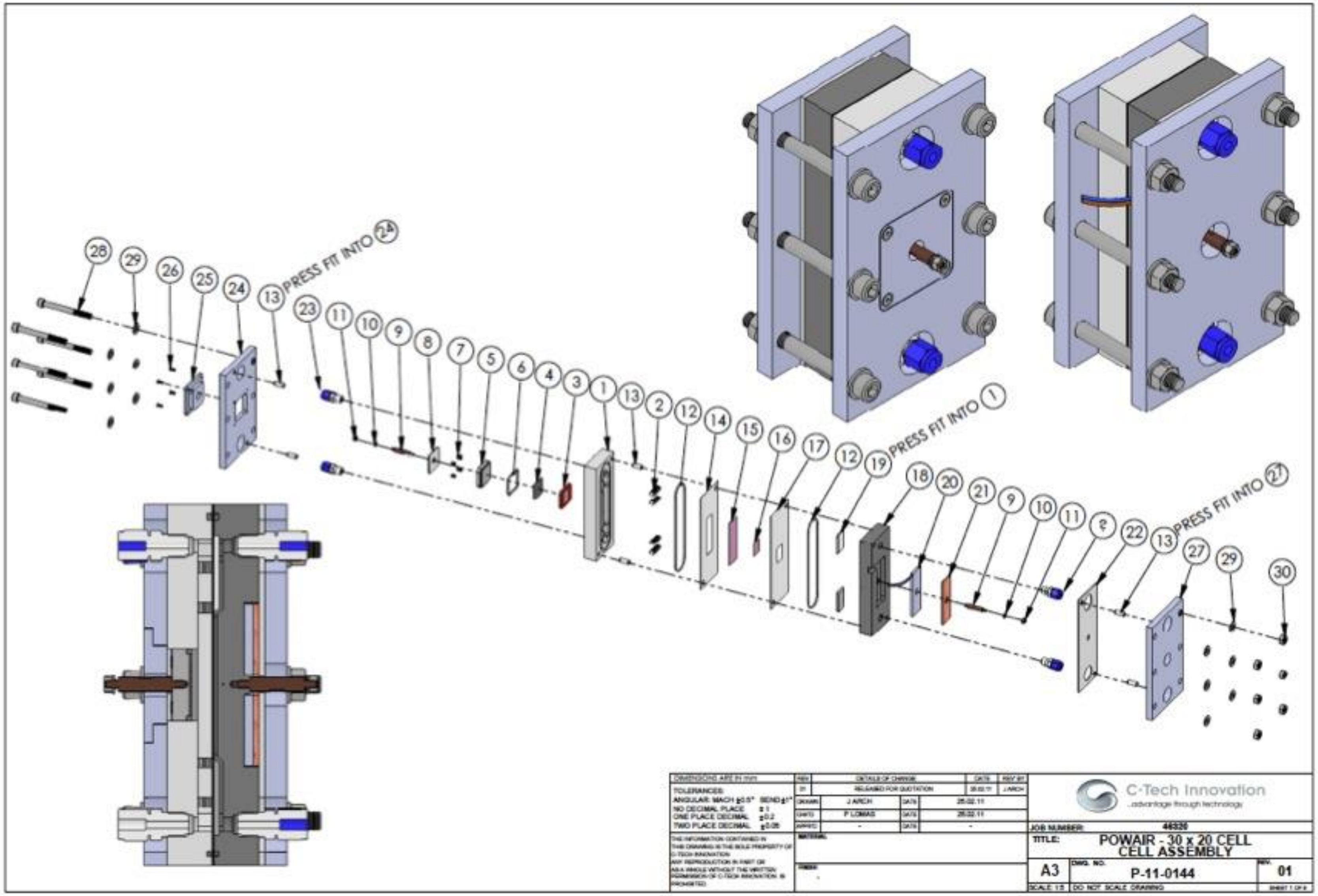

Figure 3.9 CAD drawings showing a) isometric views of the front and rear of the cell b) a cross-sectional view c) exploded view of the individual cell components 1-30.

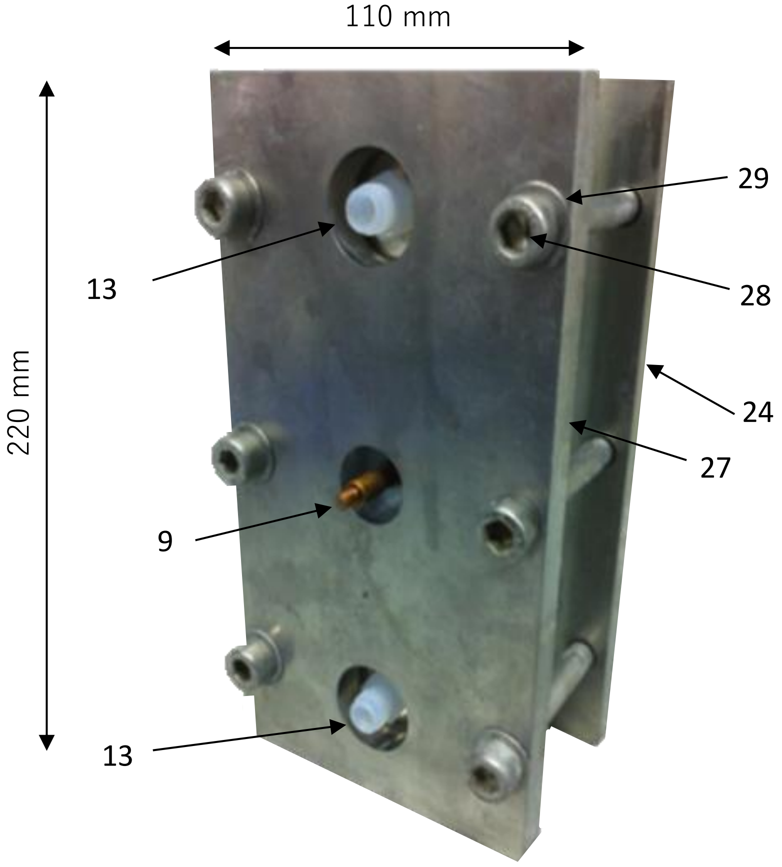

Figure 3.10 Image of the Mk I flow cell when assembled.

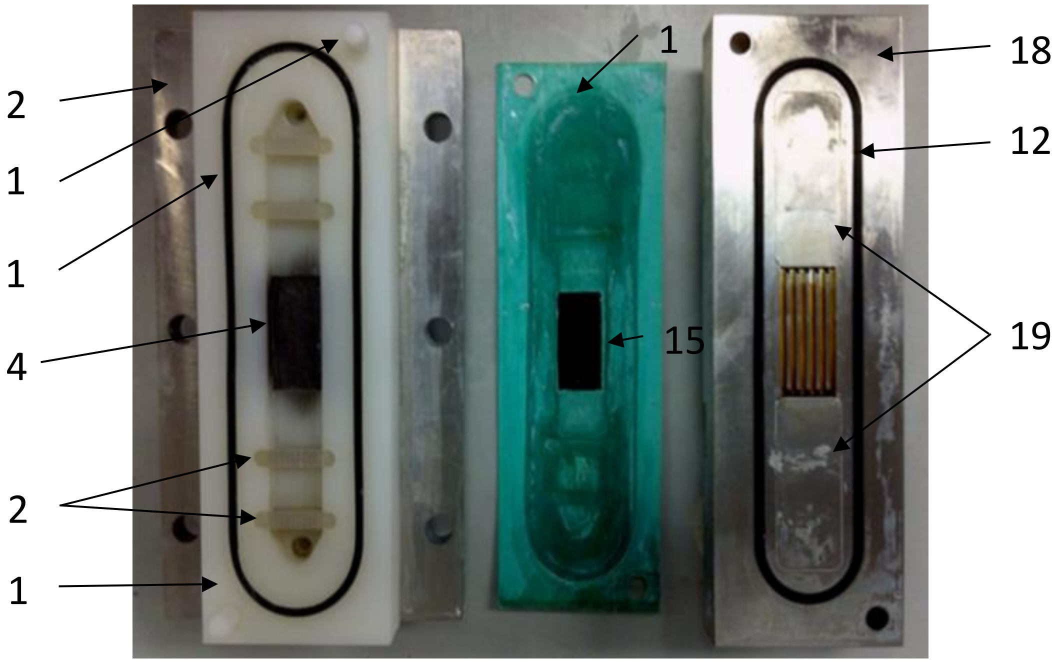

Figure 3.11 Image of the disassembled Mk I flow cell (after use) showing the internal layout of the cell.

Table 3.2 Table detailing the components shown in Figure 3.9, Figure 3.10, Figure 3.11.

Part number	Item
1	Cell body (plastic) with recess (electrolyte flow channel)
2	Electrolyte flow distributors/internal support structure
3	Rubber gasket
4	Carbon polymer composite (SGL Group) zinc electrode
5	Stainless steel plate
6,12	Viton O-ring
7,26	Metal screws
8	Plastic spacer
9	Brass rod threaded at either end
10, 29	Metal washer
11, 30	Metal nut
13	PTFE peg
14,16	Optional spacers
15	Interchangeable air-electrode
17	Cell divide with window for air-electrode
18	Carbon block with integrated gas channels
19	Stainless steel plate
20,21	Temperature sensor (not installed)
22	PTFE spacer
23	Swage lock fitting
24,27	Stainless steel end plates
25	Stainless steel plate
28	Metal bolts

The electrolyte pump was calibrated so that it was possible to equate the arbitrary pump rotation speed dial value to the volumetric electrolyte flow rate through the cell (Figure 3.12). The calibration was achieved using the pump at increasing speed settings to circulate a known quantity of fluid (500 cm^3) from the reservoir loop. The time taken to circulate a known volume (500 cm^3) of the fluid was recorded allowing calculation of an average rate. This calibration was carried out with water at 20° C to act as a reference as well as for 8 M KOH + 0.5 M ZnO at both 20° C and 60° C. This accounted for the variation in viscosity associated with temperature. At slow speed the pump had insufficient output pressure to draw a fluid through the tubing, so no flow was recorded until a pump speed setting of three, after this point, there was an approximately linear response in flow rate with increasing pump speed. A plateau in flow rate for the KOH solutions at around pump speed seven was witnessed. The plateau in rate can be attributed to the greater viscosity of the electrolyte compared to water. The operational flow rate of the electrolyte using this pump was therefore between 1 cm^3 s^{-1} and 7 cm^3 s^{-1} for an 8 M KOH + 0.5 M ZnO electrolyte. The pump was later upgraded to one with a digital display and programmable flow rates allowing for more precise control and therefore more reliable flow rates.

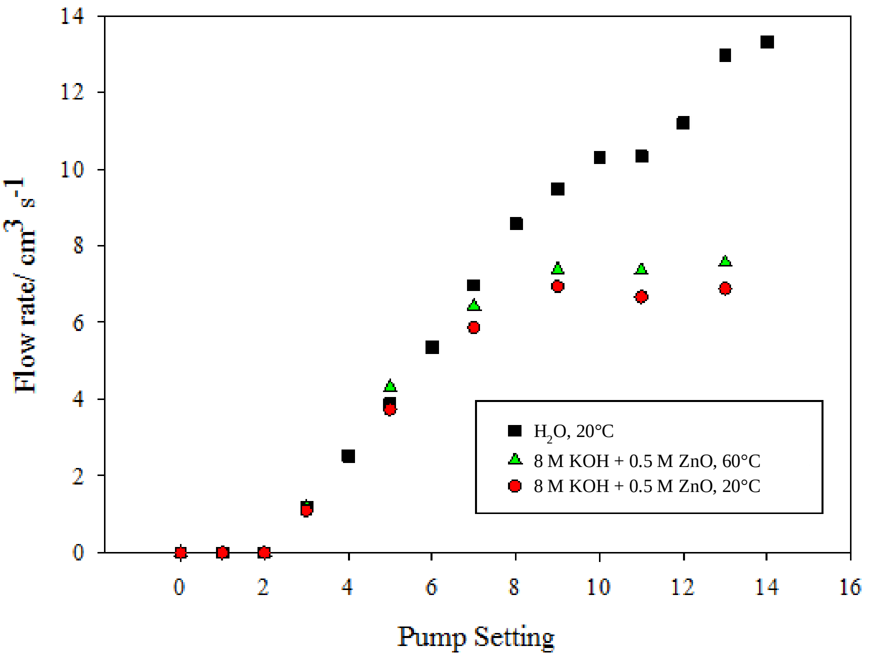

Figure 3.12 Peristaltic pump flow-rate calibration. Showing the correlation between pump rotation speed (arbitrary pump dial setting) and volumetric flow rate of electrolyte through the cell for fluids at 20˚C and 60˚C.

3.5.3.1 Developments and additions to initial design

A water-jacketed electrolyte reservoir allowing temperature control of the system was an early addition to the rig. The jacketing allowed operation at 60°C, which had been shown to be optimal for catalytic activity by the catalyst development team. On longer runs (10s of hours) at this temperature moisture from the electrolyte was evaporating. As the liquid evaporated a more concentrated solution was produced, which had the advantage of slightly increasing voltage efficiency with time, because of the increased conductivity. Excessive evaporation however could eventually result in a significantly increased viscosity as well as the possibility of the electrolyte drying out completely over time. Ultimately, this would result in significant changes in the flow properties of the fluid through the cell as well as its eventual failure. For this reason, a silicone rubber lid was fashioned for the top of the reservoir with appropriate holes for all electrodes and tubing. In the final design, the electrolyte would be sealed inside the system with inlets and outlets to add moisture and remove gas pressure as appropriate. These controls would ensure that the electrolyte was kept within desired operating parameters, for conditions such as conductivity or viscosity. Such properties could be used to monitor the system health over time. The possibility of the production of hydrogen gas as a parasitic reaction at the Zn electrode has led to the consideration of the addition of a water condenser placed over the reservoir on a laboratory-scale. Allowing the gasses produced to be extracted safely and preventing moisture from escaping. The addition of a membrane to the cell to ensure separation of any evolved hydrogen or oxygen could be considered to minimise any risk of creating an explosive mixture of gases. In the final system, these gasses could be collected and either reused, sold on or in the case of hydrogen, used in a connected fuel cell to produce energy, thus mitigating losses in efficiency through its production.

This was then replaced with a serpentine plate. Once again this was fed from bottom and then the channels which run horizontally snake up to the outlet positioned at the top.

3.5.3.2 Gaskets and separators

A variety of gasket and separator structures have been employed to ensure adequate sealing of electrodes in the flow cell. Each electrode structure required different engineering solutions to ensure no electrolyte could pass around the edges of the electrode and result in premature flooding of the gas face.

An improvement to the gasket/electrode design, was therefore required to reduce leaking and produce more representative data. All gaskets were leak tested using a metal foam electrode because this was the most difficult to seal owing to its porous structure. Carbon paper electrodes required less sealing because of their high hydrophobicity and pseudo 2-D structure. To date, no mesh or woven cloth has been sealed successfully as wicking though capillary action around the edge of the electrodes occurs rapidly.

Chapter 4: Results: Air-electrode introduction

The bifunctional air-breathing electrode is the component that contributes the biggest voltage inefficiency to the cell (see Chapter 2:). These electrodes often contain rare, expensive catalysts, such as platinum. Air-electrode development (architecture and catalyst choice) therefore has taken a leading role in this project. Studies on catalyst materials and electrode architectures spanned scales from 1 cm^2 to 600 cm^2. Rapid screening was carried out on the 1 cm^2 - 2 cm^2 scale, testing novel architectures/catalyst combinations with iterations of promising candidates leading to scale-up to the 600 cm^2 electrodes. This chapter will discuss the rationale for the materials selected and the structures pursued. Further evaluation of selected materials as well as modifications to the fabrication process to optimise electrochemical performance and stability will be discussed in subsequent chapters.

4.1 Commercial electrodes

Gaskatel, produces a series of gas diffusion electrodes under the commercial name BiPlex®.[147] Two electrodes they produce are claimed to have applications in zinc-air batteries, one with an active layer comprised of manganese dioxide and carbon (referred to as MOC). The second electrode, which utilised silver/silver oxide in place of the manganese oxide (abbreviated to OXAG).

The active layers of the Biplex® electrodes are produced using a dry mixture of catalyst and PTFE powder that is extruded into a sheet approximately 1 mm in thickness. The layer formed is then laminated onto a broad weave gold plated nickel cloth. The mass of the active layer for the OXAG electrode is approximately 120 mg cm^{-2}. The exact ratio of catalyst to carbon, is not disclosed by the manufacturer, but as silver is a component the catalyst content would need to be low to be commercially viable on a large-scale. The use of precious metals such as gold and silver suggests that the cost of the product is not the main priority. Due to its limited scale production and limited present market, the material is likely only cost effective for small-scale testing. To scale this material for kW - MW stacks is likely to prove prohibitively expensive for an application like the POWAIR system. The specific variants of the electrodes tested come with an air-breathing PTFE backing on the catalyst face to aid hydrophobicity. The backing material was not electrically conductive therefore electrodes were orientated with the backing exposed to the gas side of the cell. Consequently, electrical contact was made on the face of the electrode exposed to the electrolyte partially masking the surface. Alternatively, current could have been taken from around the perimeter of the electrode although, this method can lead to poor current distribution and spikes in current densities at contact points, particularly for larger-scale electrodes. The design of the glass cell and its insert were also not designed to accommodate electrical contact at the perimeter.

The Gaskatel electrodes were tested in the Mk II three-electrode glass cell (see section 3.5.2 for cell details). Initially, a polarization curve (linear sweep voltammogram) was obtained. The potential was swept from an upper limit of 0.30 V to a lower limit of -0.50 V *vs.* Hg/HgO reference at a scan rate of 1 mV s^{-1} in 8 M NaOH. This potential window was chosen to ensure that the ORR onset potential would be observed. Figure 4.1 presents the linear sweep voltammogram obtained for each of the two Gaskatel electrodes.

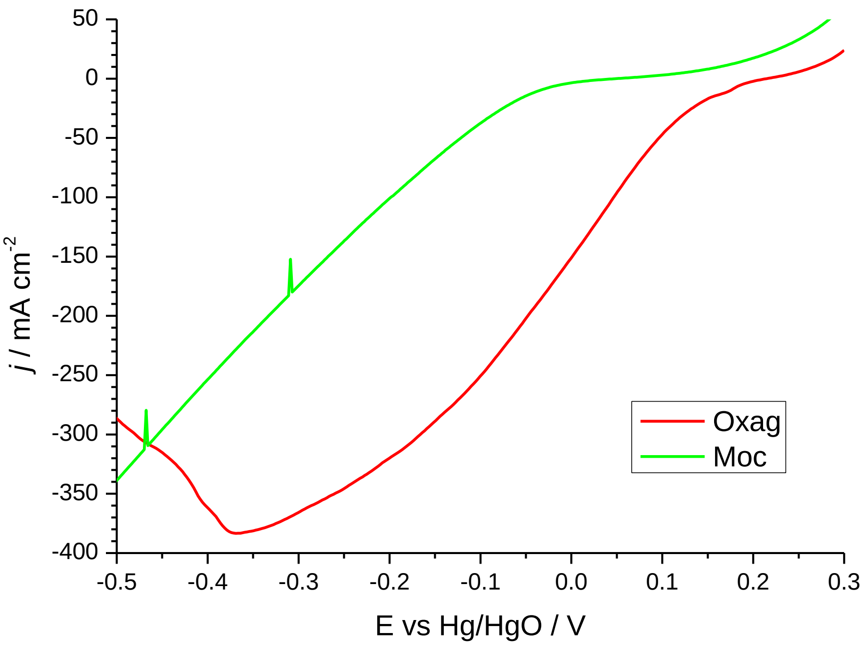

Figure 4.1 **Polarisation curves obtained for the ORR of the Gasketal 'OXAG' and 'MOC' electrodes in the Mk II glass half-cell. The potential was swept at a rate of 1 mV s^{-1} from 0.30 V to - 0.50 V *vs.* Hg/HgO. The electrolyte was unstirred 8 M NaOH thermostatically maintained at 60ºC and bottled O_2 was supplied to the rear face of the electrode at a rate of 200 cm^3 min^{-1}.**

Current densities > 300 mA cm^{-2} were recorded for both electrodes in the potential region associated with the ORR. The OXAG electrode reached 300 mA cm^{-2} at a potential of approximately - 0.15 V *vs.* Hg/HgO compared with - 0.45 V *vs.* Hg/HgO for the MOC electrode. The near linear response for the MOC electrode between potentials of - 0.1 and - 0.5 V *vs.* Hg/HgO is consistent with ohmic resistance dominated behaviour. At greater overpotentials, more negative than - 0.35 V *vs.* Hg/HgO, the reduction current observed at the OXAG electrode began to reduce. This reduction may be due to poor oxygen transport to the active catalytic sites, flooding of the gas diffusion structure or the loss of catalyst material. At potentials, more positive than 0.20 V *vs.* Hg/HgO, anodic currents were observed at both electrodes.

Because the OXAG electrode produced a lower overpotential for the ORR reaction, it was further tested using constant current (50 mA cm^{-2}) potentiometry switching between ORR and OER. The voltage *vs.* time plot is shown in Figure 4.2. The electrode was cycled in static 8 M NaOH electrolyte thermostatically maintained at 60°C. Oxygen gas was supplied via a compressed gas cylinder (regulator pressure 1 bar) and restricted to a flow rate of 200 cm^3 min^{-1}. The electrode was first subjected to 1 h of oxygen reduction, followed by 1 h oxygen evolution. Although in a functional battery, the charging (OER) reaction would be the initial step inorder to deposit metallic zinc. The ORR reaction was run first to mitigate any damage/degradation to the electrode caused by the highly positive electrode potentials and gas bubble formation within the structure during oxygen evolution.

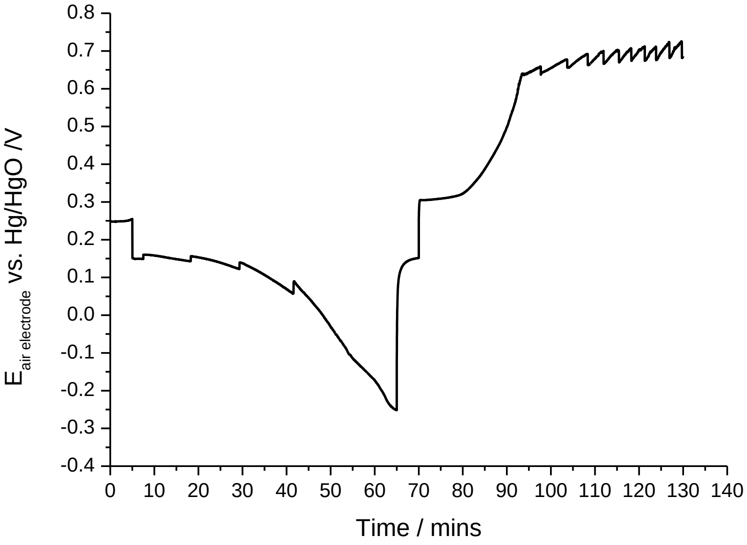

Figure 4.2 Potentiometry measurements maintained at constant current for the Gaskatel 'OXAG' electrode in static 8 M NaOH. Both the oxygen reduction and oxygen evolution reactions were observed for 1 h. The current was held at 50 mA cm^{-2} for both reactions. The electrolyte was thermostatically controlled at 60°C and O_2 was supplied to the rear face of the electrode at a rate of 200 m^3 min^{-1}. The OCP was measured for 5 minutes followed by 1 h held at a current density of -50 mA cm^{-2} afterwards the OCP was observed for a further 5 minutes before the current was raised and held at 50 mA cm^{-2} for a final hour.

A measurement of the open circuit potential (OCP) was taken preceding each step. The initial open circuit potential was approximately 0.25 V *vs.* Hg/HgO. The voltage immediately dropped to 0.15 V *vs.* Hg/HgO upon application of the reduction current. This correlates with what was seen form the LSV (Figure 4.1). During the ORR, the electrode potential dropped gradually from 0.15 V to around –0.30 V *vs.* Hg/HgO over an hour. At 50 mA cm^{-2} there was initially a strong correlation between the polarisation curve in Figure 4.1 and that from the galvanostatic measurement (Figure 4.2). This relationship was not sustained for the constant current measurements and as the time increased past 30 minutes, the potential became considerably more negative. This is possibly an artefact of the increased timescale of the galvanostatic measurement compared to the relatively short linear sweep experiment and likely indicates there is a gas diffusion limitation or degradation of the catalyst. The effects of oxygen mass-transport are more likely observed once any gas trapped in the structure has been exhausted and the supply is limited purely to the flux of new material. It is important to note this variation however, as it was observed with several of the electrode structures tested later in the thesis and highlights an experimental difficulty of correlating the intrinsic performance of small-scale catalyst development tests with operational gas diffusion electrodes. In other words, the structure of the gas diffusion layer along with the supply route of oxygen to and into the electrode is a non-trivial aspect of developing large-scale electrodes. Cai et al in a recent review highlight the fact that the majority of catalyst work in the field is performed using a (RDE) rotating disc electrode and that catalysts that show high activities in RDE testing may not perform well in actual Zn–air battery device.[148] They suggest that electrode structures and cell design are likely to prove equally as important as hight catalytic activity.

The polarisation curve was only carried out over the scale of a few minutes whereas the potentiometry used a far greater period, 1 hour. Physical degradation of the electrode was observed during the 1 h cycle testing. The electrolyte surrounding the electrode turned from clear to a grey/brown colour. A sample of the fouled electrolyte was collected, dried and examined using EDX. No Ag peak was observed to be present in the spectra, possibly because of the low detection limit of the technique, (1000 – 3000 ppm; > 10% wt.%). It is likely that any Ag would be masked by the excess of sodium hydroxide present in the sample. To gauge the true extent of dissolution of the material precise gravimetric analysis of an electrode before and after exposure to electrolyte could be used. Alternatively, a more sensitive analytical technique such as ICP-MS could be used to monitor the electrolyte composition.

After the ORR period, the applied current was stopped and the OCP was observed for 5 minutes. The potential rapidly became more positive, tending towards a plateau of 0.16 V *vs.* Hg/HgO, which was 90 mV more negative than at the start of the ORR period. Upon commencing the period of OER operation, potential is initially low (0.4 V) but quickly becomes more positive, up to 0.7 V, likely because of electrode or catalysts degradation. At the onset of the anodic current period, the electrode performance was initially favourable for oxygen evolution and gas bubbles were observed at the liquid/electrode interface. This process is exhibited in the voltammetry in the form of the saw-tooth peaks for the OER. Bubbles nucleate on the surface of the electrode, masking the surface and its active sites, reducing the surface area of the electrode. As the bubbles grow, an increasing proportion of the surface becomes engulfed while the remaining uncovered active sites pass the same current. The potential required to force this current correspondingly increases. Once the bubbles reach a critical size they detach from the electrode surface, re-exposing the active sites resulting in a rapid drop off in potential. The oxygen may therefore be evolved predominantly from the front (electrolyte facing) surface rather than being ejected from the rear (gas facing) surface.

The apparent onset-potential for the OER is lower than anticipated (ca. +0.30 V *vs.* Hg/HgO), unlikely corresponding to oxygen evolution and more likely to the oxidation of silver. Precise observation of the solubility of Ag_2O in alkaline solutions has been investigated since the 1930s for example by Johnston et al.[149] The authors showed that the solubility of Ag_2O increases linearly with the concentration of $(OH)^-$ ions in dilute alkaline solutions. At concentrations above 1 M, the solubility starts to deviate from linearity to increasing lower values. Unfortunately, the measurements of Johnston et al. were only taken up to a concentration of 6 M OH^- ions, which is lower than the typical concentrations used in this work. Johnston et al. assumed that in alkaline solution Ag_2O produces a soluble anion in the following manner:

$$Ag_2O + 2OH^- \rightarrow 2AgO^- + H_2O \qquad 4.1$$

However, the production of AgO^- species has been questioned. Evidence that the ions of monovalent silver form in alkaline solution a tri-nuclear, uni-negative complex:

$$3Ag_2O + 2OH^- + H_2O \rightarrow 2(Ag_3O\,(OH)_2)^- \qquad 4.2$$

The solubility of monovalent silver has been shown to increase with temperature. While the solubility of Ag_2O in alkaline solutions has been measured precisely in the more dilute range, more uncertainty exists with regard to the solubility of AgO. Dirkse et al. (15) have reported solubilities of AgO in alkaline solution which nearly coincide with the solubility values of Johnston et al. for Ag_2O. However, Dirkse et al. did not show that the silver species in solution was divalent, which renders the coincidence rather suspicious. Pleskov (16) has studied the instability of divalent silver ions in solution, using a rotating gold disk electrode; he found that the cathodic polarization curve of a KOH solution in contact with solid AgO only showed the diffusion current of Ag_2O. He found only indirect evidence for the presence of dissolved divalent silver in trace amounts. Solid divalent silver oxide is thermodynamically unstable in contact with alkaline solutions. Because its electrode potential is above the potential of the oxygen electrode in this environment, it decomposes to Ag_2O with evolution of oxygen:

$$Ag_2O + 2(OH)^- \leftrightarrow 2AgO + H_2O + 2e^- \ (E^0 = 0.604\ V) \qquad 4.3$$

$$2(OH)^- \leftrightarrow H_2O + {}^1\!/_2\, O_2 + 2e^- (E^0 = 0.401\ V) \qquad 4.4$$

with the first reaction proceeding in the backward direction and the second reaction in the forward direction, resulting in

$$2AgO \rightarrow Ag_2O + {}^1\!/_2\, O_2 \qquad 4.5$$

Once this process has completed (the surface is fully oxidised) the potential rapidly rises to a value of around 0.70 V *vs.* Hg/HgO and oxygen evolution is observed. This evolution of gas should be less of a problem in a flow cell arrangement as the flow of electrolyte should carry away gas bubbles from the electrode surface. Notwithstanding it does raise a safety issue; because a possible parasitic reaction on the negative electrode during zinc deposition is the evolution of hydrogen. It is therefore desirable that O_2 evolution from the liquid face is avoided in the battery system to prevent the possibility of an explosive mixture of H_2 and O_2 forming in the cell or reservoir tanks.

While the Gaskatel electrodes initially showed promise for OER and ORR under short timescale cyclic voltammetry, under prolonged periods of operation (around 60 minutes) the performance dropped considerably and the electrodes showed signs of deterioration both in physical appearance and electrochemical performance. Under the conditions of testing, the electrode did not maintain a satisfactory stability for use in a flow cell. For this reason, it was concluded that in-house electrodes would have to be manufactured to validate the flow cell design. The following sections and chapters describe the parallel cell and air-electrode development towards a functioning Zn-air flow battery.

4.2 Air-electrode substrate materials

The electrode substrate forms the backbone of the electrode, offering structural support and a scaffold onto which other materials, such as the catalyst, are applied. The substrate can also form all or part of the following roles in the electrode: current collector, gas diffusion layer or catalyst support. Therefore, factors such as electrical conductivity, porosity and stability (chemical and electrochemical) are important to consider alongside any potential performance gain when selecting materials. The materials selected for development are collated in Table 4.1. All materials were used as supplied unless otherwise stated.

Table 4.1 Electrode substrate material properties. (* http://www.goodfellow.com/E/Nickel.html)

Substrate	Supplier	Details	Porosity / pore diameter	Contact angle / degrees	Strand width / µm	Thickness* / µm	Electrical conductivity
W12722-167 Carbon paper	Johnson Matthey fuel cells®	Activated carbon coated teflonated carbon paper	Ø ~ 50 µm	132	-	200 ± 10	-
Ni foam	Goodfellow	Ni 95% purity	95%, 20 pores cm^{-2} Ø < 500 µm	N/A	Non-uniform	1600 ± 10	ρ = 6.9 µΩ cm (20° C) *
Stainless steel woven cloth (BMT50ZZ)	Haver & Boecker	Broad mesh twilled dutch weave (zig-zag)	Ø 50 µm	N/A	-	-	-
Expanded metal foil (2 Ni 4-020FA)	Dexmet Corporation	MicroGrid® Precision Expanded Metal	Ø 55 µm	98	100	75 ± 10	ρ at 20° C = 6.99x10^{-8} Ω m σ at 20° C = 1.43x10^{7} S m^{-1}
Metal coated carbon composite	Optimat®	Ni, Cu & Carbon fibre	≈ 50			19 ± 10	

* Thickness measurements made using a Mitutoyo® micrometre

Electrodes were categorised as being part of one of three groups, carbon paper, metal mesh/cloth and metal foams. Each category may refer to multiple substrates from different manufacturers but each retains the same basic structures defined by the classification. Carbon paper (Figure 4.4A) is constructed from layers of matted, randomly orientated fibres similar to the structure of paper. The fibres are bound by PTFE, which is thinly distributed throughout the electrode, however, larger concentrations are found at the intersection of fibres (Figure 4.3). The PTFE serves the additional purpose of increasing the hydrophobicity of the paper to the point that the material functions as a gas diffusion layer even without the addition of the active layer.

The metal mesh (Figure 4.4B) and cloth (Figure 4.4C) have relatively flat and smooth surfaces. This smoothness posed a challenge when applying ink/paste layers because there was little surface roughness to promote adhesion in their untreated state.

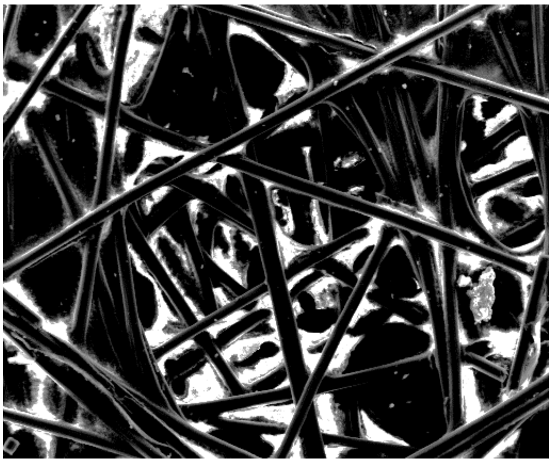

A. SEM image of carbon paper structure. The white patches show areas of fluoropolymer binder. While the black rods show the carbon fibres.

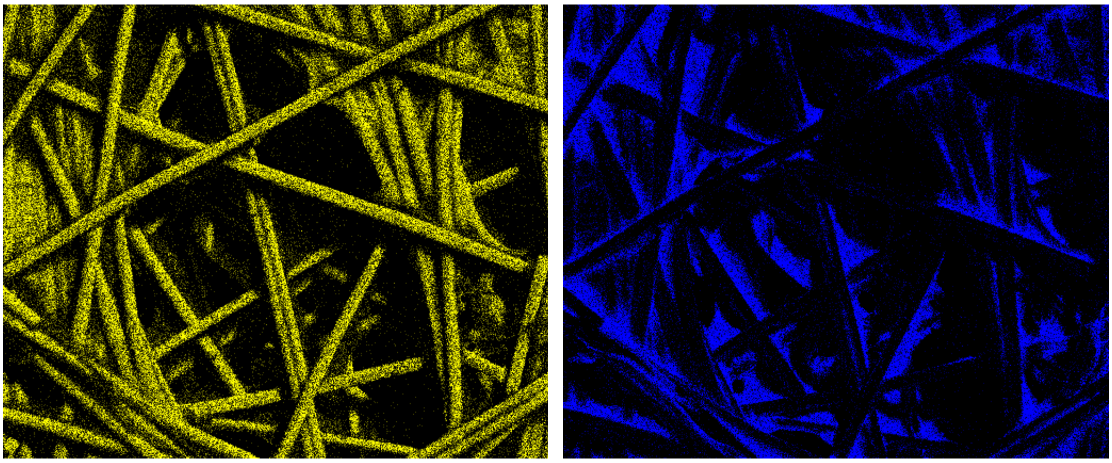

B. EDX spectral map showing the presence of carbon (yellow) representing the carbon fibres of a sample of carbon paper.

C. EDX spectral map showing the presence of fluorine (Blue) representing the presence of PTFE in a sample of carbon paper.

Figure 4.3 Spectral mapping EDX images of teflonated carbon paper showing the distribution of PTFE through the structure. Blue corresponds to high concentrations of fluorine and yellow to areas of carbon.

The foam (Figure 4.4D) is the most open and porous of the structures. The structure is truly three-dimensional compared to the planar forms of the other materials, allowing catalyst materials to penetrate deeper into the substrate. This ingression may increase the region, where a three-phase interface can occur but leads to a thicker structure. The downside to open structure is that it requires significant wet proofing to prevent the electrolyte from propagating all the way through the plane of the material. The deeply porous structure required a large amount (> 50 mg cm^{-2}) of solid material to pack the voids of the foam, ensuring hydrophobicity. The packing material could be inexpensive filler, so does not necessarily contribute to catalyst loading. Although initially promising the three-dimensional structure led to significant engineering challenges when trying to manufacture and seal the electrodes in the cell on a 10 cm^2 – 100 cm^2 scale. Most issues were resolved by modifications to the cell design rather than the electrode. Cell modification is discussed in (chapter 8-9).

A) Teflonated carbon paper

B) Dexmet corp. expanded Ni mesh

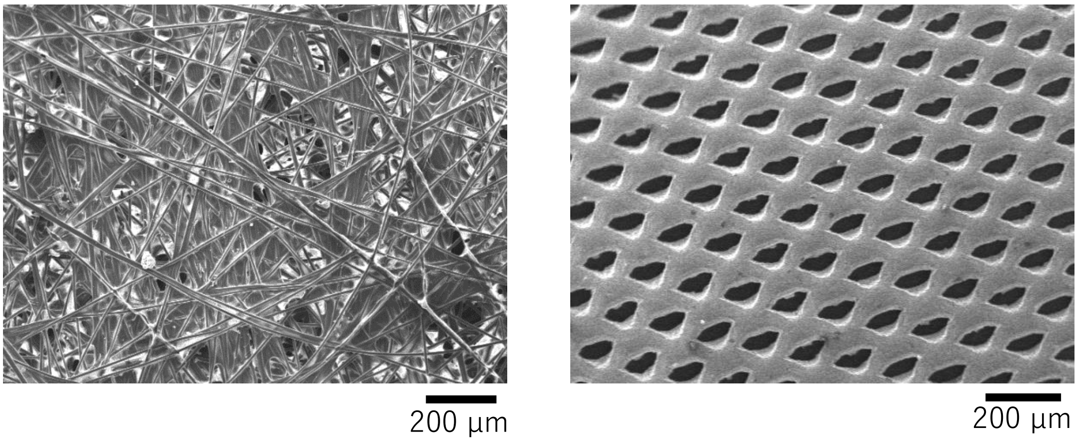

C) Stainless steel woven cloth BMT23ZZ

D) Goodfellow Ni foam

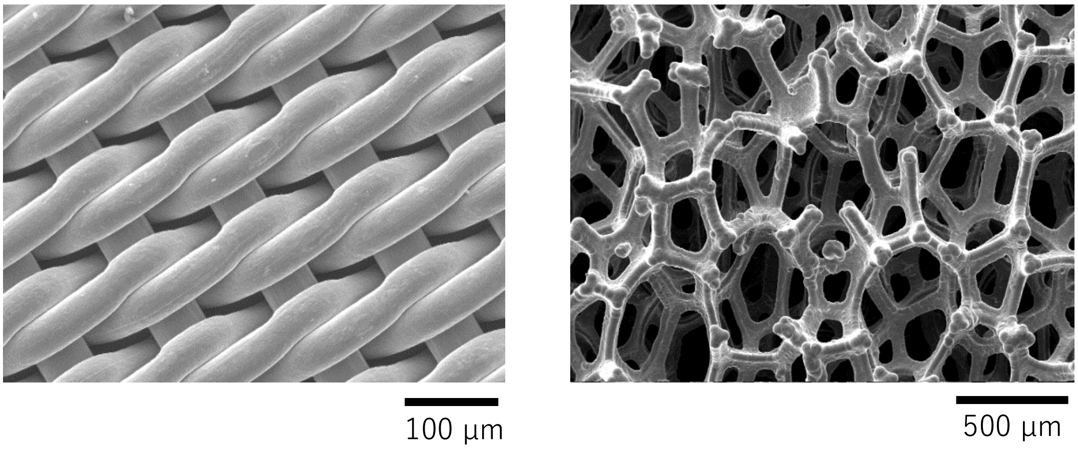

Figure 4.4. **SEM images showing the structure of the materials detailed in Table 4.1.**

4.3 Catalyst

Precious metal catalysts such as the platinum group metals show some of the highest reported activities for the ORR and so have found wide spread use as fuel cell catalysts.[66] As a consequence of extensive research by numerous research groups platinum loadings have been reduced from the few mg cm^{-2} required in the early 1990s to < 0.1 mg_{Pt}/cm^2 in more recent work while maintaining workable current densities.[66, 150, 151, 152] Despite these optimisations precious metals come at a heavy financial cost and in many instances, are of very limited terrestrial abundance. To compound matters several are not suited to the conditions associated with the potentials of the OER in alkaline media. Even with these shortcomings, there is still a significant body of academic literature, which utilise precious metals as bifunctional OER/ORR catalysts to varying success.[150, 153] A number of precious metal containing electrodes have been included in this report to act as a comparison to newer architectures. Such as Pt/C the de facto standard in fuel cell catalysis.

A more electrochemically stable and cost-effective alternative to the precious metal standard was sought for the catalyst in this research. At present, most prevalent in the literature are metal oxides and their derivatives. MnO_2 was the first to be documented and is still widespread in the literature despite questionable long-term performance.[154, 155] Mixed metal oxides are presently of great interest for this application as positive attributes specific to each component can potentially be combined, resulting in a middle ground between electrochemical activity, stability and cost. They rapidly became the focus for further investigation. Common structures include spinels, perovskites and pyrochlores. Selection of the bifunctional oxygen evolution/reduction catalyst began by ruling out materials deemed chemically unsuitable. A comparison was then made between common structures suggested in the academic literature. The materials in Table 4.2 were selected for detailed investigation. After the initial selection of catalyst material, its production moved to an in-house team to optimise its production on a small-scale 100 mg to 100 g batches. Due to the requirement of larger quantities for the 100 cm^2 electrodes manufacture was later out-sourced to C-tech Innovation, able to produce multi kg batches.

Table 4.2. Catalyst materials practically investigated in this thesis.

Catalyst	**Supplier**	**Particle size / µm**
$NiCo_2O_4$ spinel (Thermal decomposition)	Prepared in-house	≈ 0.1
$NiCo_2O_4$ spinel (Co-precipitation)	Prepared in-house	≈ 0.7
$NiCo_2O_4$ spinel (Thermal decomposition)	C-tech Innovation	≤ 20
Pt/C	Johnson Matthey	
$LaNiO_3$ Perovskite	Prepared in-house	
CoO ‘Nanocubes’	Prepared in-house	
MnO_2		
Ag/AgO	Gasketal	

There was a dramatic difference in the particle size for the two synthesis methods of producing the $NiCo_2O_4$ spinel. In house co-precipitation method produced particles with an average surface area of 70 $m^2\ g^{-1}$ compared to 10 $m^2\ g^{-1}$ for the in house thermally decomposed.

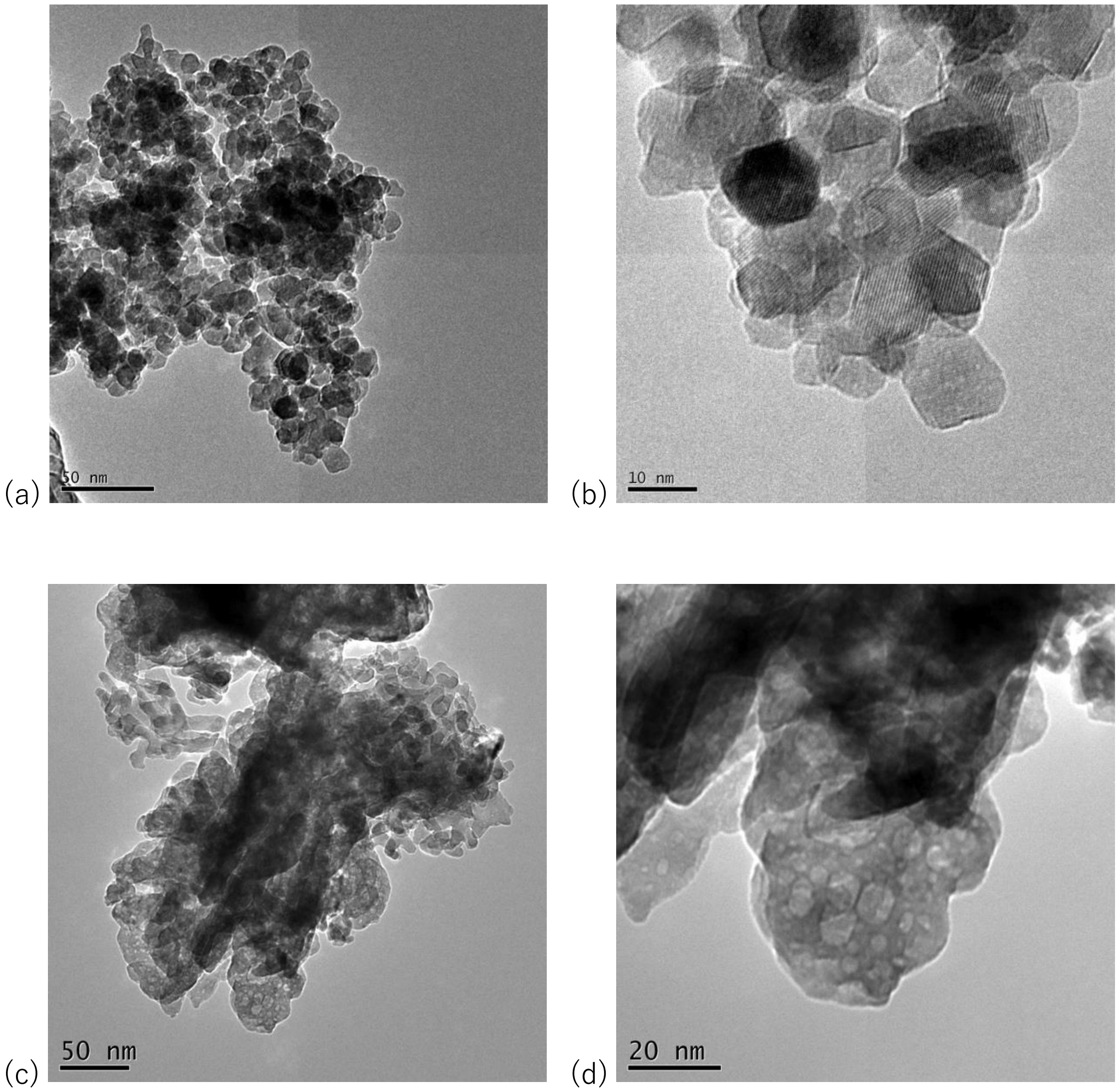

Figure 4.5 TEM micrographs of $NiCo_2O_4$ sample Co-precipitation (a & b) and Thermal decomposition (c & d) with scale bars of 50 nm on the left and 10 or 20 nm on the right. (Images acquired by S.J. Thompson as part of the Powair project)

For this reason, the co-precipitate method was favoured however this method was far more time consuming and not practical to produce on a large scale. When scaling the process up C-Tech Innovation chose for these reasons to produce the large-scale batches using ther thermal decomposition method.

4.4 Catalyst loading

Teflonated carbon paper disc electrodes were prepared with catalyst loadings between 1 mg cm^{-2} and 4 mg cm^{-2}. The catalyst ink was produced with 100 mg of thermally decomposed $NiCo_2O_4$ spinel (≤ 20 µm particle size) diluted by 0.5 mL of water and 0.1 mL of IPA. They were characterised by cyclic voltammetry (CV) and linear sweep voltammetry (LSV) to determine an optimal catalyst loading. The linear sweep voltammograms (Figure 4.6) show the correlation between catalyst loading and ORR performance. For each voltammogram, the potential was swept from 0.3 V to - 0.5 V *vs.* Hg/HgO at 1 mV s^{-1}.

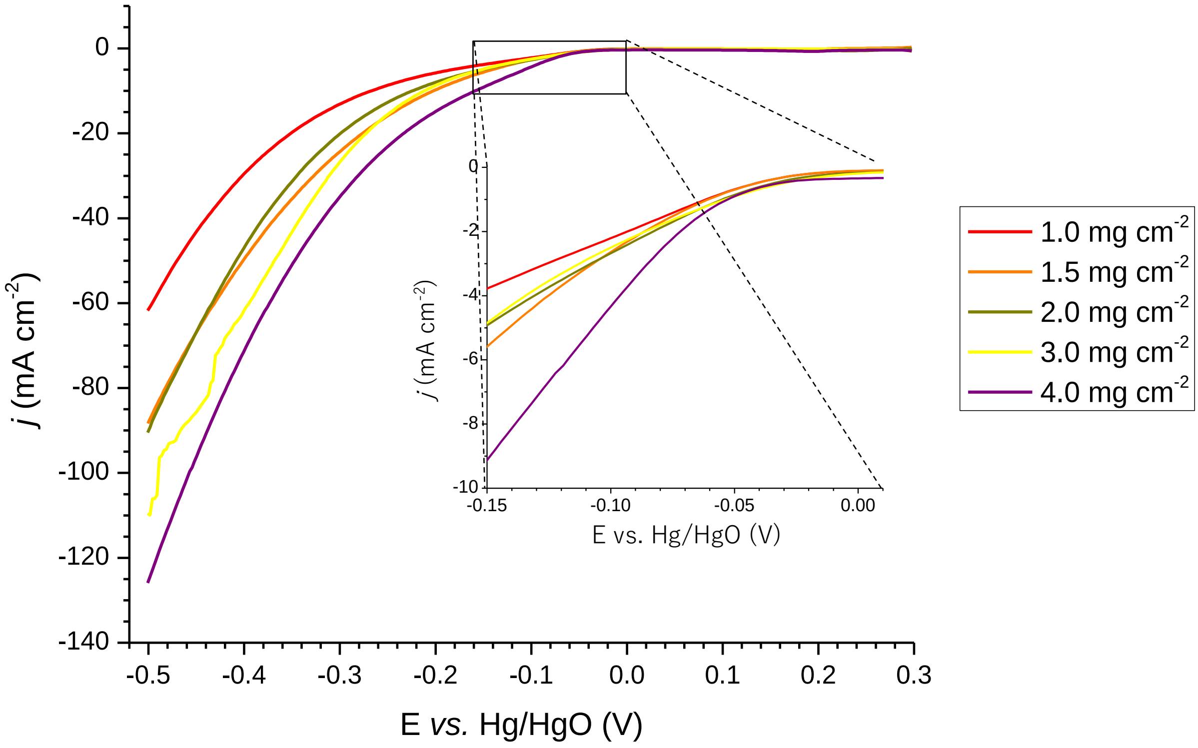

Figure 4.6 Linear sweep voltammetry for air-electrodes prepared with catalyst (⩽ 20 µm $NiCo_2O_4$ spinel, thermally decomposed) of increasing loading 1 mg cm^{-2} to 4 mg cm^{-2} (0.6 mL of water/IPA 5:1 to 100 mg of catalyst powder). The potential was swept from 0.3 V to - 0.5 V *vs.* Hg/HgO at a scan rate of 1 mV s^{-1}. Expanded section shows the onset of the oxygen reduction reaction (approx. - 0.05 V to - 0.02 V *vs.* Hg/HgO). Tested in unstirred 8 M KOH thermostatically maintained at 60° C.

All electrodes show a near identical onset potential circa - 0.05 V *vs.* Hg/HgO for the oxygen reduction reaction. This potential is an intrinsic property of the catalyst and so should be independent of loading. Whereas, the current passed approaching the lower voltage-limit, climbs steadily and diverges dependant on catalyst loading. At these potentials, other factors such as mass transport limitations become influential and so properties such as the active layer structure and the number of available active sites begin to dominate performance. The region provides a better indication of realistic electrode performance, as the conditions more closely emulate battery operation. Increasing the catalyst loading should correspond to an increased number of active sites increasing electrochemical activity and therefore current. Due to the demands of the three-phase interface however, the likely reality may be significantly more complex. Table 4.3 presents the current density at - 0.5 V *vs.* Hg/HgO for each of the electrodes. Also shown is the current density per mg of catalyst, which gives an indication of percentage catalyst utilisation. While the current density at any overpotential increases with increasing loading, the catalyst utilisation is at a maximum with a catalyst loading between 1 mg cm^{-2} and 2 mg cm^{-2}.

Table 4.3 Data extracted from Figure 4.6 showing the relationship between catalyst loading and ORR current density at - 0.5 V *vs.* Hg/HgO. The data has also been normalised to give values of catalyst utilisation.

Catalyst loading / mg cm^{-2}	*Current density at - 0.5 V vs. Hg/HgO / mA cm^{-2}*	*Normalised current density / mA cm^{-2} mg^{-1}*
1.0	- 62	- 62
1.5	- 88	- 67
2.0	- 90	- 45
3.0	- 110	- 37
4.0	- 128	- 32

Figure 4.7 presents cyclic voltammetry for the electrodes shown in Figure 4.6. For each electrode, the potential was scanned from 0.1 V *vs.* Hg/HgO in a positive direction. At 0.8 V *vs.* Hg/HgO the direction of the scan was reversed, sweeping to negative potentials. At - 0.5 V *vs.* Hg/HgO the direction of the scan was inverted once again, scanning back to the starting potential, 0.1 V *vs.* Hg/HgO. Scan rate was maintained at 25 mV s^{-1} throughout. At potentials, positive of 0.5 V *vs.* Hg/HgO the current rapidly increases corresponding to oxygen evolution. There is also a set of redox peaks at circa 0.2 V *vs.* Hg/HgO (reduction) and circa 0.4 V *vs.* Hg/HgO (oxidation). These peaks are most noticeable at 4 mg cm^{-2} and are likely due to the

Ni(II)/Ni(III) redox reaction, indicating that some of the Ni at the catalyst surface is redox active. At negative potentials, the ORR cathodic wave that was described for the linear sweep voltammograms presented in Figure 4.6 is observed. For the OER the same pattern of increasing current with increased loading does not hold true and so loading is clearly not the dominant factor controlling oxygen evolution. It should also be noted that all electrodes reached at least 50 mA cm^{-2} by 0.75 V *vs.* Hg/HgO.

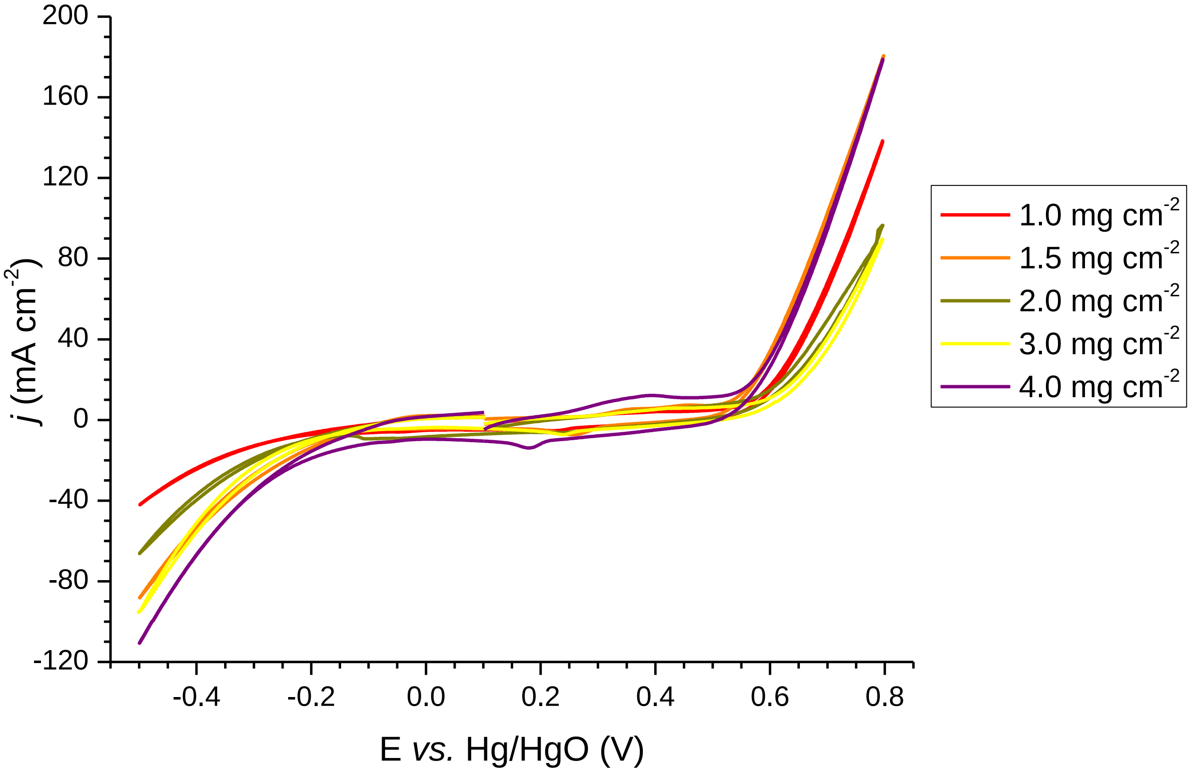

Figure 4.7 Cyclic voltammetry for the electrodes shown in Figure 4.6 prepared with different catalyst loadings (0.5 mL of water to 100 mg of ⩽ 20 μm $NiCo_2O_4$ spinel, thermally decomposed catalyst). The potential was swept positive from 0.1 V *vs.* Hg/HgO up to 0.8 V *vs.* Hg/HgO. The direction was reversed and the potential was dropped to - 0.5 V *vs.* Hg/HgO and then back to the original potential. The potential was swept at a rate of 25 mV s^{-1}. In 8 M KOH thermostatically maintained at 60°C (Mk II glass cell).

Whilst Figure 4.6 and Table 4.3 show that percentage catalyst utilisation is greatest at low (1–2 mg cm^{-2}), Figure 4.7 demonstrates that electrode performance increases with increasing catalyst loading beyond 2 mg cm^{-2}. Clearly a balance between catalyst loading and electrode performance (i.e. lowest voltage loss between OER and ORR) should be investigated. An upper limit to catalyst loading should exist, at which point the addition of more material leads to diminishing returns or no improvement at all. Electrodes with increasing catalyst loadings were manufactured. These electrodes were prepared from a single batch of ink with a dilution of 0.5 mL of water to 100 mg of catalyst (no pre-treatments) and the LSV for these are given in Figure 4.8.

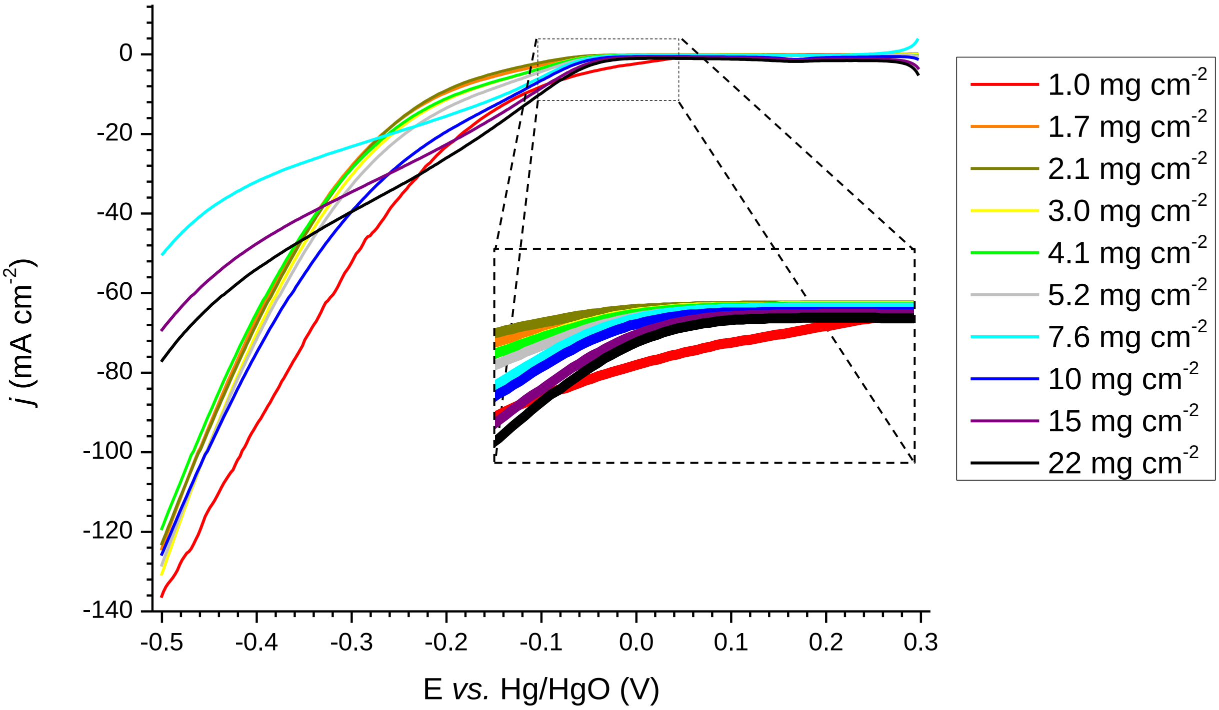

Figure 4.8 Linear sweep voltammetry for electrodes prepared with different loadings of catalyst (0.5 mL of water to 100 mg of ⩽ 20 μm $NiCo_2O_4$ spinel, thermally decomposed catalyst). Scan rate 1 mV s^{-1}. Magnified region to show the onset of oxygen reduction (approx. - 0.10 V to 0.05 V *vs.* Hg/HgO). In static 8 M KOH thermostatically maintained at 60°C (Mk II Glass cell).

Above 4 mg cm^{-2}, the relationship between catalyst loading and electrode performance is no longer straightforward. The first noteable peculiarity from the LSV is the cathodic reduction wave of the 1 mg cm^{-2} loading electrode, the onset of which is shifted by approximately + 0.1 V from the other electrodes (circa - 0.03 V) as shown in the magnification on Figure 4.8. This phenomenon is assumed to be the result of a shift in the reference electrode potential and therefore an outligher. Manually offsetting the data by - 0.1 V would bring the current density to - 96 mA cm^{-2} for - 0.5 V, which is concurrent with the established trend between catalyst loading and current density. For the graph of the CV the data for 1.0 mg cm^{-2} loading has been manually offset by - 0.1 V to demonstrate this (Figure 4.9).

The LSV for the cathodic reduction curves for the electrodes of low catalyst loadings (1–5 mg cm^{-2}) reach a value of $j_{-0.5\,V}$ at circa - 125 mA cm^{-2} showing minor variation in performance with loading. At loadings > 5 mg cm^{-2} the values for $j_{-0.5\,V}$ significantly drop to - 50 mA cm^{-2} however as the catalyst loading is increased further the performance gradually starts to recover. This is true except the 10 mg cm^{-2} loading that achieves a $j_{-0.5\,V}$ of - 126 mA cm^{-2}, which is greater than most electrodes tested. The voltammogram for the 10 mg cm^{-2} loading electrode also shows the same shaped slope for cathodic reduction as the low loading electrodes. The curve shape for the other ‘high’ loading electrodes is initially similar in form to 10 mg cm^{-2}, achieving promising current densities at potentials > - 0.2 V *vs.* Hg/HgO. But at < - 0.2 V *vs.* Hg/HgO the gradient of the curve becomes shallower suggesting a limiting factor specific to this group of electrodes.

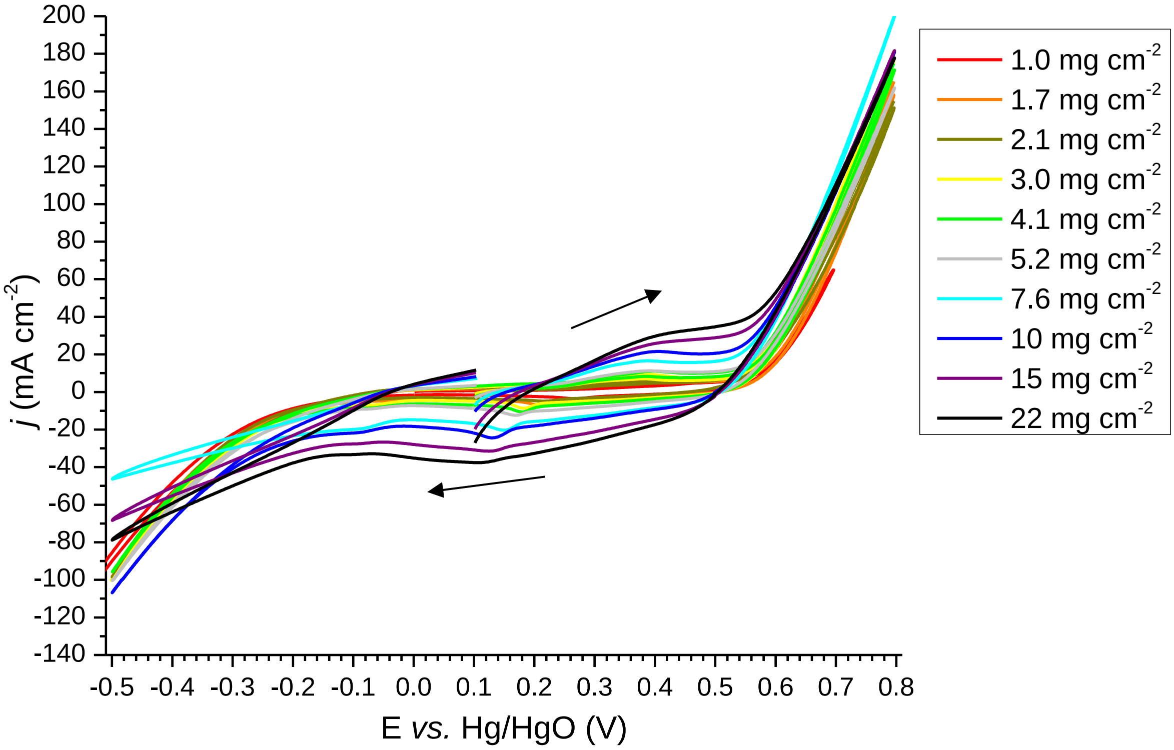

Figure 4.9 Cyclic voltammetry for electrodes prepared with different loadings of catalyst using catalyst ink of half the standard dilution (0.5 mL of water to 100 mg of ⩽ 20 µm $NiCo_2O_4$ spinel, thermally decomposed catalyst). Scan rate 25 mV s^{-1}. In static 8 M KOH thermostatically maintained at 60°C. The potential of the 1.0 mg cm^{-2} catalyst loading electrode has been offset by approximately - 0.1 V from the actual data to account for a possible systematic error; but is therefore excluded from following plots.

Figure 4.9 presents the cyclic voltammograms for the electrodes shown in Figure 4.8 with catalyst loadings between 1 mg cm^{-2} and 22 mg cm^{-2}. The same voltammetric analysis was applied to each electrode as those presented in Figure 4.7. As with Figure 4.7, at positive potentials, an anodic oxidation peak is observed commencing at circa 0.6 V *vs.* Hg/HgO that corresponds to the OER. The redox peaks at circa 0.2 V *vs.* Hg/HgO (reduction) and circa 0.4 V *vs.* Hg/HgO (oxidation) become more pronounced at the higher catalyst loadings and become broader. At negative potentials, the cathodic reduction curve is observed with the same features as described for Figure 4.7. Additionally, there is a notable difference between the current densities at the start and stop potential, 0.1 V *vs.* Hg/HgO, for each voltammogram; more so at higher catalyst loadings. Suggesting that the surface of the catalyst undergoes redox changes during the electrochemical characterisation.

The voltammetry shown in Figures 4.6-4.8 indicate that at catalyst loadings > 10 mg cm^{-2} the performance of the electrodes begins to diminish for the ORR. This can be rationalised by the fact that once the active layer reaches a critical thickness the addition of material does not contribute positively to the electrochemistry. Catalyst which was once exposed becomes isolated either physically to gas/electrolyte or electronically so that it can no longer contribute to the current. The active layer would also become physically thicker, increasing path lengths for electrical conductivity and gas transport. The cathodic reduction peaks from both the LSV and CV show that the 10 mg cm^{-2} loading electrode does not behave as expected. This one electrode is likely to be an outlier. All electrodes were produced from the same batch of ink however; the composition and homogeneity of the ink dispersion will have resulted in small fluctuations in PTFE.

One possible explanation for the apparent variation between samples could be in the application of the catalyst ink. Application method could result in differing layer thickness/number of layers require to meet the loading target. Figure 4.10 shows the number of layers of catalyst ink applied to the electrodes plotted against $j_{-0.5\ \mathrm{V}}$ achieved in LSV (Figure 4.8).

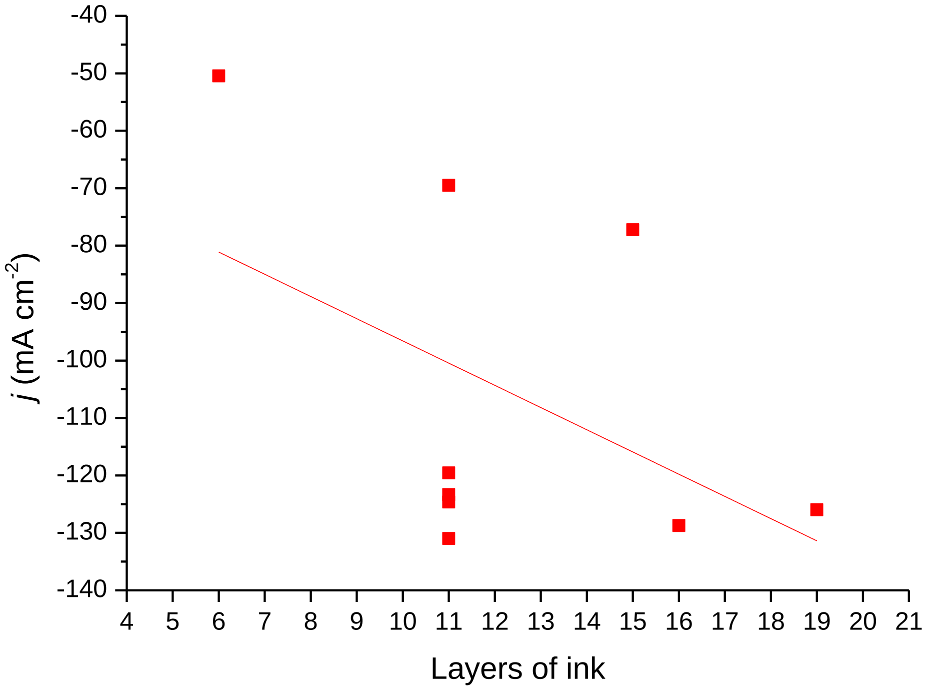

Figure 4.10 **Scatter plot of the $j_{-0.5\ V}$ for the LSV (Figure 4.8) *vs.* the layers of ink applied to the electrode.**

Despite the considerable variability in the data there is a weak correlation suggesting more layers increases for ORR performance. The fewer layers required to achieve a given loading the greater in thickness those layers will be. From this the preference would be for many thin layers over fewer thick layers. The 10 mg cm^{-2} loading electrode has the most layers (nineteen) and this may explain why it performs 75 mA cm^{-2} better than its nearest equivalent loading 7.5 mg cm^{-2} (six layers). The rationale assumed that thinner layers produced a more homogeneous active layer preventing large deposits of a single material (particularly PTFE) affecting the electrochemical surface area. It was also observed that thick layers of ink were more likely to crack during the drying process. Leading to a higher probability of delamination/flooding and interrupting electrically conductive pathways.

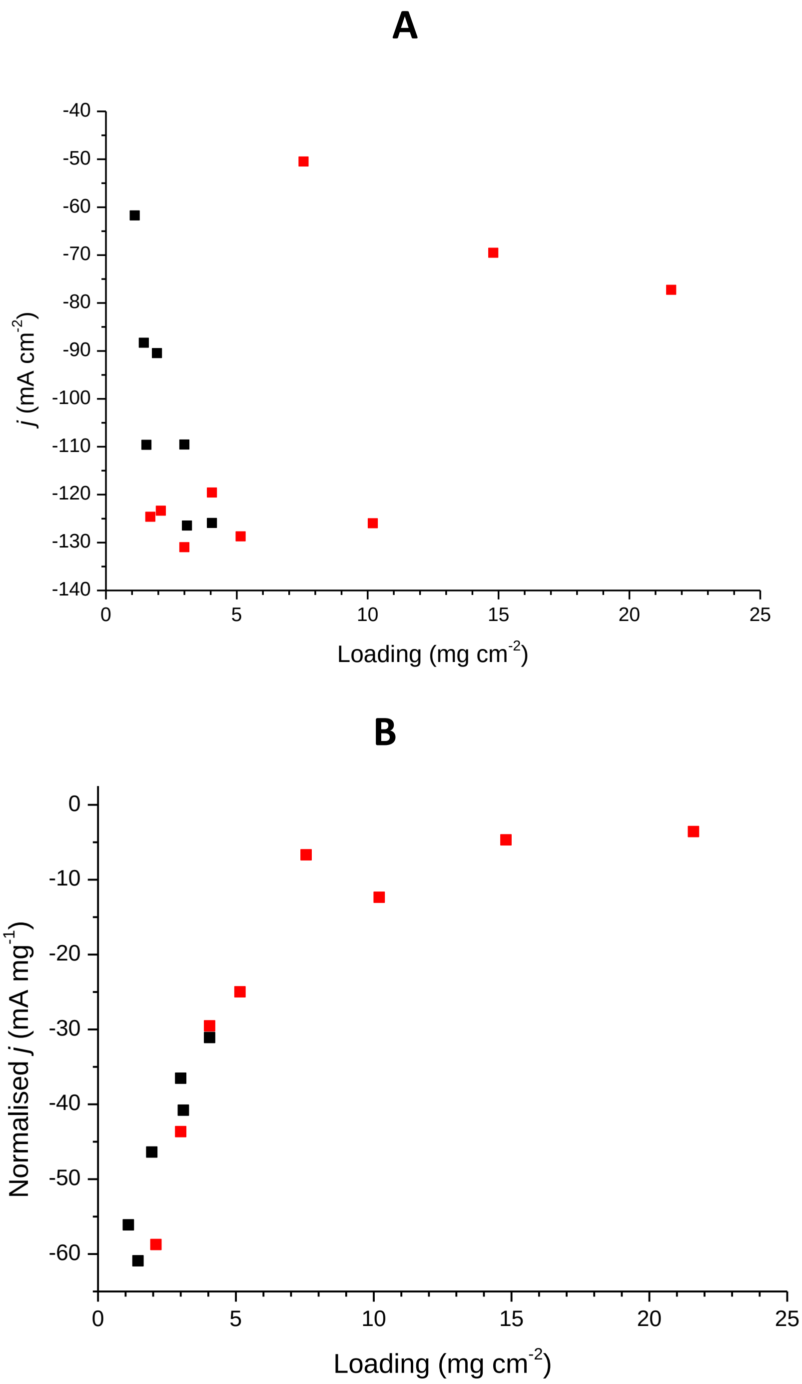

■ - Initial batch of electrodes used to produce the data in Figure 4.6

🟥 - Second batch of electrodes used to produce the data in Figure 4.8

Figure 4.11 A.) Catalyst loading of the electrode versus current density achieved at - 0.5 V, $j_{-0.5\text{ V}}$, (1 mV s^{-1} LSV) 1-4 mg cm^{-2} loading (Figure 4.6) and 1-20 mg cm^{-2} loading (Figure 4.8). B.) $j_{-0.5\text{ V}}$ normalised per mg of catalyst loading versus the loading of each electrode (1 mV s^{-1} LSV) 1-4 mg cm^{-2} loading (Figure 4.6) and 1-20 mg cm^{-2} loading (Figure 4.8).

In Figure 4.11A the values of $j_{-0.5\ V}$ for the linear sweep voltammograms of all electrodes tested in Figure 4.6 and Figure 4.8 were plotted against their catalyst loading. There is no clearly discernible pattern for this data however there is a definite cluster of points for electrodes with loadings ≤ 5 mg cm^{-2}. Most of these electrodes produced a $j_{-0.5\ V}$ between - 110 mA cm^{-2} and - 135 mA cm^{-2}. By normalising this data against the catalyst loading it is possible to gauge catalyst utilisation and observe more clearly how the addition of catalyst effects performance. In Figure 4.11B values of $j_{-0.5\ V}$ were normalised against the loading (mA per mg) and plotted against the catalyst loading of the electrodes. In this plot, there appears to be an exponential decay in the current density produced by each mg of catalyst as the loading on an electrode increases. After 7.5 mg cm^{-2} the values begin to plateau, at which point each mg of catalyst added only contributes approximately - 5 mA mg^{-1} compared to approximately - 50 mA mg^{-1} when only a single mg of catalyst is present. This neatly illustrates the notion that although electrodes with higher loading may perform comparably or better than lower loading counterparts they do so at the cost of catalyst utilisation. Catalyst loadings of ≥ 10 mA cm^{-2} are only additionally adding a few mA cm^{-2} for every mg cm^{-2} of catalyst added. Based on these results, 3 mg cm^{-2} - 5 mg cm^{-2} was selected as the optimum range of catalyst loading to continue with in the subsequent optimisation experiments. It presented a good compromise between performance, ease of application and catalyst utilisation.

4.5 Membrane

The use of a membrane to partition the battery flow chamber is not a requirement for the zinc-air flow system in contrast to many similar flow battery and fuel cell technologies. A membrane could be beneficial however as part of the air-electrode structure. This addition could aid with the maintenance of the three-phase boundary and minimise electrolyte weeping into the air-electrode. A membrane electrode assembly (MEA), which utilises a membrane as the main electrode substrate, could also be promising, as it would negate the inclusion of bulkier more complex structures.

Ion exchange membranes can discriminate which ions can pass through them in a certain direction. In the context of an electrode structure, they may also be used to add structural support, hydrophobicity, or aid in controlling the direction of gas transport away from the electrode. A range of commercial and R&D membranes were amassed for comparison. In each case, the membranes were pre-treated as prescribed by the manufacturer (soaking in a solution to hydrate the material and or exchange out elements to activate the membrane). If no pre-treatment procedure was provided by the manufacturer, they were soaked in 8 M KOH for 24 hours prior to use.

The soaked membranes were then placed in front of a Pt/C coated Toray carbon paper disc. All electrode discs used were cut from a single larger sample to ensure reproducibility. The electrodes were not hot-pressed and the membranes were simply held in contact with the electrodes by the mechanical pressure of the assembled cell. Great effort was made to ensure that there was negligible gas trapped between the two layers enabling good contact between the active layer and the membrane. The membranes investigated for this purpose, are shown in Table 4.4.

Membranes were manufactured by C-Tech Innovation, FuMA-Tech, Johnson Matthey and a team at the University of Surrey. All the membranes supplied are reported to be anion exchange membranes and so should readily conduct hydroxide ions except Nafion, which is a common proton exchange membrane. Most suppliers claim chemical stability in concentrated hydroxide at temperatures up to 50°C – 60°C. A Pt/C coated carbon paper disc without a membrane was used as a control to compare with membrane performance.

Table 4.4 Ion exchange membrane materials data and properties.

Membrane Reference Number	Membrane Name	Supplier	Thickness / µm	Stability range (supplier data)
M1	Fumapem® FAA-3	FuMA-Tech	62-84	pH 7-14 up to 60° C
M2	AM	FuMA-Tech	20-22	
M3	(MM-g-PVBz/Cl$^-$) Methylized melamine grafted poly (vinylbenzyl chloride)	C-Tech		
M4	(PTFE-AAEM) PTFE composite alkaline exchange membrane	C-Tech		
M5	CRS-PBI	C-Tech		
M6	Quaternary DABCO polysulfone	C-Tech		
M7	Nafion	Johnson Matthey	11-7	Up to 80° C
M8	AAEM (580)	University of Surrey	ca. 80 when hydrated	Up to 50° C

The membranes were tested in the three-electrode glass cell positioned on the electrolyte-facing surface of a Toray electrode coated in Pt/C catalyst. Each of the membranes were tested under the same conditions: - 20 mA cm^{-2} for 300 s in a 60° C, 8 M KOH electrolyte. Figure 4.12 shows the voltage *vs*. time plot for each membrane under ORR conditions for 300 s after a period of open circuit potential (OCP) of 30 s.

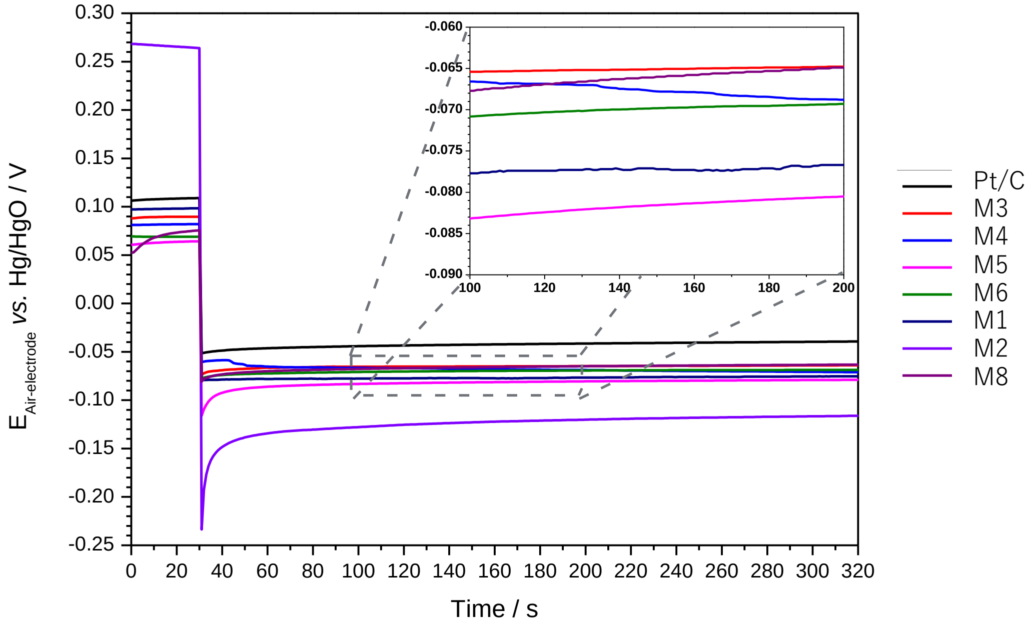

Figure 4.12 Comparison of membrane materials mechanically held in front of a carbon paper disc coated in Pt/C. Initial 30 s period of OCP followed by 300 s ORR - 20 mA cm^{-2} in static 8 M KOH electrolyte thermostatically maintained at 60°C.

An anodic current was applied after the electrochemistry shown in Figure 4.12 however as the electrodes were Pt/C based; their instability during OER meant that the data obtained was inconclusive. A dramatic jump in the evolution potential to a value of about 1.1 V occurred shortly after the current was applied for most electrodes. This elevated potential corresponds to the expected response of the carbon support and not the catalyst. Three of the electrodes tested which did not immediately degrade after the switch to evolution potentials are shown in Figure 4.13.

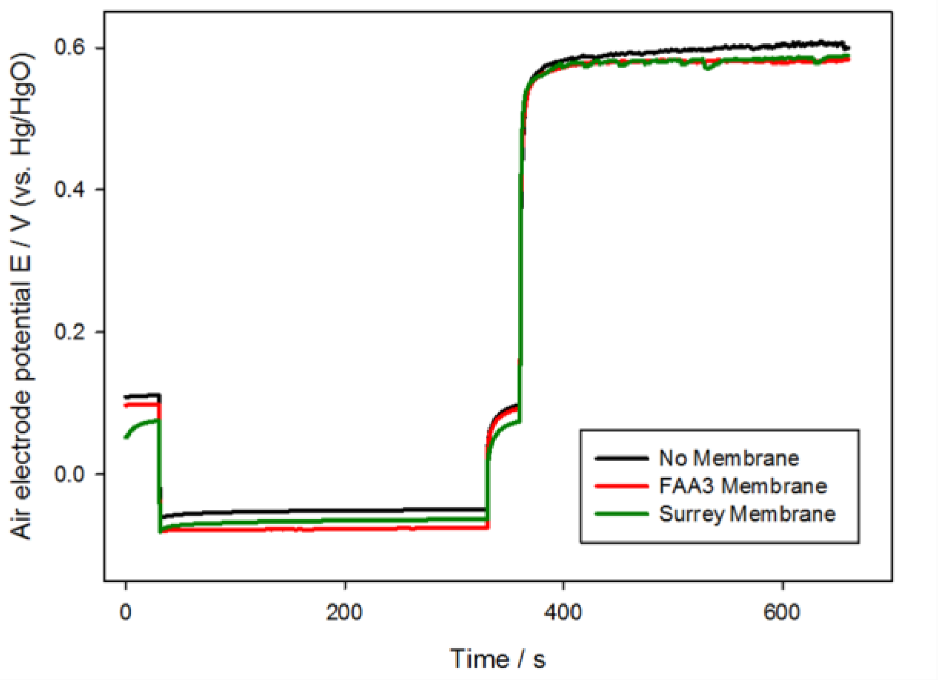

Figure 4.13 The reduction and oxidation potentials at ± 20 mA cm^{-2} for Pt catalysed electrodes with 1.) No membrane, 2.) An FAA-3 membrane clamped to the front face of the electrode, 3.) University of Surrey membrane clamped in front face of the electrode, Pt mesh CE, Hg/HgO RE, bottled O_2 supply to gas side flow rate of 200 cm^3 min^{-1}. Carried out in in the Mk II glass half-cell with static 8 M KOH thermostatically maintained at 60˚C.

All three electrodes show similar form, stable potentiometry over the relatively short timescale of a few minutes. During the ORR, all three of the samples achieved - 20 mA cm^{-2} at around - 50 mV *vs.* Hg/HgO with a modest increase in overpotential of about 20 mV associated with the addition of a membrane. On evaluation, there is only a modest performance drop 10-20 mV associated with the addition of a membrane to the samples. Performance of the electrode is not significantly hampered by the addition of a membrane at low current densities, over short timescales. It was found that all membrane covered electrodes when compared to a sample without a membrane showed a modest increase in overpotential because of the IR drop associated with the membrane. Although there are noticeable performance differences, it should be noted that none of the membranes increased the reduction potential by more than 45 mV. The exception being Nafion, which showed a large increase in potential. Degradation of the membranes with time and the need of a humidifier to control hydration at the membrane/catalyst interface are yet to be thoroughly explored.

4.6 Conclusions

The commercially sourced electrodes did not return satisfactory OER and ORR operation for more than 1 hour and as such were not investigated further. The development of the Zn-air flow battery requires a bifunctional air-electrode, which was developed in-house for the project.

Qualitative evaluation of potential substrate materials for an in-house air-electrode was carried out. Teflonated carbon paper was selected as an interim solution as it was well characterised in the fuel cell literature and came preassembled as a GDL requiring minimal modification to incorporate it into a cell.

The need for an active and cost effective catalyst which minimises the requirement of prohibitively expensive materials was established. From the academic literature, it was established that mixed metal oxides were a promising avenue to explore. An in-house team concluded that $NiCo_2O_4$ spinel could be a potential candidate and so its production was scaled up to produce sufficient quantities to produce flow cell electrodes.

The interim GDL and catalyst were used to optimise catalyst loading to maximise catalyst utilisation. Best results were found at loadings of < 10 mg cm^{-2} as the addition of catalyst after this point led to diminishing returns. Below this threshold most of the catalyst incorporated into the electrode is utilised and performance is proportional to catalyst loading. For the reasons just described a loading of 3-5 mg cm^{-2} was assessed to provide a good balance between performance and ease of manufacture while minimising catalyst use.

It was initially thought that a membrane might have been beneficial to prevent electrode flooding as well as adding mechanical protection to the active catalyst layer against the flow of electrolyte. Short time scale < 5 minutes preliminary results showed that there was a negligible overpotential increase (> 100 mV) associated with the addition of a membrane. This would allow for the inclusion of a membrane into the structure if required for safety of three-phase boundary management purposes without experiencing a significant performance penalty. Based on the initial findings efforts commenced on the development of a carbon paper based air-electrode. These findings are described in chapter 6.

Chapter 5: Results: Carbon-based air-electrode

This chapter describes the development and testing of carbon paper based air-electrodes. Despite the inherent problem of carbon corrosion at the potentials associated with oxygen evolution,[71] its use is still prevalent in the literature and there is a wealth of knowledge from fuel cell research evaluating carbon based GDLs.[27, 156] Carbon paper based GDEs were therefore the initial choice of substrate for high-throughput preliminary testing. The electrochemical properties of a carbon paper GDL prior to application of the catalyst layer was assessed using cyclic voltammetry in the glass half-cell. The electrode was a circular disc, 1.25 cm^2 geometric surface area and the electrolyte comprised 8 mol dm^{-3} KOH maintained at 60°C. Scanning towards positive potentials, an oxidation wave is observed to start at circa 1.2 V *vs.* Hg/HgO, while scanning towards negative potentials, a reduction wave is observed commencing at circa - 0.3 V *vs.* Hg/HgO. The electrode potentials observed at ± 50 mA cm^{-2} (a benchmark current density set by the POWAIR project) were - 0.54 V and 1.54 V *vs.* Hg/HgO respectively (Figure 5.1). Any of the electrodes with a catalyst layer that did not operate inside of these potentials at current densities $\leq$ 50 mA cm^{-2} were therefore defined to be inactive catalytically.

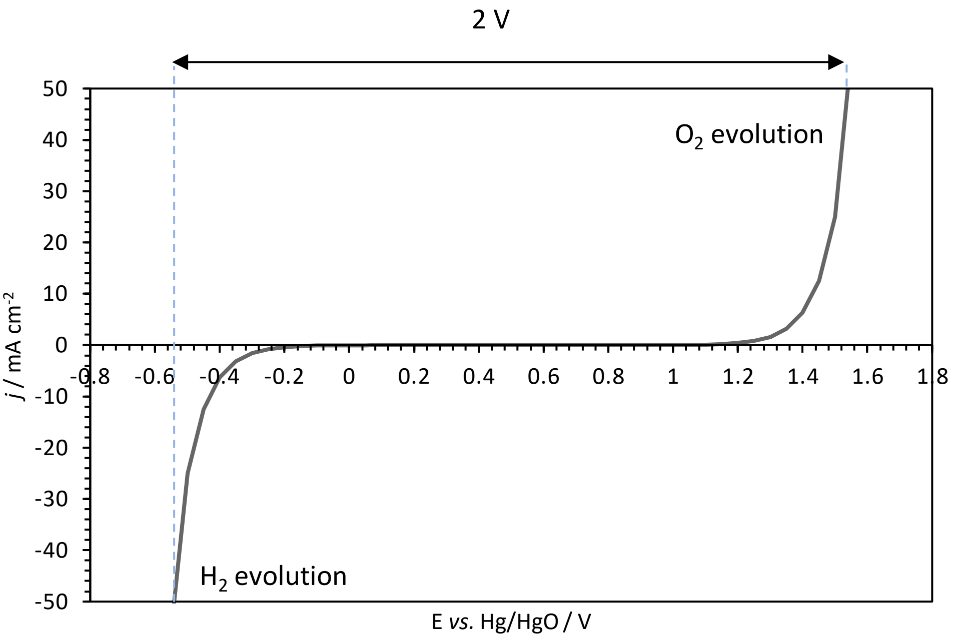

Figure 5.1 Visualisation of linear sweep voltammetry response of an uncatalyzed carbon paper GDL in 8 M hydroxide at 60˚C.

5.1 Ink composition

Electrode pre-treatments, active layer ink composition and production methods were investigated to establish best practice for producing consistently high performing electrodes. Optimising the ratio of water to IPA, in the ink, was investigated to observe its influence on ink application and performance. A series of electrodes were fabricated with inks containing varying solvent ratios, the findings are illustrated in (Figure 5.2). Each ink batch consisting of 100 mg of $NiCo_2O_4$ catalyst received a dose of 60 wt.% PTFE dispersed in H_2O. This will have contributed additional liquid to the ink, but was not considered in the ratio of solvent added, because it remained consistent for all samples and will have contributed no more than 12 µL to the overall volume. A total value on 600 µL of liquid was added comprised of different water:IPA ratios. The ink was applied with artist's brush to the activated-carbon coated carbon-paper discs and hot-pressed for 5 minutes at 180°C under a 4 kg mass. Catalyst loadings varied between samples due to the different consistencies of the ink and relative ease of application. To ensure that the results shown in Figure 5.2 were not dominated by variation in catalyst loading, the data was normalised to reflect performance per mg (not shown). Removing the effect of loading retained the same relationship between electrodes showing that in this comparison ink composition was the dominant variable.

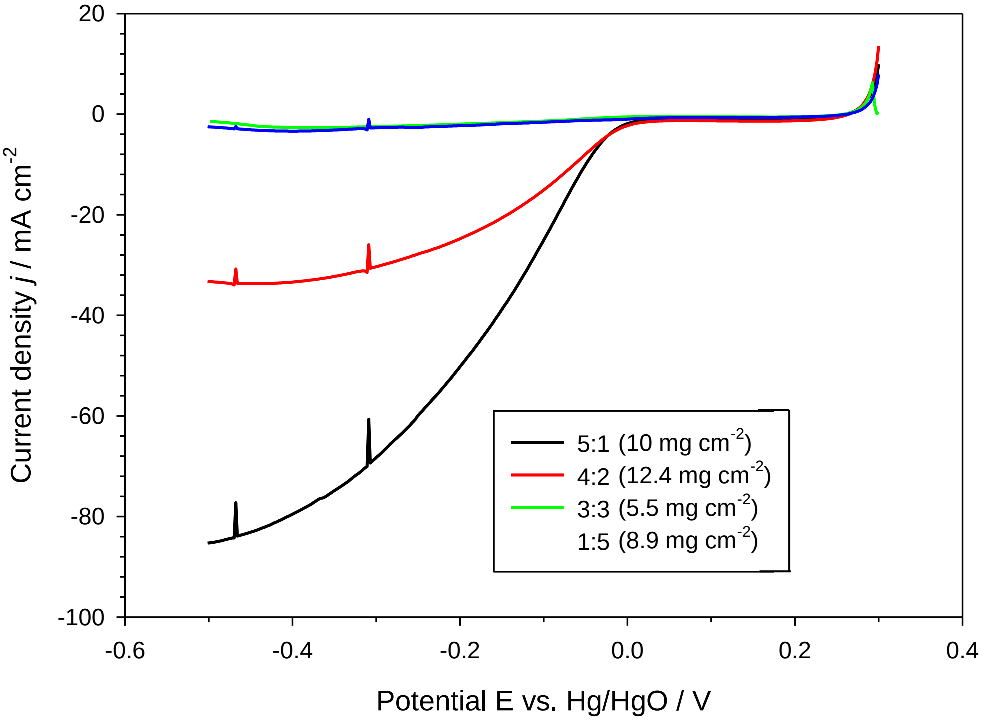

Figure 5.2 Performance of a series of carbon paper based electrodes (PTFE/ $NiCo_2O_4$ catalyst 10:3). Ink ratio H_2O:IPA was varied. Performed in Mk II glass half-cell with static 8 M NaOH thermostatically maintained at 60°C, O_2 flow 200 cm^3 min^{-1} to rear face of electrode. Linear sweep from 0.3 V to - 0.5 V at 1 mV s^{-1}.

Ink composition appears to play a substantial role in electrode performance. Inks which contain an IPA content which is greater than or equal to that of water, produce negligible ORR current, less than 5 mA cm^{-2}. Once the water content exceeded IPA and became the dominant component the performance dramatically increases. Although extrapolating this data would allude to a purely water based ink being optimal, in practice this did not prove to be the case. Preliminary work showed that an ink made solely with water, resulted in a poor suspension in which the catalyst particles rapidly separate out. Purely water based inks also tended not to wet the hydrophobic surface of the substrate and so getting initial ink layers to adhere was difficult. A certain concentration of IPA in the ink, is therefore required to ensure that subsequent layers of ink adequately wet the previous application. To reach a suitable compromise, a 5:1 ratio was selected as the standard. A valuable expansion of the data shown in Figure 5.2, would be to expand the number of ratios evaluated. Focusing on the region between a ratio of 5:1 (water: IPA) and exclusively water to see if performance can be improved, while maintaining adequate adhesion of the active layer to the substrate.

Another approach investigated to aid with ink application, was pre-wetting of the substrate surface prior to applying a layer of ink. This was achieved by dabbing the substrate surface with a lint free towel soaked in a solution of IPA and water. A batch of six electrodes (Table 5.1) were produced with a 6 mg cm^{-2} catalyst loading (≤ 20 µm particle size) to investigate the effect of substrate pre-wetting, catalyst ink on ink application and consequently electrode performance. The first three electrodes (E1-E3) were made with a catalyst ink of 0.5 mL of water to every 100 mg of catalyst and were pre-treated by wetting of the carbon paper disc with water and isopropanol in a 1:1 mixture. The next three electrodes (E4-E6) were made with 1 mL of water to every 100 mg of catalyst. The electrodes E4 and E5 were pre-wetted, as with the first three electrodes, but E6 received no pre-treatment to act as the control.

Table 5.1 Preparation conditions summarised for a batch of electrodes E1–E6.

Electrode	*H_2O volume in ink / ml*	*Catalyst in ink / mg*	*Pre-wetting*
E1	0.5	100	Yes
E2	0.5	100	Yes
E3	0.5	100	Yes
E4	1.0	100	Yes
E5	1.0	100	Yes
E6	1.0	100	No

Figure 5.3 presents the linear sweep voltammograms for the electrodes E1-E6. In each voltammogram, the potential was swept from 0.3 V *vs.* Hg/HgO to - 0.5 V *vs.* Hg/HgO at 1 mV s^{-1}. Each voltammogram shows a cathodic reduction curve associated with the ORR (commencing at circa - 0.05 V *vs.* Hg/HgO).

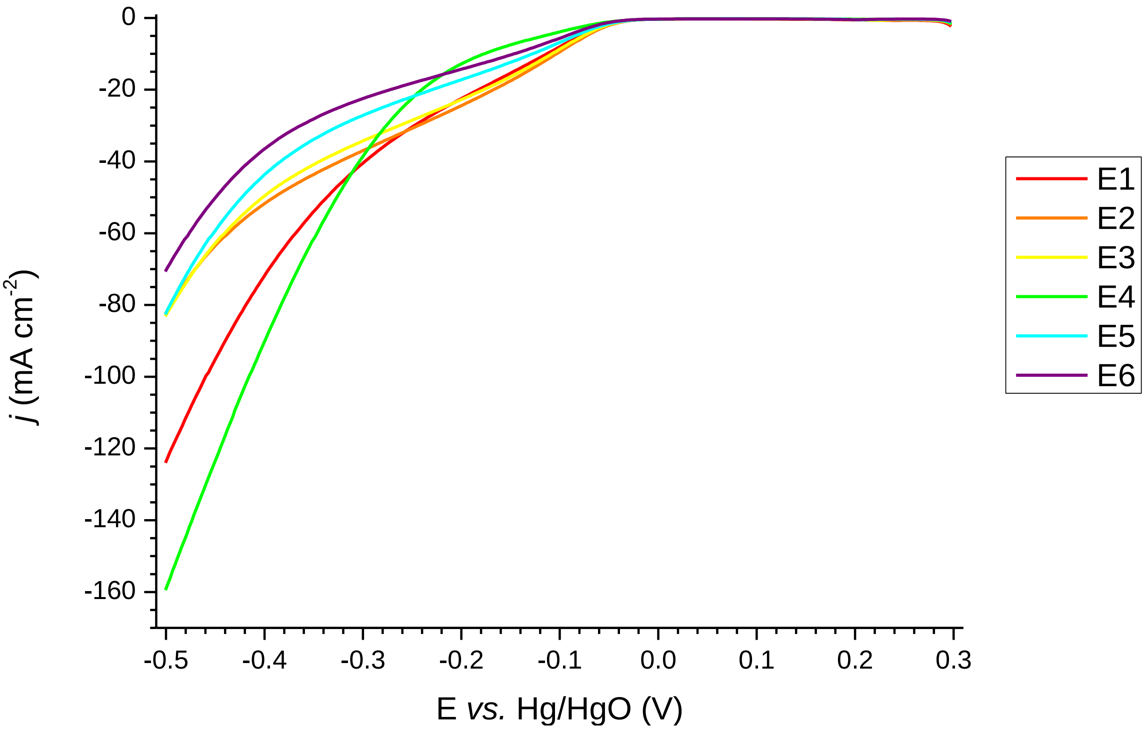

Figure 5.3 Linear sweep voltammetry for electrodes E1-E6 (Table 5.1). E1-E3 prepared using ⩽ 20 µm $NiCo_2O_4$ spinel, thermally decomposed catalyst ink of half the standard dilution and E4-E6 produced with inks diluted as standard. Scan rate 1 mV s^{-1}. In static 8 M KOH thermostatically maintained at 60˚C. All samples except E6 were pre-wetted.

In Figure 5.3, the electrode not pre-wetted, E6, performed the worst of the set, with a $j_{-0.5\,V}$ of - 71 mA cm^{-2}. Suggesting pre-wetting was beneficial to the performance of the other electrodes. Between 0.0 V and - 0.2 V *vs.* Hg/HgO current densities for all electrodes deviate minimally from each other. There are however, distinct groupings for each of the two sets of electrodes (E1-E3 and E4-E6), favouring the more concentrated ink at lower current densities. Below - 0.2 V *vs.* Hg/HgO, differences in the individual electrodes are accentuated. Electrodes E1 and E4 performed best, achieving values for $j_{-0.5\,V}$ of - 124 mA cm^{-2} and - 159 mA cm^{-2} respectively. The cathodic reduction curves for the electrodes E1 and E4, follow the shape of their ink preparation counterparts at the onset, but the gradient becomes significantly steeper circa - 0.2 V *vs.* Hg/HgO. The greater current densities achieved by electrodes E1 and E4 may be due in part to the fact that they were the first electrodes made from each batch of ink. This was notable, as these electrodes received significantly more ink layers to achieve the same loading; 15 layers for E1 (compared to 5 and 7 for E2 and E3) and 30 layers for E4 (compared to 15 and 17 for E5 and E6). This correlates with the anecdotal observation, that on initial introduction the brush absorbs a proportion of the ink which is consequently not transferred to the electrode or returned to the ink vessel. By the time it comes to a second electrode, the brush tip is becoming saturated and so ceases to absorb more of the ink. The inks composition has likely altered drastically for production of a subsequent electrode from the batch. It is therefore recommended that if an artist’s paint brush is to be used for ink application, that a fresh batch of ink is prepared for each individual sample. Alternatively, a considerably larger batch of ink could be produced so that the effect of the brush soaking up the ink will have less of an effect on the bulk ink composition. This was initially not a viable option as the catalyst could only be produced in 1-5 g batches, but became more common once the catalyst was scaled up to multi Kg batches. A final option would be to produce an initial sample from each ink batch and then discard it. All further electrodes from that batch should perform more consistently however at the cost of reduced performance.

Another method of wetting, is to ‘flood’ the electrode prior to ink application. The process which will be referred to as pre-soaking involved displacing air trapped in the structure with UHP water. This was achieved by submerging the substrate in boiling water, or by forcing the gas out of a submerged electrode in vacuo. A set of electrodes were produced to investigate the influence of small-scale paintbrush application and the effect of producing a fresh ink batch for each electrode. Eight electrodes with a 4 mg cm^{-2} catalyst loading of ≤ 20 µm particle size thermally decomposed $NiCo_2O_4$ spinel (C-tech innovation) were prepared. The ink contained a ratio of 1 mL of UHP water to every 100 mg of catalyst. The first two electrodes in this sequence (E1-E2) were made from the same batch of catalyst ink. A separate batch of catalyst ink was made up for each of the remaining electrodes (E3-E8). The paintbrush was thoroughly cleaned between painting each electrode using an ultrasonic bath. The carbon discs for (E1-E5) were pre-wetted, whereas for (E6-E8) the carbon paper pre-soaked in a 1:1 mixture of water and isopropanol. Figure 5.4 presents the linear sweep voltammograms for these electrodes (E1-E8). In each instance, the potential was swept from 0.3 V to - 0.5 V *vs.* Hg/HgO at 1 mV s^{-1}.

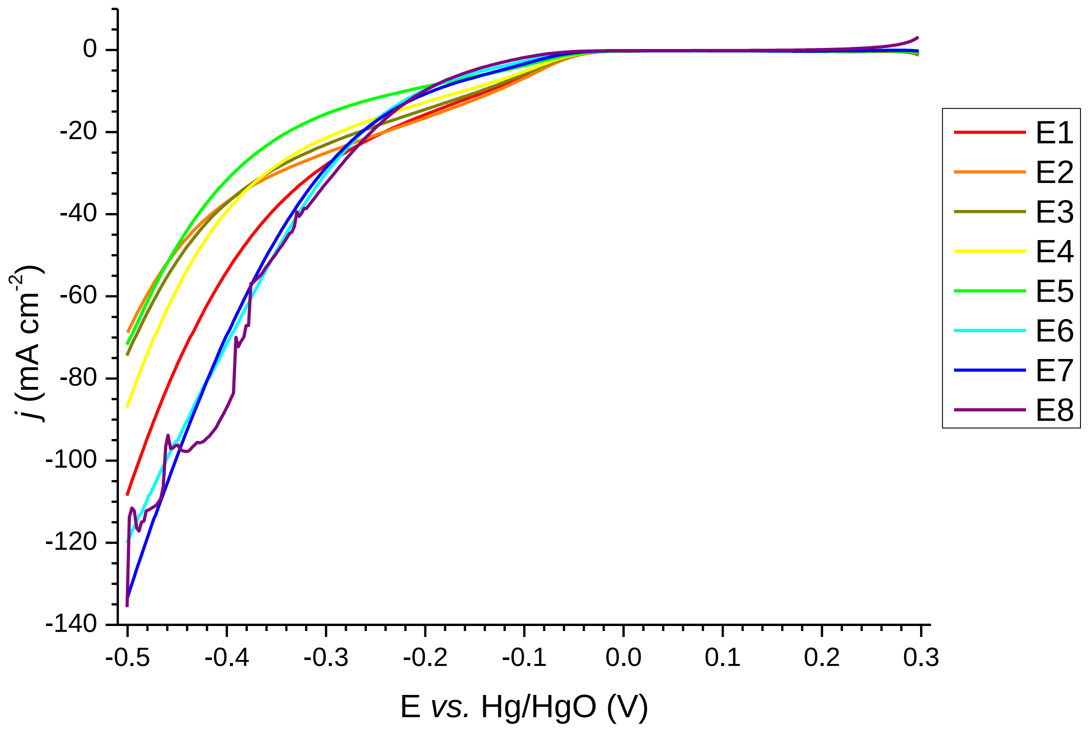

Figure 5.4 Linear sweep voltammetry for carbon paper based electrodes prepared with 4 mg cm^{-2} loading of ⩽ 20 μm $NiCo_2O_4$ spinel, thermally decomposed catalyst using the standard production method. (E1-E2) from a single batch of ink. (E1-E5) pre-wet and (E6-E8) pre-soaked. Scan rate 1 mV s^{-1}. In 8 M KOH at 60°C.

Electrode E1 (first electrode from ink batch) performed significantly better than E2 (second electrode from ink batch), with a $j_{-0.5\,V}$ of - 109 mA cm^{-2} compared to - 69 mA cm^{-2}. Adding further evidence to the suspicion that the first electrode produced from a batch of ink out performs subsequent electrodes made from the same batch. Electrodes (E3-E5) were each made from a fresh batch of ink on pre-wetted substrates. The polarisation curves for electrodes (E3-E5) are quite similar in form and values of $j_{-0.5\,V}$ lie within a range of approximately 20 mA cm^{-2}. (E3-E5) performance is not however comparable to E1 and is in fact more in line with E2 suggesting variation between non-consecutive batches or a drop in performance over time. Electrodes (E6-E8) have a much higher average $j_{-0.5\,V}$ (- 130 mA cm^{-2})

compared to those pre-wetted and retain a similar range of $j_{-0.5\ \mathrm{V}}$ (20 - 30 mA cm^{-2}) and reproducibility. Comparison of the average values of $j_{-0.5\ \mathrm{V}}$, reveal that the electrodes that were pre-soaked performed significantly better than the electrodes that were pre-wetted. To promote better performance and reproducibility, electrodes produced in subsequent optimisation experiments were made from separate batches of ink using the more diluted catalyst ink (1 mL of water per 100 mg of catalyst) and the carbon paper discs pre-soaked before the application of catalyst ink.

5.2 Hot pressing

Although teflonated carbon paper is hydrophobic, once the active layer was applied this hydrophobicity became greatly diminished. The altered wetting properties were insufficient to prevent flooding of the layer. A solution was to hot-press the electrode. There is evidence in the fuel cell literature that heating of the electrode to above the glass transition temperature (T_g) of the binder will mobilise the polymer in the layer.[157, 158] A carbon paper electrode was therefore produced and contact angle measurements were taken both before and after the electrode had been hot pressed.

Catalyst ink was applied to a carbon paper coated in activated carbon substrate. The applied catalyst ink contained 23 wt.% PTFE and 77 wt.% $NiCo_2O_4$ spinel based on the mass of the dry solids, in a 1:5 IPA to H_2O mixture. Approximately 3 mg cm^{-2} of catalyst was applied to the substrate by artist's brush. The 30 mm × 50 mm electrode was hot pressed at 180° C for 5 minutes under a 4 kg mass. Figure 5.5 shows a top down map of the electrode measured using contact angle analysis. Measurements were taken across the surface of the electrode to examine surface uniformity. Each number represents the approximate location where a measurement was made. In each instance, 1 µL of UHP water was dispensed onto the surface. The images obtained from the resulting droplets, were used to calculate the contact angle. The values for contact angle measured before and after hot pressing, can be seen in Table 5.2. Images taken by the drop shape analyser of before and after hot-pressing are shown in Figure 5.6.

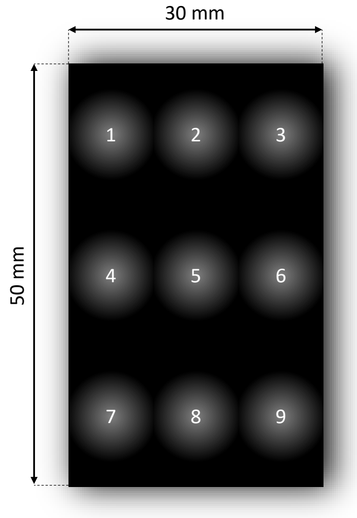

Figure 5.5 Top down map of a 30 mm by 50 mm electrode measured using contact angle. Indicating the locations 1-9 where measurements were made.

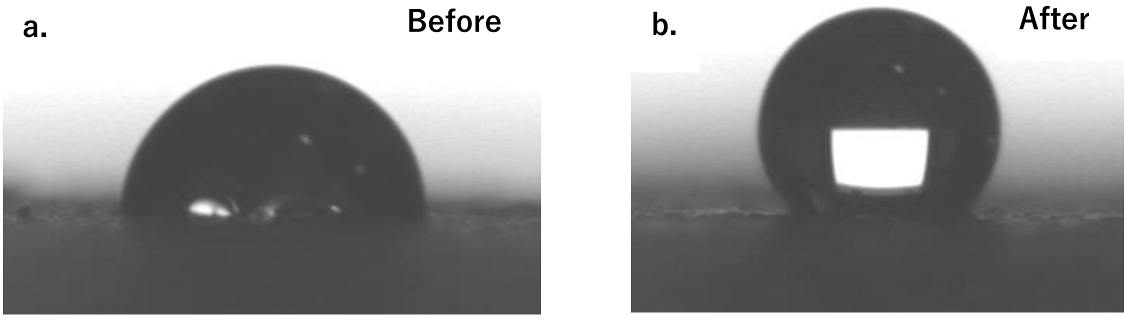

Figure 5.6 Images taken of water droplets deposited on an electrode surface a.) before and b.) after hot pressing at 180˚C under a 4 kg mass for 5 min.

Table 5.2 Contact angle data for a carbon paper electrode coated in a 10:3 catalyst to PTFE based ink, before and after hot pressing. The measurement was recorded at a range of locations across the electrode.

Location	Dose volume / µL	Before pressing		After pressing	
		Contact angle / degrees	Fit-error / µm	Contact angle / degrees	Fit-error / µm
1	1	78.80	5.47	119.90	3.61
2	1	-	-	127.60	7.13
3	1	84.40	6.00	137.40	7.81
4	1	106.30	2.90	129.50	4.99
5	1	98.10	3.61	134.70	8.94
6	1	89.20	6.68	135.40	9.28
7	1	99.80	3.05	128.00	5.91
8	1	74.50	6.60	132.70	7.36
9	1	64.30	4.72	113.10	13.80
Average	1.00	86.93	4.88	128.70	7.65

Before hot pressing, the average contact angle for the surface was 87° (Figure 5.6a) which places it on the border between hydrophobic and hydrophilic. There was a large variation of about 42° between locations, showing that there is a fair amount of variation across the surface. Once hot pressed the average increases to 129° (Figure 5.6b) placing the surface comfortably in the hydrophobic category. The variation across the surface diminished to 24°, the result of hot pressing is therefore increased hydrophobicity and greater uniformity of PTFE across the sample. At this stage, little work has been carried out to optimise hot-pressing in terms of the optimal temperature, pressure and time for which the electrodes are pressed. Preliminary work has suggested that applying too high a pressure, compressed the layer to the extent that it loses much of its porosity. Applying a temperature < 350° C resulted in the breakdown of the PTFE, lowering the hydrophobicity and producing potentially harmful by-products. Heat treatment is an area that could receive further investigation when trying to extend the lifespan of this type of electrode.

5.3 Particle size

The size of the $NiCo_2O_4$ spinel particles was a consequence of the synthesis method and conditions. These particles readily agglomerate into larger clusters of more ill-defined shape and size. All samples produced in-house were ball-milled to break up the larger clumps and then hand ground in an agate pestel and morter to form a fine free flowing powder. The resulting powder was passed through a 55 μm particle retention sieve before use. The thermally decomposed $NiCo_2O_4$ spinel samples produced by C-Tech Innovation, were ground to ≤ 20 μm, ≤ 10 μm and ≤ 6 μm particle-size tolerances. These samples were used to make comparable electrodes with different catalyst particle sizes.

Each batch was used to produce an ink comprised of catalyst and PTFE solution 10:3 dry solids and a 5:1 ratio of water to IPA. The catalyst loading for each electrode was 10 mg cm^{-2} and the substrate was activated carbon coated teflonated carbon paper. The samples were electrochemically screened in the MK II three-electrode glass cell to compare their performance.

Catalyst ink was applied to a carbon paper coated in activated carbon substrate. The applied catalyst ink contained 23 wt.% PTFE and 77 wt.% $NiCo_2O_4$ spinel based on the mass of the dry solids, in a 1:5 IPA to H_2O mixture. Approximately 3 mg cm^{-2} of catalyst was applied to the substrate by artist's brush. The 30 mm × 50 mm electrode was hot pressed at 180° C for 5 minutes under a 4 kg mass. Figure 5.5 shows a top down map of the electrode measured using contact angle. Measurements were taken across the surface of the electrode to examine surface uniformity. Each number represents the approximate location where a measurement was made. In each instance, 1 μL of UHP water was dispensed onto the surface. The images obtained from the resulting droplets were used to calculate the contact angle. The values for contact angle measured before and after hot pressing can be seen in Table 5.2. Images taken by the drop shape analyser of before and after hot-pressing are shown in Figure 5.6.

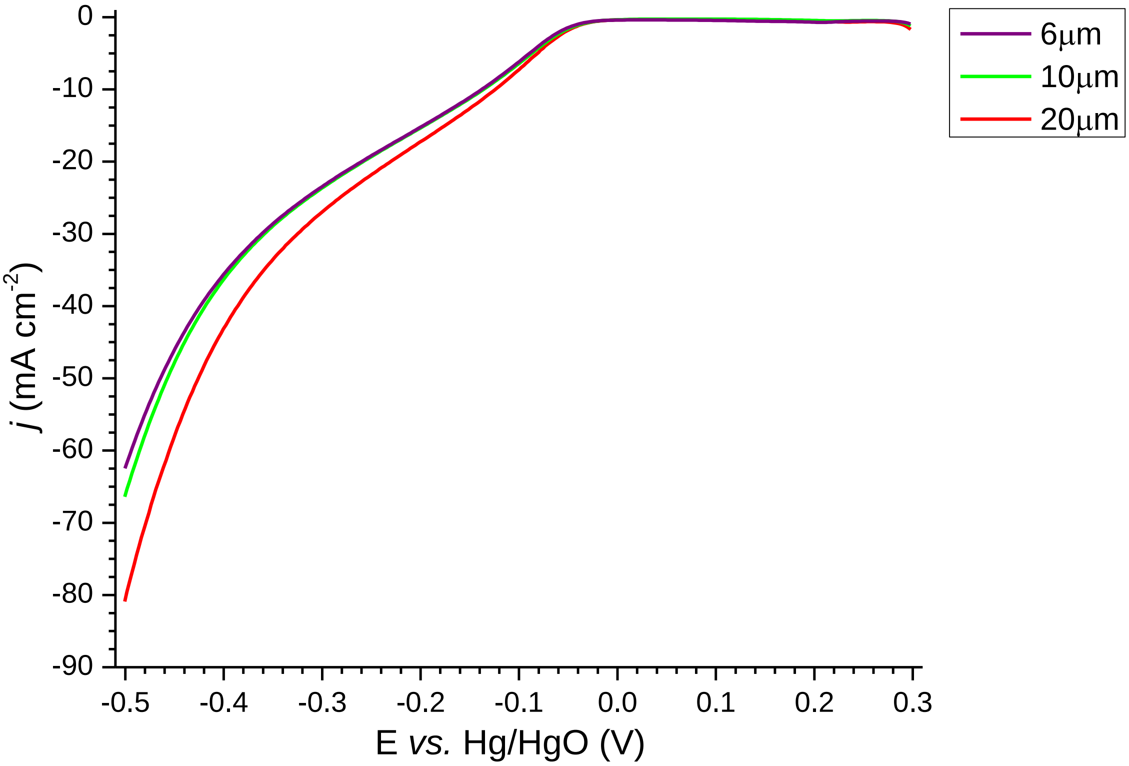

Figure 5.7 Averaged LSV from 12 electrodes made with ⩽ 20 µm $NiCo_2O_4$ spinel, thermally decomposed catalyst ground to different particle size distributions: ≤ 20 µm, ≤ 10 µm and ≤ 6 µm all at approximately 5 mg cm^{-2} catalyst loading. Scan rate 1 m s^{-1}. In static 8 M KOH thermostatically maintained at 60°C.

Figure 5.7 presents the averaged voltammograms from multiple electrodes for each catalyst particle size. The cathodic reduction curves seen, are representative of the average of four electrodes for each of the particle distributions, aiming to mitigate variation arising in the preparation of each individual electrode. The averaged LSV gives $j_{-0.5\,V}$ values of - 62 mA cm^{-2}, - 66 mA cm^{-2} and - 81 mA cm^{-2} for distributions ≤ 6 μm, ≤ 10 μm and ≤ 20 μm respectively. This suggests that the larger particle size distribution ≤ 20 μm, produces the greatest ORR performance. This finding may initially appear counterintuitive as it was assumed that the larger particles would have a lower surface area. The rationalisation for this result was that the larger variation in particle size, leads to less well ordered packing of the catalyst particals. Unordered packing leads to larger voids and better continuity of gas channels for the transport of oxygen and electrolyte to the catalyst active sites. Limitations in mass transport of oxygen to the electrode, is currently assumed to be a rate limiting factor, preventing the catalyst from achieving its true potential at higher current densities. The fact that these electrodes are also on the upper limit of what has been deemed optimal for catalyst loading (Chapter 4.4) means that the active layer will be thicker. A thicker layer will require better gas transport through the layer to maximise utilisation of the catalyst. Therefore the catalyst with a larger partical size distribution, will provide better mass transport of gas increasing catalyst utilisation. However, the increased performance can also be rationalised as the result of improved electrical conductivity in the active catalyst layer. A larger average particle size results in fewer interpartical transitions, which reduces the number of contact points (and hence contact resistance points). Following this, conductive materials were considered for inclusion in the active layer of the electrode to aid electrical conductivity and improve the electrodes performance.

The potential associated with OER is similar for all three particle-sizes. There is a consistent trend showing that increased particle size, results in a lower OER potential, however this variation is by no more than 10 mV - 20 mV which is only just above the observed variation between reproducible samples. Suggesting that particle size is not a dominant factor contributing to performance.

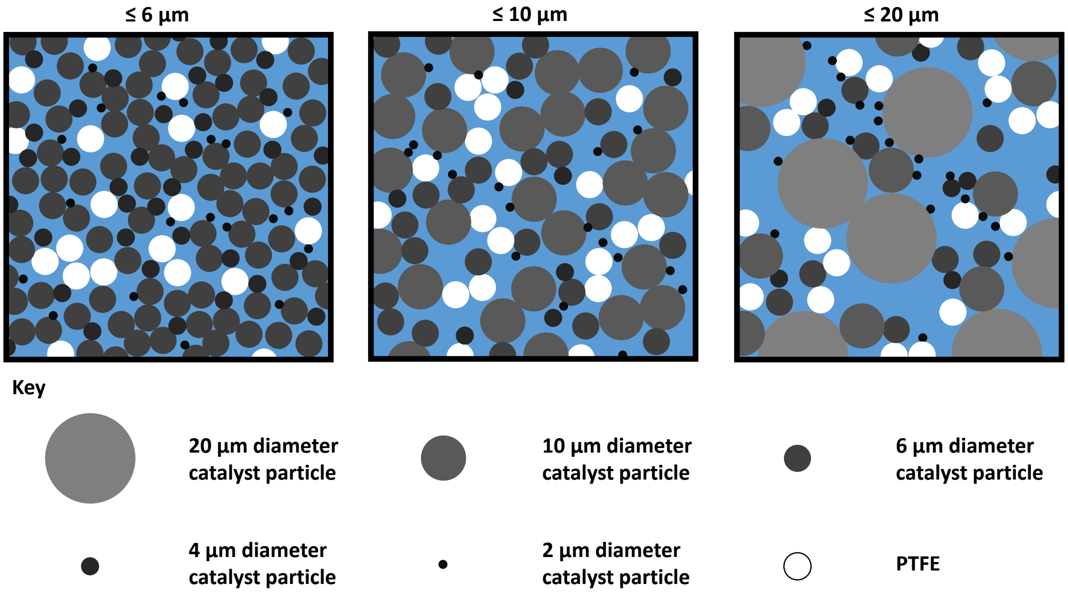

Figure 5.8 Visual representation of how the different catalyst particle size distributions might pack within the active layer and how this may affect gas and electrolyte channels (represented as the blue regions.

A series of electrodes using the thermally decomposed $NiCo_2O_4$ spinel catalysts produced by C-Tech Innovation ground to ≤ 20 µm, ≤ 10 µm and ≤ 6 µm particle-size tolerances. The inks were comprised of catalyst powder 77 wt.% and 23 wt.% PTFE dispersed in H_2O. The mixture was diluted by a solution of 5:1 water to IPA. Catalyst ink was applied to a carbon paper coated in activated carbon substrate to produce a catalyst loading of 5 mg cm^{-2}. These electrodes were characterised by constant current potentiometry at current densities of ± 10 mA cm^{-2}, ± 20 mA cm^{-2} and ± 50 mA cm^{-2} as shown in Figure 5.9. The electrolyte was static 8 M KOH maintained at 60°C. Each current step lasted for 300 s and was preceded and followed by 30 s OCP.

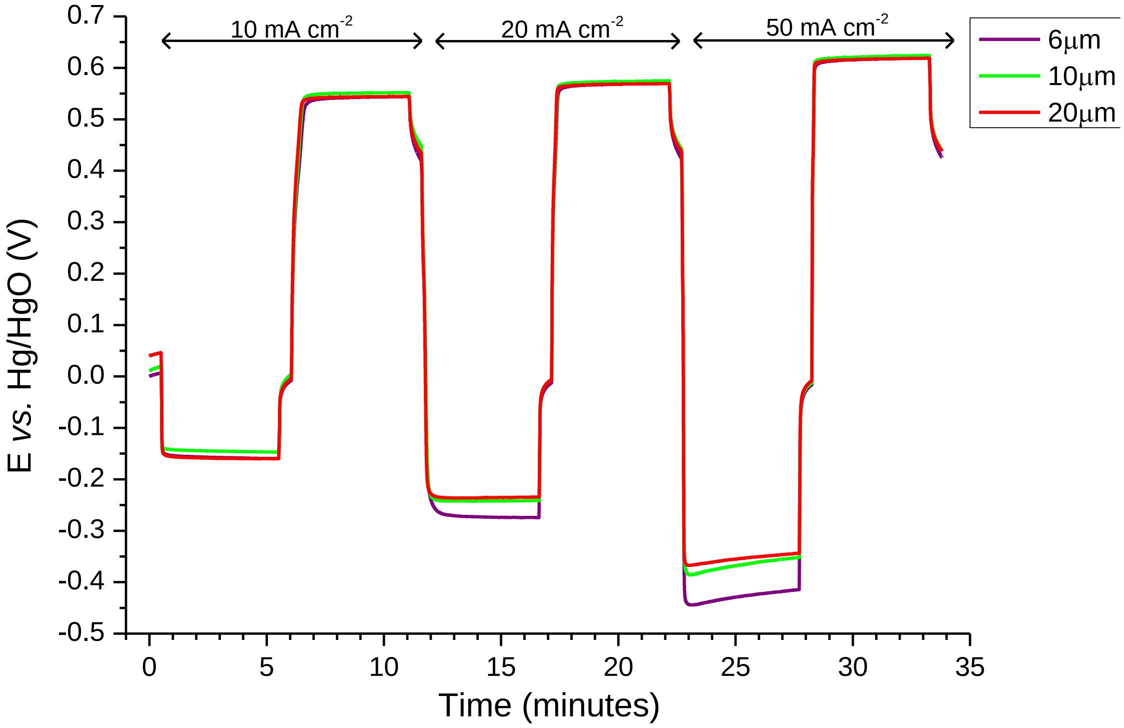

Figure 5.9 Constant current measurements at ± 10, ± 20 and ± 50 mA cm-2 for ⩽ 20 μm $NiCo_2O_4$ spinel, thermally decomposed catalyst particle size distributions: ⩽ 20 μm, ⩽ 10 μm and ⩽ 6 μm. All electrodes had a catalyst loading of 5 mg cm^{-2} and all measurements made in static, thermostatically controlled 60˚C, 8 M KOH. A 30 s period of OCP proceeded/followed each current step.

The potentials for the OER show in Figure 5.9, only display small (± 10 mV) variation between the electrodes. These differences are only just above the observed variation between reproducible samples, so any effect can be perceived as negligible. For the ORR, there appears to be a modest but noticeable reduction in overpotential associated with a larger particle size tolerance catalyst. This suggests that the effect is mass transport dependant, as the ORR is reliant on the flux of oxygen.

To eliminate the possibility this result was a by-product of the chosen loading, the experiment was repeated at 3 mg cm^{-2}, 6 mg cm^{-2} and 10 mg cm^{-2} catalyst loadings. As previously shown, layer thickness may have a critical effect on catalyst utilisation and porosity. A reduced potential gap (ΔE), the difference between oxygen reduction and evolution at a given current density, will contribute to a higher voltage efficiency in the battery. For this reason, ΔE is a good indicator of air-electrode performance taking into account both reactions of the bifunctional electrode. Values of ΔE for the electrodes are shown in (Table 5.3).

Table 5.3 Potential window values from constant current measurements at ± 10, ± 20 and ± 50 mA cm^{-2} for different particle size distributions: ≤ 20 μm, ≤ 10 μm and ≤ 6 μm at 3 mg cm^{-2}, 6 mg cm^{-2} and 3 mg cm^{-2} catalyst loading. In 8 M KOH 60ºC.

	Potential Gap ΔE (mV)								
j / mA cm^{-1}	3 mg cm^{-2}			6 mg cm^{-2}			10 mg cm^{-2}		
	Particle size / μm			Particle size / μm			Particle size / μm		
	⩽ 6	⩽ 10	⩽ 20	⩽ 6	⩽ 10	⩽ 20	⩽ 6	⩽ 10	⩽ 20
10	746	740	723	701	697	703	674	658	637
20	879	844	803	843	815	804	774	748	704
50	1059	995	969	1043	984	970	971	971	933

The results indicate that the larger particle size distribution, is still the best performing. Despite variation in the data, the ≤ 20 μm distribution had the smallest ΔE for all current densities, followed by ≤ 10 μm; the worst performing being ≤ 6 μm (Table 5.3). In general, the catalyst particle size distribution

≤ 20 μm, produced electrodes with the smallest ΔE for constant current characterisation and the lowest values of $j_{-0.5\ \mathrm{V}}$ for LSV. This particle size distribution, was selected as the optimum with which to make further electrodes.

5.4 Carbon as a catalyst support

Carbon is a common additive in fuel cell electrode active layers, to act as a catalyst support improving catalyst particle dispersion and utilisation.[159] It may also be added for its desirable attributes such as electrical conductivity or oxygen transport. Electrodes were made with $NiCo_2O_4$ spinel catalyst (thermally decomposed ≤ 20 µm, 4 mg cm^{-2} loading) and activated carbon powder (Vulcan® XC-72R) in ratios of 10:1, 4:1, 2:1 and 1:1 following the established ink procedure. The liquid component of the ink was adjusted to the total mass of dry solids (i.e. catalyst + carbon). 1 mL of water to every 100 mg of combined dry solids. The electrodes were characterised by LSV, CV and constant current. The LSV was performed in the Mk II glass half-cell filled with ~ 100 mL of 8 M KOH maintained at 60 C. The potential was swept from 0.3 V to – 0.5 V vs. Hg/HgO at a rate of 1 mV s^{-1}.

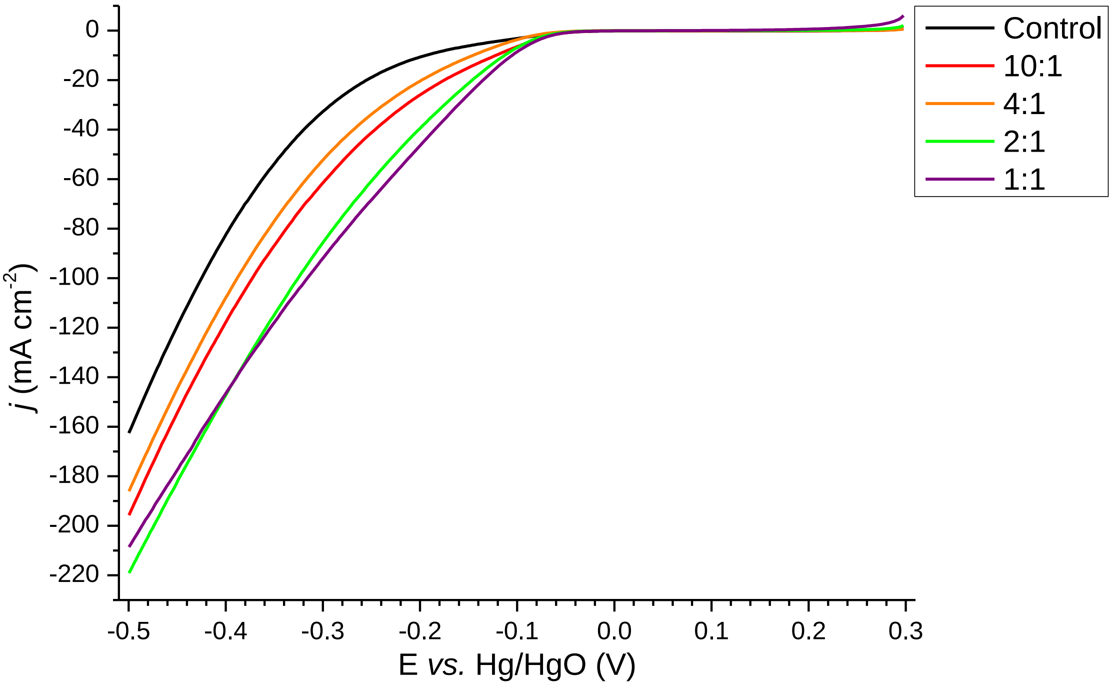

Figure 5.10 LSV for ⩽ 20 μm $NiCo_2O_4$ spinel, thermally decomposed catalyst 4 mg cm^{-2} catalyst loading electrodes with the addition of carbon in ratios 10:1, 4:1, 2:1 and 1:1 catalyst to carbon, as well as a "Control" electrode at 4 mg cm^{-2} with no carbon. Scan rate 1 mV s^{-1}. In static 8 M KOH thermostatically maintained at 60ºC.

The LSVs, presented in Figure 5.10, show high performance for all electrodes produced, values of $j_{-0.5\ V}$ range from - 163 mA cm^{-2} for the control electrode to - 219 mA cm^{-2} for the 2:1 (catalyst:carbon) electrode. Though the same procedure for electrode production was used for this set, the paintbrush had been replaced due to mechanical wear. This resulted in thinner layers and more consistent application of the ink to the surface of the carbon paper and thus better performance. There is not a perfect trend (likely due to electrode preparation variation) however there is a general tendency for reduced ORR overpotential with increasing carbon content. This indicates that a higher ratio of carbon in the catalyst ink is beneficial for the ORR. The set up as unaltered and constant current cycling at current densities of ± 10 mA cm^{-2}, ± 20 mA cm^{-2} and ± 50 mA cm^{-2} was recorded (Figure 5.11). Current steps of 300 s for the ORR followed by the OER were separated by 30 s periods of OCP.

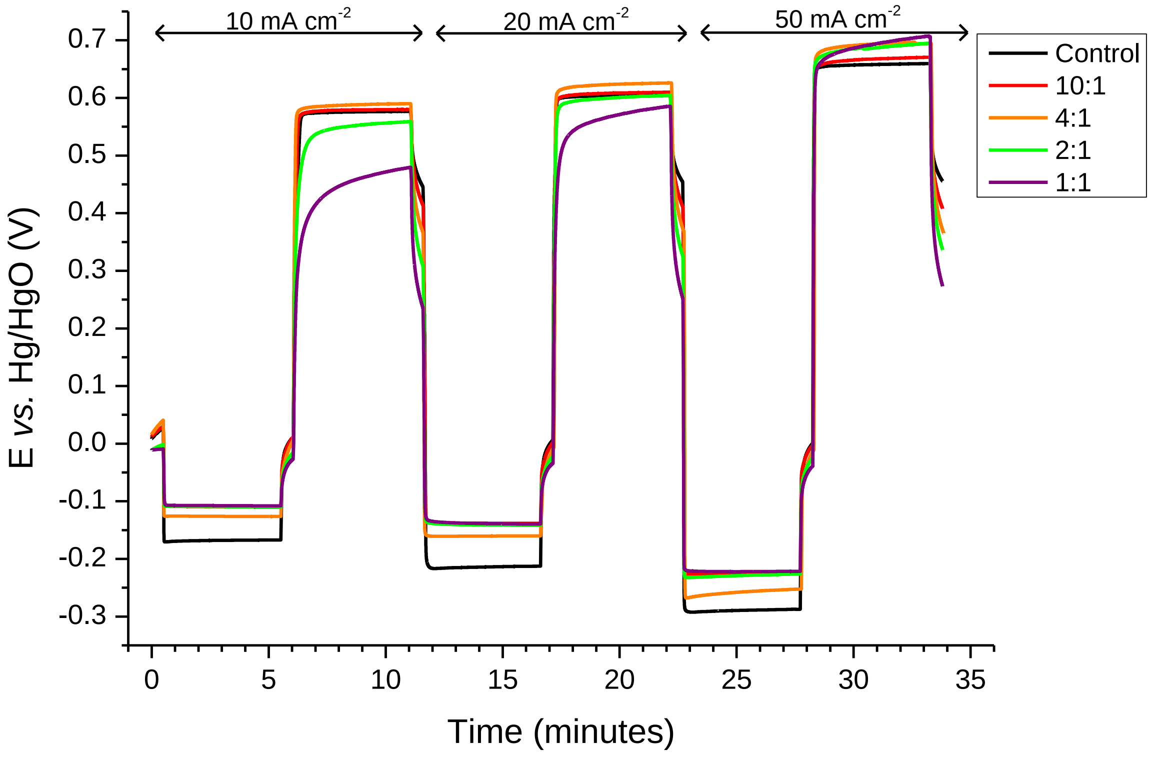

Figure 5.11 **Constant current at ± 10, ± 20 and ± 50 mA cm^{-2} for ⩽ 20 µm $NiCo_2O_4$ spinel, thermally decomposed catalyst 4 mg cm^{-2} catalyst loading electrodes with carbon inclusion in ratios 10:1, 4:1, 2:1 and 1:1 catalyst to carbon, also a “Control” electrode at 4 mg cm^{-2} with no carbon. In 8 M KOH 60ºC.**

The high carbon content electrodes, 2:1 and 1:1, show smaller values for ΔE at 10 mA cm^{-2} and 20 mA cm^{-2}. However, the performance decreases as they are subjected to higher current densities. At 50 mA cm^{-2} the 10:1 electrode has a smaller value of ΔE than either the 2:1 or the 1:1 electrode (893 mV, 918 mV and 921 mV respectively). This increase in the potential gap can be seen for the OER of the 1:1 catalyst to carbon electrode, where under constant current, the potential continues to slowly rise as the performance deteriorates; 2:1 also exhibits this behaviour though to a lesser extent. This deterioration was physically observable; after the constant current cycling, the catalyst active layer of the 2:1 and 1:1 electrodes could be seen falling away from the surface of the carbon paper discs.

The delamination is due to the deterioration of the carbon at oxygen evolution potentials. The same degradation in performance is not seen in the LSV as the electrodes were not subjected to evolution potentials and measurements were taken over a shorter time-scale. The inclusion of carbon in electrodes, although display high performance, are not stable at oxygen evolution potentials (using this method of electrode production). The 2:1 catalyst to carbon electrode performs well, and degrades more slowly than its 1:1 counterpart, though it may not prove sufficiently stable to be used in a flow cell.

5.5 Binder Stability

The PTFE present in the active layer of the electrode, acts to bind the layer and aid adhesion of the catalyst to the substrate. The effect of the binder is to increase the mechanical stability of the electrode. Without it the active layer would be exceedingly brittle and susceptible to erosion by the flowing electrolyte. Binders tend to be non-conductive and so an excess can lead to reduced conductivity and active sites become encapsulated, adversely affecting the electrochemistry. The ratio of binder to catalyst was investigated to produce a $NiCo_2O_4$ spinel and carbon electrode that could better withstand the harsh conditions at evolution potentials.

Electrodes were prepared with a catalyst loading of 4 mg cm^{-2}. The ratio of catalyst to carbon was 2:1 and the PTFE content was altered for each electrode, increasing from 10:3 to 10:6 catalyst to PTFE ratio by dry solid mass. Inks made with higher PTFE content began to behave more similar to a paste resulting in difficulties in its application. The electrodes were characterised by constant current cycling at current densities of ± 10 mA cm^{-2}, ± 20 mA cm^{-2} and ± 50 mA cm^{-2} as displayed in Figure 5.12. The electrodes were tested for longer periods in these cycles than previously, to better assess their stability over time. The electrodes are listed as their PTFE content in ratio to 100 catalyst and carbon i.e. 10:3 catalyst and carbon to PTFE becomes 30.

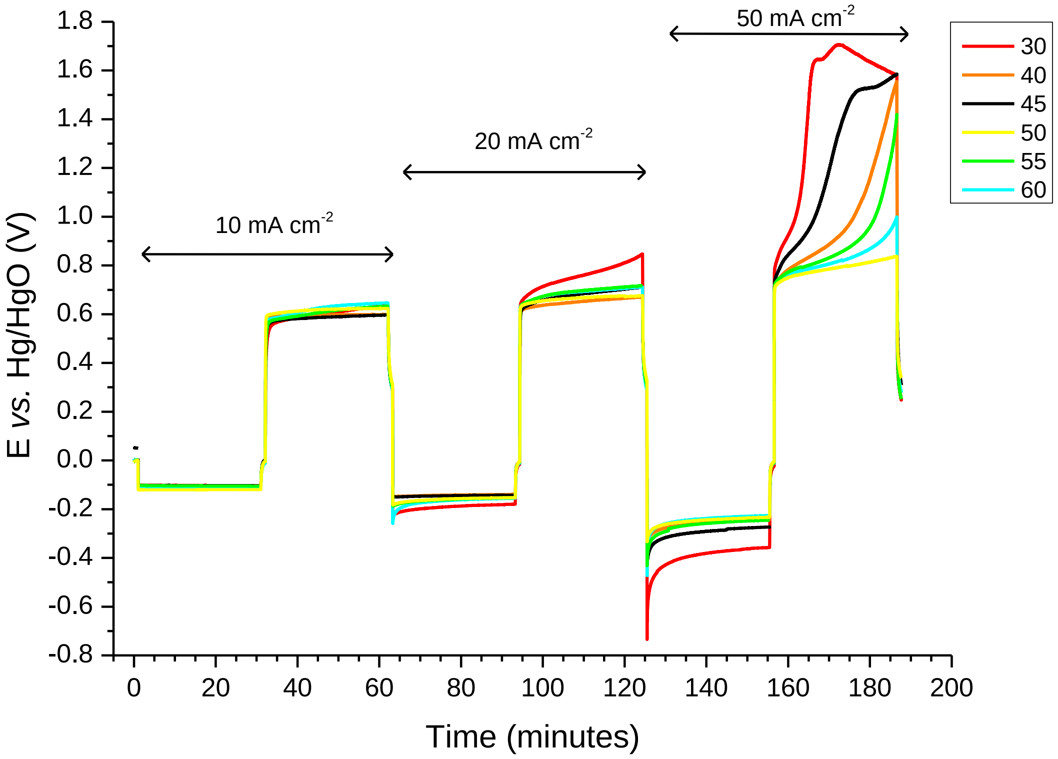

Figure 5.12 Constant current at ± 10, ± 20 and ± 50 mA cm^{-2} for different ⩽ 20 µm $NiCo_2O_4$ spinel, thermally decomposed catalyst to PTFE ratios 100:30, 100:40, 100:45, 100:50, 100:55 and 100:60 all at 4 mg cm^{-2} catalyst loading and 2:1 catalyst to carbon. In 8 M KOH 60ºC.

At 10 mA cm^{-2} the lower PTFE content electrodes (30–45) have the smallest values for ΔE, but as these electrodes are pushed to increasing oxygen evolution potentials, they begin to degrade and ΔE increases. At 50 mA cm^{-2} the lower PTFE content electrodes begin to fail, climbing to potentials associated with the corrosion of carbon as opposed to the catalysed OER. The 50 and 60 PTFE content electrodes showed more stable potentials for all values of *j,* although they both begin to degrade by the end of the cycle showing a sloping increase in oxygen evolution potential. There is a general trend that electrodes with higher PTFE contents, show improved stability, but initially hinder performance at lower current densities.

The 100:50 (catalyst:PTFE) electrodes were the peak in performance. Even higher PTFE proportions (100:55 and 100:60) electrodes showed slightly reduced stability. An explanation for this, is the consistency of the ink from which they were produced. These paste-like catalyst inks could only be applied to the substrate in thick layers, which lead to visible cracking of the surface during the drying process. The 100:50 PTFE content electrode, was taken as the best to continue with investigations. This apparent stability increase with little perceivable loss in performance for active layers with higher binder constant is counter to the conventional wisdom. Multiple sources in the literature state that the cathode active layer should contain no more than 30% PTFE.[160] Using catalyst ink with higher proportions of PTFE binder aids stability of the active layer (2:1 powder to PTFE being particularly effective), but ultimately does not entirely prevent carbon corrosion and therefore performance degradation.

5.6 Reduction only carbon electrode

The electrodes, which incorporated carbon as a supporting material, initially performed well, but proved unstable when taken to evolution potentials. Increasing the proportion of PTFE prolonged lifespan at these potentials, but could not eliminate the corrosion of the carbon in the catalyst layer. The carbon-supported electrodes could be utilised for use as reduction-only components, thereby avoiding the damaging evolution potentials. This could still be incorporated into a zinc-air flow battery by using a three-electrode setup with different catalysts for the OER and ORR (see Chapter 2.1).

Electrodes were produced with various ratios of catalyst to carbon (including a control with only catalyst) at 4 mg cm^{-2} catalyst loading (≤ 20 μm) following the standard procedure. The electrodes were characterised by LSV and constant current measurements (reduction only). Figure 5.13 shows the linear sweep voltammograms for the electrodes. Values of $j_{-0.5\text{ V}}$ ranging from - 163 mA cm^{-2} for the control to - 298 mA cm^{-2} for the 2:1 catalyst to carbon electrode were observed. The values of $j_{-0.5\text{ V}}$, reveal a clear trend of increasing cathodic current density with increasing carbon inclusion, up to the 2:1 electrode. At higher ratios of carbon, the performance remains approximately the same with $j_{-0.5\text{ V}}$ values staying in a range of 20 mA cm^{-2} from the 2:1 to the 1:2 catalyst to carbon electrodes.

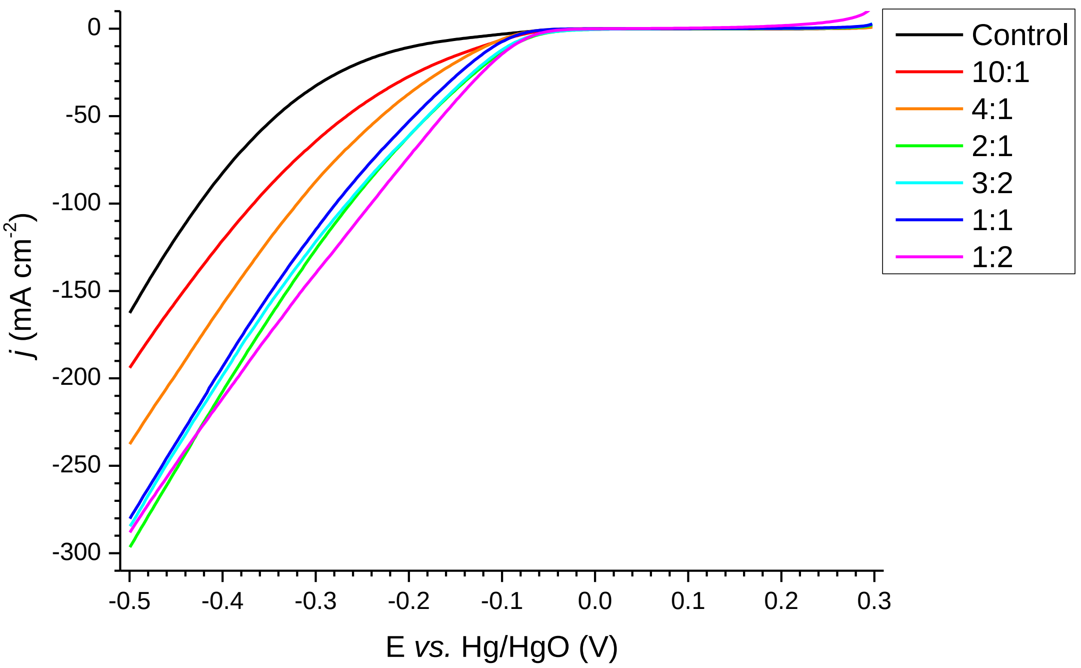

Figure 5.13 LSV for ⩽ 20 μm $NiCo_2O_4$ spinel, thermally decomposed catalyst 4 mg cm^{-2} catalyst loading electrodes with carbon inclusion in ratios 10:1, 4:1, 2:1, 3:2, 1:1and 1:2 catalyst to carbon, also a “Control” electrode at 4 mg cm^{-2} with no carbon. Scan rate 1 mV s^{-1}. In 8 M KOH 60ºC.

The electrodes performed better in LSV than those tested previously, having not first been tested by CV and so not exposed to evolution potentials. Following this, each electrode was held at current densities of - 10, - 20, - 30, - 40 and - 50 mA cm^{-2}, as displayed in Figure 5.14, and then retested at - 10 mA cm^{-2} (to compare with the initial cycle to quantify degradation occurring during testing).

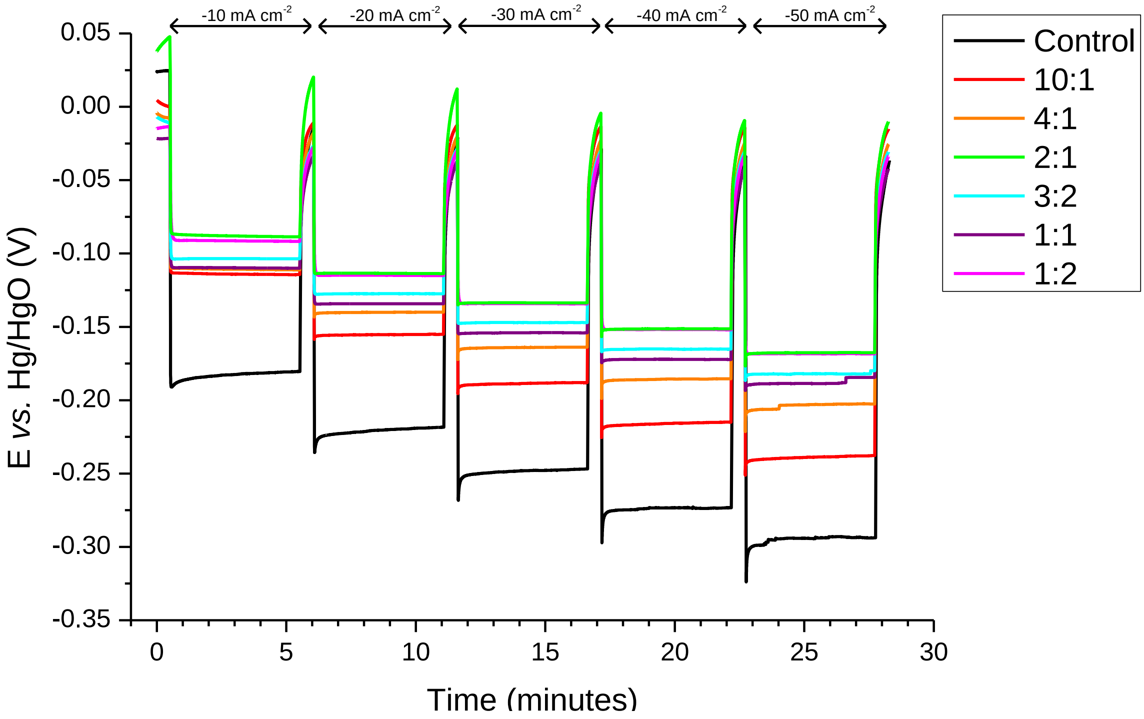

Figure 5.14 Constant current at - 10, - 20, - 30, - 40 and - 50 mA cm^{-2} for electrodes ⩽ 20 µm $NiCo_2O_4$ spinel, thermally decomposed catalyst at 4 mg cm^{-2} catalyst loading with carbon inclusion in ratios 10:1, 4:1, 2:1, 3:2, 1:1 and 1:2 catalyst to carbon, also a "control" electrode with no carbon. In 8 M KOH (at 60°C).

As with the LSV, Figure 5.14 shows the performance of the electrodes improves (cathodic reduction overpotential reduces) with increasing carbon inclusion up to 2:1 catalyst to carbon. The 3:2 and 1:1 electrodes show slightly worse performance than this although the 1:2 electrode performs equally well as the 2:1 catalyst to carbon inclusion electrode. The subsequent application of - 10 mA cm^{-2} to these electrodes, revealed no loss in performance over the course of testing. Some of the worse performing electrodes improved slightly, showing lesser potentials than for the original application of - 10 mA cm^{-2}. To illustrate this maintained performance a control electrode (no carbon inclusion) made with 4 mg cm^{-2} catalyst loading ($NiCo_2O_4$, thermal decomposition, ≤ 20 μm) was run using the following procedure.

The electrode was subjected to current densities of - 10, - 20, - 30, - 40, - 50 and - 10 mA cm^{-2} with a period of OCP measure between each current step. This procedure was carried in two consecutive runs as displayed in Figure 5.15.

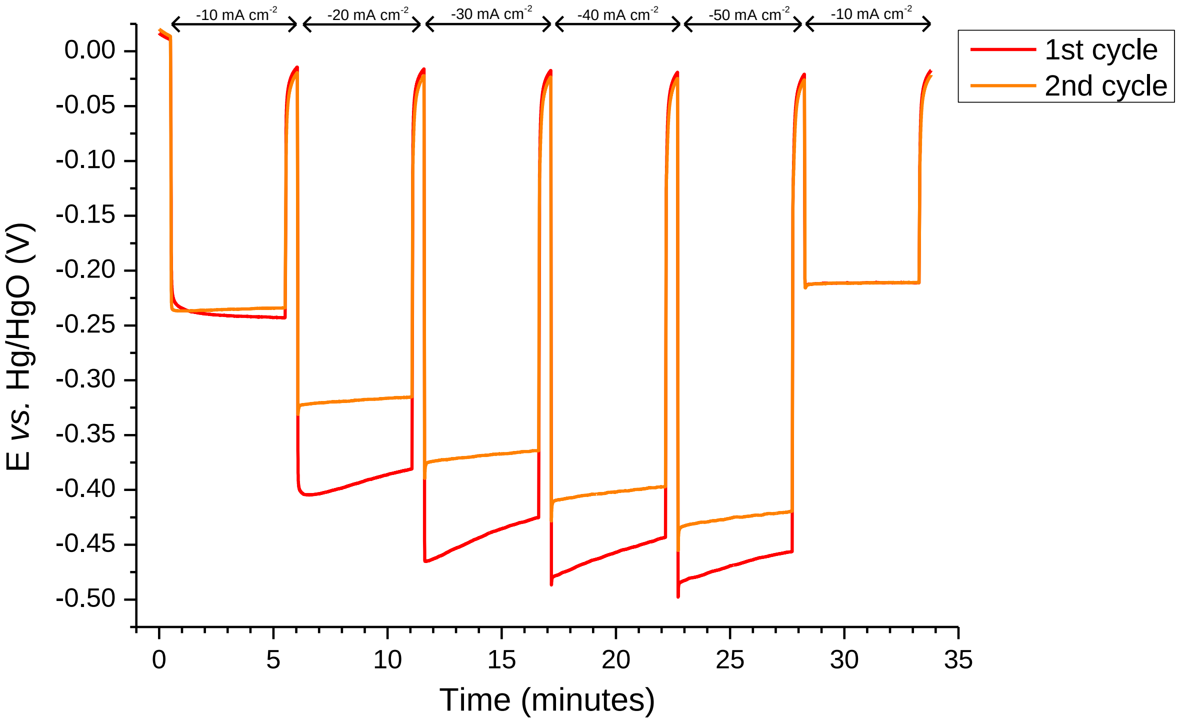

Figure 5.15 **Constant current at - 10, - 20, - 30, - 40, - 50 and - 10 mA cm^{-2} for an electrode at 4 mg cm^{-2} catalyst loading ($\leqslant$ 20 μm $NiCo_2O_4$ spinel, thermally decomposed catalyst) showing two consecutive cycles of testing. In 8 M KOH (60°C).**

Figure 5.15 shows that although this electrode does not achieve the best reduction potentials observed, for the current density applied its performance appears to improve with cycling. This suggests that electrochemical pre-treatment aids the performance of the reduction electrode. Even without this pre-treatment, the 2:1 catalyst to carbon electrode performs well as an oxygen reduction electrode and requires less material than the 1:2 electrode for the same potential. So, it was this electrode that was compared to other oxygen reduction electrodes.

If the OER does not have to be considered other catalyst materials once again become an option. For instance, platinum which shows high activity for ORR and is used in commercial fuel cell catalysts. A 20 wt.% Pt on carbon electrode was prepared with a dry solid loading of 4.1 mg cm^{-2} (Pt loading of 0.8 mg cm^{-2}) following the standard procedure (excluding isopropanol). This was used as a baseline from which to compare with a 2:1 $NiCo_2O_4$ spinel/carbon electrode and a control $NiCo_2O_4$ spinel catalyst electrode (≤ 20 μm, 4 mg cm^{-2} catalyst loading). Also prepared was an electrode with both 4 mg cm^{-2}, 20 wt.% Pt on carbon and 4 mg cm^{-2} $NiCo_2O_4$ spinel catalyst. These electrodes were characterised by LSV and constant current cycling.

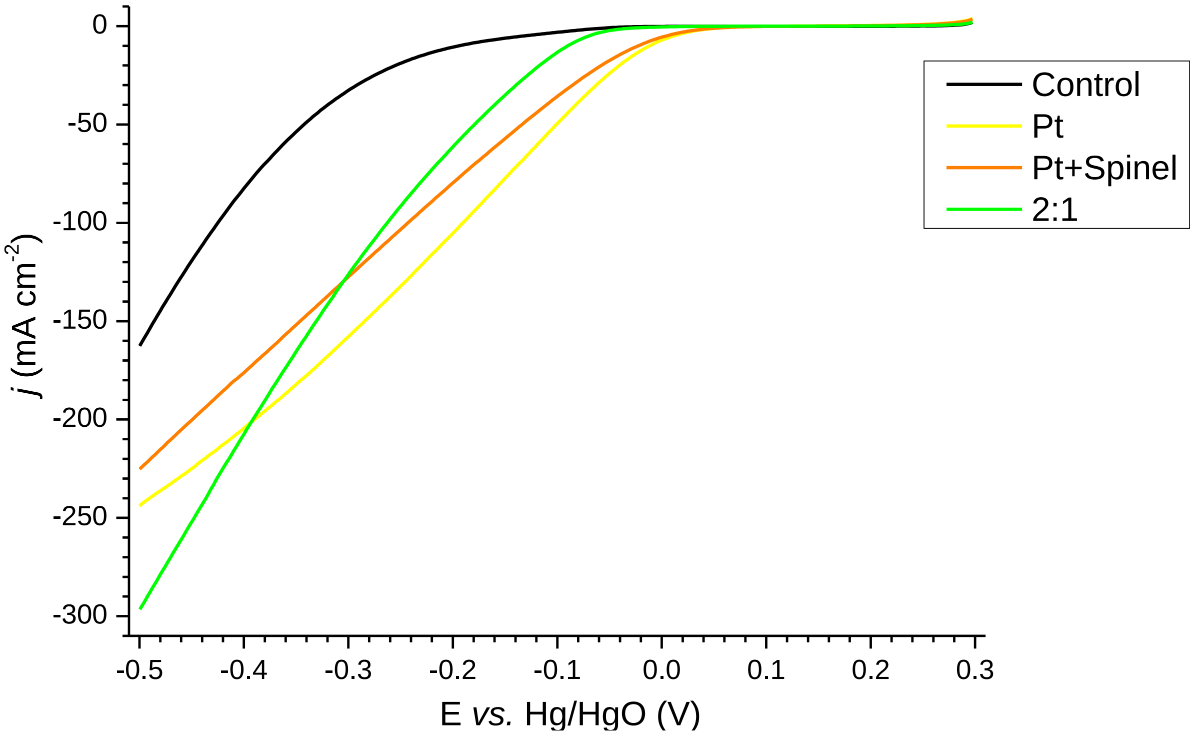

Figure 5.16 LSV for oxygen reduction form 0.3 V to -0.5 V *vs.* Hg/HgO at a scan rate of 1 mV s^{-1}. Electrodes were 20 wt.% Pt on carbon, ≤ 20 μm $NiCo_2O_4$ spinel, thermally decomposed catalyst 4 mg cm^{-2} catalyst loading in a 2:1 mixture of catalyst to carbon or a combination of the two. Performed in the Mk II glass half-cell with static 8 M KOH thermostatically maintained at 60°C.

The cathodic reduction curve of the Pt containing electrodes, commences at an earlier potential than the 2:1 electrode (circa 0.05 V and circa - 0.04 V vs. Hg/HgO respectively). But there is a steeper gradient for the reduction wave of the 2:1 electrode and at higher potentials it outperforms the Pt electrode reaching greater values of $j_{-0.5\,V}$, - 298 mA cm^{-2} compared to - 244 mA cm^{-2}.

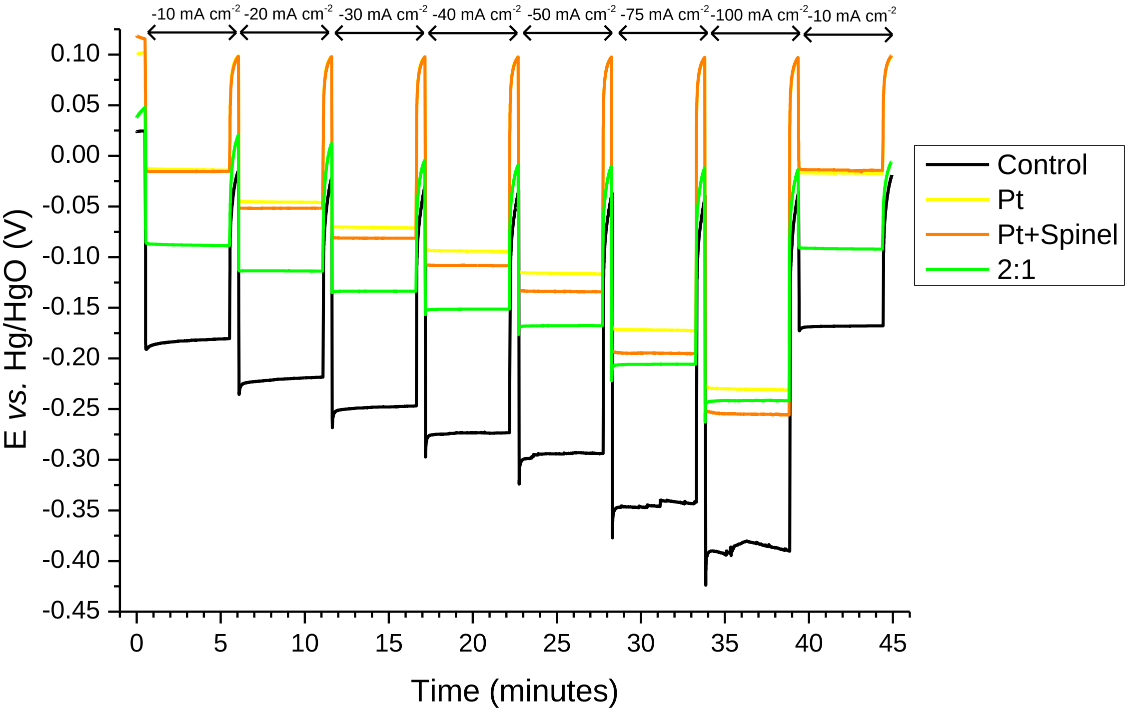

Figure 5.17 Constant current at - 10, - 20, - 30, - 40, - 50, - 75, - 100 and - 10 mA cm^{-2} for the different oxygen reduction electrodes shown in Figure 5.16. In 8 M KOH (60ºC).

Figure 5.17 presents the cycles for these electrodes, which were subjected to current densities of - 10, - 20, - 30, - 40, - 50, - 75 and - 100 mA cm^{-2} and then - 10 mA cm^{-2}. The 20 wt.% Pt on carbon electrode shows the lowest reduction potentials for all current densities. The Pt and $NiCo_2O_4$ spinel electrode shows similar potentials to the Pt electrode at - 10 and - 20 mA cm^{-2}, but drops in performance at higher current densities. The gap between their potentials raises to approximately 30 mV at - 100 mA cm^{-2}. The 2:1 electrode achieves significantly greater reduction potentials than the Pt electrode at low current densities, but as the current increases the values begin to converge. This suggests that at higher current densities the 2:1 $NiCo_2O_4$ catalyst to carbon electrode may perform comparatively to 20 wt.% Pt on carbon electrode. The 2:1 ratio $NiCo_2O_4$ catalyst to carbon electrode developed in this project, could be used as an inexpensive alternative to platinum catalyst for oxygen reduction (ideally for ≥ 200 mA cm^{-2} applications).

5.7 Nickel as a catalyst support

For developing a bi-functional electrode for oxygen evolution and reduction, nickel was also considered as a conductive material for inclusion in the catalyst layer. Electrodes at 4 mg cm^{-2} catalyst loading (≤ 20 μm), were made with different ratios of nickel powder included in the ink (following standard procedure). These electrodes were tested by LSV and constant current cycling at ± 10 mA cm^{-2}, ± 20 mA cm^{-2} and ± 50 mA cm^{-2} as displayed in Figure 5.18 and with the ΔE values shown in Table 5.4.

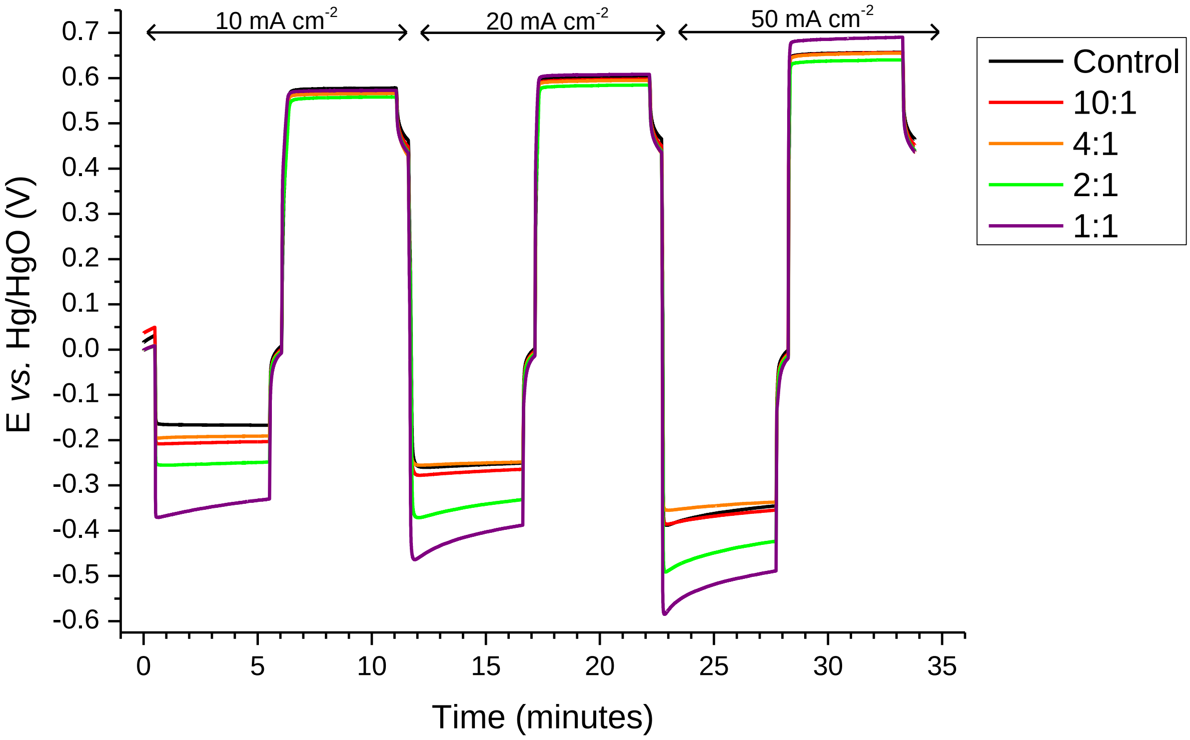

Figure 5.18 Constant current at ± 10, ± 20 and ± 50 mA cm^{-2} for ⩽ 20 μm $NiCo_2O_4$ spinel, thermally decomposed catalyst, 4 mg cm^{-2} catalyst loading electrodes with nickel inclusion in ratios 10:1, 4:1, 2:1 and 1:1 catalyst to nickel, also a “control” electrode at 4 mg cm^{-2} with no nickel. In 8 M KOH 60ºC.

Table 5.4 Depicting the results of the constant current experiment for each catalyst to nickel ratio at 4 mg cm^{-2} catalyst loading including a control electrode.

j (mA cm^{-2})	Potential Gap ΔE (mV)				
	Control	10:1	4:1	2:1	1:1
10	744	773	757	808	912
20	855	865	844	924	1009
50	1010	1018	996	1075	1193

In Figure 5.18 the electrodes with high ratios of nickel, 2:1 and 1:1 show larger values of ΔE than the control for all current densities, this is due to the significantly larger reduction potentials for these electrodes. However, the 4:1 electrode shows improved performance at both 20 and 50 mA cm^{-2}. This suggests that although large ratios of nickel inclusion are detrimental, a lower inclusion might be beneficial to the performance of the electrode.

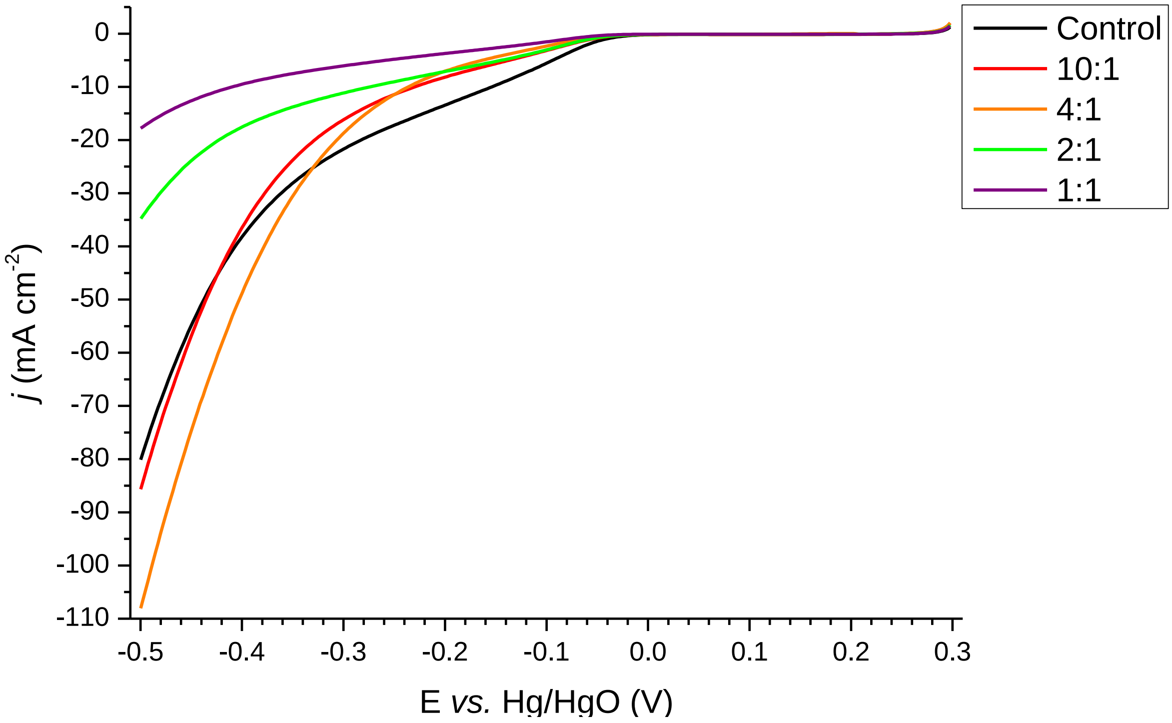

Figure 5.19 LSV for 4 mg cm^{-2} catalyst loading electrodes with nickel inclusion in ratios 10:1, 4:1, 2:1 and 1:1 ⩽ 20 μm $NiCo_2O_4$ spinel, thermally decomposed catalyst to nickel powder, also a "control" electrode at 4 mg cm^{-2} with no nickel. Scan rate 1 mV s^{-1}. In 8 M KOH 60°C.

This is reflected in the LSV presented in Figure 5.19. While the 2:1 and 1:1 electrodes, show small current densities for the potential, the 4:1 electrode begins to show promising performance reaching greater current densities than the control electrode, after circa - 0.35 V *vs.* Hg/HgO with $j_{-0.5\,V}$ - 108 mA cm^{-2} compared to - 80 mA cm^{-2}. The 4:1 catalyst to nickel electrode shows the most promise for further investigation. Electrodes with 4:1 catalyst to nickel, 10:1 catalyst to carbon and catalyst only inclusion, were prepared at 4 mg cm^{-2} (≤ 20 μm) following the standard procedure. These electrodes were subjected to constant current cycling at ± 5 mA cm^{-2} for periods of 1 hour to test their relative stabilities to reduction and evolution potentials over a long period of cycling. The constant current cycles are displayed in Figure 5.20.

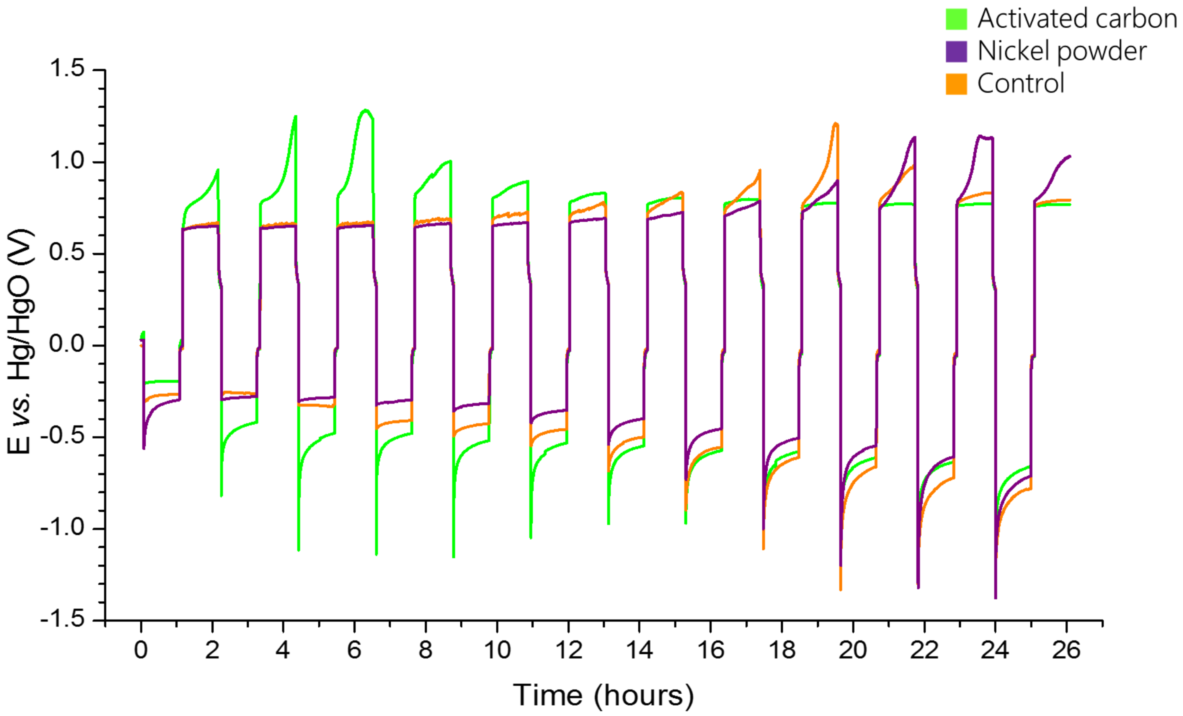

Figure 5.20 Constant current cycling ±5 mA cm^{-2} (1 hour periods) for ⩽ 20 μm $NiCo_2O_4$ spinel, thermally decomposed catalyst, 4 mg cm^{-2} catalyst loading electrodes with the addition of carbon or nickel powder in the active layer. In the Mk II glass half-cell, static 8 M KOH thermostatically controlled at 60˚C.

The 10:1 catalyst to carbon electrode reaches potentials associated with carbon corrosion following the first cycle and afterwards levels off to potentials associated with nickel (present in the cell set-up). The 4:1 catalyst to nickel electrode, shows degradation in the first period of reduction, but then recovers. Both the nickel and control electrodes show gradual loss in performance over the course of the testing, however this occurs to the nickel electrode at a lesser rate. After 4 hours of cycling the nickel electrode is the best performing, with the smallest values of ΔE, and is the last electrode to reach potentials associated with carbon corrosion (indicating the failure of the electrode).

The inclusion of nickel powder (4:1) in the catalyst active layer, has shown itself to be beneficial to the performance of the electrode, as well as an aid to stability over longer electrochemical testing. Such an electrode would be suitable for scaling up and testing in the flow cell. Alternatively, the effect of combined carbon and nickel inclusion could be investigated.

5.8 Conclusions

Carbon based air-electrodes were chosen as a starting point for electrode development, as carbon GDLs are well studied and commercially available. Teflonated carbon paper is hydrophobic in nature and so adaptations had to be made to allow catalyst inks to adequately wet the electrode surface. The addition of a small amount of IPA in the ink, improved the wetting properties and drying times for the inks. An ink containing more than 50% IPA reduces current outputs to near zero. The optimum ratio is approximately a 5:1 (water:IPA), but further investigation could result in even greater performance. The application of the ink can have a big impact on performance. In general, applying multiple thin layers is preferable to fewer thick layers. This can be achieved by diluting the ink with twice as much water/IPA mixture. In addition, pre-wetting the substrate surface appears to be beneficial.

Hot pressing the electrodes to above its glass transition temperature, mobilises the PTFE, creating a more hydrophobic and porous structure. This increases stability by preventing flooding while still maintaining adequate gas channels. In the example described the sample went from poor hydrophobicity to high hydrophobicity and variation across the sample in terms of wetting properties greatly diminished. Current suggested best practice is to heat at 180°C for 5-10 minutes, with 3-5 Kg cm^2 pressure, but this has yet to be optimised.

Although initially counterintuitive, there appears to be a modest performance boost arising from active layers made using a larger particle size range. This is believed to be a result of the less efficient packing of the particles, resulting in larger voids and increased gas channels. Promoting mass transport of oxygen to the active catalyst sites. Oxygen mass transport appears to be a limiting factor regarding maximising catalyst utilisation and reduction performance. There may also be a benefit in terms of a reduction in the number of inter-particle interactions, reducing electrical resistance. Conductivity measurements of electrodes in the future could substantiate this hypothesis.

The addition of carbon powder into the ink was shown to be beneficial, however as carbon is known to be unstable at OER potentials, the long-term stability of carbon based layers is likely to be poor. The stability can be improved by increasing the PTFE content in the active layer. However, high PTFE component active layers, lead to visible cracking of the surface during the drying process. Therefore, a balance needs to be struck as too much PTFE can diminish conductivity. Ultimately PTFE does not entirely prevent carbon corrosion and therefore performance degradation. Ni powder was another additive investigated showing increased stability with cycling. Moving away from carbon and towards a more stable scaffold such as Ni, may prove to be the key to demonstrating prolonged cycle life. Alternatively, the effect of combined carbon and nickel as a catalyst support could be investigated to combine desirable attributes.

Carbon although not stable at OER, does not hamper ORR performance. The same principles developed could be applied to purely ORR applications negating concerns over stability. Initial data suggests that $NiCo_2O_4$ spinel catalyst on carbon could be used as an inexpensive alternative to platinum for such applications. Producing minimal additional overpotential at a significantly reduced cost for ≥ 200 mA cm^{-2} applications.

Chapter 6: Metallic air-electrode

Carbon is not viewed as a long-term air-electrode material as it is susceptible to degradation at the potentials associated with oxygen evolution over prolonged time periods, as discussed in Chapter 5: . Therefore, the project focus switched to finding a more electrochemically stable GDL. As the project progressed, attention shifted toward novel alternatives to carbon for the GDL to escape carbon's inherent limitations during the OER. Various metals, polymers and composite materials were screened as potential GDL and structural components taking the forms of felts, cloths, papers, meshes, foams and membranes.

A series of metal-coated carbon fibre composite materials under the tradename Optimat® were first considered. Although it was suspected that this material would display greater electrical conductivity and stability in the alkaline environment, early electrode designs showed poor performance and stability. The delicate fibrous structure, which was thinner than the carbon paper, began to break apart and become pliable after only a few minutes in hydroxide. As the mechanical and chemical stability of the material was unsuitable interest quickly moved to purely metal structures. Metal substrates became the focus of later electrode development with carbon samples remaining as a baseline for comparison. Nickel and stainless steel (316L) materials including foams, meshes and woven cloths were used to form gas diffusion electrode (GDE) structures.

6.1 Stainless steel woven cloth

Stainless steel woven cloth was used very similarly to the carbon paper. The tight weave of the cloth meant that it required little additional wet proofing. However, the material did not have the same oxygen transport properties of the carbon and so the manufacturing process had to be altered to create a more porous active layer. A novel process which had developed while initially investigating the metallic substrates was dip coating the electrode in a bath of the catalyst precursors and then calcining the catalyst directly onto the electrode.

Two 1 cm^2 discs of BMT50 stainless steel cloth was used to produce electrodes using the same method as for the carbon paper based electrodes. The active layer consisted of a 10:3 mixture by mass of dry solids of $NiCo_2O_4$ spinel:PTFE. The samples were hot-pressed at 180°C for 300 s under a 4 Kg mass. These parameters were selected as they are regularly used for PEM fuel cell electrodes.[161] One of the electrodes was then dip coated as described in section 3.1. The two electrodes were consecutively sealed in the Mk II glass half-cell and linear sweep voltametry was performed on each electrode. The potential was swept from 0.3 V *vs.* Hg/HgO to -0.5 V *vs.* Hg/HgO at a rate of 1 mV s^{-1}. Static 8 M NaOH thermostatically maintained at 60°C was used as the electrolyte and the electrode was fed with a constant excess flow of bottled O_2.

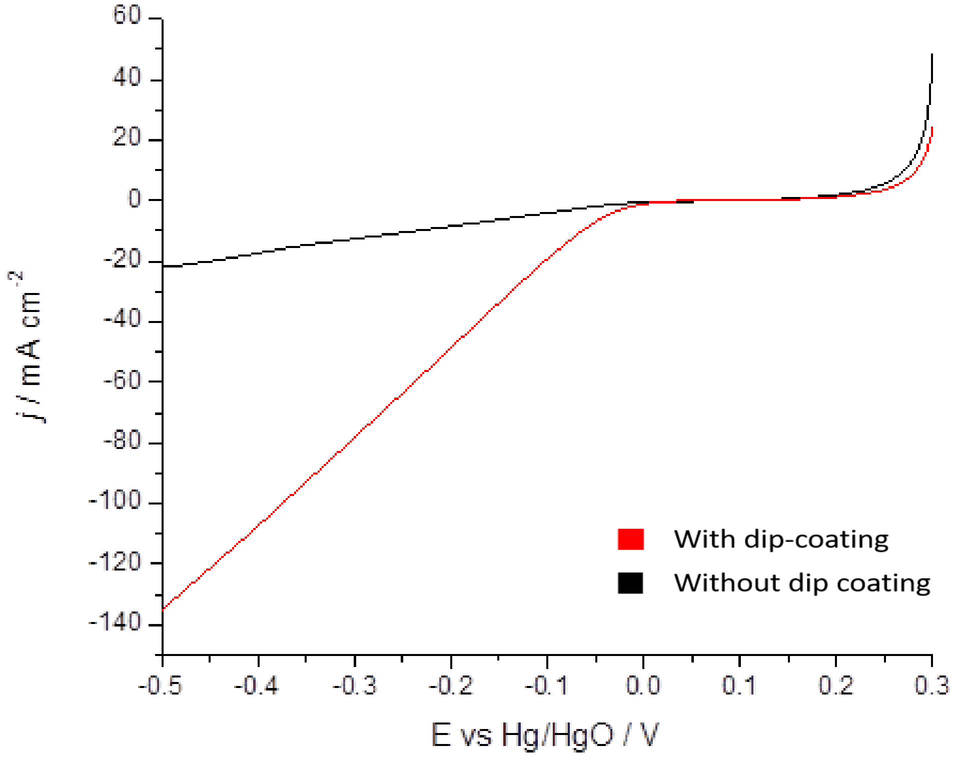

Figure 6.1 Linear sweep voltametry in the Mk II glass half-cell fitted with BMT50 stainless steel woven cloth based electrodes utilising $NiCo_2O_4$ spinel as a catalyst. The electrolyte was 8 M NaOH thermostatically maintained at 60°C and the electrode was fed with a constant excess of bottled O_2. The potential was swept from 0.3 V *vs.* Hg/HgO to -0.5 V *vs.* Hg/HgO at a rate of 1 mV s^{-1}. The black line represents a control electrode whereas the red line shows an electrode which has been produced with the addition of a dip-coating step.

The non dip-coated sample shows relatively little activity maxing out at 21 mA cm^{-2} at - 0.5 V. The dip-coated sample displays much higher activity reaching 134 mA cm^{-2} at - 0.5 V, a more than six-fold increase. It should be noted that the dip-coated electrode has additional catalyst and so there is an expected increase however the dip-coating only adds a thin layer to the surface and so this increase is disproportionately greater than would be expected purely from the addition of catalyst.

It is claimed in the academic literature that it is possible to increase the porosity and therefore oxygen mass transport though the air-electrode by adding a pore former into the active layer.[22, 134] This is then dissolved or combusted at a later stage in the manufacturing process leaving behind voids where the material used to be. One such pore former is Na_2SO_4. Two electrodes were produced as described previously one with the addition of a 10% Na_2SO_4 in the active layer one without. Both samples were dip coated before being run in the Mk II glass half-cell. Static 8 M NaOH thermostatically maintained at 60°C was the electrolyte and the air-electrode was fed with an excess of bottled O_2. The two electrodes were consecutively sealed in the Mk II glass cell and linear sweep voltametry was performed on each electrode. The potential was swept from 0.3 V *vs.* Hg/HgO to - 0.5 V *vs.* Hg/HgO at a rate of 1 mV s^{-1}.

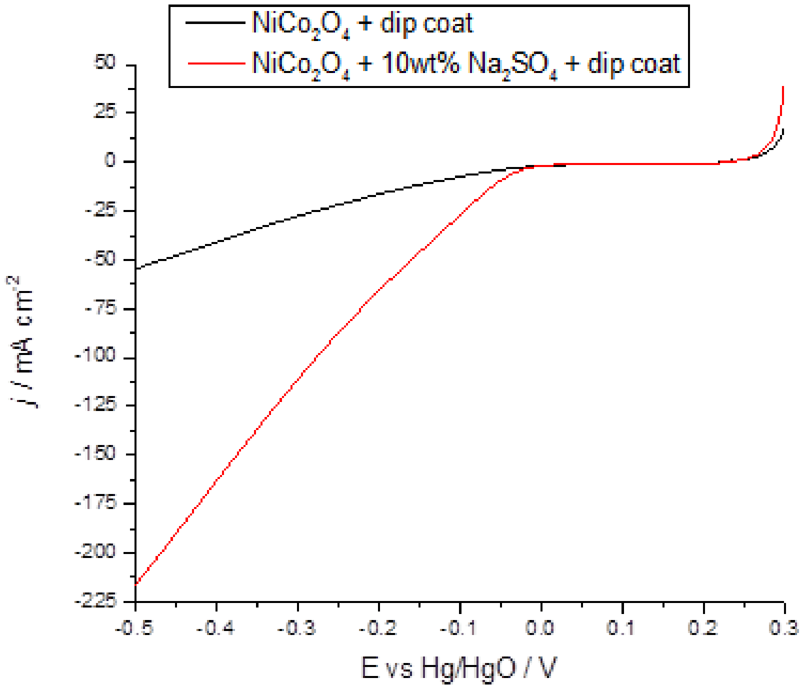

Figure 6.2 Linear sweep voltametry in the Mk II glass half-cell fitted with BMT50 stainless steel woven cloth based electrodes utilising $NiCo_2O_4$ spinel as a catalyst. The electrolyte was 8 M NaOH thermostatically maintained at 60°C and the electrode was fed with a constant excess of bottled O_2. The potential was swept from 0.3 V *vs.* Hg/HgO to -0.5 V *vs.* Hg/HgO at a rate of 1 mV s^{-1}. The black line represents a control electrode whereas the red line shows an electrode which has been produced with the addition of a pore forming step.

The current density achieved for the sample without the pore former was only about half of the value seen for the comparable electrode tested in the previous experiment. This suggests that the dip coating process requires greater controls to ensure reproducibility. Despite this a comparison between the sample with and without the pore former is still observable. The *j* value at - 0.5 V *vs.* Hg/HgO for the sample with pore former is 215 mA cm^{-2}, significantly greater than either of the samples produced without it. The electrodes were then run under constant current conditions for the ORR followed by the OER at 10, 20 and 50 mA cm^{-2} with 30 s periods of OCP preceding each current step. The results are shown in Figure 6.3.

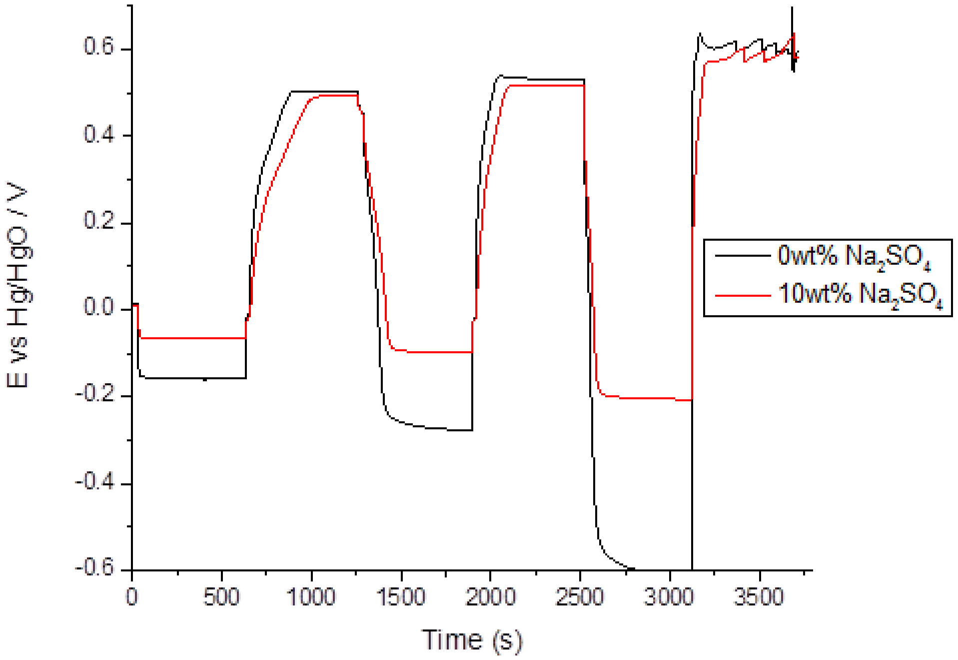

Figure 6.3 Constant current potentiometry in the Mk II glass half-cell fitted with BMT50 stainless steel woven cloth based electrodes utilising $NiCo_2O_4$ spinel as a catalyst. The electrolyte was 8 M NaOH thermostatically maintained at 60°C and the electrode was fed with a constant excess of bottled O_2. The electrodes were then run under constant current conditions for the ORR followed by the OER at 10, 20 and 50 mA cm^{-2} with 30 s periods of OCP preceding each current step. The black line represents a control electrode whereas the red line shows an electrode which has been produced with the addition of a pore forming step.

For the OER the sample utilising the pore former shows a minimal reduction in overpotential over the sample without, approximately 10 mV cm^{-2}. There is also a far more pronounced slope before reaching a plateau. For both electrodes at

50 mA cm^{-2} there is a distinctive ‘sawtooth’ pattern, which represents the evolved gas becoming trapped on the electrolyte face of the electrode. Due to the design of the Mk II glass cell insert (see Figure 3.7) there is a lip which extends out passed the electrode surface. Evolved gas would rise and become trapped by this lip. As more gas was evolved the gas would collect as bubble caught between the electrode and the lip. As the bubble grew it was mask an increasingly large area of the electrode from the electrolyte effectively reducing the geometric area of the electrode. This corresponded to an increase in potential to maintain a constant current over what was now a smaller area and a lower number of active sites. Once the bubble reached sufficient size it would detach from the surface and escape the lip. This effectively lead to the electrodes area returning to the original dimensions and so the voltage rapidly returns to its previous level prior to bubble formation. This entire process would occur repeated leading to the jagged pattern in the data. It was possible to minimise the effect by tilting the cell to allow evolved gas to more readily leave the electrode surface however this did not entirely remedy the problem. Ultimately this phenomenon would not occur to the same extent in a flow battery as the constant flow of electrolyte should remove any trapped gas bubbles formed on the electrode surface. For the ORR, there is a clear difference between the sample with and without pore former. The sample without the pore former is approximately 100 mV greater overpotential than the one with at 10 mA cm^{-2}. The samples then both increase linearly with current density. For the sample with the pore former approximately 20 mV per 10 mA cm^{-2}. For the sample without pore former it is approximately 100 mV per 10 mA cm^{-2}. Overall it is apparent that the introduction of additional gas channels facilitated by the pore former has a significant benefit on air-electrode performance. The fact that the performance

delta is greatest for the ORR suggests that the main benefit of the pore former is the fact that it aids the mass transport of gas as this is a limiting factor for the ORR but does not affect the OER. A suggestion as to the minor performance gain for the OER is a small increase in surface area allowing both the dip coat and the electrolyte to penetrate slightly further into the structure.

6.2 Mesh

MicroGrid® nickel mesh sourced from Dexmet as described in Chapter 4: was initially investigated as it was already being used as a current collector material and was readily commercially available in metre squared quantities. The porous Ni-mesh required the addition of a hydrophobic backing but was otherwise unaltered. A 1.54 cm^2 disc of nickel mesh was mounted in front of a teflonated carbon paper disc (to act as a GDL) in the Mk II glass cell insert (Figure 3.7). It was assumed that the O-ring placed in front of the nickel mesh would not prevent electrolyte expanding past its perimeter as the openings in the mesh were large enough to prevent a water tight seal. In this instance, therefore the exposed geometric surface-area was approximated to be the geometric surface-area of the electrode. The resulting potential at - 50 mA cm^{-2} (ORR) was - 912 mV and 1124 mV at 50 mA cm^{-2} (OER). This potential window was similar in magnitude to pure carbon although shifted positive by a few hundred millivolts so unsurprisingly pure nickel would not prove a viable catalyst.

To overcome the lack of wet proofing an additional layer was required. Early attempts to simply apply a thicker active layer to the mesh were unsuccessful as the smooth surface and flexible nature of the mesh led to delamination of the active layer. It was not possible to apply a thin active layer which was hydrophobic enough to prevent flooding. A solution was to coat the gas face of the electrode with a layer of PTFE. This prevented the majority of wicking/weeping of electrolyte through the electrode but produced an electrically inert surface. This however created the need for the current collector to be repositioned. The simplest way to achieve this in the Mk II glass half-cell was to take current off the electrolyte face of the electrode. Although this presently solves the issue this may be more difficult to implement in a flow cell and could result in the need to collect current via the perimeter or a tab which could increase electrical path lengths and produce uneven current distribution.

A 1.2 cm^2 disc of Dexmet MicroGrid® nickel mesh was used to produce an electrode with the same method as for the carbon paper based electrodes. The ink for this electrode was produced using an FAA3 based ionomer solution provided by Fuma Tech. The FAA3 binder was found to have little or no benefit over PTFE and so was only used for a short period. The thin active layer (~2 mg cm^{-2}) consisted of $NiCo_2O_4$ spinel: FAA3 in a 10:3 mixture by mass of dry solids. The sample was hot-pressed at 180°C for 300 s under a 4 Kg mass. A thin layer of PTFE dispersed in water was then painted onto the opposite face of the electrode to the catalyst. The electrode was then run in the Mk II glass half-cell and linear sweep voltametry was performed (Figure 6.4). The potential was swept from 0.3 V *vs.* Hg/HgO to - 0.5 V *vs.* Hg/HgO at a rate of 1 mV s^{-1}. Static 8 M NaOH thermostatically maintained at 60°C was used as the electrolyte and the electrode was fed with a constant 200 cm^3 min^{-1} flow of bottled O_2.

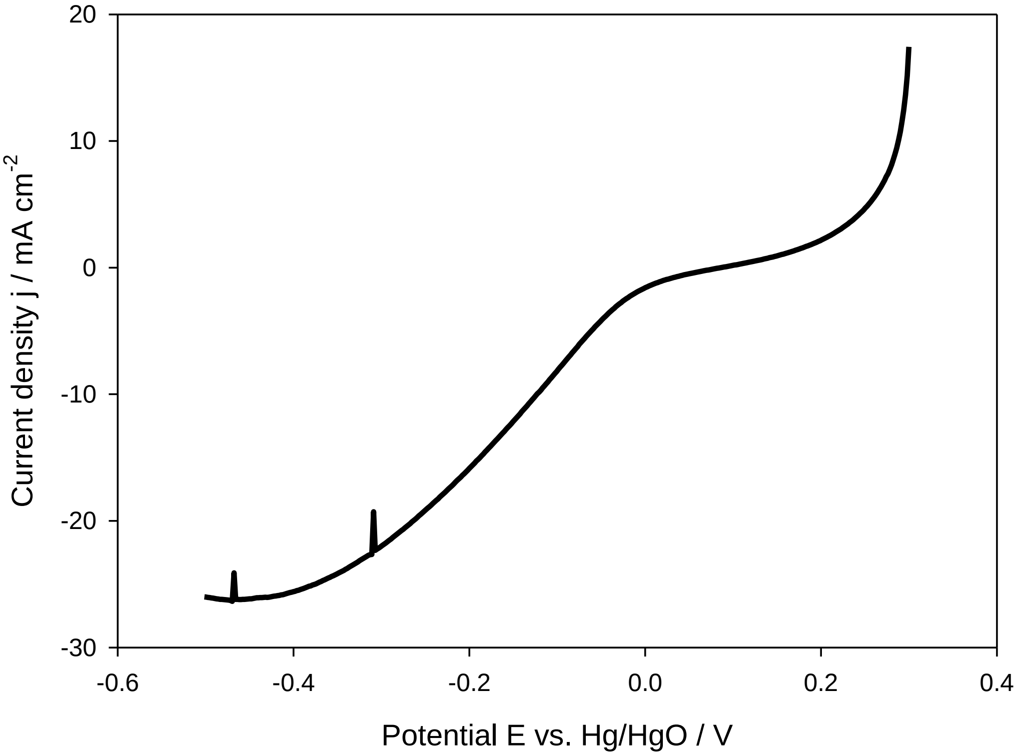

Figure 6.4 Linear sweep voltametry in the Mk II glass half-cell fitted with a Dexmet MicroGrid® nickel mesh based electrode utilising $NiCo_2O_4$ spinel as a catalyst and FAA3 as a binder. The electrolyte was 8 M NaOH thermostatically maintained at 60°C and the electrode was fed with a constant 200 cm^3 min^{-1} of bottled O_2. The potential was swept from 0.3 V *vs.* Hg/HgO to -0.5 V *vs.* Hg/HgO at a rate of 1 mV s^{-1}.

Figure 6.4 shows that the sample had relatively little activity maxing out at 26 mA cm^{-2}. This is similar to the comparable sample produced on the stainless steel woven cloth. There are two noticeable spikes in the LSV data which are caused by an incorrect selection of the current range in the GPES software. In this instance, the system fell back on to auto ranging and the two spikes occur at points at which the current range is switched. The current then rapidly returns to its actual value. The electrode was then run under constant current conditions for the

ORR (300 s) followed by the OER (300 s) at 10 mA cm^{-2} with 30 s periods of OCP preceding each current step. The results are shown in Figure 6.5.

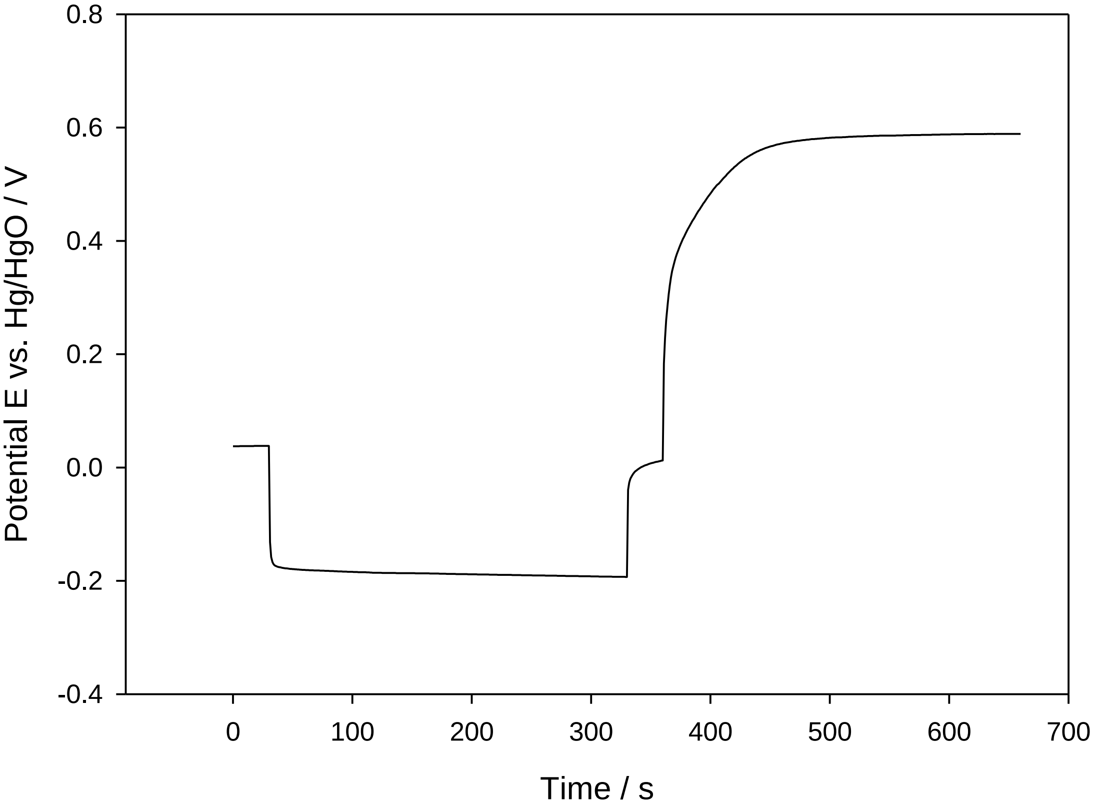

Figure 6.5 Constant current potentiometry in the Mk II glass half-cell fitted with a Dexmet MicroGrid® nickel mesh based electrode utilising $NiCo_2O_4$ spinel as a catalyst and FAA3 as a binder. The electrolyte was 8 M NaOH thermostatically maintained at 60°C and the electrode was fed with a constant 200 cm^3 min^{-1} of bottled O_2. The electrode was then run under constant current conditions for the ORR followed by the OER at 10 mA cm^{-2} with 30 s periods of OCP preceding each current step.

For the OER the potential plateaus at 580 mV *vs.* Hg/HgO. The ORR potential is - 200 mV *vs.* Hg/HgO giving a potential window of 780 mV overall. The performance is stable and potentials are acceptable for a non-optimised electrode. Ultimately due to the limitations associated with the substrate material and subsequently electrode manufacture few operational electrodes were produced using this mesh. This combined with its performance equalling the stainless-steel cloth led to it being dropped as a substrate and other materials were considered.

6.3 Ni Foam

Nickel foams such as those supplied by Goodfellow were next explored for use in metal based air-electrodes; their 3-D structure allowed for far greater adhesion of the active layer to the substrate than there comparatively 2-D mesh/cloth based counterparts. The deeply porous structure required a significant quantity (> 50 mg cm^{-2}) of material to be packed into the voids of the foam to ensure adequate wet proofing. For this reason, the manufacturing process had to be altered greatly as detailed in Section 3.1. The electrode is fabricated by pre-forming a PTFE-bonded nickel powder layer on a nickel foam substrate followed by deposition of $NiCo_2O_4$ spinel electrocatalyst by dip coating in a nitrate solution and thermal decomposition. The nickel powder/PTFE paste was used as a filler for the foam. Although it was possible to pack the foam with catalyst material, 50-150 mg cm^{-2} was required which would prove prohibitively expensive even for a non-precious metal catalyst. This is significantly larger than the 3-10 mg cm^{-2} required for the carbon paper based electrodes and the < 1 mg cm^{-2} of precious metals used in fuel cell electrodes. What is more due to the nature of the three-phase boundary only a small subsection of the filler material would meet the conditions required to facilitate the electrochemistry. The dip coating method which had already proven to be effective for the stainless-steel cloth was applied to the packed foam to create a more acceptable catalyst loading. The loading of

$NiCo_2O_4$ from the dip-coat was estimated to be ~ 3 mg cm^{-2} by weight increase, which is comparable to the carbon paper based electrodes.

Figure 6.6 shows the potential *vs.* time responses for oxygen reduction and evolution at a constant current density of 20 mA cm^{-2} for the nickel foam based GDE. A commercial Pt/carbon GDE (Johnson Matthey Fuel Cells, 15 wt.% Pt with loading 4 mg cm^{-2}) used as received was also tested as a comparison. Static 8 M NaOH thermostatically maintained at 60°C was used as the electrolyte and the electrode was fed with a constant 200 cm^3 min^{-1} flow of bottled O_2.

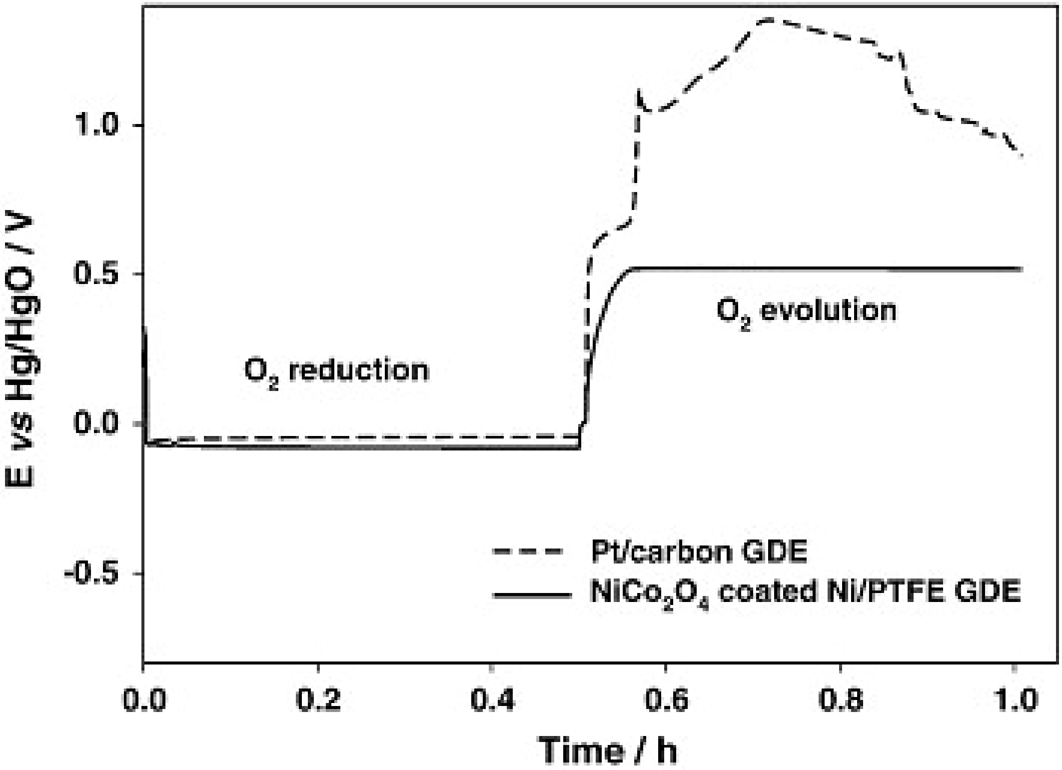

Figure 6.6 Comparison of potential *vs.* time responses during constant current density cycling of spinel-coated Ni/PTFE Ni foam GDE and a commercial Pt/C GDE. Cathodic and anodic currents both 20 mA cm^{-2}. Electrolyte: 8 M NaOH at 60°C. Oxygen feed rate: 200 cm^3 min^{-1}.

The potential quickly reaches a constant value during both oxygen reduction and evolution. The steady state potentials are separated by only 620 mV which is comparable with the best carbon paper based electrodes. The data for the commercial Pt/carbon GDE illustrates how favourably the $NiCo_2O_4$ spinel compares to Pt during the ORR. When an initial cathodic current is passed, the Pt catalysed GDE performs well, giving a slightly lower overpotential (~ 40 mV) for oxygen reduction than observed with the spinel. During oxygen evolution, however the sample containing Pt and carbon begins to degrade almost instantly, highlighting the benefit of a carbon free air-electrode structure. A further foam based electrode was produced as described previously and run in the Mk I flow cell (see section3.5.3) at 10 mA cm^{-2} for 1 h charge cycles followed by the corresponding discharges (a 300 s period of OCP was left between steps).

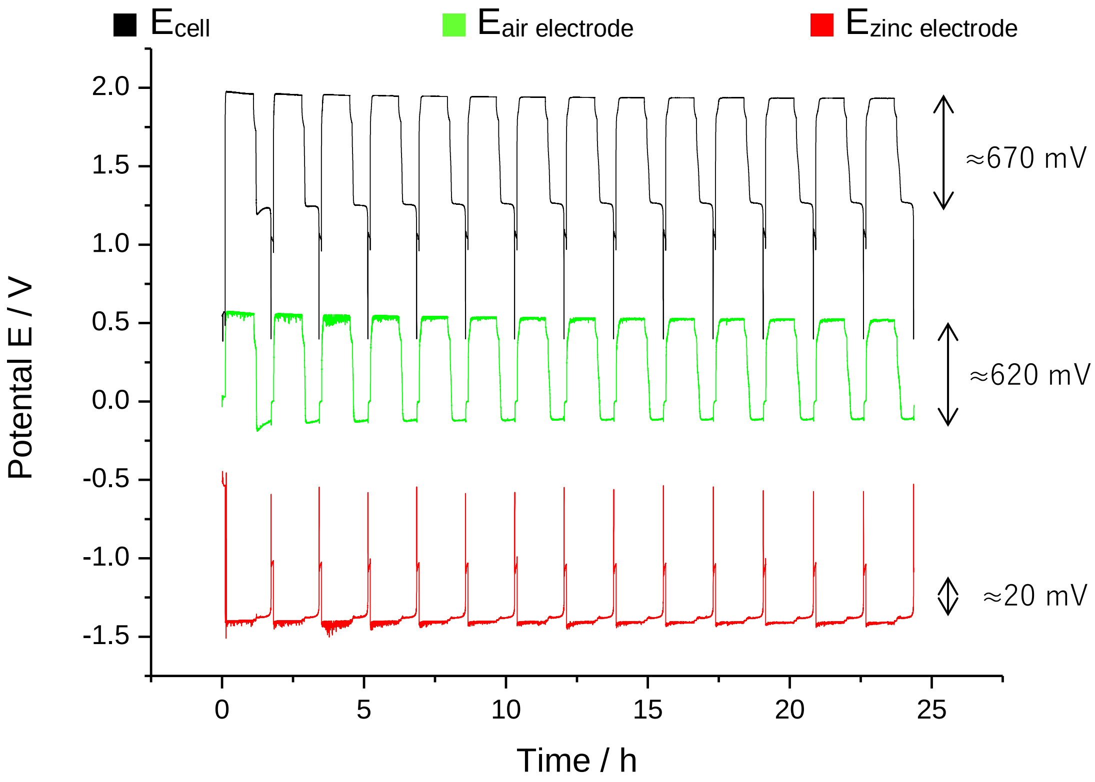

Figure 6.7 Charge/discharge cycling at 10 mA cm^{-2} in the Mk I flow cell for fourteen 1 h charging period cycles. Cell fitted with an 8 cm^2 $NiCo_2O_4$ spinel coated Ni foam packed with Ni powder/PTFE GDE. Electrolyte: 1 L of 8 M NaOH + 0.5 ZnO thermostatically maintained at 60°C (approx. 400 cm^3 min^{-1} flow rate). Gas supply: bottled O_2 (approx. 250 cm^3 min^{-1} flow rate). A 300 s period of OCP preceded each step in the testing program.

Figure 6.7 shows both the charge/discharge cell data and values for the individual electrodes. Performance slowly improved with cycling which is common for electrodes which do not degrade or leak. For this reason peak cell performance was taken as the performance of the final cycle. For the zinc electrode the potential window observed was 20 mV which added very little to the combined overpotential. The air-electrode had a potential window of 620 mV which correlates with performance shown in the glass half-cell. These combined with other minor ineffecencies resulted in a potential window of 670 mV for the operation the cell. This translates into a voltage efficiently of ~ 65% which is around the threshold of system viability. Stability is respectable but the cell did suffer from leaking most probably as a result of not forming an adequate seal round the electrode. The three-dimensional nature of the structure led to significant engineering challenges when trying to manufacture and seal the electrodes into a cell on a 10 cm^2 – 100 cm^2 scale. The charge efficiency is considerably lower than would be expected at ~ 55%. Assuming that the zinc-electrode is functioning properly charge efficiency should be > 90%.

A second nickel foam based electrode was manufactured and tested in the Mk II flow cell. Figure 6.8 presents a series of three charge-discharge cycles using the Ni-foam positive electrode with incremental increases in current densities with successive cycles, 10, 20 and 50 mA cm^{-2}. The data is summarised in Table 6.1.

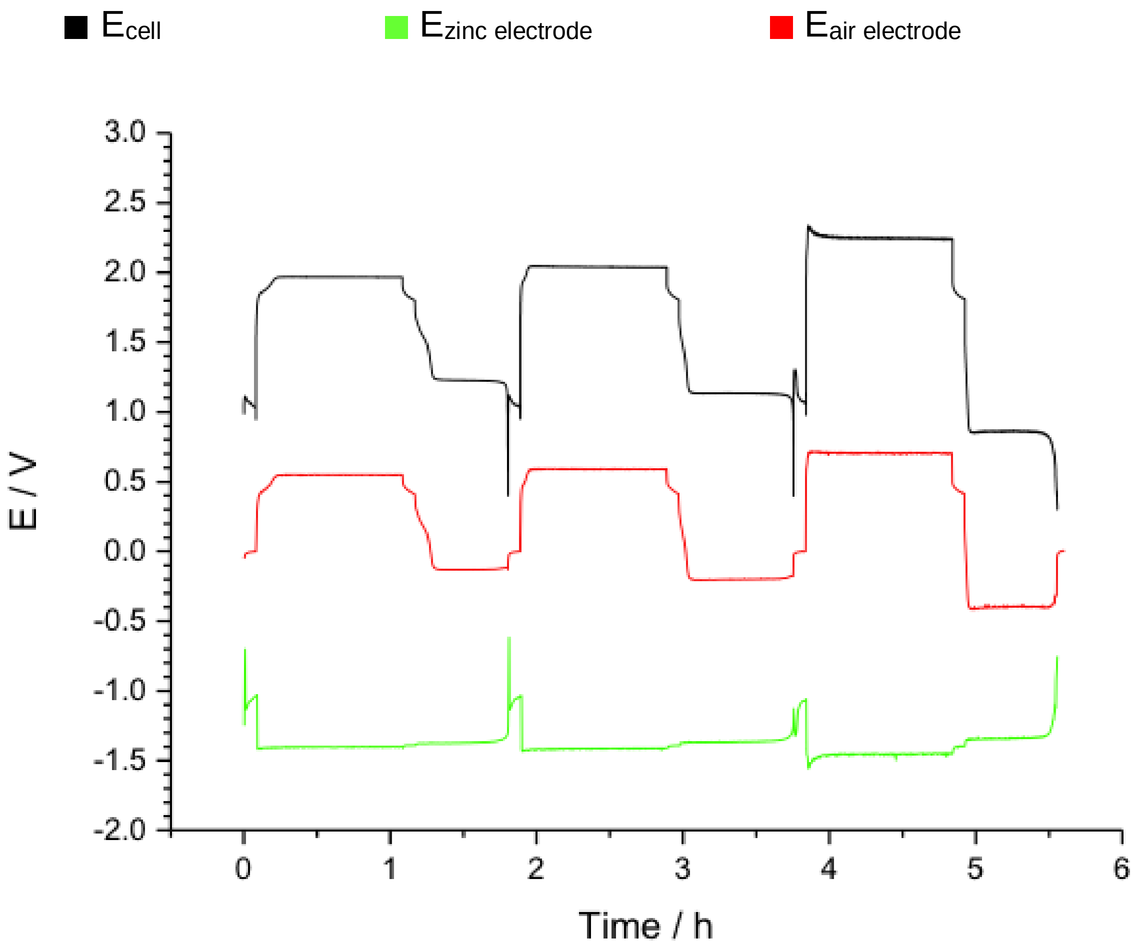

Figure 6.8 Charge/discharge data from the Mk I flow cell fitted an 8 cm^2 $NiCo_2O_4$ spinel coated Ni foam packed with Ni powder/PTFE GDE. The cell was cycled at 10 mA cm^{-2}, 20 mA cm^{-2} and 50 mA cm^{-2}. Electrolyte: 1 L of 8 M NaOH + 0.5 ZnO thermostatically maintained at 60˚C (approx. 400 cm^3 min^{-1} flow rate). Gas supply: bottled O_2 (approx. 250 cm^3 min^{-1} flow rate). A 300 s period of OCP preceded each step in the testing program.

Table 6.1 Efficiency data calculated for the flow cell cycling shown in Figure 6.8.

Current density, j / mA cm^{-2}	Charge Voltage / V			Discharge voltage / V			Voltage efficiency / %	Charge efficiency / %
	Cell	Electrode		Cell	Electrode			
		+	-		+	-		
10	1.969	0.553	-1.404	1.227	-0.131	-1.380	62.3	63.7
20	2.043	0.590	-1.416	1.130	-0.203	-1.368	55.3	78.3
50	2.246	0.710	-1.453	0.865	-0.395	-1.344	38.5	63.2

The charging and discharging potentials for the cell increase linearly with current density. There is approximately a 70 mV increase in charging overpotential of each 10 mA cm^{-2} increase and an approximately a 90 mV increase in discharge overpotential of each 10 mA cm^{-2} increase. the additional increase during discharge is likely associated with oxygen mass transport limitations. Correspondingly the voltage efficiency drops by approximately 6% per 10 mA cm^{-2} increase. The charge efficiency is slightly higher than seen in the previous experiment but still lower than anticipated. There is also an inexplicable jump of 15% for the second cycle which disappears on the third. Clearly further optimisation of the zinc electrode is required however this falls outside the scope of this thesis. As stated in equation 1.8 the E_{cell} should equate to the difference between the individual electrode potentials. From the data collected this appears to be the case to a rough approximation. For example, the charging potential measured for the cell at 10 mA cm^{-2} was 1.969 V where as the calculated value form the two electrodes was 1.957 V. This is a total disparity of 12 mV which is negligible however the gap between experimentally measured from the cell and the combination of the individual electrodes increases consistently with current density. The samples measured at 50 mA cm^{-2} the difference is ~80 mV.

6.4 Comparison of structures with an example of the current best architecture

Figure 6.9 shows a comparison of air-electrode structures investigated in the Mk II glass half-cell at 20 mA cm^{-2}. Although the geometric area of the electrodes was kept constant and the same electrochemical conditions are maintained the surface area, catalyst loading and compositions vary greatly between the different electrode types. Galvanostatic potentiometric measurements were recorded for each electrode in turn. After an initial period of OCP (30 s) a negative j of -20 mA cm^{-2} was applied for 300 s to observe the ORR. This was followed by a further 30 s of OCP. The current was then increased to 20 mA cm^{-2} and applied for 300 s. 8 M NaOH at 60° C was used as the electrolyte for all tests and a constant flow of 200 cm^3 min^{-1} O_2 was supplied to the rear face of the air-electrode.

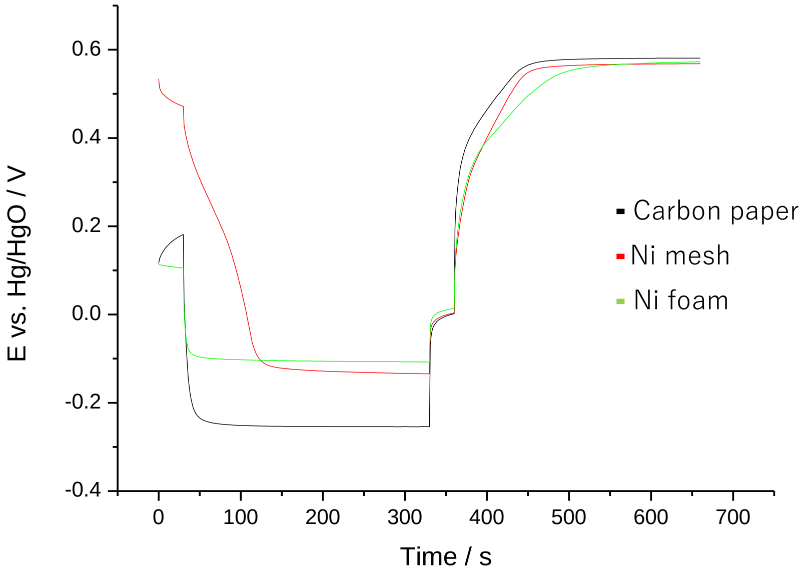

Figure 6.9 Comparison of three electrodes based on a carbon paper, Dexmet Ni mesh an Goodfellow Ni foam substrates. Galvanostatic potentiometry run at 20 mA cm^{-2} for both cathodic and anodic currents with 30 s periods of OCP in between current steps. 8 M NaOH at 60°C was used as the electrolyte for all tests at constant flow of 200 cm^{3} min^{-1}, with bottled O_2 supplied to the rear face.

Once the first current step was applied the potential for all samples began to drop. Both the carbon paper and the foam samples dropped rapidly to steady state potentials of approximately - 260 mV and - 100 mV *vs.* Hg/HgO respectively. The Ni mesh however dropped in potential far more gradually than the other two samples before settling at approximately - 120 mV *vs.* Hg/HgO. This more gradual decrease results from the fact that the surface has been oxidised and so a reduction of the surface species is occurring before oxygen reduction is achieved. For the OER, there is minor variation between the samples as the reaction is independent of oxygen mass transport properties the electrode architecture is far less influential on performance. Although based on the comparison the carbon paper is electrochemically the weakest of the electrodes are rapid and practical to manufacture at a laboratory scale. They also utilise modest quantities of catalyst ($\leq$ 10 mg cm^{-2}) making them an efficient use of potentially limited catalyst supplies. The carbon electrode therefore maintains a utility for development and optimisation of other cell components however in terms of raw performance and stability the Ni foam appears superior. For optimal performance, these are the electrodes to operate.

6.5 Conclusions

Carbon is not a suitable air-electrode material as it is susceptible to degradation at the potentials associated with oxygen evolution therefore purely metal based structures were explored as a substitute. After a brief period of screening Nickel and stainless steel (316L) materials were selected as suitable alternatives to consider for gas diffusion electrode (GDE) structures.

Tight weave BMT50 stainless steel woven cloth required little additional wet proofing and so could be substituted directly into the carbon paper manufacture process. However, the material did not have the same oxygen transport properties of the carbon and so required alterations to create a more porous active layer. A process which had been developed concurrently with metal substrate development was dip coating electrodes in a bath of the catalyst precursors and then form the catalyst directly onto the electrode by calcination. This process was used to increase stainless steel electrode performance by a factor of six achieving an ORR activity of 134 mA cm^{-2} at - 0.5 V *vs.* Hg/HgO.

A second claim was that the addition of a pore former which could be extracted after the formation of the active layer would increase porosity and therefore oxygen mass transport. 10% Na_2SO_4 was added to the active layer during production and soaked out during dip coating. Despite variability between samples caused by the dip coating process the *j* value at - 0.5 V *vs.* Hg/HgO for the sample with pore former was increased yet further over the base electrode to 215 mA cm^{-2}.

MicroGrid® nickel mesh sourced from Dexmet was also investigated as a substrate material. Due to the large pores in the material it required additional wet proofing to prevent flooding. A solution was to coat the gas face of the electrode with a layer of PTFE. Initial electrodes showed relatively little activity maxing out at 26 mA cm^{-2} similar to the comparable stainless steel woven cloth electrodes. Due to the limitations associated with the substrate material and subsequently electrode manufacture few operational electrodes were produced using this mesh. This combined with its performance equalling the stainless-steel cloth led to it being dropped as a substrate and other materials were considered.

Nickel foams such as those supplied by Goodfellow were next explored for use in metal based air-electrodes; their 3-D structure allowed for far greater adhesion of the active layer to the substrate than there comparatively 2-D mesh/cloth based counterparts. The deeply porous structure required a significant quantity (> 50 mg cm^{-2}) of material to be packed into the voids of the foam to ensure adequate wet proofing. For this reason, the manufacturing process had to be altered greatly. To increase wet proofing and reduce the amount of catalyst required the foam was packed with a PTFE-bonded nickel powder layer. The $NiCo_2O_4$ spinel electrocatalyst could then be applied to this pre-formed GDL by dip coating in a nitrate solution and thermal decomposition. The loading of $NiCo_2O_4$ from the dip-coat was estimated to be ~ 3 mg cm^{-2} by weight increase, which is comparable to the carbon paper based electrodes.

For constant current potentiometry at 20 mA cm^{-2} in the glass half-cell the potential quickly reaches a constant value during both oxygen reduction and evolution. The steady state potentials are separated by only 620 mV which is comparable with the best carbon paper based electrodes. The electrode was compared to a commercial Pt/carbon fuel cell GDE. The Pt catalysed GDE gave a slightly lower overpotential (~ 40 mV) for oxygen reduction than observed with the spinel/Ni foam electrode. During oxygen evolution, however the sample containing Pt and carbon begins to degrade almost instantly, highlighting the benefit of a carbon free air-electrode structure.

A similar nickel foam electrode was cycled in the flow cell at 10 mA cm^{-2} for 24 hours with no drop in performance. The air-electrode had a potential window of 620 mV between charge and discharge which correlates with performance shown the glass half-cell. The resulting potential window for the cell was 670 mV which translates into a voltage efficiently of ~ 65% which is around the threshold of system viability. The charge efficiency was considerably lower than would be expected at ~ 55%. A second nickel foam based electrode was manufactured and cycled in the Mk II flow cell at current densities of 10, 20 and 50 mA cm^{-2}. The voltage efficiency dropped by approximately 6% per 10 mA cm^{-2} increase. The charge efficiency again was erratic and lower than anticipated. Clearly further optimisation of the zinc electrode is required however this falls outside the scope of this thesis.

Comparing the three main types of electrode (carbon paper, metal mesh/cloth and metal foam) at 20 mA cm^{-2} in the glass half-cell showed minor variation for the OER. The three electrodes utilise the same catalyst with similar loadings and as the reaction is independent of oxygen mass transport electrode architecture appears to have little effect. For the ORR, however the carbon paper reaches a steady state potential at approximately – 260 mV *vs.* Hg/HgO compared to the metal electrodes at approximately - 100 mV *vs.* Hg/HgO. Based on this comparison the carbon paper is electrochemically the weakest of the electrodes and so would not be recommended for further scale-up/commercialisation. Despite this it is simple and rapid to produce on a laboratory scale so is still worth considering for development and optimisation of other cell components on a small scale however in terms of raw performance and stability the Ni foam is superior. Despite present manufacturing and material issues for optimal performance, metallic foam is the electrode to operate.

Chapter 7: Flow cell optimisation

This chapter details the construction, development, calibration and testing of a unit flow cell for evaluation of novel electrode structures and proof of concept operation. As progress was made on a smaller scale, the findings were fed into flow cell development, however, these activities were run concurrently so initial flow cell work was carried out using non-optimised catalysts and GDE structures.

7.1 Electrolyte

7.1.1 Effect of zincate on the air-electrode

Electrolyte for the flow cell was prepared by dissolving ZnO (0.5 M equivalent) into 8 M hydroxide. This addition is essential, as it provides the active material for the zinc half-cell (Equation 7.2). For air-electrode half-cell testing, zinc was not included in the electrolyte (Chapter 4-6) as this would add unnecessary complexity. The zinc oxide reacts with the hydroxide solution to produce zincate, $Zn(OH)_4^{2-}$, which is deposited as metallic zinc during charging (Equations 7.1). In Equation 7.1 potassium hydroxide is used as an example.

$$ZnO + H_2O + 2KOH \leftrightarrow K_2[Zn(OH)_4] \qquad 7.1$$

$$Zn(OH)_4{}^{2-} + 2e^- \leftrightarrow Zn + 4OH^- \ (E^0 = -1.25\ V) \qquad 7.2$$

ZnO has a low solubility in water ($< 1\ g\ L^{-1}$). The solubility of a substance is fundamentally dependant on three factors:

- The solvent and its properties
- Pressure
- Temperature

Due to the need for OH^- charge carriers the solvent in this instance has been limited to hydroxide. Properties including concentration and the metal ion can be varied but fundamentally the solvent cannot be drastically altered. Due to the additional complexity, expenses and safety implications associated with varying and maintaining pressure this was not chosen to be explored. The delicate interface of the three-phase boundary at that air-electrode will also be dramatically effected by a deviation in pressure which would have to be balanced by the gas flow on the opposing face. The only other parameter which can be varied is temperature and so this was used as the route to increased solubility. The ZnO solubility can be increased dramatically when the temperature is raised to 60°C. The solubility in 10 mol dm^{-3} KOH at 60°C is 0.87 mol dm^{-3}.

To assess the effect of zincate on the air-electrode and the Mk II glass half-cell a 2:1 catalyst to carbon ratio electrode (4 mg cm^{-2} loading) was made following the established procedure. It was sealed in the glass cell and a constant current of - 10 mA cm^{-2} was applied for two 15 minute periods followed by open circuit. The electrode was kept below evolution potentials to minimise degradation. During the period of open circuit, the 8 M KOH electrolyte was stirred and 0.1 M of ZnO was added and allowed to dissolve. A constant current of - 10 mA cm^{-2} was then applied once again for 15 minutes. This process of adding ZnO was repeated until the electrolyte contained 0.7 M zinc oxide (near the limit of solubility in 8 M KOH). Figure 7.1 displays the resulting E *vs.* Hg/HgO plotted against the concentration of ZnO added.

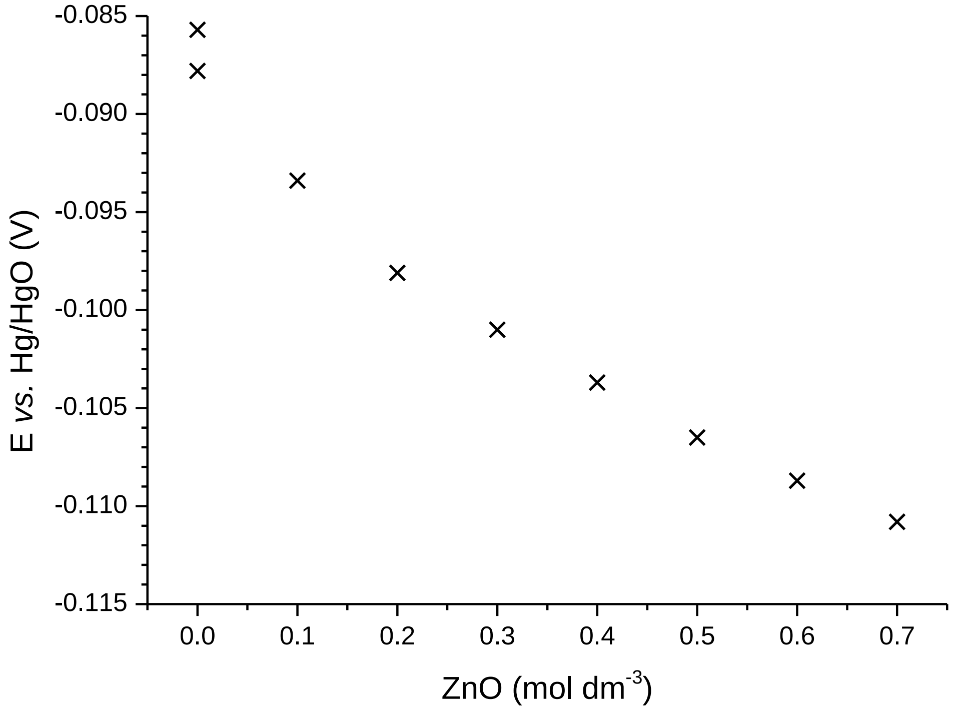

Figure 7.1 Plot of potentials for an air-electrode (4 mg cm^{-2} 2:1 NiCo2O4 catalyst to carbon powder active layer) measured at a constant current of -10 mA cm^{-2} versus the concentration of ZnO added to the 8 M KOH (60°C) electrolyte.

The potential of the electrode for each of the - 10 mA cm^{-2} periods decrease minimally with the addition of ZnO. The potential drops by 23 mV over the course of the experiment. This equates to a decrease in potential of 2-5 mV per 0.1 M ZnO addition and is present even between the two initial measurements which occurred before the addition of zinc oxide. This performance drop therefore appears to be more closely related to electrode deterioration over the > 2 h period rather than an effect of the zincate concentration. Agitation of the electrolyte used to aid zinc dissolution may also have played a role in eroding the electrode surface as the electrolyte had remained static in glass cell tests to this point. Before the electrode was removed from the cell the electrolyte was replaced with fresh 8 M KOH and a current of - 10 mA cm^{-2} was applied for 5 minutes. The electrode potential recovered from a low of – 0.111 V *vs.* Hg/HgO to – 0.092 V *vs.* Hg/HgO showing that the Zn present in the electrolyte may have minimal effect on electrode potential. To explore this further, a set of four carbon paper GDL electrodes were produced with a 4 mg cm^{-2} loading of 2:1 catalyst to carbon following the established procedure with the additional step of grinding catalyst and carbon together before addition to the ink. This procedural tweak was believed to increase homogeneity of the ink improving the reproducibility of the electrodes. Each of these electrodes was characterised by LSV and constant current (reduction potentials only) in a different electrolyte. The electrolytes used were 8 M KOH with 0.2 M, 0.4 M or 0.6 M Zn (zincate/zinc oxide).

The electrodes were first characterised by LSV to determine how comparable they were to one another. The electrodes showed strong and reproducible performance with $j_{-0.5\,V}$ values within 15 mA cm^{-2} of one another (- 296 mA cm^{-2} to - 310 mA cm^{-2}) and current densities remaining within a close range at all potentials observed. Satisfied with this, each electrode was subjected to current densities of - 10 mA cm^{-2}, - 20 mA cm^{-2} and - 50 mA cm^{-2} each for the shorter time of 5 minutes (to minimise the effects of electrode degradation over time). The results are displayed in Figure 7.2 and tabulated in Table 7.1.

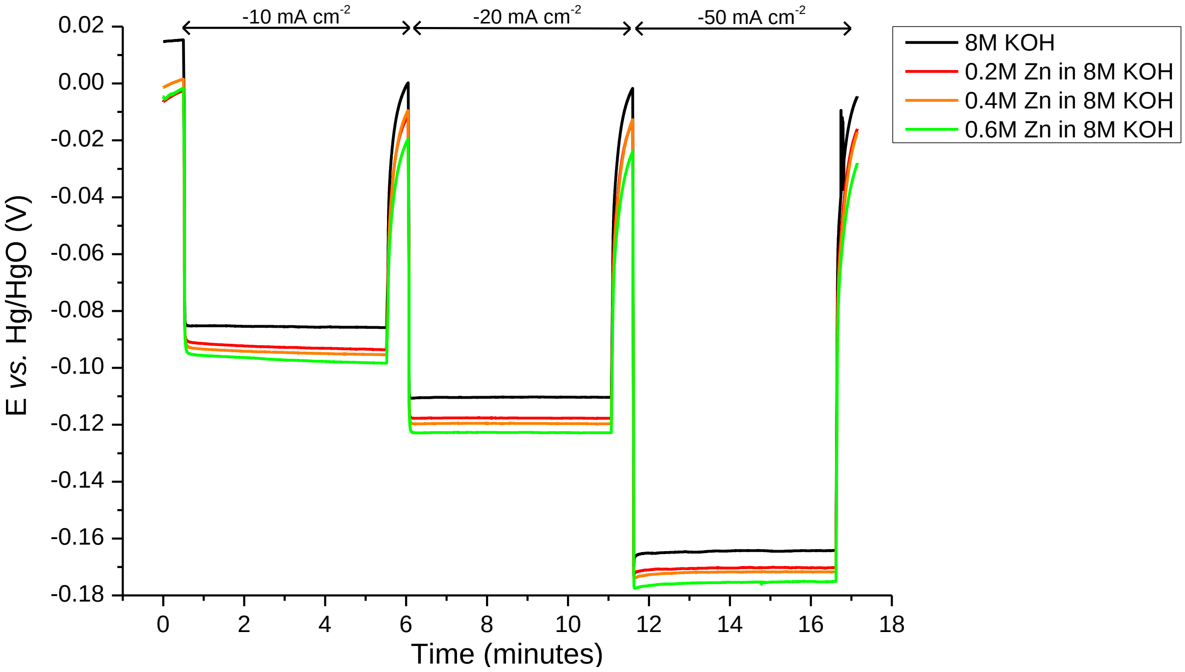

Figure 7.2 Constant current at - 10, - 20 and - 50 mA cm^{-2} for 4 mg cm^{-2} 2:1 catalyst to carbon electrodes versus the concentration of ZnO added to the 8 M KOH (at 60°C).

Table 7.1 Constant current (reduction only) for 4 mg cm^{-2} 2:1 catalyst to carbon electrodes in different concentrations of ZnO in 8 M KOH.

	Potential E *vs.* Hg/HgO (mV)				
j (mA cm^{-2})	8 M KOH	0.2 M Zn in 8 M KOH	0.4 M Zn in 8 M KOH	0.6 M Zn in 8 M KOH	Range of potential
- 10	- 85	- 92	- 94	- 96	11
- 20	- 110	- 118	- 120	- 123	13
- 50	- 164	- 170	- 172	- 176	12

For each current density, the performance drops with increasing concentration of zincate/zinc oxide (Zn). The difference in potential between the electrode in pure 8 M KOH and 0.6 M Zn in 8 M KOH was approximately 11 mV for all current densities (11 mV, 13 mV and 12 mV). The increase in potential between electrolytes, did not scale with increasing current density, suggesting it was independent of this factor. The consistent difference in potential between the electrolytes implies that the loss in performance (increase in cathodic reduction potential for the same current density) is linked to an intrinsic property of the zincate electrolyte, potentially producing an unfavourable interaction at the surface of the electrode. Alternatively, the addition of zinc oxide will effectively reduce the concentration of potassium hydroxide to produce the zincate. The depletion of KOH will reduce the pH of the solution and its effectiveness as an electrolyte; hence the consistent decrease in performance. Ultimately this minor increase will impact minimally on overall cell efficiency and so is not of imminent concern.

7.1.2 Effect of electrolyte temperature

Based on the Arrhenius equation (Equation 7.3), the rate constant for a reaction increases exponentially with temperature.

$$k = Ae^{-Ea/(RT)} \qquad 7.3$$

Therefore, an increase in temperature should improve cell performance. However increased temperature may have negative impacts for the zinc electrode such as increased solubility of Zn in the electrolyte increasing self-discharge. The surface of the Zn is gradually oxidized to the sub-surface while a battery is in storage at a state of partial discharge. This takes place via the hydrogen evolution reaction (HER) by reaction below.[162, 163, 164]

$$Zn + 2H_2O \rightarrow Zn(OH)_2 + H_2 \uparrow \qquad 7.4$$

A lower limit of 25°C was chosen to represent ambient conditions since any temperature below this would require cooling, add complexity, expend energy and ultimately reduce system efficiency with no evidence at present to suggest a tangible benefit. An upper limit of around 70°C was selected, as above this temperature electrolyte evaporation becomes an issue and so additional containment measures would have to be implemented. There are also safety and cost implications associated with elevated temperatures.

Figure 7.4 presents cell voltage versus time plots from the Mk I flow cell fitted with a carbon paper based oxygen electrode. The electrolyte was maintained at temperatures between 25°C and 65°C progressively increasing in 10°C increments. A current density of 10 mA cm^{-2} was used for the charge and discharge periods. The flow cell was operated with a fresh air-electrode and electrolyte for each temperature. The test plan used is outlined in Table 7.2.

Table 7.2 Battery testing procedure followed for cell operation described for Figure 7.4 for each temperature evaluated.

Step	action	Period / s	Data
1	OCP	60	Discarded
2	Charging at 10 mA cm^{-2}	900	Discarded
3	OCP	60	Discarded
4	Discharge at 10 mA cm^{-2}	900 or $E \leqslant 0.4$ V (whichever was greater)	Discarded
5	OCP	60	Figure 7.4
6	Charging at 10 mA cm^{-2}	900	Figure 7.4
7	OCP	60	Figure 7.4
8	Discharge at 10 mA cm^{-2}	900 or $E \leqslant 0.4$ V (whichever was greater)	Figure 7.4

Each experiment consisted of two charge-discharge cycles comprising 60 s of open circuit potential, followed by 900 s charging, 60 s at open circuit and a period of discharge, with the cycle being terminated at a cut off voltage of 0.4 V (Table 7.2). The data shown was collected from every second cycle to allow the system to equilibrate after each temperature rise. The sample was $NiCo_2O_4$ spinel (co-precipitation) / PTFE (10:3) with IPA / water (1:5) ink catalyst loading ~3 mg cm^{-2} on activated carbon coated teflonated carbon paper (50 mm × 30 mm geometric area). The electrode was hot pressed at 180° C for 300 s under a mass of 4 kg. A stainless-steel plate (1.5 mm thick) with a 20 mm × 40 mm window, was used to frame the electrode ensuring an adequate seal. A single sheet of Dexmet® Ni mesh was mechanically sandwiched between the plate and the electrode exposed to the electrolyte by the window in the plate (total inter-electrode gap 10 mm). The mesh was insulated from the stainless-steel plate by a thin strip of PTFE to prevent the whole plate from acting as the electrode (Figure 7.3).

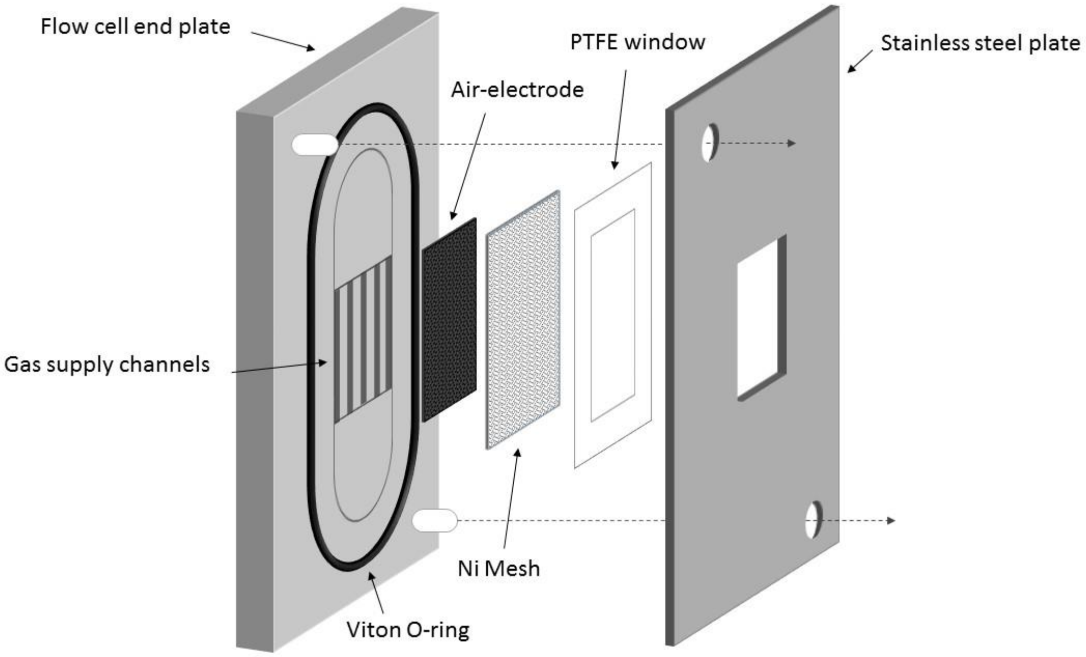

Figure 7.3 Exploded diagram showing how the air-electrode was sealed inside the Mk I flow cell.

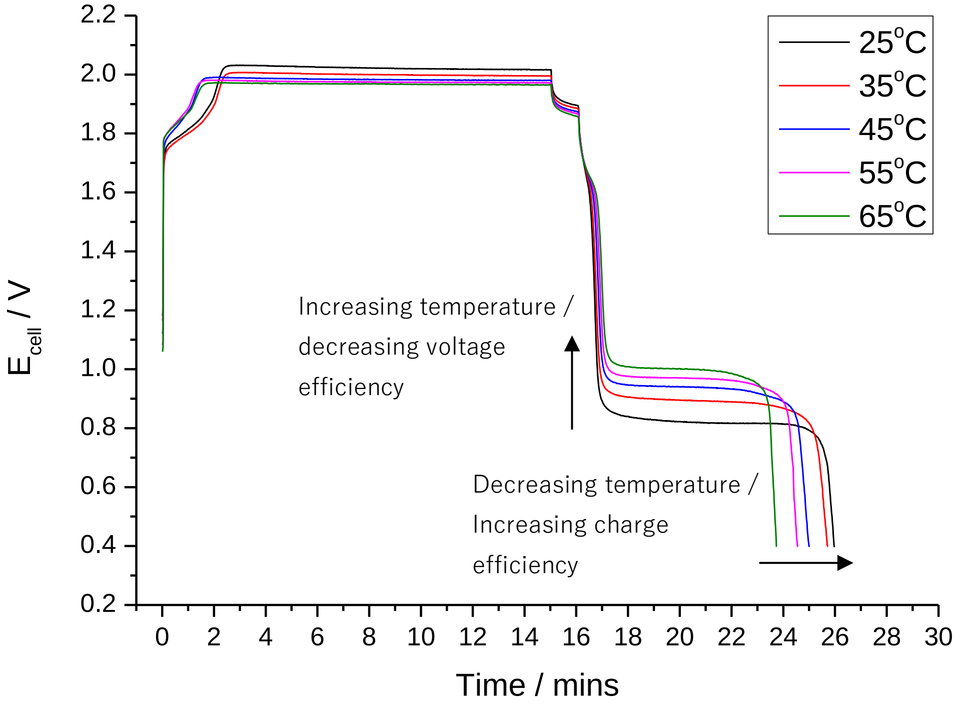

Figure 7.4. Cell voltage *vs.* time plots for the MK I flow cell fitted with a ~3 mg cm^{-2} $NiCo_2O_4$ spinel (co-precipitation preparation method) catalyst carbon paper electrode. The cell as charged and discharged at increasing temperatures 25, 35, 45, 55 and 65˚C.

It can be seen in Figure 7.4 that as temperature increases so does the discharge potential and correspondingly the voltage efficiency of the cell. Conversely, as the temperature increases the discharge period decreases resulting in decreased charge efficiency. This could be because of increased self-discharge caused by the zinc more readily dissolving back into the electrolyte. This is particularly relevant to lower current density cell operation as there is a considerably smaller deposit of zinc, so the surface area to volume ratio of the deposit will be greater. Alternatively, the increase in temperature may affect the deposition of the zinc metal in the first place. At the end of discharge, the voltage rapidly drops off, indicating that the zinc deposit has been exhausted. By contrast the voltage efficiency is dominated by the difference in potential between oxygen evolution and oxygen reduction at the positive electrode. The kinetics of the OER and ORR reactions significantly improve at elevated temperatures.[165] There is likely to be an upper limit to this where by additional heat begins to be a determent.[166] This can be seen in, which presents the average voltages for the cell, positive and negative electrodes along with charge efficiency.

Table 7.3. Calculation of efficiency metrics for the flow cell experiments shown in Figure 7.4.

Temperature / K	**Charging potential / V**	**OCP / V**	**Discharge potential / V**	**Potential gap / V**	**Voltage efficiency / %**	**Charge efficiency / %**	**Energy efficiency / %**
25	2.02	1.90	0.82	1.20	41	66	27
35	2.00	1.89	0.90	1.10	45	64	29
45	1.98	1.87	0.94	1.04	48	59	28
55	1.98	1.87	0.97	1.01	49	56	27
65	1.97	1.86	1.00	0.97	51	51	26

The competing effects of voltage and charge efficiency, as a function of temperature, will mean that the optimum temperature for energy efficiency, will be a compromise of positive and negative electrode performances. As shown in Figure 7.4 and Table 7.3, for this cell setup the optimum temperature of operation is 45° C. Both the voltage and charge efficiencies for the system are ~ 50% showing that improvement is required at both electrodes to reach higher energy efficiency as 25-30% does not represent viable battery operation.

7.1.3 NaOH *vs*. KOH

A key differentiator between the two electrolytes other than cost (NaOH being considerably less expensive than KOH) is zinc oxide solubility. The availability of zinc in solution will affect how readily it is plated during charging as well as how readily it will strip during discharge and open circuit. The amount of zinc will also affect properties of the electrolyte such as conductivity and viscosity.

The experimentally obtained values for ZnO solubility in NaOH and KOH at 25°C, are shown in Figure 7.5. 100 mL of each concentration electrolyte was prepared and 0.1 M ZnO was added at a time and dissolved using a magnetic stirrer bar. This process was repeated until no more ZnO would dissolve (defined as visible sediment remaining after 12 hours of continuous stirring).

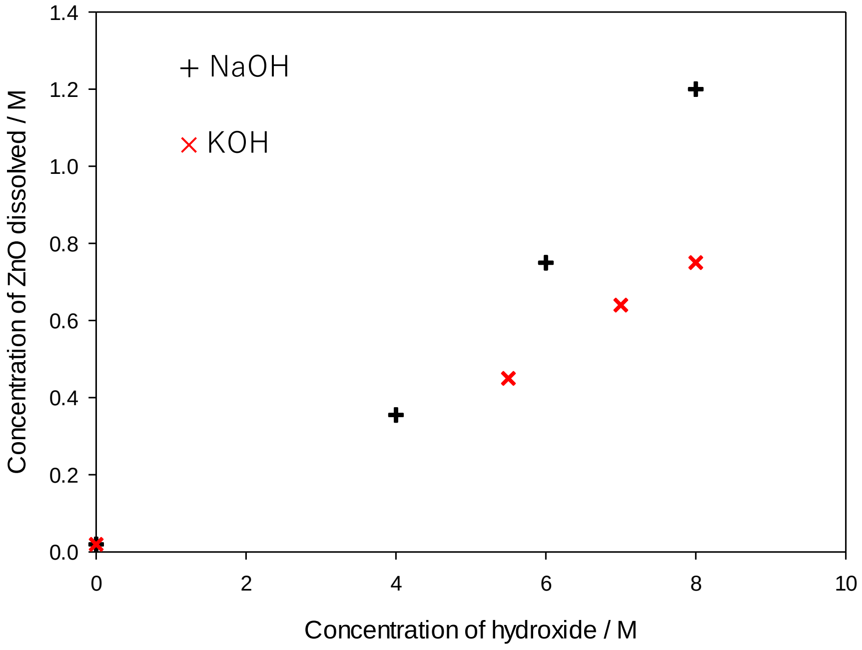

Figure 7.5. **A comparison of the solubility of ZnO in NaOH (black) and KOH (red) at different concentrations at 25˚C.**

The solubility of ZnO in pure water and < 3 M hydroxide is poor (< 0.2 M, ZnO), however, as the concentration increases so does the ZnO solubility. Around 0.75 M ZnO is soluble in 8 M KOH, meaning that a sensible operating level is around 0.5 M ZnO in 8 M KOH to allow for variation in the electrolyte over the course of cycling and to allow for a small amount of water loss. 1.2 M ZnO appears to be achievable in 8 M NaOH, showing an almost two-fold increase in the ZnO solubility, therefore 1 M ZnO is a reasonable operating value for NaOH. This increased solubility for NaOH should aid zinc deposition as it will be more readily available at the electrode surface. The ability to operate at a reduce NaOH concentration while maintaining sufficient Zn in solution may be attractive for system scale-up as there are financial and safety benefits. A useful expansion to this study would be to observe the solubility at the elevated temperatures of the operational cell as this should further increase solubility.

The effect of these zincate solutions was assessed in the context of flow cell performance. A series of charge / discharge cycles were run in the Mk I flow cell with the electrolytes described in Table 7.4 to see if the increased Zn content translated into enhanced charge efficiency. A $NiCo_2O_4$ spinel/PTFE on activated carbon coated carbon paper electrode ~3 mg cm^{-2} catalyst loading was produced and cycled in the flow cell at increasing temperatures (25°C - 65°C). The voltage and charge efficiencies at each temperature were recorded.

Table 7.4 Electrolyte compositions used in Figure 7.6 and Figure 7.7.

Hydroxide	Hydroxide concentration / M	ZnO concentration / M
KOH	8.0	0.5
NaOH	8.0	0.5
NaOH	8.0	1.0

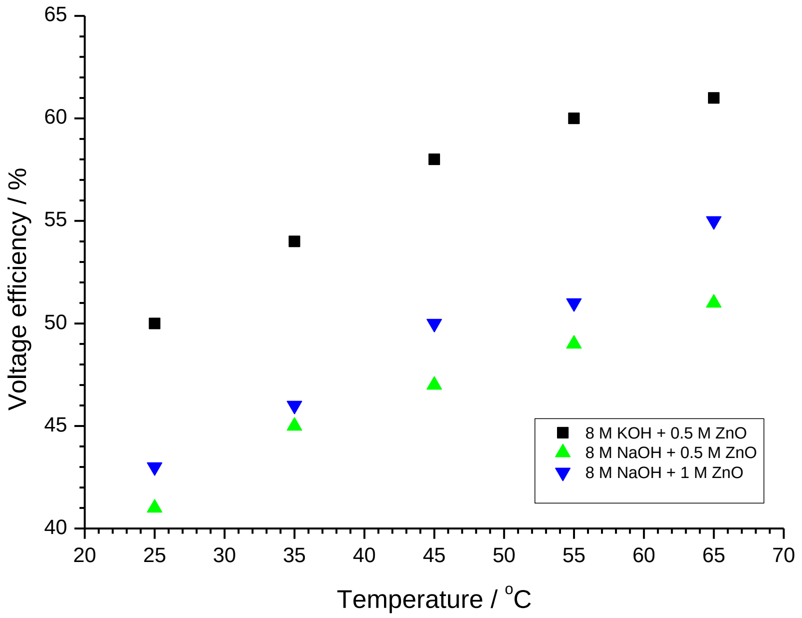

Figure 7.6. Voltage efficiency as a function of temperature for carbon paper based electrodes with ~3 mg cm^{-2} $NiCo_2O_4$ spinel loading produced in the same batch. The first electrode was run in the Mk I flow cell in a solution of 8 M KOH + 0.5 M ZnO. The second was run in a solution of 8 M NaOH + 0.5 M ZnO. The volumetric flow rate of the electrolyte was ~2.5 × 10^{-6} m^3 s^{-1}.

Figure 7.6 shows the voltage efficiencies for the electrodes described above. At 25° C voltage efficiency is poor 41% and 43% for the NaOH electrolytes and 50% for KOH. Voltage efficiency increased with temperature in all cases and the differences between electrolytes remain constant, however there were signs that the rate of increase as a function of temperature began to slow down above 50°C particularly for the KOH sample. There is consistently a 1-3% boost in voltage efficiency at all temperatures for the doubling of Zn content. Higher concentrations of zinc do appear to be beneficial, however a much larger benefit ~10% is seen from using potassium hydroxide as opposed to sodium hydroxide.

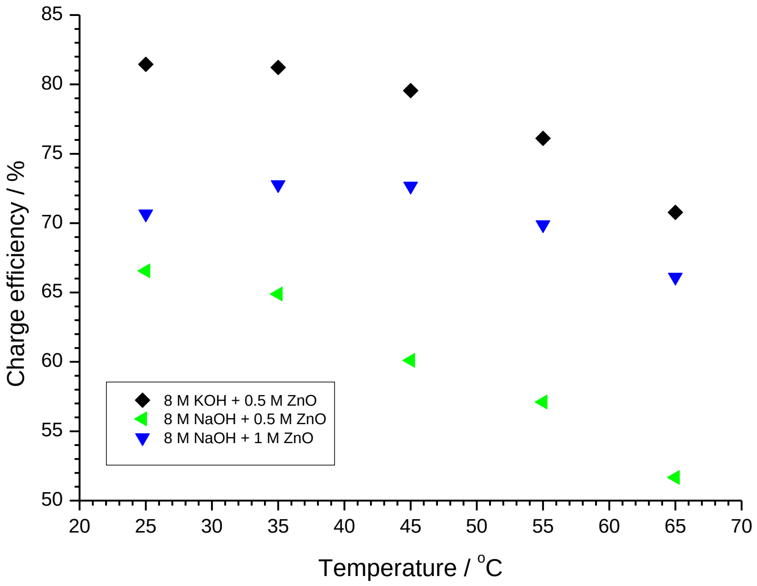

Figure 7.7. The variation in charge efficiency *vs.* temperature for the same conditions outlined for Figure 7.6.

The charge efficiency, as shown in Figure 7.7 however, for both 0.5 M ZnO solutions decreases with increasing temperature. The gap in efficiency between NaOH and KOH (0.5 M ZnO) is 15% - 20% and so a significant gain is associated with the KOH. The increase to 1 M ZnO afforded by the NaOH does show an improvement over the lower concentration NaOH solution and a much smaller variation with temperature, however the performance is still worse than that of its KOH alternative. Although there appears to be a benefit from running in NaOH at temperatures $\leq$ 35° C after this point performance in NaOH rapidly decreases with increasing temperature. The KOH based electrolyte provides greater energy efficiencies than the NaOH. A contributing factor to this is the increased conductivity of KOH. One solution to try and mitigate this performance drop, would be to reduce the inter electrode gap so that losses through the electrolyte could be minimised.

7.1.4 Electrolyte flow rate

To evaluate the effect of the electrolyte flow rate on efficiency, the MK I flow cell was run through a series of charge/discharge cycles at a current density of 10 mA cm^{-2}. The electrolyte was 8 M NaOH (0.5 M ZnO) maintained at 60^{o}C. The air-electrode was supplied with a constant 4 cm^{3} s^{-1} flow of bottled O_2. With each increasing cycle, the speed of the peristaltic electrolyte pump flow rate was increased by 2.0 cm^{3} s^{-1} however, as the speed of the pump approached its maximum the increase in flow rate did not scale linearly and so topped out at around 7.5 cm^{3} s^{-1}. The charge/discharge potential *vs.* time plot for flow rates of 2.0 cm^{3} s^{-1}, 5.0 cm^{3} s^{-1}, 7.0 cm^{3} s^{-1} and 7.5 cm^{3} s^{-1} (linear flow rate 1 cm s^{-1} - 3.75 cm s^{-1}) are shown in Figure 7.8. Examples in similar flow battery studies appear to have used comparable flow rates suggesting that 3 cm^{3} s^{-1} - 5 cm^{3} s^{-1} (linear flow rate 1.11 cm s^{-1} – 1.85 cm s^{-1}) is optimal.[167] However in the highlighted study it is apparent that they are constrained by the upper limit of 5 cm^{3} s^{-1} which can be provided by their pump. Therefore there may be benefit to higher flow rates.

Table 7.5 Battery testing procedure followed for cell operation described for Figure 7.8.

Step	action	Period / s	Volumetric Flow rate / $cm^3\ s^{-1}$	Linear flow rate /$cm\ s^{-1}$
1	OCP	60	2.0	1.0
2	Charging at 10 mA cm^{-2}	900	2.0	1.0
3	OCP	60	2.0	1.0
4	Discharge at 10 mA cm^{-2}	900 or $E \leqslant 0.4$ V (whichever was greater)	2.0	1.0
5-8	Repeat steps 1-4 at new flow rate		5.0	2.5
9-12	Repeat steps 1-4 at new flow rate		7.0	3.5
13-16	Repeat steps 1-4 at new flow rate		7.5	3.8
17-20	Repeat steps 1-4		2.0	1.0

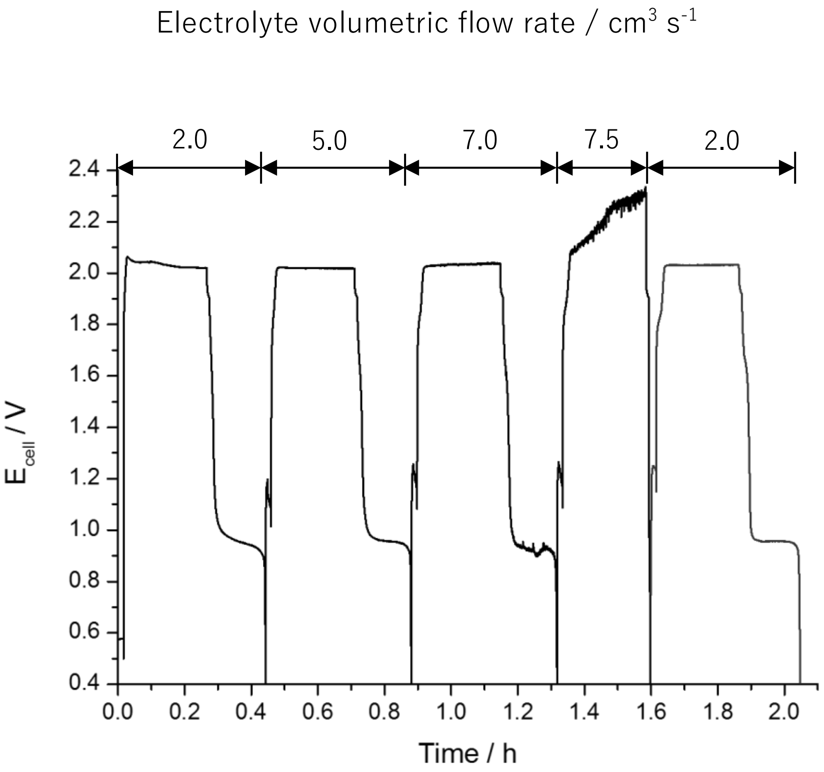

Figure 7.8. **Carbon paper Toray electrode cycled in the flow cell at increasing electrolyte flow rates with a steady gas flow rate. The final cycle shows a repeat of the first cycle run at the end of the test run on the same electrode with no other modifications to the arrangement.**

For the first three speeds 2.0 cm^3 s^{-1} - 7.0 cm^3 s^{-1}, charging occurs at ~ 2 V and discharge at ~ 1 V (~ 50% voltage efficiency). There is minor variation in performance between these three cycles. For the initial charge, there is a ‘bedding in’ period possibly associated with the nucleation of zinc on the electrode surface however, after a few minutes the potential settles. During discharge at 7.0 cm^3 s^{-1} and charging at 7.5 cm^3 s^{-1} the observed potential data becomes noticeably noisier. At 7.5 cm^3 s^{-1} the charging potential also begins to increase sharply to 2.3 V and no discharge potential is observed as the system hits its voltage cut off immediately. The pump speed was lowered back down to its original flow rate of 2.0 cm^3 s^{-1} as shown, to assess if the electrode had received irreversible damage. There is a negligible difference in performance between the initial scan and the repeat showing that the electrode has not been detrimentally affected by the increased flow rate. For the Mk I flow cell with the attached pump there is an electrolyte flow limit of just below 7.0 cm^3 s^{-1} before there are noticeable adverse effects on performance. These higher flow rates may produce turbulence in the cell perturb mossy zinc deposition and creating inhomogeneity in the electrolyte. The most probable cause is the pump itself which as shown previously in Figure 3.12 may be struggling to pump the viscous electrolyte at higher pump speeds. This may result in intermittent flow. From the individual cell data, it is clear to see that the increased charging potential is predominantly associated with the zinc electrode. This suggests that at high flow rates zinc deposition is inhibited, which would correspond to the subsequent failure to discharge. 5.0 cm^3 s^{-1} gave the highest efficiency and the most stable potentials so will be the standard moving forward. This is approximately equivalent to the gas flow rate of 4.0 cm^3 s^{-1}. This validates preliminary data which suggested that balancing the fluid pressure and flow on either face of the electrode would help maintain the three-phase boundary.

7.1.5 Additives

Electrolytes based on KOH and NaOH were evaluated in the Mk I flow cell with and without the addition of an additive to promote the zinc deposition/dissolution reactions. The aim of using the additive, was to promote the reactions occurring at the zinc electrode at the elevated temperatures previously shown to be beneficial for air-electrode performance. The additive was suggested by project partners CEST based on their investigation of the negative half-cell (Zn electrode) using a rotary Hull Cell. The additive in question was Lugalvan® P (BASF) a basic brightener for alkaline zinc plating baths. To evaluate the effect of this additive on flow cell performance, electrolytes with and without additive were used to charge/discharge cycle comparable electrodes. Carbon paper electrodes with $NiCo_2O_4$ spinel catalyst (< 10 mg cm^{-2} loading) in a 10:3 ratio with PTFE were used. As discussed in section 7.1.2 only the second 10 mA cm^{-2} charge / discharge cycle was recorded for each test. Figure 7.9 shows an example of a typical charge discharge cycle regime for one such cell arrangement. The individual electrode potentials have also been plotted to show their contribution to the overall cell performance.

Table 7.6 Flow cell dest plan for the data shown in Figure 7.9.

Step	Action	Period / s	Temp / °C	O_2 flow rate / cm^3 min^{-1}	OH^- flow rate / cm^3 min^{-1}
1	OCP	60	25	220	180
2	Charging at 10 mA cm^{-2}	900	25	220	180
3	OCP	60	25	220	180
4	Discharge at 10 mA cm^{-2}	900 or $E \leqslant 0.4$ V (whichever was greater)	25	220	180
5-8	Repeat steps 1-4		25	220	180
9-16	Repeat steps 1-8		35	220	180
17-24	Repeat steps 1-8		45	220	180
25-32	Repeat steps 1-8		55	220	180
33-40	Repeat steps 1-8		65	220	180

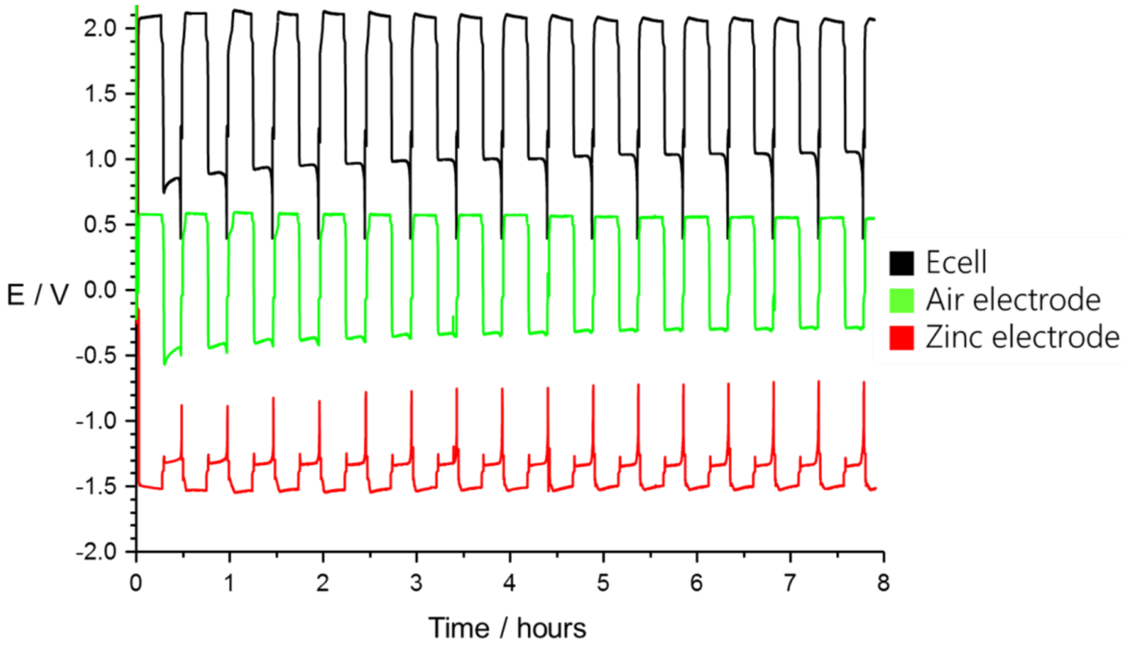

Figure 7.9 An example of the data collected for a carbon paper electrode at 10 mA cm^{-2} in 8 M NaOH + 1 M ZnO + electrolyte additives. Showing cell performance as well at the performance of the individual cell components.

Figure 7.9 shows an example of the data obtained from testing an electrode, in this instance the parameters were 10 mA cm^{-2} in 8 M NaOH + 1 M ZnO + electrolyte additives. Comparable data sets were collected for the other electrolyte/additive combinations the key performance metrics have been summarised in Figure 7.10, Figure 7.11 and Figure 7.12 for comparison. Both the cell potential and the individual electrode potentials were recorded. By plotting all three on the same axis, it becomes immediately apparent which electrode is contributing the greatest inefficiency to the system. The zinc-electrode (red line) shows no more than approximately 250 mV difference between charge and discharge and remains constant across cycles. The air-electrode potential (green line) on the other hand, starts with a gap of > 1.1 V for the initial cycle, reducing to approximately 0.85 V as the temperature is elevated to 65°C. The potential window between charge and discharge for the air-electrode is in this instance more than three times that of the zinc-electrode. Therefore, the air-electrode remains one of the key components requiring further development, as it represents one of the largest contributions to inefficiency. For all electrolytes tested, a similar response was witnessed in that the potential associated with the zinc electrode remained constant, while the oxygen electrode varied as a function of temperature. The breakdown of the voltage and charge efficiencies are shown in, Figure 7.10 and Figure 7.11.

There is a trend that increasing temperature reduces charge efficiency as seen previously. The peak appears to be between 25°C and 40°C for all electrolyte/additives combinations tested. After this point, all instances show a steady decrease in charge efficiency. For KOH at ≤ 45°C there are very similar observed charge efficiencies for the electrolyte with and without additive. Above this temperature however, cell performance decays more dramatically with the increasing temperature without the additive than when it is present. This is encouraging as it suggests that for KOH the addition of the additive can increase charge efficiency in the temperature region which is preferential for air-electrode operation.

Because NaOH can more readily dissolve ZnO, there is firstly the comparison between 0.5 M and 1 M ZnO. As expected there is a clear benefit to increasing the ZnO concentration. The benefits are accentuated at the higher end of the temperature range. At 25°C there is only a 5% difference between the two electrolytes however, at 65°C this increases more than threefold to 16%. This is not a trivial difference in efficiency and would suggest that for the benefit of the zinc electrode when running an NaOH based electrolyte at elevated temperatures, the

ZnO concentration should be as great as practicable. When comparing the 8 M NaOH + 0.5 M ZnO electrolyte with and without the addition of the additive, there is a definitive difference. Both electrolytes show very similar responses to temperature showing a similar form on the plot however, there is a large improvement of 15-20% at every temperature evaluated for the electrolyte with the addition of the additive. A very similar relationship is observed of the 1 M solutions whereby they show similar shaped response to temperature, but there is a consistent performance bump associated with the addition of the additive.

Overall there is a noticeable improvement in terms of charge efficiency with the addition of the additive for both electrolytes. The enhancements are more dramatic for NaOH bringing the charge efficiency in line with and in the most extreme case surpassing the efficiencies for KOH. Figure 7.10 shows the voltage efficiencies recorded for the experiments discussed.

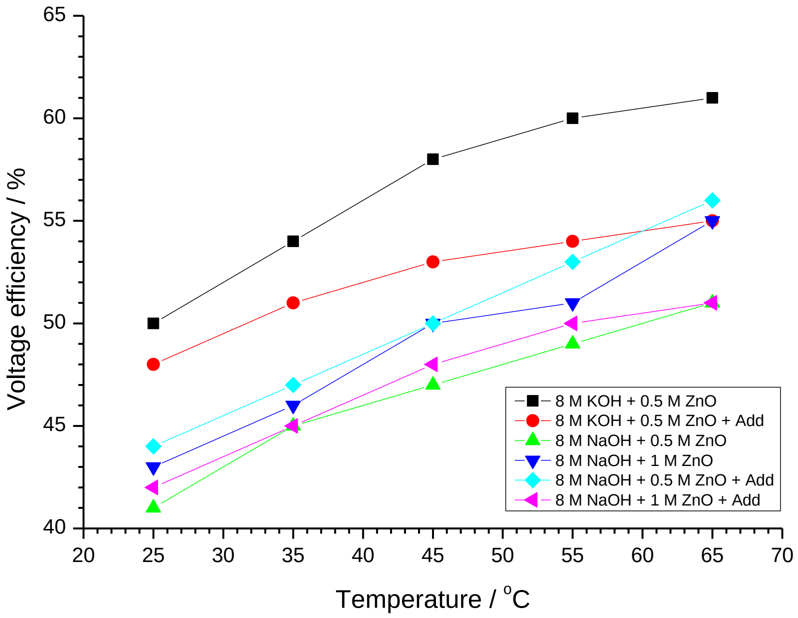

Figure 7.10. Voltage efficiency data as a function of temperature displayed by a Toray® carbon paper based electrode coated in a PTFE based

active layer with a $NiCo_2O_4$ spinel catalyst loading of approximately 3 mg cm^{-2}. (Exposed geometric area 8 cm^2). Bottled O_2 flow rate of 220 cm^3 min^{-1} and an electrolyte flow rate of 180 cm^3 min^{-1}. The charging period for each cycle was 15 mins and the cell was then allowed to discharge until it reached a 0.4 V cut-off voltage. Each period of charging/discharging, was followed by a period of 60 s OCP. Two cycles were performed at each temperature and the second of these was used to calculate efficiencies.

Once again there is a clear trend that increasing temperature increases voltage efficiency. The largest performance gains appear between 25°C and 45°C, after this point certain electrolyte/additive combinations show a slowing in improvement of voltage efficiency. For the KOH based electrolytes there is a noticeable reduction in voltage efficiency for the electrolyte with additive and performance diverges as the temperature increases. This is practically the opposite response to the trend seen for charge efficiency where the use of an additive improved efficiency at elevated temperatures. For NaOH there is a small bump in voltage efficiency going from 0.5 M and 1 M ZnO, further validating that an increase in ZnO concentration is beneficial for cell performance. When comparing the NaOH electrolytes with and without the addition of the additive, there is no clear trend indicating a benefit. All electrolytes show very similar responses within 5% of one another which would suggest that for the NaOH based electrolytes the addition of the additive has minimal influence on voltage efficiency.

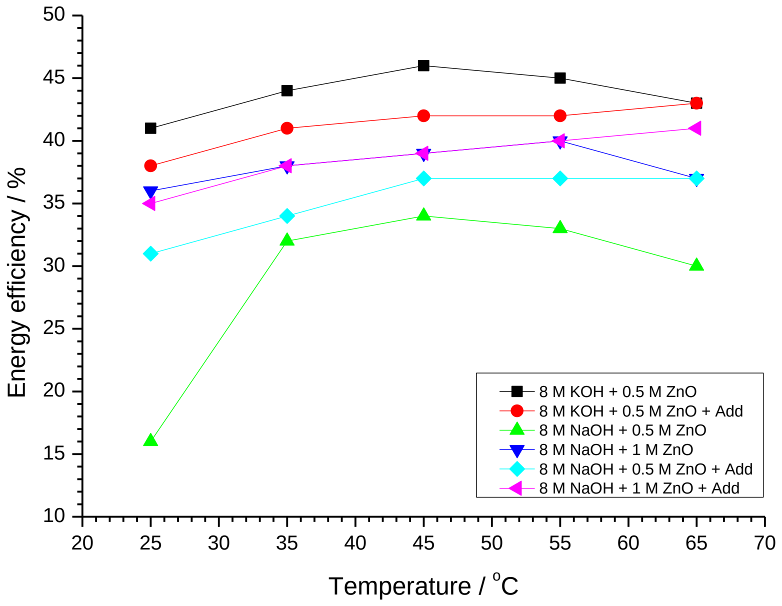

Figure 7.11. Energy efficiency data as a function of temperature displayed by a Toray® carbon paper based electrode coated in a PTFE based active layer with a $NiCo_2O_4$ spinel catalyst loading of approximately 3 mg cm^{-2}. (Exposed geometric area 8 cm^2). Bottled O_2 flow rate of 220 cm^3 min^{-1} and an electrolyte flow rate of 180 cm^3 min^{-1}. The charging period for each cycle was 15 mins and the cell was then allowed to discharge until it reached a cut off of 0.4 V. Each period of charging/discharging was followed by a period of 60 s OCP. Two cycles were performed at each temperature and the second of these was used to calculate efficiencies.

Figure 7.11 shows the energy efficiency which is the combination of the charge and voltage efficiencies. For KOH, the addition of the additive has a detrimental effect on energy efficiency below 65°C. As shown previously voltage efficiency was hindered by the additive and charge efficiency only aided at temperatures above 40°C. Above this temperature, the two electrode effects appear to balance each other out and performance with and without the additive is near identical. There is an upward trend for the run including additive matching cell performance without the additive at 65°C. Extrapolating this, the assumption would be that as the temperature of the electrolyte was increased past 65°C, there may be a benefit to its inclusion, but this is highly speculative.

The benefit from increasing the ZnO concentration is made apparent once again when viewing the two NaOH electrolytes without additive. At 25°C the energy efficiency more than doubles when the ZnO concentration is doubled. The efficiency for the higher concentration electrolyte remains significantly higher across the temperature range. In terms of the effect of the additive for the samples with 0.5 M NaOH, there is a jump in performance when the additive is used, however this improvement disappears for the 1.0 M samples. This seems to suggest that when the ZnO content is lower and Zn-electrode performance is correspondingly hampered the additive serves a purpose. When the Zn concentration is increased the zinc-electrode can perform more efficiently and so the additive has a negligible effect. Despite improvements from increased Zn concentration and the aid of the additive the KOH electrolytes still out perform all the tested permeations of the NaOH electrolyte. Proposed best practice would therefore be to utilise KOH based electrolytes with as great a Zn content as is practicable and only consider using Lugalvan® P as an additive if it the intention is to operate at ≥65°C.

7.2 Bottled O_2 *vs.* laboratory air

A factor which commonly leads to premature failure of zinc-air systems is carbonate poisoning from CO_2 in the air.[3] For this reason, testing in the flow cell has predominantly taken place with pure oxygen rather than air to eliminate this variable. It is possible to strip CO_2 from the air prior to entering the cell using a CO_2 scrubber, however this is an aspect of the system which has not been explored.[168] To assess how the system may perform on air as a source as well as to simulate what might happen in the event of a CO_2 scrubber failure, the following test was performed. A standard carbon paper based electrode (10 mg cm^{-2}) was sealed in the Mk I flow cell. The same electrode was run firstly with laboratory air or two cycles followed by two cycles with bottled O_2. In each case the second of the two cycles was recorded to allow the system to equilibrate. Conditions are outlined in Table 7.7.

Table 7.7 Battery tester test plan for the data shown in Figure 7.12.

Step	Action	Period / s	Gas	O_2 flow rate / cm^3 min^{-1}	Electrolyte Temp / ° C	OH$^-$ flow rate / cm^3 min^{-1}
1	OCP	60	Air	200	60	180
2	Charging at 10 mA cm^{-2}	900	Air	200	60	180
3	OCP	60	Air	200	60	180
4	Discharge at 10 mA cm^{-2}	900 or E ⩽ 0.4 V (whichever was greater)	Air	200	60	180
5-8	Repeat steps 1-4 (record data)		Air	200	60	180
9-12	Repeat steps 1-4 (discard data)		O_2	200	60	180
13-16	Repeat steps 1-4 (record data)		O_2	200	60	180

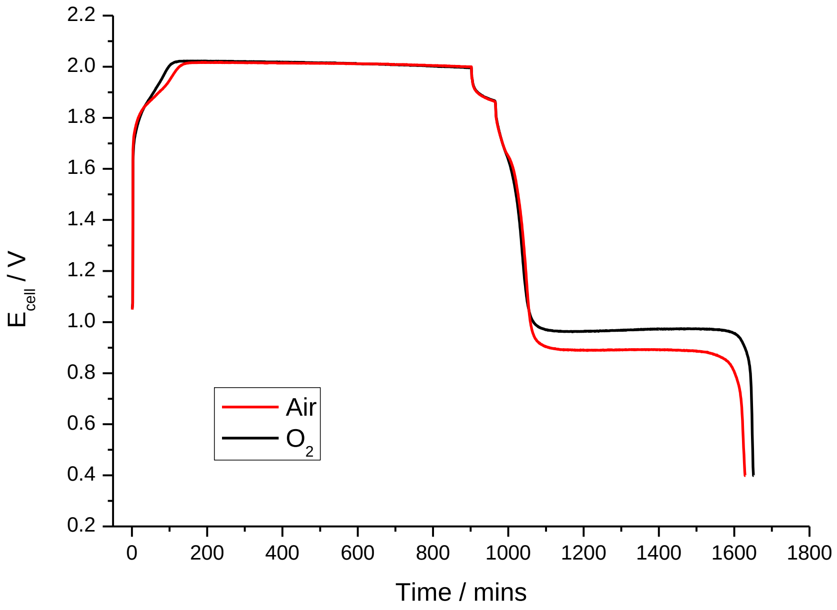

Figure 7.12 15 min charging period charge/discharge cycles of a carbon paper based electrode coated in a 10:3 $NiCo_2O_4$ spinel/PTFE ink (dry catalyst loading ca. 10 mg cm^{-2}). 8 M NaOH with 0.5 M ZnO electrolyte maintained at 60°C. Displayed are the second of two concurrently run cycles for each of the gas compositions with O_2 being run before air on the same electrode.

Table 7.8 Efficiency data collected from the charge discharge cycling shown in Figure 7.12.

Gas composition	Charge efficiency / %	Voltage efficiency / %	Energy efficiency / %
Bottled O_2	77	48	37
Laboratory air	74	44	33

The charging period is very similar for both gases. The potential immediately jumps from an open circuit of around 1.1 V, to approximately 1.7 V. The potential then slowly climbs to about 2 V. The potential then remains near constant during the remainder of the charging period. The potentials only start to deviate once a stable discharge potential is achieved. At this point, there is a roughly 100 mV gap between air and bottled oxygen. This is a noticeable drop, however the air has roughly a fifth of the oxygen content so this is promising. There is also a small drop in the discharge period and so correspondingly a drop-in charge efficiency. Based on all efficiency metrics bottled, O_2 appears to be superior, but by no more than 4%. The fact that the O_2 cycles were run after the air and the performance increases suggests the CO_2 has little effect over this time scale. To evaluate how CO_2 might affect cycling over a longer period, a fresh electrode was run for multiple cycles over an 18-hour period.

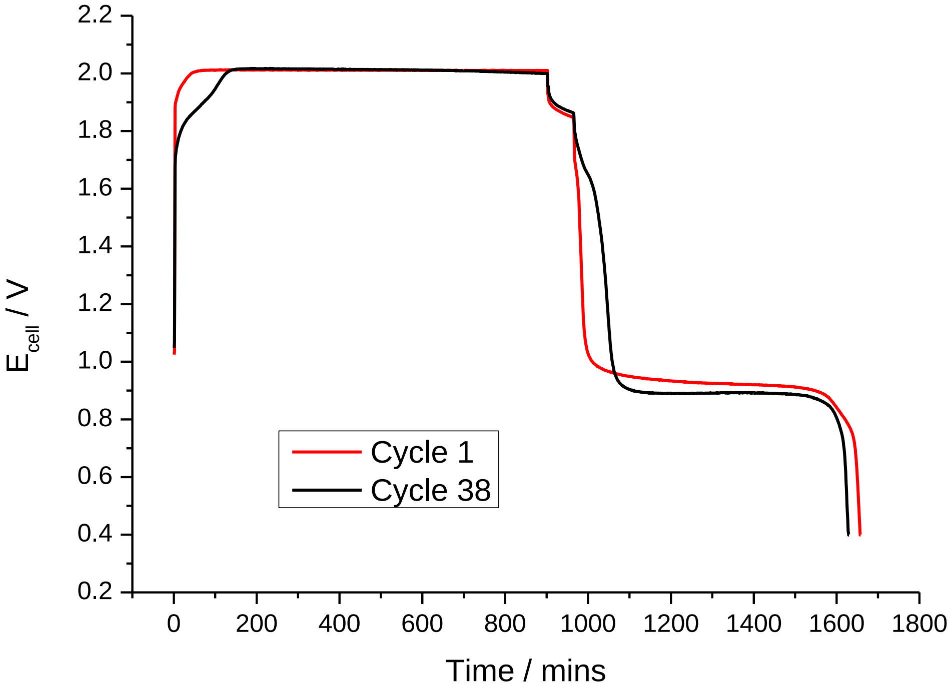

Figure 7.13 15 min charging period charge/discharge cycles of a carbon paper based electrode coated in a 10:3 $NiCo_2O_4$ spinel/PTFE ink (dry catalyst loading ca. 10 mg cm^{-2}). 8 M NaOH with 0.5 M ZnO electrolyte maintained at 60°C. Supplied with laboratory air.

Although the charge/discharge plots change in form, there is only a minimal drop in performance over the 18-hour period. Such a small change over the period could be associated with multiple causes. Therefore, over the relatively short time scales that have been evaluated in this study, typically $\leq$ 24 hours of cycling it could be suggested that carbonate formation has a negligible impact on performance. Carbonate formation is an issue which would be better addressed once stable cycling over weeks or months was achieved and the outlook was focused on system longevity as opposed to optimizing initial operation.

7.3 Charging period

Most of the flow cell tests to this point have covered relatively short cycle times. However, this only represents a small proportion of the potential capacity of the cell and in realistic operation charging periods will likely be far longer. To evaluate how performance will change dependent on depth of charge, an electrode was cycled with increasing charging periods (15, 30, 60 and 120 minutes). A carbon paper based electrode coated in a 10:3 $NiCo_2O_4$ spinel/PTFE ink (dry catalyst loading ca. 10 mg cm^{-2}) was used as the air-electrode. The electrolyte was 8 M NaOH with 1 M ZnO electrolyte and the additive Lugalvan® P thermostatically maintained at 60°C. The resulting charge/discharge cycles are shown in Figure 7.14.

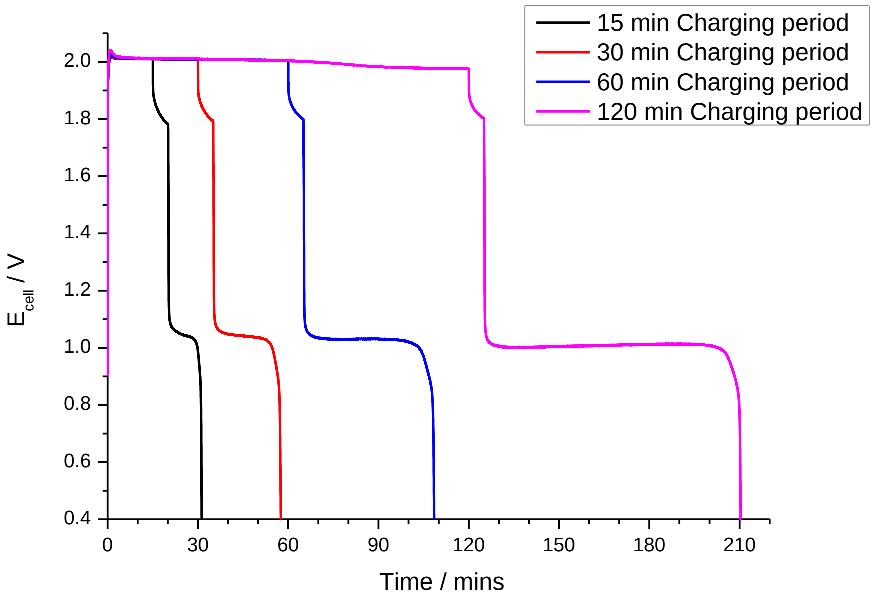

Figure 7.14 Successive charge/discharge cycles with varying charging period for a carbon paper based electrode coated in a 10:3 $NiCo_2O_4$ spinel/PTFE ink (dry catalyst loading ca. 10 mg cm^{-2}). The electrolyte used was 8 M NaOH with 1 M ZnO electrolyte with additive at 60°C. A discharge cut off voltage of 0.4 V was used.

All cycles showed near identical charging performance, jumping rapidly to 2 V from OCP and reducing gradually as charging period increases. Once switched back to OCP the potential drops back to a value of 1.78 V after 300s. When the cell is discharged the potential immediately drops to around 1 V, however there is approximately a 10 mV drop in discharge potential with each increase in charging period. A certain proportion of this drop may be associated with electrode degradation as all cycles were run sequentially on the same electrode. Ultimately such a small variation in discharge potential only equates to 1-2% variation in voltage efficiency as shown in Table 7.9.

Table 7.9 Calculated efficiencies for the flow cell cycling data shown in Figure 7.14.

Charging period / Mins	Charge efficiency / %	Voltage efficiency / %	Energy efficiency / %
15	75	52	39
30	75	52	39
60	73	51	37
120	71	50	36

As cycle length is increased, efficiency does reduce with extended charging period, however only by a few percent. Eventually there may be a point at which a large enough percentage of the zinc in solution will have been plated out that it becomes increasingly difficult. Due to the excess electrolyte supplied by the external storage tanks, a more likely scenario would be that metallic zinc fills the interelectrode gap to such an extent that either it prevents electrolyte flow, or causes an electrical short circuit. By monitoring the composition of the electrolyte and the potential of the cell, it would be possible to anticipate either of these two out comes and create shut off mechanisms before they occur.

7.4 Scale up

As electrode manufacturing techniques were developed it was possible to make larger geometric area air-electrodes (>100 cm^2). To test these electrodes a larger flow cell was designed and constructed in collaboration with C-tech innovation (Flow cell Mk II). The cell shared many of the same features of the Mk I cell with a few minor alterations. Firstly, instead of straight gas channels, a serpentine design was milled out of a metal plate. Electrical contact for the air-electrode was made via a metal tab on the gas channel plate which protruded from the cell. The other key difference is that to accommodate the larger electrolyte flow channel the manifolds with in the cell had to be redesigned.

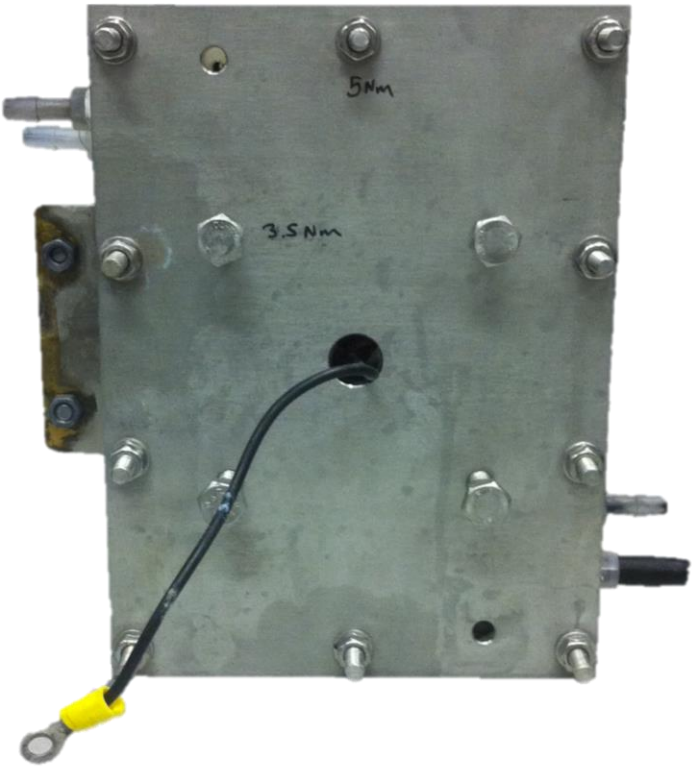

Figure 7.15 Photograph of the Mk II flow cell

Figure 7.16 Air-electrode for the Mk II air-electrode (geometric area 150 x 150 mm, electrolyte exposed area 110 cm^2 exposed electrode area) post cycling. The central darker region shows the area exposed to electrolyte.

The cell was assembled with a Ni foam based air-electrode 110 cm^2 exposed geometric surface area. The electrolyte was 8 M NaOH thermostatically maintained at 60°C and circulated at a flow rate of 0.25 L min^{-1}. Bottled O_2 was supplied to the gas face of the air-electrode at 1 L min^{-1} flow rate at a pressure of 1 bar.

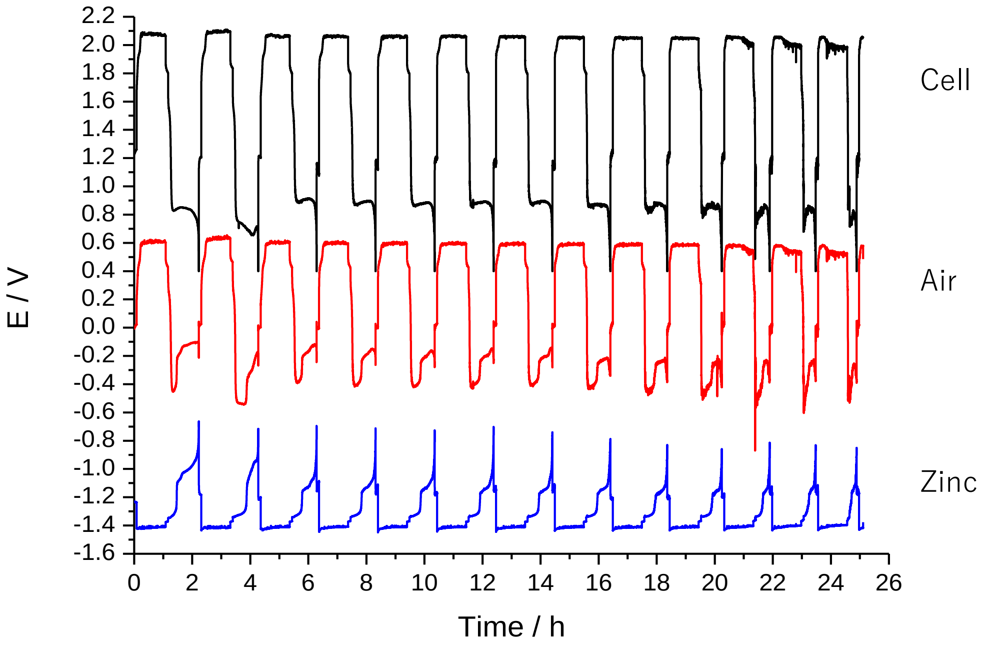

Figure 7.17 MK II flow cell cycling at 10 mA cm^{-2}. The cell was assembled with a Ni foam based air-electrode 110 cm^2 exposed geometric surface area. The electrolyte was 8 M NaOH thermostatically maintained at 60°C and circulated at a flow rate of 0.25 L min^{-1}. Bottled O_2 was supplied to the gas face of the air-electrode at 1 L min^{-1} flow rate. Individual electrode potentials were recorded as well as the cell.

The cell cycled similarly to its predecessor. Charging at approximately 2 V and discharging at around 0.9-0.7 V. The cell continued to cycle for over 24 hours, however by this point charge efficiency had decreased and the discharge potential was steadily dropping. Most of these issues were likely associated with leaking of electrolyte around the air-electrode perimeter. As the cell was designed for rapid interchange of electrodes, sealing was non-ideal and over time electrolyte would weep through/around the air-electrode.

Table 7.10 Performance data extracted from Figure 7.17.

Metric	Value	Units
Charging potential	2.06	V
Discharging potential	0.90	V
Potential gap	1.16	V
Peak voltage efficiency	45	%
Peak charge efficiency	> 90	%
Peak energy efficiency	41	%

Charge efficiency was initially good, but deteriorated with cycling. Voltage efficiency was poor, 5-10% lower than seen for similar electrodes in the Mk I cell. Despite this the results are encouraging, as the larger cell brings additional issues such as longer electrical path lengths and the risk of the electrodes bowing or warping effecting electrical contact and increasing the chance of leaks.

Ultimately the flow cell will contain more than one cell in a stack, in order to boost the power of the system. It is intended for such stacks to be bipolar in design. Therefore, to test this concept, a rudimentary two cell stack was constructed. A zinc plate was used in place of a zinc electrode, as the cell was unoptimized and used a static electrolyte to reduce complexity. To prevent the zinc plate from being completely dissolved, cycles were kept to 5 minute bursts of discharge.

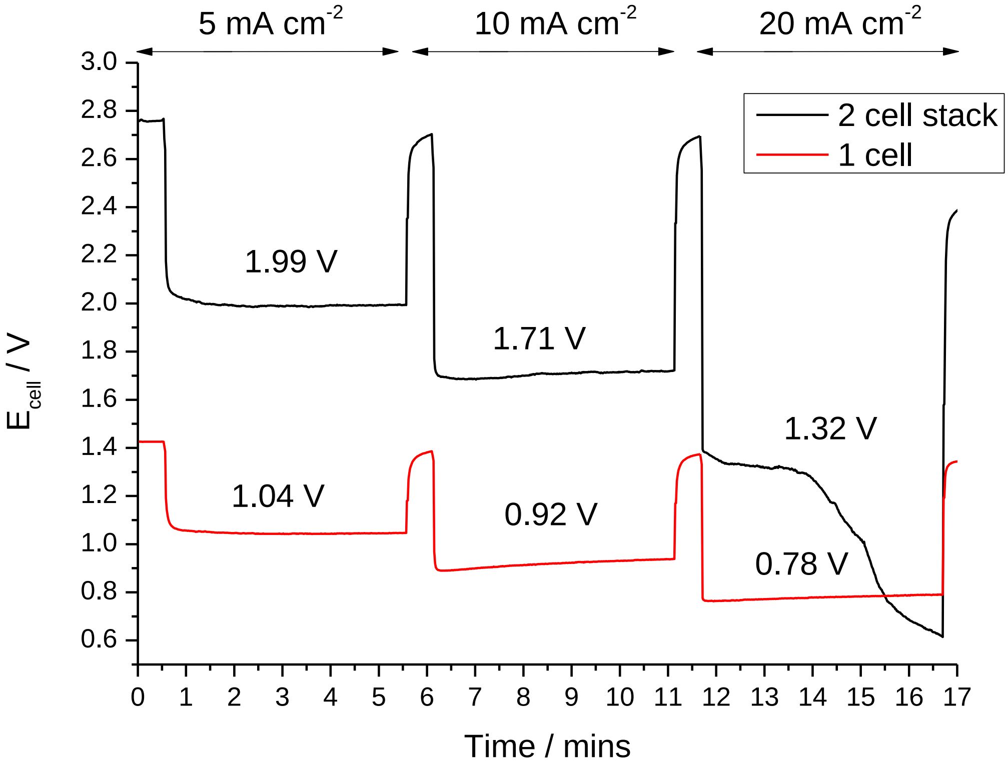

Figure 7.18 Discharge potentials at 5, 10 and 20 mA cm^{-2} for carbon paper based electrodes in a rudimentary one and two cell bipolar stack. The electrolyte was static 8 M NaOH at 25°C. Bottled O_2 was supplied to the gas face of the air-electrode. A Zinc plate was used as the (negative) zinc electrode.

The current densities observed are small and the potentials are low. This being in part due to the non-optimal set up. The key observation however, is that is that the current approximately doubles going from one to two cells. Showing that for the two-cell bipolar stack both cells are contributing to the voltage and in approximately equal amounts and that there is not a prohibitively high resistance through the stack when bi polar elements are utilised.

7.5 Conclusions

The solubility of ZnO in < 3 M hydroxide is poor (< 0.2 M, ZnO), however, as the hydroxide concentration increases, so does the ZnO solubility. Around 0.75 M ZnO is soluble in 8 M KOH meaning that a sensible operating level is around 0.5 M ZnO in 8 M KOH to allow for variation in the electrolyte over the course of cycling and to allow for a small amount of water loss. 1.2 M ZnO is achievable in 8 M NaOH showing an almost two-fold increase in the ZnO solubility therefore 1 M ZnO is a reasonable operating value for NaOH.

Testing in the Mk II glass half-cell, showed that running the air-electrode in zincate as opposed to pure KOH, had a nominal effect on overpotential. The addition of 0.1 M increments of ZnO, equated to an increase of ≤ 5 mV in air-electrode overpotential independent of current density. However, when considering the cell, doubling Zn concentration in the electrolyte can boost voltage efficiency 1-3% independent of temperature. KOH based electrolyte provides ~10% greater energy efficiencies than the NaOH despite the superior Zn solubility of NaOH most likely due to the increased conductivity of KOH.

An electrolyte temperature increase from 25°C to 65°C, showed a reduction in discharge overpotential, but shortened the discharge period. A probable culprit being increased self-discharge of the zinc electrode. Increasing the temperature of the electrolyte therefore increased voltage efficiency but led to a reduction in charge efficiency. To achieve the best energy efficiency a compromise between the conflicting positive and negative electrodes must be struck. Therefore, for the MK I cell set up the best compromise is the mid-point 45°C.

In most tests at ≤50 mA cm^{-2}, the zinc-electrode shows no more than 250 mV difference between charge and discharge and remains consistent across cycles. The best potential gap shown by an air-electrode in the Mk I flow cell is >800 V. Therefore, the air-electrode remains one of the key components requiring further development as it represents one of the largest contributions to inefficiency.

Electrolyte flow rate appeared to have little effect on cell cycling performance in the Mk I flow cell within the normal operating limits of the peristaltic pump used. If the flow was high enough to ensure the flux of fresh material to the electrodes, there was little benefit to flowing faster. 5.0 cm^3 s^{-1} gave the highest efficiency and the most stable potentials so is the recommended rate for the cell. What appears to be crucial is balancing gas and electrolyte flow rates to maintain the three-phase boundary.

Lugalvan® P (BASF) was evaluated as an electrolyte additive in the Mk I flow cell for KOH and NaOH electrolytes to promote the zinc deposition/dissolution reactions. There is a noticeable improvement in terms of charge efficiency with the addition of the additive for both electrolytes. The enhancements are more dramatic for NaOH bringing the charge efficiency in line with and in the most extreme case surpassing the efficiencies for KOH. By contrast for the KOH based electrolytes, there is a noticeable reduction in voltage efficiency for the electrolyte with additive. When comparing the NaOH electrolytes with and without the addition of the additive, there is no clear trend indicating a benefit to voltage efficiency. Overall for KOH, the addition of the additive has a detrimental effect on energy efficiency below 65°C. Above this temperature, the two electrode effects appear to balance each other out and performance with and without the additive is near identical.

For NaOH electrolytes with the Zn concentration near the saturation point the additive has a negligible effect. KOH electrolytes still out perform all tested permeations of the NaOH electrolyte. Proposed best practice would therefore be to utilise KOH based electrolytes with the greatest practicable Zn concentration and only consider using Lugalvan® P as an additive if it the intention is to operate at ≥ 65°C.

Testing in the flow cell has predominantly used pure oxygen in place of air as a CO_2 scrubber was not incorporated into the system design. To assess how the system may perform on air as a source the same electrode was run firstly with laboratory air and then bottled O_2. There was a small drop in both voltage and charge efficiency associated with using air, however based on all efficiency metrics by no more than 4% in short term testing. Cycling over an 18-hour period on laboratory air, there is only a minimal drop in performance. But there is likely to be some effect over the months or years a commercial system may be operated over.

To evaluate how performance will change dependent on depth of charge, an electrode was cycled with increasing charging periods (15, 30, 60 and 120 minutes). As cycle length is increased, all measurements of efficiency are reduced by ≤2% with each doubling of charge length. When the cell is discharged, the potential immediately drops to around 1 V, there is then an approximately 10 mV drop in discharge potential with each increase in charging period. A certain proportion of this drop may be associated with electrode degradation as all cycles were run sequentially on the same electrode. Ultimately such a small variation in discharge potential only equates to 1-2% variation in voltage efficiency.

As electrode manufacturing techniques were developed, it was possible to make larger geometric area air-electrodes (>100 cm^2). To test these electrodes a larger flow cell was designed and constructed in collaboration with C-tech innovation (Flow cell Mk II). The cell cycled similarly to its predecessor. Charging at approximately 2 V and discharging at around 0.9-0.7 V. The cell continued to cycle for over 24 hours, however by this point charge efficiency had decreased and the discharge potential was steadily dropping. Most of these issues were likely associated with the non-ideal sealing of the cell design. Charge efficiency was initially good but deteriorated with cycling. Voltage efficiency was poor 5-10% lower than seen for similar electrodes in the Mk I cell.

The viability of turning the system into a bipolar in design was tested in a rudimentary two cell stack. The discharge voltage was observed to approximately double going from one to two cells, showing that for the two-cell bipolar stack, both cells are contributing to the voltage and there is not a prohibitively high resistance through the stack when bi polar elements are utilised.

Chapter 8: Conclusion

The initial intention to source a commercially available air-electrode for flow cell calibration was unsuccessful. As testing, did not return satisfactory oxygen reduction and evolution operation of > 1 hour periods. Work therefore began on a novel in-house bifunctional air-electrode, for use in the project. Qualitative evaluation of potential substrate materials for an in-house air-electrode was carried out. Teflonated carbon paper was selected as an interim solution as it was well characterised in the fuel cell literature and came preassembled as a GDL requiring minimal modification to incorporate it into a cell. The need for an active and cost effective catalyst which minimised the requirement of precious metals was established. Based on the academic literature, mixed metal oxides were isolated as a promising avenue to explore. An in-house team concluded that $NiCo_2O_4$ spinel could be a potential candidate and so its production was scaled up to produce sufficient quantities to produce flow cell electrodes.

Anion exchange membranes were evaluated as an electrode component to prevent flooding as well as adding mechanical protection to the active catalyst layer against the flow of electrolyte. Short time scale < 300 s tests showed that there was a negligible oxygen reduction overpotential increase (≤ 20 mV) associated with the addition of a membrane. Therefore a membrane could be incorporated into a GDE structure if required for safety or three-phase boundary management purposes without experiencing a significant performance penalty. This was not however pursued.

The interim GDL and catalyst were used to evaluate GDE optimisations and maximise catalyst utilisation. Best results were found at loadings of < 10 mg cm^{-2} as the addition of catalyst after this point led to diminishing returns. Below this threshold, most of the catalyst incorporated into the active layer is utilised and performance was proportional to catalyst loading. For the reasons just described a loading of 3-10 mg cm^{-2} was assessed to provide a balance between performance and ease of manufacture while minimising catalyst use.

Teflonated carbon paper is hydrophobic in nature and so adaptations had to be made to allow catalyst inks to adequately wet the substrate surface. The addition of a small quantity of IPA in the ink improved the wetting properties and drying times for the inks. The proportion of IPA in the ink must be less than 50% to produce effective electrodes. The optimum ratio is approximately 5:1 (H_2O: IPA). The application of the ink can have a big impact on performance. In general, applying multiple thin layers is preferable to fewer thick layers. This can be achieved by using a more dilute ink. In addition, pre-wetting the substrate surface appears to be beneficial by aiding adhesion of the initial catalyst layer.

Hot pressing the electrodes to above the glass transition temperature of the binder mobilises the PTFE creating a more hydrophobic and porous structure. This increases stability and activity by preventing flooding while increasing gas channels. In the examples tested the samples went from poorly hydrophobic to highly hydrophobicity based on contact angle measurements. Variation across the sample in terms of wetting properties greatly diminished as the PTFE was more evenly distributed. Present best practice is to heat at 180°C for 5-10 minutes with 3-5 Kg cm^2 pressure but this has yet to be fully optimised.

Although initially counterintuitive there appears to be a modest performance boost arising from active layers made using a larger particle size distribution catalyst. This is believed to be a result of the less efficient packing of the particles resulting in larger voids and increased oxygen mass transport. There may also be a benefit in terms of a reduction in the number of inter-particle interactions reducing electrical resistance. Conductivity measurements of electrodes in the future could substantiate this hypothesis.

The addition of carbon powder into the ink was shown to be electrochemically beneficial, however as carbon is known to be unstable at OER potentials the long-term stability of carbon based layers is likely to be poor. The stability can be improved by increasing the PTFE content in the active layer. However, high PTFE component active layers' lead to visible cracking of the surface during the drying process. A balance needs to be struck as too much PTFE can diminish conductivity. Carbon although not stable during the OER is not effected by the ORR. Electrodes based on carbon could therefore have an alternate application in systems which operate only under ORR conditions such as fuel cells. Initial data suggests that $NiCo_2O_4$ spinal catalyst on carbon could be used as an inexpensive alternative to platinum for such applications. Producing minimal additional overpotential at a significantly reduced cost for $\geq$ 200 mA cm^{-2} applications.

Ni powder was another active layer additive investigated showing increased stability with cycling. Moving away from carbon and towards a more stable scaffold such as Nickle powder may prove to be the key to demonstrating prolonged cycle life. Alternatively, the effect of combining carbon and nickel as a catalyst support could be investigated to combine desirable attributes. A summary of best practice for production and preparation of carbon paper based air-electrodes can be found in Table 8.1.

Table 8.1 summary of best practice for production and preparation of carbon paper based air-electrodes.

Property	Recommendation
$NiCo_2O_4$ spinel catalyst loading (carbon paper GDL)	3-10 mg cm^{-2}
Addition of a membrane to air-electrode structure	Preliminarily data so that this adds < 20 mV to ORR potential
A catalyst ink water to IPA ratio	5:1
Layers of ink applied	A greater number of thin players is preferable to fewer thick layers.
Ink dilution	More dilute
Substrate preparation	Pre-soke in water
Increasing hydrophobicity	Hotpress at 180°C for 300 s under a force of 4 kg cm^{-2}
Ni powder dispersed in the active layer	Increases stability
Catalyst particle size	Freshly ground to ≤ 20 μm particle size
Addition of an anion exchange membrane	Adds a tolerable overpotential if required to aid structurally or to act as a separator

Despite the production of workable GDE structures carbon is not a desirable air-electrode material as it is susceptible to degradation at the potentials associated with oxygen evolution. Purely metal based structures were therefore explored as a substitute. After a brief period of screening nickel and stainless steel (316L) based materials were selected as suitable alternatives to consider for gas diffusion electrode structures.

Tightly woven BMT50 stainless steel cloth was a material which required little additional wet proofing and so could be substituted directly into the carbon paper manufacture process. However, the material did not have the same oxygen transport properties of the carbon and so required alterations to create a more porous active layer. A process which had been developed concurrently with metal substrate development was dip coating electrodes in a bath of the catalyst precursors and forming the catalyst directly onto the electrode by calcination. This process was used to increase stainless steel electrode performance by a factor of six achieving an ORR activity of 134 mA cm^{-2} at - 0.5 V *vs.* Hg/HgO. A second development was that the addition of a pore former which could be extracted after GDE formation would increase porosity and therefore oxygen mass transport. 10% Na_2SO_4 was added to the active layer during production and soaked out during the dip coating process. Despite variability between samples associated with the dip coating process the j value at - 0.5 V *vs.* Hg/HgO for the sample with pore former was increased yet further over the base electrode to 215 mA cm^{-2}.

MicroGrid® nickel mesh sourced from Dexmet was also investigated as a substrate material. Due to the large pores in the material it required additional wet proofing to prevent flooding. A solution was to coat the gas face of the electrode with a layer of PTFE. Initial electrodes showed relatively little activity maxing out at 26 mA cm^{-2} similar to the unmodified stainless steel woven cloth electrodes. Due to limitations associated with the substrate material and subsequently electrode manufacture, few operational electrodes were produced using this mesh.

Nickel foams such as those supplied by Goodfellow were next explored for use in metal based air-electrodes; their 3-D structure allowed for far greater adhesion of the active layer to the substrate. The deeply porous structure required a significant quantity (> 50 mg cm^{-2}) of material to be packed into the voids of the foam to ensure adequate wet proofing. For this reason, the manufacturing process had to be altered greatly. To increase wet proofing and reduce the amount of catalyst required the foam was packed with a PTFE-bonded nickel powder layer. The $NiCo_2O_4$ spinel electrocatalyst could then be applied to this pre-formed GDL by dip coating in a nitrate solution and thermal decomposition. The loading of $NiCo_2O_4$ from the dip-coat was estimated to be ~ 3 mg cm^{-2} by weight increase, which is comparable to the carbon paper based electrodes. When evaluated using constant current potentiometry at the potential rapidly reached steady state values during both oxygen reduction and evolution. The potential window between oxygen reduction and oxygen evolution at 20 mA cm^{-2} was 620 mV. Compared to a commercial Pt/carbon fuel cell GDE the Ni foam/ $NiCo_2O_4$ spinal GDE had an additional overpotential of ~ 40 mV for oxygen reduction. During oxygen evolution, however the sample containing Pt and carbon began to degrade almost instantly, highlighting the benefit of a carbon free air-electrode structure.

A similar nickel foam electrode was cycled in the Mk I flow cell at 10 mA cm^{-2} for 24 hours with no drop in performance. The resulting potential window for the cell was 670 mV which translates into a voltage efficiently of ~ 65% which is around the threshold of system viability. The charge efficiency was considerably lower than would be expected at ~ 55%. A second nickel foam based electrode was manufactured and cycled in the Mk I flow cell at current densities of 10, 20 and 50 mA cm^{-2}. An approximately 6% drop in voltage efficiency per 10 mA cm^{-2} increase in current density was observed. The charge efficiency again was erratic and lower than anticipated. Clearly further optimisation of the zinc electrode is required however this falls outside the scope of this thesis.

Comparing the three main types of electrode (carbon paper, metal mesh/cloth and metal foam) at 20 mA cm^{-2} in the glass half-cell showed little variation for the OER. The three electrodes utilise the same catalyst with similar loadings and as the reaction is independent of oxygen mass transport electrode architecture appears to have little effect. For the ORR, however the carbon paper reaches a steady state potential at approximately – 260 mV *vs.* Hg/HgO compared to the metal electrodes at approximately - 100 mV *vs.* Hg/HgO. Although based on this comparison the carbon paper is electrochemically the weakest of the electrodes it is the simplest/cheapest to manufacture and has acceptable catalyst loadings $\leq$ 10 mg cm^{-2}. The carbon electrode is still worth considering for development and optimisation of other cell components however in terms of raw performance and stability the Ni foam is superior. Despite manufacturing and material issues for optimal performance, these are the electrodes to operate.

Table 8.2 summary of best practice for production and preparation of metal based air-electrodes.

Property	**Recommendation**
'Dip coating' thermally decomposing the catalyst directly onto the electrode surface	Allows for increased activity while minimising catalyst loading. ~3 mg cm^{-2} depending on structure
Addition of a pore former to the active layer	10% Na_2SO_4 is beneficial for increasing porosity and surface area
Weeping electrode	A PTFE coating can be applied to the gas face of the electrode to prevent wicking through the electrode structure but produces an electrically insulating surface
Foam electrode filler	Ni powder mixed with PTFE can be used to make a hydrophobic layer within the structure
Carbon paper based electrodes	Simple and rapid to manufacture. Suitable for low current density, short time scale operation or exclusively under oxygen reduction conditions.
Nickle foam based electrodes	Complex to produce/seal in cell. Display present best performance and stability.

Proof of concept electrodes have been scaled up from 1-2 cm^2 to up to 225 cm^2. Electrodes larger than these are beyond the scope of this thesis and not achievable at the University of Southampton based on current manufacturing techniques due to equipment restrictions on site.

The solubility of ZnO in < 3 M hydroxide is poor (< 0.2 M, ZnO), however, as the hydroxide concentration increases so does the ZnO solubility. Around 0.75 M ZnO is soluble in 8 M KOH at 25°C, consequently 0.5 M ZnO in 8 M KOH was selected as a sensible operating level to allow for variation over the course of cycling. 1.2 M ZnO is achievable in 8 M NaOH showing an almost two-fold increase in the ZnO solubility therefore 1 M ZnO is a reasonable operating value for NaOH.

Testing in the Mk II glass half-cell showed that running the air-electrode in zincate as opposed to pure KOH had a nominal effect on overpotential. The addition of 0.1 M increments of ZnO equated to an increase of ≤ 5 mV in air-electrode overpotential independent of current density. However, when considering the flow cell as a whole, doubling Zn concentration in the electrolyte may subtly boost voltage efficiency 1-3% independent of temperature. From all comparable data collected KOH has been shown to promote ~10% greater efficiencies in the flow cell than NaOH at 25-65° C despite the superior Zn solubility of NaOH. Part of this performance gain may simply be due to ionic conductivity in the solution.

An electrolyte temperature increase from 25°C to 65°C showed a reduction in discharge overpotential but shortened the discharge period. A probable culprit being increased self-discharge of the zinc electrode. Increasing the temperature of the electrolyte therefore increased voltage efficiency but led to a reduction in charge efficiency. To achieve the best energy efficiency a compromise between the conflicting positive and negative electrodes must be struck. Therefore, for the MK I cell set up the best compromise is the mid-point 45°C.

In most tests at $\leq$ 50 mA cm^{-2} the zinc-electrode shows no more than 250 mV difference between charge and discharge and remains consistent across cycles. The best potential gap shown by an air-electrode in the Mk I flow cell is 670 mV. Therefore, the air-electrode remains one of the key components requiring further development as it represents one of the largest contributions to inefficiency.

Electrolyte flow rate appeared to have little effect on cell cycling performance in the Mk I flow cell within the normal operating limits of the peristaltic pump used. If the flow was high enough to ensure the flux of fresh material to the electrodes there was little benefit to flowing faster. 5.0 cm^3 s^{-1} gave the highest efficiency and the most stable potentials so is the recommended rate for the cell. What appears to be crucial is balancing gas and electrolyte flow rates to maintain the three-phase boundary.

Observed charge efficiencies have been unexpectedly low possibly due to deterioration with extended use without replacement. This should be rectifiable use knowledge from the platting industry. Assuming a >90 charge efficiency had been constantly achieved 50-60% energy efficiency is comfortably attainable at $\leq$ 50 mA cm^{-2}. Lugalvan® P (BASF) was evaluated as an electrolyte additive in the Mk I flow cell for KOH and NaOH electrolytes to promote the zinc deposition/dissolution reactions. There is a noticeable improvement in terms of charge efficiency with the addition of the additive for both electrolytes. The enhancements are more dramatic for NaOH bringing the charge efficiency in line with KOH. By contrast voltage efficiency with the additive is the same or worse than without it. Overall for KOH, the addition of the additive has a detrimental effect on energy efficiency below 65°C. For NaOH electrolytes with the Zn concentration near the saturation point the additive has a negligible effect. KOH electrolytes still out perform all tested permeations of the NaOH electrolyte. Proposed best practice would therefore be to utilise KOH based electrolytes with as great a Zn content as is practicable and only consider using Lugalvan® P as an additive if the intention is to operate at ≥65°C.

Testing in the flow cell has predominantly used pure oxygen in place of air as a CO_2 scrubber was not incorporated into the system design. To assess how the system may perform on air as a source the same electrode was run firstly with laboratory air and then bottled O_2. There was a small drop in both voltage and charge efficiency associated with using air however, based on all efficiency metrics by no more than 4% in short term testing. The long-term effect is currently unknown. Additional areas of future investigation relating to the gas supply could include gas supply temperature, humidity and composition (such as O_2 enriched air).

To evaluate how performance will change dependent on depth of charge an electrode was cycled with increasing charging periods (15, 30, 60 and 120 minutes). As cycle length is increased efficiency reduces with extended charging period however only by a few percent. When the cell is discharged the potential immediately drops to around 1 V however there is approximately a 10 mV drop in discharge potential with each increase in charging period. A certain proportion of this drop may be associated with electrode degradation as all cycles were run sequentially on the same electrode. Ultimately such a small variation in discharge potential only equates to 1-2% variation in voltage efficiency.

As electrode manufacturing techniques were developed it was possible to make larger geometric area air-electrodes (>100 cm^2). To test these electrodes a larger flow cell was designed and constructed in collaboration with C-Tech Innovation (Flow cell Mk II). The cell initially cycled similarly to its predecessor. Charging at approximately 2 V and discharging at 0.9-0.7 V. The cell continued to cycle for over 24 hours however by this point charge efficiency had decreased and the discharge potential was steadily dropping. Most of these issues were likely associated with the non-ideal sealing of the cell design. Charge efficiency was initially good but deteriorated with cycling. Voltage efficiency was poor 5-10% lower than seen for similar electrodes in the Mk I cell.

The viability of turning the system into a bipolar stack was tested in a rudimentary two cell stack. The discharge voltage was observed to approximately double going from one to two cells. Showing that for the two-cell bipolar stack both cells are contributing to the voltage and there is not a prohibitively high resistance through the stack when bi polar elements are utilised.

To conclude as there was not a viable commercially available air-electrode available a novel GDE had to be produced. Carbon paper based GDEs utilising $NiCo_2O_4$ spinel as a catalyst and PTFE as a binder proved rapid to manufacture and provided reasonable performance for assessing other cell components. Carbons inherent susceptability to corrosion during the OER led to a search for an alternative. Several metal based GDEs were explored and tested however ultimately a novel fabrication method centred around a porous nickel foam showed the best performance and stability. Both electrode types were scaled up to $> 100\ \text{cm}^2$ and incorporated into proof of concept a flow cell. The laboratory-scale demonstration system was characterised using the novel air-electrodes and short-time scale cycling was demonstrated at reasonable efficiencies.

8.1 Future work

It is apparent that significant optimisation is still required to develop the gas diffusion electrode for long life cycle applications. However, structures which show minimal efficiency losses over 10s of hours of charge/discharge cycling at current densities $\leq 50\ \text{mA cm}^{-2}$ can be reproducibly manufactured. This level of performance is satisfactory for development and characterisation of a flow cell structure. Despite producing a functioning flow battery prototype many of the cell components and control systems were not fully fleshed out and with optimisation could lead to significant advancements particularly focusing on stability and life span.

Further investigation into real time electrolyte composition analysis could prove fruitful. Properties such as viscosity, conductivity and pH measured during cell operation could be used to monitor state of charge and system health. The rate of self-discharge should also be evaluated by charging a cell and then leaving it for a period of time at OCP before discharging it to see what proportion of its capacity has been lost compared to immediate discharge. The effect of cycle regime on energy efficiency should also be evaluated. To measure the effect of charging rate, depth of discharge or current density on cycle life and energy efficiency. If the system were to be paired with a renewable energy source, power generation is likely to be intermittent and so combinations of partial charge and discharge cycles should be considered.

Little evaluation of the physical structure of the air-electrode was made other than visual observation. As many of the electrode iterations produced failed in testing due to leaking, active layer delamination, poor conductivity, shorting or a manner of unknown failure mechanisms it would be of interest to take a sample which is known to be reliable and image it before and after prolonged operation or at various states of charge to observed any physical changes to the structure. This could be performed by imaging cross-sections of the electrodes using SEM. Ideally to obtain a more complete image of the electrode structure x-ray tomography could be used to penetrate deep into the structure without damaging it producing a fully three dimensional representation of the internal structure.

Appendices

Table 8.3 Published literature and conference attendance from the project

Authors	Title	Journal/event	Date
Xiaohong Li, Derek Pletcher, Andrea E. Russell, Frank C. Walsh, Richard G.A. Wills, Scott F. Gorman, Stephen W.T. Price and Stephen J. Thompson	A novel bifunctional oxygen GDE for alkaline secondary batteries	Electrochem. Comm.	25 June 2013
Stephen W.T. Price, Stephen J. Thompson, Xiaohong Li, Scott F. Gorman, Derek Pletcher, Andrea E. Russell, Frank C. Walsh, Richard G.A. Wills	The fabrication of a bifunctional oxygen electrodes without carbon components for alkaline secondary batteries	Journal of Power Sources	15 February 2014
Scott F Gorman	Development of Zinc-Air Flow Batteries for Energy Storage in Electrical Power Distribution Networks (Poster)	63rd Annual meeting of the international society of electrochemistry (Prague, 2012)	19-24 August, 2012
Scott F Gorman	Development of a Zinc-Air Flow Battery Operating with an Alkaline Electrolyte (Talk)	65th Annual meeting of the international society of electrochemistry (Lausanne, 2014)	31 August – 5 September, 2014

List of References

1. Leung, P.; Li, X.; Ponce De Leon, C.; Berlouis, L.; Low, C. T. J.; Walsh, F. C., Progress in redox flow batteries, remaining challenges and their applications in energy storage. *RSC Advances* **2012,** *2* (27), 10125-10156.
2. Yang, Z.; Zhang, J.; Kintner-Meyer, M. C. W.; Lu, X.; Choi, D.; Lemmon, J. P.; Liu, J., Electrochemical Energy Storage for Green Grid. *Chemical Reviews* **2011,** *111* (5), 3577-3613.
3. Li, Y.; Dai, H., Recent advances in zinc-air batteries. *Chemical Society Reviews* **2014,** *43* (15), 5257-5275.
4. Mears, D.; Gotschall, H.; Kamath, H. *EPRI-DOE handbook of energy storage for transmission & distribution applications*; Electric Power Research Institute: 2003.
5. Davidson, C. R.; Kissel, G.; Srinivasan, S., Electrode kinetics of the oxygen evolution reaction at $NiCo_2O_4$ from 30% KOH - dependence on temperature. *Journal of Electroanalytical Chemistry* **1982,** *132* (Jan), 129-135.
6. *Handbook of batteries*. Third Edition ed.; McGraw-Hill: 2002.
7. Borbely, A.; Molla, J., Cathode for zinc air cells. Google Patents: 1990.
8. Deane, J. P.; Ó Gallachóir, B. P.; Mckeogh, E. J., Techno-economic review of existing and new pumped hydro energy storage plant. *Renewable and Sustainable Energy Reviews* **2010,** *14* (4), 1293-1302.
9. Doughty, D. H.; Butler, P. C.; Akhil, A. A.; Clark, N. H.; Boyes, J. D., Batteries for large-scale stationary energy storage. *The Electrochemical Society Interface* **2010,** *19* (3), 49-53.
10. Perrin, M.; Saint-Drenan, Y. M.; Mattera, F.; Malbranche, P., Lead–acid batteries in stationary applications: competitors and new markets for large penetration of renewable energies. *Journal of Power Sources* **2005,** *144* (2), 402-410.
11. Hassenzahl, W. V., Superconductivity, an enabling technology for 21st century power systems? *Ieee Transactions on Applied Superconductivity* **2001,** *11* (1), 1447-1453.
12. Change, D. O. E. C., Planning our electric future: a White Paper for secure, affordable and low-carbon electricity. Change, D. O. E. C., Ed. The Stationery Office Limited: UK, 2011.
13. Chen, H.; Cong, T. N.; Yang, W.; Tan, C.; Li, Y.; Ding, Y., Progress in electrical energy storage system: A critical review. *Progress in Natural Science* **2009,** *19* (3), 291-312.

14. Kong, F., Synthesis of rod and beadlike Co_3O_4 and bi-functional properties as air/oxygen electrode materials. *Electrochimica Acta* **2012,** *68* (0), 198-201.

15. Halls, J. E.; Hawthornthwaite, A.; Hepworth, R. J.; Roberts, N. A.; Wright, K. J.; Zhou, Y.; Haswell, S. J.; Haywood, S. K.; Kelly, S. M.; Lawrence, N. S.; Wadhawan, J. D., Empowering the smart grid: can redox batteries be matched to renewable energy systems for energy storage? *Energy & Environmental Science* **2013,** *6* (3), 1026-1041.

16. Dunn, B.; Kamath, H.; Tarascon, J.-M., Electrical energy storage for the grid: A battery of choices. *Science* **2011,** *334* (6058), 928-935.

17. Secours, C.; Essiembre, S.; Marsan, B.; Celis, J. P., Electrodeposition of Ni and spinel oxide particles for the oxygen evolution reaction in alkaline medium. In *New Materials for Electrochemical Systems IV. Extended Abstracts of the Fourth International Symposium on New Materials for Electrochemical Systems*, 2001.

18. Li, X.; Pletcher, D.; Russell, A. E.; Walsh, F. C.; Wills, R. G. A.; Gorman, S. F.; Price, S. W. T.; Thompson, S. J., A novel bifunctional oxygen GDE for alkaline secondary batteries. *Electrochemistry Communications* **2013,** *34* (0), 228-230.

19. Chakrabarti, M. H.; Hajimolana, S. A.; Mjalli, F. S.; Saleem, M.; Mustafa, I., Redox flow battery for energy storage. *Arabian Journal for Science and Engineering* **2013,** *38* (4), 723-739.

20. Lan, C. J.; Chin, T. S.; Lin, P. H.; Perng, T. P., Zn-Al alloy as a new anode-metal of a zinc-air battery. *Journal of New Materials for Electrochemical Systems* **2006,** *9* (1), 27-32.

21. Neburchilov, V.; Wang, H. J.; Martin, J. J.; Qu, W., A review on air cathodes for zinc-air fuel cells. *Journal of Power Sources* **2010,** *195* (5), 1271-1291.

22. Cifrain, M.; Kordesch, K. V., Advances, aging mechanism and lifetime in AFCs with circulating electrolytes. *Journal of Power Sources* **2004,** *127* (1-2), 234-242.

23. Shevchenko, V. V.; Gumennaya, M. A., Synthesis and properties of anion-exchange membranes for fuel cells. *Theoretical and Experimental Chemistry* **2010,** *46* (3), 139-152.

24. Leung, P. K.; Ponce De Leon, C.; Walsh, F. C., An undivided zinc–cerium redox flow battery operating at room temperature (295 K). *Electrochemistry Communications* **2011,** *13* (8), 770-773.

25. Maja, M.; Orecchia, C.; Strano, M.; Tosco, P.; Vanni, M., Effect of structure of the electrical performance of gas diffusion electrodes for metal air batteries. *Electrochimica Acta* **2000,** *46* (2-3), 423-432.

26. Jiratchayamaethasakul, C.; Srijaroenpramong, N.; Bunyangyuen, T.; Arpavate, W.; Wongyao, N.; Therdthianwong, A.; Therdthianwong, S., Effects of anode orientation and flow channel design on performance of refuelable zinc-air fuel cells. *Journal of Applied Electrochemistry* **2014,** *44* (11), 1205-1218.
27. Sapkota, P.; Kim, H., Zinc-air fuel cell, a potential candidate for alternative energy. *Journal of Industrial and Engineering Chemistry* **2009,** *15* (4), 445-450.
28. Gulzow, E.; Kaz, T.; Reissner, R.; Sander, H.; Schilling, L.; Von Bradke, M., Study of membrane electrode assemblies for direct methanol fuel cells. *Journal of Power Sources* **2002,** *105* (2), 261-266.
29. Witherspoon, R. R., A mechanically rechargeable 1-KW zinc-air battery. SAE International: 1969; 10.4271/690204.
30. Goldstein, J. R.; Koretz, B., Tests of a full-sized mechanically rechargeable zinc-air battery in an electric vehicle. *IEEE Aerospace and Electronic Systems Magazine* 1993, pp 34 - 38.
31. De Geeter, E.; Mangan, M.; Spaepen, S.; Stinissen, W.; Vennekens, G., Alkaline fuel cells for road traction. *Journal of Power Sources* **1999,** *80* (1-2), 207-212.
32. Lee, S. M.; Kim, Y. J.; Eom, S. W.; Choi, N. S.; Kim, K. W.; Cho, S. B., Improvement in self-discharge of Zn anode by applying surface modification for Zn–air batteries with high energy density. *Journal of Power Sources* **2013,** *227*, 177-184.
33. Wang, W.; Luo, Q.; Li, B.; Wei, X.; Li, L.; Yang, Z., Recent progress in redox flow battery research and development. *Advanced Functional Materials* **2013,** *23* (8), 970-986.
34. Lund, H.; Mathiesen, B. V., Energy system analysis of 100% renewable energy systems-The case of Denmark in years 2030 and 2050. *Energy* **2009,** *34* (5), 524-531.
35. Heise, G. W. Air-depolarized primary battery. 28 Feb 1933, 1933.
36. Bacon, F. T., Fuel cells, past, present and future. *Electrochimica Acta* **1969,** *14*, 569-585.
37. Kubo, D.; Tadanaga, K.; Hayashi, A.; Tatsumisago, M., Multifunctional inorganic electrode materials for high-performance rechargeable metal–air batteries. *Journal of Materials Chemistry A* **2013,** *1* (23), 6804.
38. Hilder, M.; Winther-Jensen, B.; Clark, N. B., The effect of binder and electrolyte on the performance of thin zinc-air battery. *Electrochimica Acta* **2012,** *69*, 308-314.

39. Caramia, V.; Bozzini, B., Materials science aspects of zinc–air batteries: A review. *Materials for Renewable and Sustainable Energy* **2014,** *3* (2), 28.

40. Li, Y.; Gong, M.; Liang, Y.; Feng, J.; Kim, J.-E.; Wang, H.; Hong, G.; Zhang, B.; Dai, H., Advanced zinc-air batteries based on high-performance hybrid electrocatalysts. *Nature Communications* **2013,** *4*, 1805.

41. Borbely, A.; Molla, J. Cathode for zinc air cells. US Patent 4894296, 1990.

42. Chi, B.; Li, J. B.; Han, Y. S.; Chen, Y. J., Effect of temperature on the preparation and electrocatalytic properties of a spinel $NiCo_2O_4$/Ni electrode. *International Journal of Hydrogen Energy* **2004,** *29* (6), 605-610.

43. Gouérec, P.; Poletto, L.; Denizot, J.; Sanchez-Cortezon, E.; Miners, J. H., The evolution of the performance of alkaline fuel cells with circulating electrolyte. *Journal of Power Sources* **2004,** *129* (2), 193-204.

44. Bockris, J. O.; Minevski, Z. S., ELECTROCATALYSIS - PAST, PRESENT AND FUTURE. *Electrochimica Acta* **1994,** *39* (11-12), 1471-1479.

45. Suntivich, J.; Gasteiger, H. A.; Yabuuchi, N.; Nakanishi, H.; Goodenough, J. B.; Shao-Horn, Y., Design principles for oxygen-reduction activity on perovskite oxide catalysts for fuel cells and metal-air batteries. *Nat. Chem.* **2011,** *3* (7), 546-550.

46. Arlt, T.; Schroder, D.; Krewer, U.; Manke, I., In operando monitoring of the state of charge and species distribution in zinc air batteries using X-ray tomography and model-based simulations. *Physical chemistry chemical physics : PCCP* **2014,** *16* (40), 22273-22280.

47. Ang, L. M.; Hor, T. S. A.; Xu, G. Q.; Tung, C. H.; Zhao, S. P.; Wang, J. L. S., Decoration of activated carbon nanotubes with copper and nickel. *Carbon* **2000,** *38* (3), 363-372.

48. Gregory Zhang, X., *Corrosion and Electrochemistry of Zinc*. 1996.

49. Ramesh Bapu, G. N. K.; Devaraj, G.; Ayyapparaj, J., Studies on non-cyanide alkaline zinc electrolytes. *Journal of Solid State Electrochemistry* **1998,** *3* (1), 48-51.

50. Kavitha, B.; Santhosh, P.; Renukadevi, M.; Kalpana, A.; Shakkthivel, P.; Vasudevan, T., Role of organic additives on zinc plating. *Surface and Coatings Technology* **2006,** *201* (6), 3438-3442.

51. Naik, Y. A.; Venkatesha, T. V., A new condensation product for zinc plating from non-cyanide alkaline bath. *Bulletin of Materials Science* **2005,** *28* (5), 495-501.

52. Pereira, M. S.; Barbosa, L. L.; Souza, C. a. C.; De Moraes, A. C. M.; Carlos, I. A., The influence of sorbitol on zinc film deposition, zinc dissolution

processand morphology of deposits obtained from alkaline bath. *Journal of Applied Electrochemistry* **2006,** *36* (6), 727-732.

53. Lee, C. W.; Eom, S. W.; Sathiyanarayanan, K.; Yun, M. S., Preliminary comparative studies of zinc and zinc oxide electrodes on corrosion reaction and reversible reaction for zinc/air fuel cells. *Electrochimica Acta* **2006,** *52* (4), 1588-1591.
54. Lee, C. W.; Sathiyanarayanan, K.; Eom, S. W.; Kim, H. S.; Yun, M. S., Novel electrochemical behavior of zinc anodes in zinc/air batteries in the presence of additives. *Journal of Power Sources* **2006,** *159* (2), 1474-1477.
55. Lee, C. W.; Sathiyanarayanan, K.; Eom, S. W.; Kim, H. S.; Yun, M. S., Effect of additives on the electrochemical behaviour of zinc anodes for zinc/air fuel cells. *Journal of Power Sources* **2006,** *160* (1), 161-164.
56. Pan, J.; Ji, L.; Sun, Y.; Wan, P.; Cheng, J.; Yang, Y.; Fan, M., Preliminary study of alkaline single flowing Zn-O-2 battery. *Electrochemistry Communications* **2009,** *11* (11), 2191-2194.
57. Hamann, C. H.; Hamnett, A.; Vielstich, W., *Electrochemistry*. Wiley-VCH: Weinheim, 1998.
58. Jörissen, L., Bifunctional oxygen/air electrodes. *Journal of Power Sources* **2006,** *155* (1), 23-32.
59. Mclean, G. F.; Niet, T.; Prince-Richard, S.; Djilali, N., An assessment of alkaline fuel cell technology. *International Journal of Hydrogen Energy* **2002,** *27* (5), 507-526.
60. Bidault, F.; Brett, D. J. L.; Middleton, P. H.; Brandon, N. P., Review of gas diffusion cathodes for alkaline fuel cells. *Journal of Power Sources* **2009,** *187* (1), 39-48.
61. Gülzow, E., Alkaline fuel cells: a critical view. *Journal of Power Sources* **1996,** *61* (1–2), 99-104.
62. Laudse, R. A.; Kolb, E. D., The solubility of zincite in basic hydrothermal solvents. *The American Mineralogist* **1963,** *48*, 642-648.
63. Rolla, A.; Sadkowski, A.; Wild, J.; Zóltowski, P., On the problem of ageing of carbon—air electrodes in alkaline electrolytes. *Journal of Power Sources* **1980,** *5* (2), 189-196.
64. Bertolotti, B.; Chikh, L.; Vancaeyzeele, C.; Alfonsi, S.; Fichet, O., Assemblies of protective anion exchange membrane on air electrode for its efficient operation in aqueous alkaline electrolyte. *Journal of Power Sources* **2015,** *274* (0), 636-644.

65. Yang, C. C., Preparation and characterization of electrochemical properties of air cathode electrode. *International Journal of Hydrogen Energy* **2004,** *29* (2), 135–143.

66. Acres, G. J. K.; Frost, J. C.; Hards, G. A.; Potter, R. J.; Ralph, T. R.; Thompsett, D.; Burstein, G. T.; Hutchings, G. J., Electrocatalysts for fuel cells. *Catalysis Today* **1997,** *38* (4), 393-400.

67. Martin, J. J.; Neburchilov, V.; Wang, H.; Qu, W., Air cathodes for metal-air batteries and fuel cells. *2009 IEEE Electrical Power & Energy Conference (EPEC 2009)* **2009,** 10.1109/epec.2009.5420955.

68. Bender, S. F.; Cretzmeyer, J. W.; Reise, T. F., *Handbook of batteries and fuel cells*. McGraw-Hill: New York, 1995.

69. Dey, A. N., Primary Li/$SOCl_2$ cells VIII. Effect of type of carbon on the performance. *Journal of the Electrochemical Society* **1979,** *126* (12), 2052-2056.

70. Kivisaari, J.; Lamminen, J.; Lampinen, M. J.; Viitanen, M., Preparation and measurement of air electrodes for alkaline fuel cells. *Journal of Power Sources* **1990,** *32* (3), 233-241.

71. Ross, P. N.; Sattler, M., The corrosion of carbon black anodes in alkaline electrolyte III. The effect of graphitization on the corrosion resistance of furnace blacks. *Journal of the Electrochemical Society* **1988,** *135* (6), 1464-1470.

72. Watanabe, M.; Tomikawa, M.; Motoo, S., Experimental analysis of the reaction layer structure in a gas diffusion electrode. *Journal of Electroanalytical Chemistry and Interfacial Electrochemistry* **1985,** *195* (1), 81-93.

73. Hacker, V.; Wallnofer, E.; Baumgartner, W.; Schaffer, T.; Besenhard, J. O.; Schrottner, H.; Schmied, M., Carbon nanofiber-based active layers for fuel cell cathodes - preparation and characterization. *Electrochemistry Communications* **2005,** *7* (4), 377-382.

74. Clarke, R. L.; Harnsberger, S. K., New electrically conductive ceramic - a fundamental advance in electrode technology. *American Laboratory* **1988,** *20* (6A), 8-10.

75. Gusev, A. A.; Avvakumov, E. G.; Medvedev, A. Z.; Masliy, A. I., Ceramic electrodes based on magneli phases of titanium oxides. *Science of Sintering* **2007,** *39* (1), 51-57.

76. Wu, C.-Y.; Wu, P.-W.; Lin, P.; Li, Y.-Y.; Lin, Y.-M., Silver-carbon nanocapsule electrocatalyst for oxygen reduction reaction. *Journal of the Electrochemical Society* **2007,** *154* (10), B1059-B1062.

77. Yu, P. T.; Gu, W.; Makharia, R.; Wagner, F. T.; Gasteiger, H. A., The impact of carbon stability on PEM fuel cell startup and shutdown voltage degradation. *ECS Transactions* **2006,** *3* (1), 797-809.

78. Wenzhen, L.; Changhai, L.; Jieshan, Q.; Weijiang, Z.; Hongmei, H.; Zhaobin, W.; Gongquan, S.; Qin, X., Carbon nanotubes as support for cathode catalyst of a direct methanol fuel cell. *Carbon* **2002,** *40* (5), 787–803.

79. Mathias, M. F.; Makharia, R.; Gasteiger, H. A.; Conley, J. J.; Fuller, T. J.; Gittleman, C. J.; Kocha, S. S.; Miller, D. P.; Mittelsteadt, C. K.; Tao, X.; Yan, S. G.; Yu, P. T., Two fuel cell cars in every garage? *Electrochemical Society Interface* **2005,** *14* (3), 24-35.

80. Tang, H.; Qi, Z.; Ramani, M.; Elter, J. F., PEM fuel cell cathode carbon corrosion due to the formation of air/fuel boundary at the anode. *Journal of Power Sources* **2006,** *158* (2), 1306-1312.

81. Meyers, J. P.; Darling, R. M., Model of carbon corrosion in PEM fuel cells. *Journal of the Electrochemical Society* **2006,** *153* (8), A1432-A1442.

82. Ndzebet, E. Manganese oxide based electrode for alkaline electrochemical system and method of its production. U.S. Patent 6780347, **2004**.

83. Koshiba, N.; Hayakawa, H.; Momose, K.; Ohta, A. Air cell electrode and process for preparing its cataylist. U.S. Patent 4595643, **1986**.

84. Wang, X.; Li, W. Z.; Chen, Z. W.; Waje, M.; Yan, Y. S., Durability investigation of carbon nanotube as catalyst support for proton exchange membrane fuel cell. *Journal of Power Sources* **2006,** *158* (1), 154-159.

85. Golovin, N. Manganese-based oxygen reduction catalyst, metal-air electrode including said catalyst and methods for making the same. U.S. 6444609 B1, 3 sep 2002, 2002.

86. Sun, X.; Li, R.; Villers, D.; Dodelet, J. P.; Desilets, S., Composite electrodes made of Pt nanoparticles deposited on carbon nanotubes grown on fuel cell backings. *Chemical Physics Letters* **2003,** *379* (1-2), 99-104.

87. Li, W. Z.; Liang, C. H.; Zhou, W. J.; Qiu, J. S.; Zhou, Z. H.; Sun, G. Q.; Xin, Q., Preparation and characterization of multiwalled carbon nanotube-supported platinum for cathode catalysts of direct methanol fuel cells. *J. Phys. Chem. B* **2003,** *107* (26), 6292-6299.

88. Steigerwalt, E. S.; Deluga, G. A.; Lukehart, C. M., Pt-Ru/carbon fiber nanocomposites: Synthesis, characterization, and performance as anode catalysts of direct methanol fuel cells. A search for exceptional performance. *J. Phys. Chem. B* **2002,** *106* (4), 760-766.

89. Bessel, C. A.; Laubernds, K.; Rodriguez, N. M.; Baker, R. T. K., Graphite nanofibers as an electrode for fuel cell applications. *J. Phys. Chem. B* **2001,** *105* (6), 1115-1118.

90. Steigerwalt, E. S.; Deluga, G. A.; Cliffel, D. E.; Lukehart, C. M., A Pt-Ru/graphitic carbon nanofiber nanocomposite exhibiting high relative performance as a direct-methanol fuel cell anode catalyst. *J. Phys. Chem. B* **2001,** *105* (34), 8097-8101.

91. Kohler, D.; Zabasajja, J.; Rose, F.; Tatarchuk, B. J., Metal-carbon composite electrodes from fiber precursors. *Journal of the Electrochemical Society* **1990,** *137* (6), 1750-1757.

92. Tatarchuk, B. J.; Rose, M. F.; Krishnagopalan, A. Preparation of mixed fiber composite structures U.S. Patent 5304330, **1994**.

93. Ahn, S.; Tatarchuk, B. J., Air electrode: Identification of intraelectrode rate phenomena via AC impedance. *Journal of the Electrochemical Society* **1995,** *142* (12), 4169-4175.

94. Ahn, S.; Tatarchuk, B. J., *COMPOSITE ELECTRODE STRUCTURES FOR FUEL-CELL APPLICATIONS*. 1990; p 287-292.

95. Ahn, S.; Tatarchuk, B. J., Fibrous metal-carbon composite structures as gas diffusion electrodes for use in alkaline electrolyte. *Journal of Applied Electrochemistry* **1997,** *27* (1), 9-17.

96. Tatarchuk, B. J.; Rose, M. F.; Krishnagopalan, G. A.; Zabasajja, J. N.; Kohler, D. A. Preparation of mixed fibre composite structures. U.S. Patent 5304330, 1994.

97. Gao, X. P.; Lan, Y.; Pan, G. L.; Wu, F.; Qu, J. Q.; Song, D. Y.; Shen, P. W., Electrochemical hydrogen storage by carbon nanotubes decorated with metallic nickel. *Electrochemical and Solid State Letters* **2001,** *4* (10), A173-A175.

98. Ioroi, T.; Siroma, Z.; Fujiwara, N.; Yamazaki, S.; Yasuda, K., Sub-stoichiometric titanium oxide-supported platinum electrocatalyst for polymer electrolyte fuel cells. *Electrochemistry Communications* **2005,** *7* (2), 183-188.

99. Walsh, F. C.; Wills, R. G. A., The continuing development of Magnéli phase titanium sub-oxides and Ebonex® electrodes. *Electrochimica Acta* **2010,** *55* (22), 6342-6351.

100. Chen, G. Y.; Bare, S. R.; Mallouk, T. E., Development of supported bifunctional electrocatalysts for unitized regenerative fuel cells. *Journal of the Electrochemical Society* **2002,** *149* (8), A1092-A1099.

101. Garci´A, B. L.; Fuentes, R.; Weidner, J. W., Low-temperature synthesis of a PtRu/$Nb_{0.1}Ti_{0.9}O_2$ electrocatalyst for methanol oxidation. *Electrochemical and Solid State Letters* **2007,** *10* (7), B108-B110.
102. Chhina, H.; Campbell, S.; Kesler, O., An oxidation-resistant indium tin oxide catalyst support for proton exchange membrane fuel cells. *Journal of Power Sources* **2006,** *161* (2), 893-900.
103. Suzuki, Y.; Ishihara, A.; Mitsushima, S.; Kamiya, N.; Ota, K. I., Sulfated-zirconia as a support of Pt catalyst for polymer electrolyte fuel cells. *Electrochemical and Solid State Letters* **2007,** *10* (7), B105-B107.
104. Ioroi, T.; Senoh, H.; Yamazaki, S. I.; Siroma, Z.; Fujiwara, N.; Yasuda, K., Stability of corrosion-resistant magneli-phase Ti4O7-supported PEMFC catalysts at high potentials. *Journal of the Electrochemical Society* **2008,** *155* (4), B321-B326.
105. Ellis, K.; Hill, A.; Hill, J.; Loyns, A.; Partington, T., The performance of Ebonex® electrodes in bipolar lead-acid batteries. *Journal of Power Sources* **2004,** *136* (2), 366-371.
106. Ellis, K. Manufacturing method. U.S. Patent 0,231,938A1 2007.
107. Bartholomew, R. F.; Frankl, D. R., Electrical properties of some titanium oxides. *Phys. Rev.* **1969,** *187* (3), 828-832.
108. Kao, W. H.; Patel, P.; Haberichter, S. L., Formation enhancement of a lead/acid battery positive plate by barium metaplumbate and Ebonex®. *Journal of the Electrochemical Society* **1997,** *144* (6), 1907-1911.
109. Graves, J. E.; Pletcher, D.; Clarke, R. L.; Walsh, F. C., The electrochemistry of magneli phase titanium-oxide ceramic electrodes - Part I. the deposition and properties of metal coatings. *Journal of Applied Electrochemistry* **1991,** *21* (10), 848-857.
110. Smith, J. R.; Walsh, F. C.; Clarke, R. L., Electrodes based on Magneli phase titanium oxides: the properties and applications of Ebonex® materials. *Journal of Applied Electrochemistry* **1998,** *28* (10), 1021-1033.
111. Vračar, L. M.; Krstajić, N. V.; Radmilović, V. R.; Jakšić, M. M., Electrocatalysis by nanoparticles – oxygen reduction on Ebonex/Pt electrode. *Journal of Electroanalytical Chemistry* **2006,** *587* (1), 99-107.
112. Vracar, L. M.; Gojkovic, S. L.; Elezovic, N. R.; Radmilovic, V. R.; Jaksic, M. M.; Krstajic, N. V., Magneli phase titanium oxides as catalyst support - Electrochemical behavior of Ebonex/Pt catalysts. *Journal of New Materials for Electrochemical Systems* **2006,** *9* (2), 99-106.

113. Slavcheva, E.; Nikolova, V.; Petkova, T.; Lefterova, E.; Dragieva, I.; Vitanov, T.; Budevski, E., Electrocatalytic activity of Pt and PtCo deposited on Ebonex by BH reduction. *Electrochimica Acta* **2005,** *50* (27), 5444-5448.
114. Bavykin, D. V.; Walsh, F. C., Elongated titanate nanostructures and their applications. *European Journal of Inorganic Chemistry* **2009,** 10.1002/ejic.200801122 (8), 977-997.
115. Friesen, C. A.; Friesen, G.; Krishnan, R.; Trimble, T. Electrochemical cell with diffuser. US 2011/0189551 A1, 2011.
116. Kraft, A., Doped diamond: a compact review on a new, versatile electrode material. *International Journal of Electrochemical Science* **2007,** *2* (5), 355-385.
117. Peckova, K.; Musilova, J.; Barek, J., Boron-doped diamond film electrodes-new tool for voltammetric determination of organic substances. *Critical Reviews in Analytical Chemistry* **2009,** *39* (3), 148-172.
118. Suryanarayanan, V.; Noel, M., A comparative evaluation on the voltammetric behavior of boron-doped diamond (BDD) and glassy carbon (GC) electrodes in different electrolyte media. *Journal of Electroanalytical Chemistry* **2010,** *642* (1), 69-74.
119. Szunerits, S.; Boukherroub, R., Investigation of the electrocatalytic activity of boron-doped diamond electrodes modified with palladium or gold nanoparticles for oxygen reduction reaction in basic medium. *Comptes Rendus Chimie* **2008,** *11* (9), 1004-1009.
120. El Roustom, B.; Sine, G.; Foti, G.; Comninellis, C., A novel method for the preparation of bi-metallic (Pt-Au) nanoparticles on boron doped diamond (BDD) substrate: application to the oxygen reduction reaction. *Journal of Applied Electrochemistry* **2007,** *37* (11), 1227-1236.
121. Nikolova, V.; Iliev, P.; Petrov, K.; Vitanov, T.; Zhecheva, E.; Stoyanova, R.; Valov, I.; Stoychev, D., Electrocatalysts for bifunctional oxygen/air electrodes. *Journal of Power Sources* **2008,** *185* (2), 727-733.
122. Lu, Y.-C.; Xu, Z.; Gasteiger, H. A.; Chen, S.; Hamad-Schifferli, K.; Shao-Horn, Y., Platinum-gold nanoparticles: A highly active bifunctional electrocatalyst for rechargeable lithium-air batteries. *Journal of the American Chemical Society* **2010,** *132* (35), 12170-12171.
123. Hu, W.-K.; Noreus, D., Lab-size rechargeable metal hydride-air cells. *Journal of Power Sources* **2010,** *195* (17), 5810-5813.
124. Lee, H. K.; Shim, J. P.; Shim, M. J.; Kim, S. W.; Lee, J. S., Oxygen reduction behavior with silver alloy catalyst in alkaline media. *Materials Chemistry and Physics* **1996,** *45* (3), 238-242.

125. Matsuki, K.; Kamada, H., Oxygen reduction electrocatalysis on some manganese oxides. *Electrochimica Acta* **1986,** *31* (1), 13-18.

126. Roche, I.; Chainet, E.; Vondrak, J.; Chatenet, M., Durability of carbon-supported manganese oxide nanoparticles for the oxygen reduction reaction (ORR) in alkaline medium. *Journal of Applied Electrochemistry* **2008,** *38* (9), 1195-1201.

127. Reddy, R. N.; Reddy, R. G., Synthesis and electrochemical characterization of amorphous MnO_2 electrochemical capacitor electrode material. *Journal of Power Sources* **2004,** *132* (1-2), 315-320.

128. Zhu, T.; Liu, Y.; Hu, Z.; Wang, C.; Wen, Z., Preparation and characterization of mesoporous Co_3O_4 electrode material. *Journal of Materials Science-Materials in Electronics* **2011,** *22* (11), 1649-1655.

129. Soares, C. O.; Carvalho, M. D.; Melo Jorge, M. E.; Gomes, A.; Silva, R. A.; Rangel, C. M.; Da Silva Pereira, M. I., High surface area $LaNiO_3$ electrodes for oxygen electrocatalysis in alkaline media. *Journal of Applied Electrochemistry* **2012,** *42* (5), 325-332.

130. Burchardt, T.; Ngamga, R. F. Charging method for metal-air battery involves applying pulse charge to metal-air battery, and returning to charging metal-air battery using charge profile after pulse charge has been applied. US2011199054-A1; WO2011098916-A2; WO2011098916-A3.

131. Burchardt, T.; Ngamga, R. F. Methods for charging metal-air cells. US 2011/0199054 A1, Aug. 18, 2011, 2011.

132. Appleby, A. J.; Yeager, E. B., Solid polymer electrolyte fuel cells (SPEFCs). *Energy* **1986,** *11* (1-2).

133. Bidault, F.; Kucernak, A., Cathode development for alkaline fuel cells based on a porous silver membrane. *Journal of Power Sources* **2011,** *196* (11), 4950-4956.

134. Zhang, H.; Meng, H.; Sun, D.; Yu, H., An energy-saving method of electrolysis preparation for emd using oxygen reduction electrode. **2012**.

135. Ji, M. B.; Wei, Z. D.; Chen, S. G.; Zhang, Q.; Wang, Y. Q.; Qi, X. Q.; Li, A. L., A more flooding-tolerant oxygen electrode in alkaline electrolyte. *Fuel Cells* **2010,** *10* (2), 289-298.

136. Merle, G.; Wessling, M.; Nijmeijer, K., Anion exchange membranes for alkaline fuel cells: A review. *Journal of Membrane Science* **2011,** *377* (1-2), 1-35.

137. Wilson, M. S.; Gottesfeld, S., Thin-film catalyst layers for polymer electrolyte fuel-cell electrodes. *Journal of Applied Electrochemistry* **1992,** *22* (1), 1-7.

138. Taylor, P.; Bolton, R.; Stone, D.; Zhang, X.-P.; Martin, C.; Upham, P. *Pathways for Energy Storage in the UK*; 27/03/2012, 2012.
139. Fowkes, F. M., *Contact Angle, Wettability, and Adhesion*. AMERICAN CHEMICAL SOCIETY: 1964; Vol. 43, p 404.
140. Yuan, Y.; Lee, T. R., Contact Angle and Wetting Properties. In *Surface Science Techniques*, Bracco, G.; Holst, B., Eds. Springer Berlin Heidelberg: Berlin, Heidelberg, 2013; 10.1007/978-3-642-34243-1_1pp 3-34.
141. Yuan, Y.; Randall Lee, T., *Surface Science Techniques*. 2013; Vol. 51.
142. Friess, B. R.; Hoorfar, M., Development of a novel radial cathode flow field for PEMFC. *International Journal of Hydrogen Energy* **2012,** *37* (9), 7719-7729.
143. Wang, J.; Wang, H., Discrete approach for flow field designs of parallel channel configurations in fuel cells. *International Journal of Hydrogen Energy* **2012,** *37* (14), 10881-10897.
144. Tsai, B.-T.; Tseng, C.-J.; Liu, Z.-S.; Wang, C.-H.; Lee, C.-I.; Yang, C.-C.; Lo, S.-K., Effects of flow field design on the performance of a PEM fuel cell with metal foam as the flow distributor. *International Journal of Hydrogen Energy* **2012,** *37* (17), 13060-13066.
145. Jyothi Latha, T.; Jayanti, S., Ex-situ experimental studies on serpentine flow field design for redox flow battery systems. *Journal of Power Sources* **2014,** *248* (0), 140-146.
146. Chen, K.; Li, X., Accurate determination of battery discharge characteristics – a comparison between two battery temperature control methods. *Journal of Power Sources* **2014,** *247*, 961-966.
147. http://www.gaskatel.de/eng/produkte/biplex/eng_biplex_index.html. http://www.gaskatel.de/eng/produkte/biplex/eng_biplex_index.html.
148. Cai, X.; Lai, L.; Lin, J.; Shen, Z., Recent advances in air electrodes for Zn-air batteries: electrocatalysis and structural design. *Materials Horizons* **2017,** 10.1039/C7MH00358G.
149. Johnston, H. L.; Cuta, F.; Garrett, A. B., The Solubility of Silver Oxide in Water, in Alkali and in Alkaline Salt Solutions. The Amphoteric Character of Silver Hydroxide. *Journal of the American Chemical Society* **1933,** *55* (6), 2311-2325.
150. Goh, F. W. T.; Liu, Z.; Ge, X.; Zong, Y.; Du, G.; Hor, T. S. A., Ag nanoparticle-modified MnO_2 nanorods catalyst for use as an air electrode in zinc–air battery. *Electrochimica Acta* **2013,** *114* (0), 598-604.
151. Qi, Z.; Kaufman, A., Low Pt loading high performance cathodes for PEM fuel cells. *Journal of Power Sources* **2003,** *113* (1), 37-43.

152. Ralph, T. R.; Hards, G. A.; Keating, J. E.; Campbell, S. A.; Wilkinson, D. P.; Davis, M.; St - Pierre, J.; Johnson, M. C., Low Cost Electrodes for Proton Exchange Membrane Fuel Cells: Performance in Single Cells and Ballard Stacks. *Journal of The Electrochemical Society* **1997,** *144* (11), 3845-3857.

153. Cohn, G.; Starosvetsky, D.; Hagiwara, R.; Macdonald, D. D.; Ein-Eli, Y., Silicon–air batteries. *Electrochemistry Communications* **2009,** *11* (10), 1916-1918.

154. Neburchilov, V.; Wang, H.; Martin, J. J.; Qu, W., A review on air cathodes for zinc–air fuel cells. *Journal of Power Sources* **2010,** *195* (5), 1271-1291.

155. Chen, Z.; Yu, A.; Ahmed, R.; Wang, H.; Li, H.; Chen, Z., Manganese dioxide nanotube and nitrogen-doped carbon nanotube based composite bifunctional catalyst for rechargeable zinc-air battery. *Electrochimica Acta* **2012,** *69*, 295-300.

156. Arico, A. S.; Srinivasan, S.; Antonucci, V., DMFCs: From Fundamental Aspects to Technology Development. *Fuel Cells* **2001,** *1* (2), 133-161.

157. Andersen, S. M.; Dhiman, R.; Larsen, M. J.; Skou, E., Importance of electrode hot-pressing conditions for the catalyst performance of proton exchange membrane fuel cells. *Applied Catalysis B: Environmental* **2015,** *172–173*, 82-90.

158. Litster, S.; Mclean, G., PEM fuel cell electrodes. *Journal of Power Sources* **2004,** *130* (1–2), 61-76.

159. Schmidt, T. J.; Gasteiger, H. A.; Stäb, G. D.; Urban, P. M.; Kolb, D. M.; Behm, R. J., Characterization of High - Surface - Area Electrocatalysts Using a Rotating Disk Electrode Configuration. *Journal of The Electrochemical Society* **1998,** *145* (7), 2354-2358.

160. Zhu, W. H.; Poole, B. A.; Cahela, D. R.; Tatarchuk, B. J., New structures of thin air cathodes for zinc–air batteries. *Journal of Applied Electrochemistry* **2003,** *33* (1), 29-36.

161. Brooker, R. P.; Rodgers, M. P.; Bonville, L. J.; Kunz, H. R.; Slattery, D. K.; Fenton, J. M., Effect of Spray Parameters on Electrode Surface and Performance. *ECS Transactions* **2010,** *28* (27), 51-59.

162. Chakkaravarthy, C.; Waheed, A. K. A.; Udupa, H. V. K., Zinc—air alkaline batteries — A review. *Journal of Power Sources* **1981,** *6* (3), 203-228.

163. Lee, S.-M.; Kim, Y.-J.; Eom, S.-W.; Choi, N.-S.; Kim, K.-W.; Cho, S.-B., Improvement in self-discharge of Zn anode by applying surface modification for Zn–air batteries with high energy density. *Journal of Power Sources* **2013,** *227*, 177-184.

164. Beverskog, B.; Puigdomenech, I., Revised pourbaix diagrams for zinc at 25–300 ° C. *Corrosion Science* **1997,** *39* (1), 107-114.

165. Miles, M. H.; Kissel, G.; Lu, P. W. T.; Srinivasan, S., Effect of Temperature on Electrode Kinetic Parameters for Hydrogen and Oxygen Evolution Reactions on Nickel Electrodes in Alkaline Solutions. *Journal of The Electrochemical Society* **1976,** *123* (3), 332-336.

166. Wong, W. Y.; Daud, W. R. W.; Mohamad, A. B.; Loh, K. S., Effect of temperature on the oxygen reduction reaction kinetic at nitrogen-doped carbon nanotubes for fuel cell cathode. *International Journal of Hydrogen Energy* **2015,** *40* (35), 11444-11450.

167. Mohamed, M. R.; Leung, P. K.; Sulaiman, M. H., Performance characterization of a vanadium redox flow battery at different operating parameters under a standardized test-bed system. *Applied Energy* **2015,** *137*, 402-412.

168. Goldstein, J. R.; Harats, Y.; Sharon, Y.; Naimer, N., Scrubber system for removing carbon dioxide from a metal-air or fuel cell battery. Google Patents: 1997.